10-1-2011

Event horizons, gravitational waves and astrophysical kicks in black-hole spacetimes

J. Marcelo Ponce Castro

Event Horizons, Gravitational Waves and Astrophysical Kicks in Black-Hole Spacetimes

---

Ph.D. *Doctor of Philosophy*

in Astrophysical Sciences and Technology

M.Sc. *Marcelo Ponce C.*

Rochester Institute of Technology

Rochester, New York

October 2011

ASTROPHYSICAL SCIENCES AND TECHNOLOGY
COLLEGE OF SCIENCE
ROCHESTER INSTITUTE OF TECHNOLOGY
ROCHESTER, NEW YORK

CERTIFICATE OF APPROVAL

Ph.D. DEGREE DISSERTATION

The Ph.D. Degree Dissertation of *J. Marcelo Ponce Castro* has been examined and approved by the dissertation committee as satisfactory for the dissertation requirement for the Ph.D. degree in Astrophysical Sciences and Technology.

Dr. Douglas Meadows, Committee Chair

Dr. Manuela Campanelli, Committee Member

Dr. Joshua A. Faber, Committee Member

Dr. Joel Kastner, Committee Member

Dr. Carlos Lousto, Committee Member

Dr. Jorge Pullin, Committee Member

Professor Dr. Yosef Zlochower, Thesis Advisor

Date _____

EVENT HORIZONS, GRAVITATIONAL WAVES
AND ASTROPHYSICAL KICKS IN BLACK HOLES SPACETIMES

By

J. Marcelo Ponce Castro

A dissertation submitted in partial fulfillment of the
requirements for the degree of Ph.D. in Astrophysical
Sciences and Technology, in the College of Science,
Rochester Institute of Technology.

October, 2011

Approved by

Prof. Andrew Robinson	Date
Director, Astrophysical Sciences and Technology	

Para *ALI*

Acknowledgments

I want to express my most profound gratitude and admiration to my advisor, Prof. Yosef Zlochower, who has been not only and incredible mentor, but who also has expended large amounts of time teaching me the science behind the numerical simulations. I have learnt a lot from him not only in our research field but also in the motivation, dedication and passion that he has for his work. Many thanks for his scientific guidance that generated many interesting discussions, questions, and pushing the goals of our research. Thanks so much for reading this thesis "thousands of times" and the editorial assistance in writing it. It has been an honor and a enormous pleasure for me to work with him.

Very special thanks to Prof. Manuela Campanelli and Prof. Carlos Lousto for giving me the chance and honor of belonging to the CCRG, for enlightening discussions and for the high quality science developed within the CCRG.

Many thanks to all the members from CCRG: faculties, postdocs and students. Special thanks to Prof. Hans-Peter Bischof, for his help with the visualizations, Imagine RIT and for being always so nice with me.

Many thanks to Prof. Joshua Faber and Prof. Jamie Lombardi. It has been a pleasure to work with them. Thanks for many interesting discussions and forthcoming projects...

Thanks to the faculty of the AST program at RIT, from who I have learnt most of the astrophysics I known.

To the members of this committee, for accepting the hard task of reading and evaluating this thesis.

I gratefully acknowledge NSF for financial support from grants PHY-0722315, PHY-0653303, PHY-0714388, PHY-0722703, DMS-0820923, PHY-0929114, PHY-0969855, PHY-0903782, and CDI-1028087. and NASA for financial support from grants NASA 08-ATFP-0093, 07-ATFP07-0158 and HST-AR-11763. This research was supported in part by the National Science Foundation through TeraGrid resources provided by NCSA and TACC under grant numbers TG-PHY080040N, TG-PHY060027N and TG-AST100048. Computational resources were provided by Ranger cluster at TACC, Lincoln cluster at NCSA and by NewHorizons at

RIT.

I gratefully acknowledge financial support from the Astrophysical Sciences and Technology (AST) program at RIT, and the Graduate Student Office at RIT.

I gratefully acknowledge travel awards from the American Physical Society (APS): Division of Astrophysics (DAP) and Topical Group in Gravitation (GGR).

To all my fellows graduate student for sharing a really enjoyable ride. I found amazing people and friends that I hope to keep close.

To RIT, for allowing me to pursue my dreams, to live in an amazing place, to enjoy the snow one more time, to play rugby again... go TIGERS!!!

I want to thank my family in Uruguay for their support and unconditional love: my aunt Alicia, my parents Hector and Griselda, my cousins Sebi and Andre, my grand-mother Mamaela, and to the rest of all my family that in our very own and particular way we keep our ties strong!

To all my pets: I miss you a lot guys! The most beautiful and sweet white kitty in the world 'enana', this little and sweetie buddy Newton and the greatest dog in the whole world Ernita who will be always in my thoughts.

I want to specially thank to my lovely and beautiful fiancée, friend and future wife, Luciana, that has decide to come and join me in what will be an amazing and incredible journey for the rest of our lives, not only to reach our most challenging goals but also to begin our own family. Without her all this effort will not make any sense at all. Thanks darling for being there and being here for me! I love you!

Abstract

In this thesis we use computational techniques (numerical simulations) to study different stages of black hole mergers. A first project describes topological properties of the main performer of this play, the black hole and its event horizon. We investigate three configurations: a continuum ring singularity, a "discretized" ring (black holes arranged on a ring), and a linear distribution of black holes. We evolve each of the corresponding spacetimes forward and then backwards in time, searching for the respective event horizons. We find some evidence, based on configurations of multiple BHs arranged in a ring, that this configuration leads to singular limit where the horizon width has zero size, possibly indicating the presence of a naked singularity, when the radius of the ring is sufficiently large.

In a second project, we study the dynamics of a hydrodynamical accretion disk around a recoiling black hole, which models the behavior of an accretion disk around a binary just after the merger, using "smoothed-particle hydrodynamics" techniques. We simulated different recoil angles between the accretion disk and the recoil velocity of the black hole. We find that for more vertical kicks ($\theta \lesssim 30°$), a gap remains present in the inner disk, while for more oblique kicks ($\theta \gtrsim 45°$), matter rapidly accretes toward the black hole. There is a systematic trend for higher potential luminosities for more oblique kick angles for a given black hole mass, disk mass and kick velocity, and we find large amplitude oscillations in time in the case of a kick oriented 60° from the vertical.

Key-words: Computational Astrophysics, Numerical Relativity, Smooth Particle Hydrodynamics, Event Horizons, Ring Singularity, Black Holes, Gravitational Recoils, Accretion Disk.

Contents

List of Figures

List of Tables

Chapter 1

Introduction

1.1 General Relativity

Einstein's General Theory of Relativity (1915) represents one of the most complete, mathematically elegant and beautiful physical theories. It describes the most general systems where masses and energies are important, and in the limiting cases of slow speeds and low masses recovers the Newtonian concepts. The theory of Special Relativity (Einstein, 1905) represents the unification of the Electromagnetism and Classical Newtonian Mechanics, based on two simple principles: i) the Principle of Relativity, which states that all inertial observers are equivalent; and ii) the Principle of the Invariance of the Speed of Light, which states that the speed of light is the same for all observers [2, 3, 4, 5]. As an immediate consequence of these two principles, a maximum speed for propagation of all information is set: the speed of the light. General Relativity goes further and generalizes the concepts of a 4-dimensional *spacetime*, where space and time play dynamical roles with the same relevance. The theory of General Relativity marries Special Relativity and Gravitation. Even more interesting, General Relativity is based on one principle: the *General Principle of Relativity*, which states that the laws of physics should be the same for all observers, which is a generalization of the Principle of Relativity. General Relativity is one of the most elegant and beautiful mathematical descriptions where space and time evolve together, affecting each other in a dynamical way. The following sections are a review of the field, and more details can be found in the Refs.[2, 3, 4, 5].

General Relativity can be thought of as a *gauge theory*, meaning that there is a freedom inherent in the theory, in this case, the freedom lies in the coordinate system. As was mentioned previously, the laws of physics should be the same for any observer in any reference frame. This represents the freedom of the theory regarding coordinate changes, more technically the so-called *diffeomorphism invariance*.

1.1.1 Einstein Field Equations

Einstein's Equations of General Relativity are the equations that describe the evolution of the spacetime itself. As General Relativity is a "*geometrical* theory of gravitation", the "gravitational force" (attraction between bodies) is not a *force* or interaction among bodies but instead is due to the *curvature* of a 4 dimensional spacetime. Freely falling bodies move in trajectories ruled by the principle of least action, or more accurately, stationary action, called *geodesics*. A geodesic between two events is described as the curve joining those two events which has the maximum possible length in time (for a timelike curve) or the minimum possible length in space (for a spacelike curve).[1] Mathematically the geodesic is the generalization of the concept of "straight line" in flat space to curved space. The length of a curve in spacetime is given by $l = \int \sqrt{|g_{\mu\nu}\dot{x}^\mu \dot{x}^\nu|} ds$, where $g_{\mu\nu}$ are the spacetime metric components. By applying the Euler-Lagrange equations (from the least action principle), it is possible to obtain the geodesic equation: $\Gamma^\lambda_{\mu\nu}\dot{x}^\mu\dot{x}^\nu + \ddot{x}^\lambda = 0$; where $\Gamma^\lambda_{\mu\nu}$ are *connection coefficients* that account for changes in the metric components along the curve; and the " $\dot{}$ " represents derivatives with respect to an affine parameter that parametrizes the curve (d/ds). The affine parameter can be the proper time for timelike geodesics, but it must be something else for null-curves (lightlike) because for these curves, the proper time is always zero. Under the new prescription of General Relativity, all small free bodies (and also light) will move following geodesics. Einstein's equations relate the geometry of the spacetime (curvature and hence how the bodies move) with the energy or masses present in the 4d-manifold, the curvature tells the bodies how to move. Conversely the motion of the bodies describes the energy and mass distribution in the

[1] The denomination of *spacelike*/*timelike*/or/*null* is determined by the line-element: $ds^2 = g_{\mu\nu}dx^\mu dx^\nu$. Whether ds^2 is positive, negative or identically zero, defines if the line-element is spacelike, timelike or null respectively (under the assumption of having a metric with signature: $(-,+,+,+)$).

manifold: i.e. mass and energy distribution bends and warps the spacetime. This intricate and profound relation between spacetime (geometry) and energy/matter is a clear indication of the deep and complicated relation of the elements in the theory.

More specifically, Einstein equations can be written [2]

$$R_{\mu\nu} - \frac{1}{2}Rg_{\mu\nu} = \frac{8\pi G}{c^4}T_{\mu\nu}, \tag{I-1}$$

where μ and ν are free indices representing the coordinates of the 4d-manifold ($\mu = 0, 1, 2, 3$ corresponds to ct, x, y, z respectively); $g_{\mu\nu}$ is the metric of the manifold, i.e., it contains the information of how the coordinates (t, x, y, z) distances are related to physical distance; $R_{\mu\nu}$ is the Ricci tensor of the manifold, which can be defined as a contraction of a more general tensor: $R^{\rho}{}_{\sigma\mu\nu}$, the Riemann curvature tensor (it basically indicates whether the manifold is intrinsically flat or not: i.e. $R^{\rho}{}_{\sigma\mu\nu}(x^{\alpha}) = 0$ if and only if the spacetime is locally flat at x^{α}); R is the curvature scalar defined as the contraction of the Ricci tensor,

$$R = R^{\mu\nu}g_{\mu\nu}; \tag{I-2}$$

$T_{\mu\nu}$ is the *energy-momentum tensor* (also known as stress energy tensor), which describes the energy and mass distribution on the manifold; and G is the gravitation universal constant and c is the speed of light.

The left hand side of Eq.(I-1) is usually known as the Einstein tensor, $G_{\mu\nu} = R_{\mu\nu} - \frac{1}{2}Rg_{\mu\nu}$, which is related to the geometry of the spacetime. The right hand side of Eq.(I-1) basically describes the distribution of mass and energy given by the energy-momentum tensor $T_{\mu\nu}$. The components of the $T_{\mu\nu}$ can be heuristically interpreted as follows: $T_{00} = T_{tt}$ measures the energy density; $T_{i0} = T_{xt}, T_{yt}, T_{zt}$ measures how fast the matter is moving, i.e. the momentum density; $T_{ii} = T_{xx}, T_{yy}, T_{zz}$ measures the pressure in each of the three directions; $T_{ij} = T_{xy}, T_{xz}, T_{yz}$ measures the stresses in the matter.

[2] More general formulations of Einstein equations are given when considering cosmological constants or torsion: for instance, Eq.(I-1) is generalized as $R_{\mu\nu} - \frac{1}{2}Rg_{\mu\nu} + g_{\mu\nu}\Lambda = \frac{8\pi G}{c^4}T_{\mu\nu}$ when considering a cosmological constant Λ [6] – which is also related to questions about *dark energy* [7]. In this thesis we assume General Relativity in a torsion-free description and we do not include the contribution of a cosmological constant.

An important special case of the Einstein equations is that when there is no matter present, or the matter is not self-gravitating, then the energy-momentum tensor vanishes, and Eq.(I-1) becomes,

$$R_{\mu\nu} = 0. \tag{I-3}$$

We will see in Sec. 1.5, that even this particular case leads to important unusual predictions of the theory, e.g. the existence of black holes, wormholes, etc. Furthermore solving this "simple" equation is actually a complex problem that has kept physicists working for almost a century. The set of equations given by Eq.(I-3) is usually known as *vacuum Einstein equations*.

In addition to the algebraic symmetries of the Riemann tensor[3] (which constrain the number of independent components at any point); the Riemann tensor obeys a differential identity, which constrains its relative values at different points,

$$\nabla_{[\lambda} R_{\rho\sigma]\mu\nu} = 0, \tag{I-4}$$

known as the *Bianchi identity*[4].

In four dimensions the Einstein tensor can be thought of as a trace-reversed version of the Ricci tensor, $G_{\mu\nu} = R_{\mu\nu} - \frac{1}{2} R g_{\mu\nu}$. When considering the Bianchi identity, Eq.(I-4), and contracting twice, one obtains

$$\nabla^{\mu} G_{\mu\nu} = 0. \tag{I-5}$$

Thus the Einstein tensor is a divergence-free tensor (and therefore the energy momentum tensor too), which will lead to important consequences. When combined with the Gauss theorem, Eq.(I-5), can be used to construct conserved quantities. This in particular will raise the question whether energy is a conserved quantity in the context of General Relativity (in general it is not conserved).

Einstein's system of equations –Eq.(I-1)– is a system of 10 coupled, non-linear, partial

[3] More details about the Riemann tensor are given in Sec.2.1.1.6.

[4] For a general connection there would be additional terms involving the torsion tensor. It is also closely related to the Jacobi identity and can be rewritten in a similar way.

differential equations (elliptic and hyperbolic), for 10 metric components (in an arbitrary coordinate system it can contain thousand of terms). [5]

Mathematically the Einstein equations as given by Eq.(I-1) are *fully covariant*, hence there is no distinction between space and time (in the sense that looking at the full expression of Einstein equations there is no difference between space and time coordinates). Space and time are promoted to dynamical players at the same level, and this not only represents a beautiful and elegant mathematical detail but also sets a 'democratic' (equitable) principle in the theory. On the other hand, there is a very important distinction between time and space components of the metric. For example, in a local Cartesian frame the metric has the form $\mathrm{diag}(-1,+1,+1,+1)$ and it is easy to prove in general that the metric determinant must be negative always $g = det(g) < 0$; otherwise certain issues regarding causality, closed timelike curves and time travel may arise. [6]

But as is described in Sec. 1.4, these same properties come with certain difficulties when trying to solve the Einstein equations. So far, there are thousands of publications on exact solutions to the Einstein equations [10], and most if not all of them are found using particular symmetries.

1.2 Gravitational Radiation

One of the main consequence of General Relativity is the theoretical prediction of the existence of *Gravitational Waves* [11]. This prediction of the theory claims that the spacetime can be

[5] There are several different ways to mathematically describe General Relativity, but one that is of maximal elegance and simplicity is via differential geometry and differential forms. In such approach, all the elements in the theory are geometrical and the theory can be formulated almost completely using topology [8].

[6] Additionally in Classical General Relativity there are 3 spatial (bidirectional) dimensions and only 1 time (unidirectional) dimension. Considering a space of $n = (N + T)$-dimensions, where N is the number of spatial dimensions and T the number of time dimensions, some heuristic arguments rule out all cases except $N = 3$ and $T = 1$ – which happens to describe the world about us [9]. Curiously, the cases $N = 3$ or 4 have the richest and most difficult geometry and topology. There are, for example, geometric statements whose truth or falsity is known for all N except one or both of 3 and 4. $N = 3$ was the last case of the Poincaré conjecture to be proved. On the other hand, other alternatives theories argue the existence of extra-dimensions, in general spatial ones. For instance, String theory hypothesizes that matter and energy are composed of tiny vibrating strings of various types, most of which are embedded in dimensions that exist only on a scale no larger than the Planck length. Hence $N = 3$ and $T = 1$ do not characterize string theory, which embeds vibrating strings in coordinate grids having 10, or even 26, dimensions.

rippled and twisted in much the same way as the fluid in a pond.

Mathematically, the existence of gravitational waves can be described by a technique known as 'Linearized Gravity', which basically consists of taking a linear expansion of the metric ($g_{\mu\nu} \approx \eta_{\mu\nu} + h_{\mu\nu}$) around a Minkowski metric. By substituting this expansion in Einstein equations, and under certain assumptions related to the reference frame, it is possible to show that these equations lead to a wave equation for the metric perturbation. This phenomenon has all the characteristics of a wave phenomenon, including propagation and transportation of energy and momentum. The unique feature here is that the 'medium' in this case is the spacetime itself, and the perturbation (i.e. the gravitational wave) propagates at the speed of light. As for other wave phenomena, the gravitational waves can be polarized in two fundamental directions (polarizations). These waves, propagating at the speed of light, can be considered as intermediaries in this case of gravity (analogous to the electromagnetic case where the electromagnetic waves are carriers of the electromagnetic fields; actually the relation in both cases is much more complex, with a cause-and-effect feedback loop). Furthermore, the analogy can be pushed even further given that, in the same way as photons are considered "carriers" of the electromagnetic force, quantum theories of gravitation have proposed the existence of a theoretical particle named "graviton" as the carrier of gravity. Such hypothetical particle should be massless and have spin 2. Actually it can be shown that any massless spin-2 field would be indistinguishable from the 'graviton', because a massless spin-2 field must couple to (interact with) the stress-energy tensor in the same way that the gravitational field does. This result suggests that if a massless spin-2 particle is discovered, it must be the graviton, so that the only experimental verification needed for the graviton may simply be the discovery of a massless spin-2 particle [2, 12].

Currently, Gravitational waves are of great importance, but their existence so far has been proven only indirectly. There are now several very large experiments [13, 14, 15, 16, 17, 18, 19] to detect them directly [20, 21, 22, 23, 24]. The indirect proofs are the precise concordance between computations of the energy radiated by a binary pulsar system and the measured change in the orbits of the binary [25, 26, 27, 28, 29, 30, 31, 32]. The direct detection of

gravitational waves, and therefore the existence of gravitational waves, will be an additional proof in favor of the validity of General Relativity in the strong gravity regime. On the other hand, an absence of a direct detection –which may be even more tricky to claim than a detection itself, because of all the technical challenges involved– would open a new window for the so-called "alternative theories of gravity", such as generalizations of General Relativity modifying the action by including higher-order derivatives of the metric among many others possibilities (e.g. gravitational scalar fields, "strange" matter, etc.). With the target of a positive detection, many gravitational wave detectors are working in a cohesive network to detect relative perturbations of the order of 10^{-22}. This variation is the relative change in the length of the arms of the interferometer due to the passage of the gravitational wave. The reason for such small values, requiring among the most precise and accurate measurements ever, is that gravity couples to matter so weakly and the amplitude of the gravitational waves scales as the inverse to the distance to the source. Likewise the amplitude of the gravitational radiation also scales proportional with the mass and speed of the source. Thus the most promising and relevant sources of gravitational waves for detection purposes appear to be astrophysical events, such as, black hole mergers, mergers of binary white dwarfs or neutron stars systems, or any other highly massive dynamical system without spherical symmetry [7].

Gravitational waves are the result of time variations of second and higher order multipole moments of mass and mass "current", in the same way that electromagnetic waves are the result of changes of first and higher order electric and magnetic multipole moments (charge, dipole, ..., electric current density, etc.). More precisely, the gravitational wave produced by an isolated nonrelativistic object is proportional to the second derivative of the quadrupole moment of the energy density. In contrast, the leading contribution in electromagnetic radiation comes from the changing dipole moment of the charge density. The origin of the difference arises from the different nature of both interactions, although in both cases it is "accelerated" objects that radiate. The dominant moment for gravitational waves emission is the mass quadrupole,

[7] The strongest astrophysical sources are likely to have masses on the order of our sun, or perhaps a few factors of ten larger, with internal velocities between 10% of the speed of light and larger, and will be located (at the closest) at roughly the distance to the center of the Virgo cluster of galaxies. Consequently, the strongest gravitational waves arriving at the Earth will have upper limits to their amplitudes h of the order of 10^{-20}m (see Eq.(I-6)).

$M_2 \sim Mr^2$, where M is the source's total mass and r is the average length scale of its deviations from spherical symmetry. Actually this is the reason why systems with spherically symmetric mass distributions cannot radiate. A good approximation for the contributions to the two polarizations of the gravitational waves due to the quadrupole moment is, $h_\times \sim h_+ \sim \left(\frac{G}{c^4 r}\right) \frac{d^2 M_2}{dt^2}$, where h is the strain amplitude of the wave. The strain h distorts the distance between two freely falling objects by an amount proportional to strain and the mean distance between them. For compact relativistic sources, the second derivative of the quadrupole mass moment can be approximated by Mv^2 (where v is the average internal velocity of the source) which is equal to the kinetic energy associated with internal, nonspherical motions of the source, E_{Kin}^{nonSph}. Consequently, the amplitude of the oscillations of the gravitational components, $h_\times$ and h_+, can be expressed as:

$$h \approx \frac{G E_{Kin}^{nonSph}}{c^4 r} \approx 10^{-20} \frac{E_{Kin}^{nonSph}}{M_\odot c^2} \frac{10\text{MPc}}{r}, \tag{I-6}$$

where $M_\odot$ is the solar mass and 10 megaparsecs (Mpc), or 30 million light years, is the distance to the Virgo cluster of galaxies (the nearest large cluster of galaxies to our own Milky Way galaxy).

Because of the enormous amount of mass concentrated in a singular point of the spacetime in a Black Hole, and recalling that the energy radiated in a gravitational wave scales with the mass and speed of the 'source', it turns out that the merger of binary black holes are among the most promising gravitational wave sources [33, 34]. Despite having a technically challenging signal-to-noise ratio, the sensitivity reached in successive stages of improvements by the gravitational wave detectors is expected to be large enough that a detection in the next few years is likely. Equally important in such attempts is to have template banks with waveforms in order to filter the signals and perform parameter estimation for localizing and identifying the origins and astrophysical nature of the source. Currently several techniques are being tested in order to obtain a wider template bank [35, 36, 37, 38, 39]. Some of this techniques consists of semi-analytical approaches and approximations (e.g. post-Newtonian approx., effective one-body, effective field theory). In spite of all the recent advances in the

area, the most reliable and precise way to generate an appropriate waveform is full numerical simulations. Even in the case of full numerical simulations, there are important questions about accuracy and precision of the waveform generated.

Furthermore, gravitational waves are of great importance not only for their theoretical implications, but also because they play a fundamental role in gravitational recoils of black holes (see Sec.1.3.1). Additionally, it has been proposed that gravitational radiation can imprint particular signatures in surrounding matter, leading to modulations in electromagnetic emissions [40]. This type of study forms the core of one our projects (see Chapt.4).

1.3 Astrophysical Applications

General Relativity is important for understanding many (if not the most important) astrophysical processes in the universe. Because of its validity in systems with large masses and energies it is required for understanding the large scale structure of the universe [41, 42], as well as dark matter and dark energy [7], and cosmology [43, 44, 45]. Different proposed metrics allow for the study of the large structure of the Universe [46] (e.g. Friedmann-Lemaître-Robertson-Walker [47, 48, 49, 50, 51]). Even Special Relativity is important for understanding electromagnetic radiation processes and the observational electromagnetic spectrum.

More directly related to General Relativity, several direct consequences are important not only for understanding and learning more about our Universe, but also how it is "populated". The theoretical predictions from General Relativity include: black holes, gravitational waves, and also other effects such as GR precession, gravitational lensing, gravitational recoils, the Lense-Thirring effect, gravitational redshift, time delay, frame dragging for spinning black holes, and the cosmological constant (dark energy), among many others that have been or might soon be found.

There are many astrophysical questions that remain to be answered in the regime where General Relativity is expected to be valid. For instance, how astrophysical jets are produced and fueled from compact objects[8] [52, 53, 54], as well as how Active Galactic Nuclei are

[8]Astrophysical jets can be defined as well-collimated outflows from a compact object. Jets are commonly

powered [55, 56], or how Supernovae explosions occur [57, 58, 59, 60, 61, 62, 63].

Even when it may not have direct implications, General Relativity is useful for understanding other relevant astrophysical questions such as dark matter [64, 65, 66, 67, 68, 69] (among the observational evidence for the existence of dark matter are the galactic rotational velocity profiles, the gravitational lensing and Cosmic Microwave Background power spectrum anisotropy [70, 71, 72]) – or even its absence [73] [9], the Big Bang modeling [77] and inflation scenarios [78, 79, 80] (or even more exotic possibilities [81, 82]), the "final parsec problem" [83, 84, 85], etc.

1.3.1 Gravitational Recoils

One of the most outstanding recently discovered consequences of General Relativity, is the *Gravitational Recoils* that could occur after the merger of a binary system of black holes [86, 87, 88, 89, 90, 91, 92, 93, 94, 95, 96, 97, 98, 99, 100, 101, 102, 103, 104, 105, 106, 107]. This effect is based on the asymmetric emission of gravitational radiation, leaving a net overall momentum in the remnant black hole. Interestingly enough, this effect has no precedent in classical mechanics, and the maximum recoil occurs when the black holes are spinning. Furthermore, the effect was first discovered numerically due to the breakthrough of the numerical simulations, demonstrating super-"kick" velocities up to thousands of kilometers per second [91, 92]. Many attempts have been made to model these kicks through analytical descriptions like perturbation theory, post-Newtonian approximations, etc. Remarkably, it has been found that it is possible to model the recoil using a 'simple' phenomenological formula inspired by post-Newtonian theory and fitted via numerical simulations [108, 107, 93, 109]. Furthermore, the most up-to-date studies show that the maximum recoil could be reached

bipolar, with two back-to-back jets streaming away from the central compact object. There are two main types of astrophysical jets: Young stellar jets, which are seen near newly forming stars; and, Extragalactic jets, which are seen near the nuclei of radio galaxies and quasars. Despite the very different length scales and velocities for the two types of jets, the basic physics involved is the same. Long, highly collimated flows originate in a compact object, and appear to be perpendicular to an accretion disk. In addition to a force that counteracts the gravitational force of the central compact object, the formation of a jet requires a 'nozzle' to shape the gas flow into a narrow jet.

[9] Alternatives theories to dark matter include 'Modified Newtonian Dynamics' (MOND) [74], and formulations trying to recover it from a General Relativity basis, known as 'Tensorial-Vector-Scalar Gravity' (TeVeS) [75, 76].

for spins partially aligned with the orbital angular momentum [110], so-called "hangup kicks", pushing the recoil velocities up to 5000km/s. Additionally in the last years several observational studies claim to have found candidates supporting evidence of such enormous kicks [111, 112, 113, 114, 115, 116].

The discovery of super-kicks and the observational evidence that support this, constitute astonishing new results. The astrophysical implications are profound: supermassive black holes may even escape their host galaxies and roam the Universe. Furthermore galaxy mergers have already been observed [117, 118, 119, 120], which provides a probable scenario for black hole mergers [121, 122]. If these merger configurations are such the remnant black hole reaches the super-kicks regime, then it could produce a black hole that oscillates, not only sharpening the structure of the recent merger host galaxy but furthermore ejecting it from its own host galaxy.

Understanding the consequences of these kind of phenomena is of great importance and of current interest, not only theoretically and astrophysically, but also because of the potential electromagnetic counterpart signature of such events. For that reason one of the projects developed within this thesis is devoted to the study of kicked black holes surrounded by accretion disks (see Chapter 4).

1.4 Numerical Relativity

Numerical Relativity was initially born as a sub-field of General Relativity that emerged with the aim of finding numerical solutions to the Einstein Equations in more general and realistic cases than the usual analytic solutions [123, 124, 125, 126, 127].

The discipline of Numerical Relativity started around 60 years ago, with the pioneering works looking for new formulations of the theory of relativity [128]. Some early attempts at black holes simulations were tried a few years after the new formulations were published for very simple cases [129]. For nearly 20 years following the initial attempts, there were few other published results in numerical relativity, probably due to the lack of sufficiently powerful com-

puters to address the problem. [10]The first attempts, in the mid-sixties, of the 2-dimensional axisymmetric collision of black holes were not successful. The efforts on the 2-dimensional problem of colliding black holes was continued during the 1970's including gravitational radiation and the first visualizations as well [130, 131, 132]. By the mid seventies, the first "head-on" collision (in 2-D) was tried [133]. At that time ('60s & '70s) the computing power was on the order of MegaFlops for processing speed and MegaBytes in memory allocation. By the end of the '80s, with a factor of 10^2 improvement in computer resources, the 1-dimensional spherical symmetry black hole was the target. Following this, there were attempts to evolve: 2-dimensional axisymmetric distorted black holes, 2-dimensional axisymmetric collisions of black holes, and 2-dimensional axisymmetric rotating black holes. Each of these problems allowed Numerical Relativity gain expertise and solve more complicated problems. By the early '90s, the simulations were tackling scenarios such as: 1-dimensional spherical symmetric black hole in 3-D, 2-dimensional distorted black hole in 3-D, 3-dimensional colliding black holes in 3-D; i.e. many of the problems previously tackled but now in one more dimension. Additionally the first approach to 3-dimensional gravitational wave propagation was done. By the late '90s, the processor's speed arrived to the GigaFlops, and the memory to the GigaBytes ranges. It was in the late 1990s when the Binary Black Hole Grand Challenge Alliance successfully simulated a full 3-dimensional "head-on" binary black hole collision for the first time. As a post-processing step the event horizon for the spacetime was computed. At the end of the century, the computational power was in the order of TeraFlops and TeraBytes for processing speed and memory respectively. For the sake of comparison, currently we talk about high performance computers with distributed resources, parallel computing, multiple cores in the Peta-scale range.

Among the first attempts to solve the Einstein equations in three dimensions were focused on a single Schwarzschild black hole, which is described by a static and spherically symmetric solution to the Einstein field equations. This provides an excellent test case in numerical relativity because it has a closed-form solution so that numerical results can be compared to

[10]The following description is based on the "Numerical Relativity Timeline" chart available at http://archive.ncsa.illinois.edu/Cyberia/NumRel/NumRelTimeline.html.

an exact solution, because it is static, and because it contains one of the most numerically challenging features of relativity theory, a physical singularity. But still the lack of computers with sufficient memory and computational power to perform well resolved calculations of 3D spacetimes appeared to be a limiting issue at that time. In the years that followed, not only did computers became more powerful, but also various research groups developed alternate techniques to improve the efficiency of the calculations. With respect to black hole simulations specifically, two techniques were devised to avoid problems associated with the existence of physical singularities in the solutions to the equations: "excision" [134, 135], and the "puncture" method [136, 137, 138]. Additionally, adaptive mesh refinement techniques, already used in computational fluid dynamics were introduced to the field of numerical relativity.

It was in the last 6 to 7 years, when there were several breakthroughs that allowed Numerical Relativity to go from simulations where was just hardly possible to simulate some simple cases up to the point where the simulations crashed; to the current state of the art where the most sophisticated and complex simulations are feasible with high accuracy, precision and control [139, 140, 141].

By the same token, the computational simulations performed are likely among the most demanding, complicated, complex, sophisticated and challenging ones ever. The reason for that, is not only that the system of equations that need to be solved are a non-linear set of coupled partial differential equations with mathematical issues when discretized. But as it was mentioned before in Sec. 1.1, General Relativity promotes space and time as a unique entity, although in order to perform numerical simulations that unification must be broken. This is the only way in what numerical evolutions can be achieved: via time evolution schemes through consecutive time steps either forward or backward in time. The 3D manifold (t=constant) changes dynamically as the coordinate description of the points in the manifold. These dynamical changes in the coordinates are represented by new variables, called the 'lapse' function and the 'shift' 3-vector.

Furthermore, having a theory which is described in such dynamical way also faces the problem of how to compare results, i.e. in which coordinate system are the results expressed.

Moreover, the field of numerical relativity is not just coding and running simulations but also a lot of work has been done in obtaining formulations of the theory [128, 142, 143, 144, 145, 146, 147, 148]. Basically these formulations take the Einstein equations and rewrite them in a way that makes traditional numerical evolutions possible. Building a numerical spacetime on the computer means solving equations. The equations that arise in numerical relativity are typically multidimensional, nonlinear, coupled, partial differential equations in space and time, as such they share the usual difficulties encountered when solving this type of mathematical problems numerically. However, solving Einstein's equations includes some additional complications that are unique to General Relativity. Among the most important are: the choices of coordinates, the treatment of physical singularities (actually the key element is perform the evolution in such a way that the singularity can be avoided in the course of the simulation), the matching of very different regions (e.g. the far-field, radiation, zone for extracting gravitational radiation; and the strong-field central region where the source lays), time and spatial resolutions, among others. Chapter 2 describes and discuss the mathematical and technical details of the theory behind the numerical simulations.

Currently Numerical Relativity, is a discipline that has matured and that not only involves numerical techniques and General Relativity, but also due to the computational resources involved, disciplines such as Computer Sciences, Mathematical Relativity, Computational Astrophysics among many others, share important areas of research and interest.

Additionally, many other disciplines has grown based on the results obtained by Numerical Relativity and their simulations, i.e. black-hole Astrophysics, and especially the detection of Gravitational Waves.

1.4.1 3+1 Decomposition

One of the most astonishing ideas from General Relativity is the concept of *spacetime*, which is a peculiar entity that geometrically can be thought as a 4-dimensional manifold. This beautiful and fundamental idea, is propagated to the Einstein equations eliminating any sort of predominant role of space vs time, or vice versa. Furthermore, any spatial or temporal

nature of the components is completely hidden in the theory.

While this represents a unified prescription of the theory, there are several reasons why it may be necessary to abandon this perspective. Somehow, it is the same freedom and beauty inherent to the basics origins of the theory of General Relativity, that from the numerical side makes things more complicated, and this freedom needs to be broken in order to make possible the implementation of numerical computations.

In the case of Numerical Relativity, the goal is to recover a more intuitive picture and make possible standard time evolutions schemes. There are other reasons in addition to obtain a dynamical classical evolution in time, why it may be useful to recover the usual picture of a 3-dimensional space with a 1-dimensional time direction[11]. Either for recovering a more intuitive picture, or trying a quantization approach as in quantum field theory, the goal will be to recover a classical picture of a 3-dimensional spatial-type space plus a 1 dimensional time coordinate. Therefore it is necessary to break the new 4-dimensional geometrical manifold defined in General Relativity of the spacetime, by splitting it into the spatial and temporal components.

Having a «3+1» formulation also allows one to perform evolutions of the system for given initial data via defining a well-posed Cauchy problem. As described in more detail in Chapter 2, the idea behind this will be to use a Hamiltonian formulation and recover the equations of motion.

1.5 Black Holes

General Relativity itself gives birth to one of the most intriguing and enigmatic inhabitants of the universe: black holes. It is only in General Relativity (as well as generalizations and/or extensions, or alternative theories of gravity) where this particular type of solution to Einstein equations uniquely emerges (i.e. this can not be found in Newtonian gravity[12]). Using

[11] Likewise there are different arguments to recover a standard space and time description, there are also different ways to proceed and implement this splitting according to the field and interest underneath (e.g. Ashtekar variables [149], tetrads [150], etc.)

[12] Sometimes the term of "Newtonian Black Hole" is also employed in the literature, although this denomination is not completely appropriate: in Newtonian dynamics, light can not be bent by gravity and therefore

spherical symmetry arguments and assuming static spacetime, it is possible to obtain a particular solution of Einstein equations, i.e. a special metric which satisfies Einstein equations: more precisely vacuum Einstein Equations –Eq.(I-3)–. This particular solution is known as Schwarzschild black hole, and represents the spacetime metric in a vacuum, static, spherically symmetric spacetime. It was found just a month after the theory of General Relativity was published. It has been proven via Birkhoff's theorem that actually this is the most general solution for a vacuum, spherical symmetric spacetime. Even more interesting was to notice that this particular solution has unique and unprecedented features: the solution contains a *singularity*, i.e. for a given point in the spacetime the metric components as many other quantities diverge. Nevertheless Newtonian point particles are also singular, this is mainly due to the fact that Newton's inverse-square law diverges mathematically as the distance goes to zero. However the caveat here is as far as it is known, the singularity in the Newtonian theory is related to the mathematical breakdown of the theory. Meanwhile, General Relativity allows for singularities either as mathematical solutions of the theory or real physical singularities (i.e. black holes).

The original mathematical prediction of the existence of black holes was first obtained theoretically within months after the publication of General theory of Relativity. Because of their particular nature, black holes have never been directly observed, although predictions of their effects have matched observations. One of the strongest evidence of black holes detection may lay in the center of our own galaxy: Sagittarius A* (pronounced "Sagittarius A-star", standard abbreviation Sgr A*) is a bright and very compact astronomical radio source at the center of the Milky Way Galaxy. Sagittarius A* is believed to be the location of a supermassive black hole [151], which are now generally accepted to be at the centers of many spiral and elliptical galaxies. Observations of the star S2 in orbit around Sagittarius A* have been used to show the presence of, and deduce data about, the Milky Way's central supermassive black hole, and have led to the conclusion that Sagittarius A* is the site of that black hole [152]. Over 16 years, the orbits of 28 stars in the Milky Way's central region have been meticulously tracked by astronomers, allowing them study the hidden black hole that influences the stars'

it can escape from the "singularity".

movements. The black hole cannot be seen directly, but its nature can be inferred from the pattern of motion of the stars that surround it. In particular there are more than a century of observations from one of the closest companions of SgrA: a variable star named S2 (or So-2), because of its magnitude the first records are from 1850 [153]. The star S2 follows an elliptical orbit with a period of 15.2 years and a pericenter (closest distance) of 17 light hours (1.8×10^{13}m) from the center of the central object. From the motion of star S2, the central object's mass can be estimated between 3.7 and 4.1 million solar masses. The radius of the central object must be significantly less than 17 light hours, because otherwise, S2 would either collide with it or be ripped apart by tidal forces. In fact, recent observations indicate that the radius is no more than 6.25 light-hours, about the diameter of Uranus' orbit. The only known type of object which can contain 4.1 million solar masses in a volume that small is a black hole. The orbit of S2 will give astronomers an opportunity to test for various General Relativistic and even extra-dimensional effects. Given a recent estimate of the mass of Sagittarius A* and S2's close approach, this makes S2 the fastest known ballistic orbit, reaching speeds exceeding 5000 km/s or 2% of the speed of light and accelerating at about 1.5m/s^2 or almost one-sixth of Earth's surface gravity.

Currently there are several techniques that allow for the measurement of the effects of strong gravitational fields (e.g. gravitational lensing, X ray emission, etc.). For example, in some fraction of galaxies, large amounts of gas are inferred to be falling into the black hole [154, 155, 156]. Any small rotation of the gas is amplified as it falls towards the black hole, and the gas eventually forms a disk which orbits around the black hole. Such a disk is called an accretion disk. As the gas slowly spirals through the accretion disk towards the black hole, it releases a large amount of energy. The accretion disk acts like a power plant generator, converting the kinetic energy of the gas into large amounts of infra-red, optical, ultraviolet and X-ray light. Galaxies with this powerful radiation sources at their center are called active galaxies. A large fraction of the energy released by the gas as it falls onto the black hole is converted into X-rays. It is thought that the X-rays come from material that is very close to the black hole (i.e. at distances of just a few times the event horizon size).

Observations with X-ray telescopes allow astronomers to test and measure the conditions in this very interesting region of space. Of particular interest is when iron atoms in the accretion disk become 'excited' by absorbing X-rays. The response to such excitation is to emit X-ray of their own, but with a very particular frequency: X-ray emission at this special frequency is called iron line emission. The observed frequency of these X-rays is strongly influenced by the orbital motion of the gas around the black hole by Doppler shift. Also, as predicted by Einstein's theory, the gravitational redshift lowers the frequency of the X-rays that are emitted near the black hole. Both of these effects can be detected when observing the iron emission line [157, 158, 159].

Astrophysically, it is expected that black holes are born when very massive stars die and collapse; the collapse of the mass to the center of the star generates sufficiently strong gravitational fields that a singularity is formed [160, 161]. Interestingly enough, thanks to Chandrasekar's studies, it is possible to know what masses and compactnesses are required in order to turn an object into a black hole [162, 163, 164]. Considering arguments about the electron degeneracy pressure and assuming a non-relativistic star (e.g. a white dwarf), it is possible to obtain an approximate expression for the critical mass necessary for collapsing into a black hole,

$$\begin{cases} M_c \approx \frac{1}{m_p^2}\left(\frac{\hbar c}{G}\right)^{3/2} \\ R_c \approx \frac{1}{m_e m_p}\left(\frac{\hbar^3}{Gc}\right)^{3/2}, \end{cases} \tag{I-7}$$

which is the *Chandrasekar limit*, where m_p is the mass of the proton, m_e is the electron mass, and $\hbar$ is Planck's constant divided by 2π. A more detailed calculation gives $M_c \approx 1.4 M_\odot \sim 10^{30}$kg as the upper bound mass for a stable white dwarf star. On the other hand, in order to produce a black hole from the Earth's mass, the entire mass should be reduced to a volume the size of a marble.

There are different ways to classify black holes. From the theoretical point of view (i.e. mathematical solutions to Einstein equations) there are 4 types of stationary black holes: Schwarzschild (spherical symmetry vacuum spacetime), Kerr (which is a rotating black hole), Reissner-Nordström (which is a electrically charged non-rotating, spherically symmetric body),

and Kerr-Newman (which arises from a rotating, electrically charged, axisymmetric solution to Einstein equations [13]). Of course, in addition to these solutions, many other analytic solutions have been found using symmetry arguments and in some cases peculiar distributions of matter and/or energy.

From the astrophysical point of view, black holes are classified according to their masses (or, less precisely, by their radii [14]): micro black holes (with masses much smaller than the solar mass and sizes of the order of a mm), stellar black holes (which have masses in the range of tenth to hundred of solar masses and sizes of the order of a km), intermediate-mass black holes (with masses of thousands of solar masses and sizes of thousands of km), supermassive black holes (with mass ranges running from hundred of thousands up to billions of solar masses, and sizes of the order of hundred of millions of km $\approx 1AU$). Additionally in the astrophysical arena, there are references to primordial black holes, which refers to black holes that could have been formed at the time of the big bang in regions where there were tremendous excesses of densities. Micro-black holes have been suggested as possible candidates for this primordial and ancient habitants of the Universe, but also much attention has been focused in these "little guys" when discussing possible consequences of high-energy colliders and particle physics [165, 166, 167, 168, 169]. The argument arises, that when considering possible extensions of the theory to higher dimensions[6] ($\gtrsim 5$) [170], where the gravitational force[15] is stronger, micro-black holes of very small size can be produced in high energy collisions. It has been also argued that if such objects may exist they would 'live' for a very small period of time. Another mystery which still remains unsolved in the astrophysical arena is the fact that there is less evidence for the existence of intermediate-mass black holes (IMBH) than for either stellar-mass or supermassive black holes [171]. The key question is whether this type of black hole mass distribution is actually detectable (observable) or if there is a more profound

[13] Formally speaking, when mentioning the solution to electrically charge spacetimes, the appropriate denomination should be *Maxwell-Einstein* equations, which are the equations of General Relativity including the electromagnetism's Maxwell equations in its covariant formulation.

[14] Assuming for instance the validity of Schwarzschild solution, it is immediate to give a relation between the mass of the black hole and its *Schwarzschild radius*, $r_S = 2GM(r)/c^2$.

[15] As mentioned in Sec. 1.1 gravity is not more a force itself but instead the consequence of the bending of the spacetime and its curvature. In spite of that, the reader must be aware that in this work it will appear many time references as 'gravitational force' but it should be recall as the motion under the geodesics of the spacetime instead.

and fundamental reason why such BH mass scales are not allowed.

Some ultra-luminous X ray sources in nearby galaxies are suspected to be IMBHs, with masses of a hundred to a thousand solar masses [172]. The ultra-luminous X ray sources are observed in star forming regions (e.g., in the starburst galaxy M82 [173]), and are seemingly associated with young star clusters which are also observed in these regions. However only a dynamical mass measurement from the analysis of the optical spectrum of the companion star[16] can unveil the presence of an IMBH as the compact accretor of the ultra-luminous X ray sources.

If IMBHs form in young dense stellar clusters, they can be fed by Roche lobe overflow from a tidally captured massive stellar companion. After the donor leaves the main sequence it forms a compact remnant, which spirals in due to gravitational wave emission [176]. Observations of gravitational radiation emitted by these compact remnants would provide additional evidence for the existence of IMBHs.

In addition the *M-sigma* relation[17] [178, 179, 180] predicts the existence of black holes with masses of 10^4 to 10^6 solar masses in low-luminosity galaxies.

IMBH are too massive to be formed by the collapse of a single star, which is how stellar black holes are thought to form. Their environments lack the extreme conditions –i.e., high density and velocities observed at the centers of galaxies– which seemingly lead to the formation of supermassive black holes. There are three popular formation scenarios for IMBHs. The first, is the merging of stellar mass black holes and other compact objects by means of accretion. The second one is the runaway collision of massive stars in dense stellar clusters and the collapse of the collision product into an IMBH. The third is that they are primordial black holes formed in the big bang.

Black holes have transcended the fields of General Relativity and Astrophysics turning into

[16] It is not clear whether IMBHs can exist in systems with individual stellar companions. However, most of the reference in the literature talk about a stellar companion in a binary system [174, 175]. So it looks like most of the reference either because of an observational bias or maybe for a more fundamental reason, require that.

[17] The *M-sigma* (or $M_{BH} - \sigma$) relation is an empirical correlation between the stellar velocity dispersion σ of a galaxy bulge and the mass M of the supermassive black hole at the galaxy's center. The relation can be expressed mathematically as $M \propto \sigma^{\alpha}$. A recent study, based on a complete sample of published black hole masses in nearby galaxies [177], gives $\log(M/M_{\odot}) = 8.12 \pm 0.08 \ + \ (4.24 \pm 0.41) \log(\sigma/200 \text{ km } s^{-1})$.

a modern paradigm for *alternatives theories of gravity* and *unification schemes* (e.g. string theory, quantum gravity [181], extra-dimensions, etc.); and even for information paradox (the black hole information paradox [182] results from the combination of quantum mechanics and General Relativity when using the concept of black hole as a potential mechanism for 'destroying' information[18]). Moreover Black holes have turned out to be key elements also in astrophysics, working as unique laboratories where it is possible to study the fundamental processes of strong gravity, stellar dynamics and star formation, etc.

1.5.1 Definition of Horizons

Black holes are probably the most surprising objects emerging from General Relativity, and a more formal definition of them involves the concept of mathematical singularities. A *physical singularity* is one that can not be avoided via a coordinate transformation (otherwise it will be a coordinate singularity not a physical one). The defining property of a black hole is that it has a *horizon*, a surface through which matter can fall in, but from which no matter or information can escape. Naively it could be expected that a black hole, because its singular nature would be a very complicated object to describe mathematically, but on the contrary, black holes turn out to be the most "perfect" macroscopic objects. It has been proven (*No-Hair theorems* [183, 184, 185]) that a black hole can be described by only three quantities: mass, electric charge, and angular momentum (often referred to as "spin"). Of course the position and linear momentum of the black hole must be included in this set, but not as intrinsic parameters of the black hole itself.

Additionally, there arises the question of what is the size of a black hole? Moreover, one of the main properties that defines a black hole is not the singularity by itself but instead, a singularity surrounded by a surface of "no return" that isolates the singularity (interior of

[18]The black hole information paradox suggests that physical information could disappear in a black hole, allowing many physical states to evolve into the same state. This is a contentious subject since it violates a commonly assumed tenet of science–that in principle complete information about a physical system at one point in time should determine its state at any other time. A postulate of quantum mechanics is that complete information about a system is encoded in its wave function, an abstract concept not present in classical physics. The evolution of the wave function is determined by a unitary operator, and unitarity implies that information is conserved in the quantum sense. In General Relativity, all the information that falls into a black hole is seemingly destroyed when the black hole evaporates.

the black hole) from the exterior (outside of the black hole). The area of this region is an important measure of the "size" of the black hole and can be useful to characterize and describe the black hole (it is directly related to its mass). This concept is immediately related to the definition of a *horizon* of the black hole. Likewise, the concept of black hole horizon is not only interesting for its mathematical implications but also for practical applications in numerical simulations.

There are several definitions and concepts related to horizons in the context of General Relativity: event horizons, apparent horizons, Killing horizons, isolated horizons, trapped surfaces, etc [186, 187].

1.5.1.1 Event Horizon

An *event horizon* is a hypersurface in spacetime that defines the boundary between the points where signals and information can escape and those where signals are trapped (can not escape away from the black hole). It is a global quantity in the sense that it extends not only in space but also in time, that is why it is difficult to obtain this object. The event horizon, as a boundary in the spacetime, separates events that can and cannot affect distant observers. This particular property plays a key role in some numerical evolution schemes which use this idea to "ignore" the spacetime inside a black hole.

The event horizon is the best way to define the boundary of a black hole, but in order to locate the event horizon (assuming that it exists), the entire history of the spacetime must be provided. An event horizon is therefore a non-local notion.

1.5.1.2 Apparent Horizon

In order to give the appropriate definition of an apparent horizon, first we must define the notion of trapped surfaces. A *trapped surface* is a set of points defined as a closed (compact, orientable, spacelike) surface on which the outward-pointing light rays are actually converging (moving inwards). In practice trapped surfaces can be located by examining at the components of the metric on a given slice.

An *apparent horizon* can be defined as the outermost marginally trapped surface in the spacetime. Apparent horizons are local quantities, which presents a major difference with respect to event horizons, which are global and intrinsic properties of the spacetime. Apparent horizons depend on the "slicing" of the spacetime. That is, the location and even existence of an apparent horizon depends on the way that the spacetime is split into space and time. In general apparent and event horizons will differ, especially when the spacetime is highly dynamical (e.g. during the merger of black holes). Nevertheless, near equilibrium the two horizons will coincide to high accuracy. For our purposes the main advantages of apparent horizons is that they are easy to compute numerically.

In the simple picture of stellar collapse leading to the formation of a black hole, an event horizon forms before an apparent horizon. As the black hole settles down, the two horizons approach each other, and asymptotically become the same surface.

Under the reasonable assumptions that the dominant energy condition holds, it has been proven that if the apparent horizon exists, it will necessarily lie inside of the event horizon [19] .

More technical and mathematical precise definitions, concepts and discussions are presented in Chapter 3.

Other horizon-related definitions and concepts. From a theoretical perspective, event horizons provide a safety barrier in the sense that they 'hide' the singularity from the rest of the universe and observers. Singularities without horizons could be observed but have only been proposed as theoretical objects so far. For instance it has been proposed that a naked singularity might magnify the effect in gravitational lensing, allowing for a particular

[19] The so-called *energy conditions* are not physical laws as such, but they are rather assumptions about how any reasonable form of matter should behave. Energy conditions are coordinate-invariant restrictions on the energy-momentum tensor. The *dominant energy condition*, implies that the energy density (for instance thinking about a perfect fluid) must be non-negative and greater than or equal to the pressure, $\rho \geq |p|$. The *null energy condition*, implies that the energy density plus the pressure (again considering a perfect fluid) must be greater or equal zero, $\rho + p \geq 0$. The energy density may be negative, so long as there is a compensating positive pressure. Most ordinary classical form of matter, including scalar fields and electromagnetic fields, obey the dominant energy condition, and hence less restrictive conditions (weak energy condition, null energy condition, null dominant energy condition). The strong energy condition is useful to prove some singularity theorems, but can be violated by certain forms of matter, such as a massive scalar field. The energy conditions are not, strictly speaking, related to energy conservation; the Bianchi identity guarantees $\nabla_\mu T^{\mu\nu} = 0$ regardless of any additional constraint imposed on $T^{\mu\nu}$. Rather, they serve to prevent certain "unphysical" properties.

imprint for its detection [188]. In the context of General Relativity, a *naked singularity* is a gravitational singularity, without an event horizon. If a BH exists, the singularity cannot be directly observed. A naked singularity, by contrast, is observable from the outside. The theoretical existence of naked singularities [189, 190, 191, 192] is important because their existence would mean that it would be possible to observe the collapse of an object to infinite density. It would also cause foundational problems for General Relativity, because in the presence of a (timelike) naked singularity, General Relativity cannot make predictions about the future evolution of the spacetime. Some research has suggested that if loop quantum gravity is correct, then naked singularities could exist in nature, [193, 194, 195] implying that the cosmic censorship hypothesis does not hold. Numerical calculations [196] and some other arguments [197] have also hinted at this possibility. The presence of a naked singularity not only jeopardizes fundamental aspects of the theory but also any possibly intended numerical computation [198, 199, 200, 201]. So far, no naked singularities (and no event horizons) have been observed.

Singularities theorems exist in many forms, proceeding from various different sets of assumptions. Typically, time-dependent solutions in General Relativity usually end (or begin, e.g. the Big Bang) at singularities. This represents a problem for General Relativity, in the sense that the theory does not really apply to singularities themselves, whose existence may represent an incompleteness of the description. Among the possible solutions to this issue is the popular belief that a more general unification theory would tackle this incompleteness (e.g Quantum Gravity, String Theory, etc.) by removing the singularity.

The *Cosmic Censorship conjecture* [202, 203, 204, 205, 206, 207] states that naked singularities cannot form in gravitational collapse from generic, initially nonsingular states in an asymptotically flat spacetime obeying the dominant energy condition[19] (for a perfect fluid $-T^{\mu\nu} = (p+\rho)u^\mu u^\nu + pg^{\mu\nu}-$, the energy density must be nonnegative, and greater than or equal to the magnitude or the pressure, $\rho \geq |p|$).

As noted in [5], the Cosmic Censorship conjecture refers to the formation of naked singularities, not their existence: there are certainly solutions in which spacelike naked singularities

exist in the past (e.g. Schwarzschild white hole) or timelike singularities exist for all times (e.g. super-extremal charged black hole). Also a rotating Kerr black hole can produce a naked singularity when the spin of the black hole exceeds the square of the mass of the black hole. The cosmic censorship conjecture has not been proven, although a lot of effort has gone into finding convincing counterexamples. The requirement of the initial data to be "generic" plays an important role, as some numerical experiments have shown that finely tuned initial conditions are able to give rise to naked singularities. Nevertheless, a formal and precise proof of some form of the cosmic censorship conjecture remains as one of the open questions and problems of classical General Relativity [208, 209, 210].

A related property, previously mentioned, about the existence and location of the apparent and event horizons, can be restated under the assumption of the cosmic censorship conjecture's validity. If the cosmic censorship conjecture holds, and the *null energy condition*[19] is satisfied, then the presence of an apparent horizon implies the existence of an event horizon that lies outside, or coincides with, the apparent horizon.

Additionally a consequence of the cosmic censorship is that the areas of classical black holes never shrink. This is known as Hawking's area theorem.

1.5.2 Gas Dynamics around BHs

There is a growing body of optical observations of active galactic nuclei (AGN) [211, 212] in which different emission regions, particularly those responsible for the broad-line and narrow-line components [111, 213], are observed at significantly different velocities. Many different theoretical models for these systems have been proposed [214, 215], nearly all of which involve binary supermassive black holes (SMBH) [216], particularly those shortly before or immediately after a gravitational wave-driven merger. At present, theoretical and numerical simulations of these systems are still in their infancy, and there is a noticeable lack of observational criteria that can distinguish between pre-merger binaries, post-merger systems, and other dynamical configurations [217, 218, 219, 220, 113].

Supermassive black holes, which are supposed to reside at the centers of nearly all galaxies

[221], are likely the most important tracers to study galaxy formation and evolution throughout cosmological time [222]. SMBH mergers, driven at first by dynamical friction with stars and gas and later [223], once they approach close enough, by angular momentum losses via gravitational radiation [224], are likely to be the main cosmological source of low frequency gravitational waves [225, 226, 227]. There is a growing body of observational results indicating that AGNs containing either merging SMBHs or newly merged SMBHs, may have already been detected [117, 118, 119, 120]. Unfortunately, interpreting observations of dynamically perturbed AGNS has proven difficult [228], in large part due to an incomplete theoretical modeling and understanding predictions of what one is expected to see when observing such systems.

The past few years have seen tremendous advances in the theoretical study of merging supermassive binary black holes and the kicks imparted to the larger SMBH that results, which can recoil at speeds up to 4000 km/s for optimal system configurations [91]. Additionally there are studies of the statistical probabilities of spins and recoil velocities distributions for dry [229] and wet mergers [109]. Simultaneously, several systems have been observed that might be examples of this process. Beginning with SDSSJ092712.65+294344.0 [111], an AGN in which the broad-line emission appears blueshifted by 2650 km/s with respect to the narrow-line emission, there are now several sources that show substantial redshift differences between broad and narrow-line emission regions. These include SDSS J105041.35+345631.3 (3500km/s) [114], CXOC J100043.1+020637 (1200km/s) [115], and E1821+643 (2100 km/s) [116]. To date, none of these has been confirmed to represent an accretion disk around a recoiling SMBH, in part because it remains unclear how to distinguish such a source from other models including broadline emission from the smaller SMBH within a binary surrounded by a disk [214, 215], a pair of SMBHs at the respective centers of interacting galaxies [216], and even chance spatial coincidence [112]. Still, the post-merger scenario remains entirely plausible, and several theoretical simulations of post-merger disks have been performed, using a variety of numerical techniques, and a relatively coherent picture is emerging.

More than any other factor, interpreting observations of dynamically perturbed AGNs is

inhibited by the uncertainty in how to distinguish a system prior to merger from a post-merger one. There have been theoretical studies of binaries surrounded by up to three disks, one bound to each of the SMBH and a circumbinary disk surrounding the binary. Smoothed particle hydrodynamics studies [219, 230] have shown that the inner disks will be fed by mass transfer from the circumbinary disk, as the $m = 2$ azimuthal gravitational perturbation induces an elongation in the outer disk. For circular orbits, the mass transfer rate is relatively constant, while for elliptic binaries the mass transfer takes on a more periodic character. Finally, once the binary begins its gravitational radiation-driven plunge, the binary decouples form the outer disk, and mass transfer basically ceases. Schnittman and Krolik in [226], found that the inner edge of the circumbinary disk was likely to occur at roughly $1000M$, in typical relativistic units where $G = c = 1$, with the value dependent on disk parameters like the assumed α-parameter [218].

Other systems demonstrate clear indications of dynamical interactions in their observed emission. OJ287 is a blazar that undergoes quasi-periodic outbursts on a roughly 12-year cycle, with a double peak occurring roughly 1 year apart [231, 232]. It is difficult to constrain the exact system properties, since we see only the jet and not the surrounding disk, but a detailed analysis of the timing of the bursts indicates that they are consistent with the passage of a "small" SMBH with mass $M_2 = 1.2 \times 10^8 M_\odot$ on an orbit with eccentricity $e = 0.66$ through the accretion disk of a substantially larger one of mass $M_1 = 1.8 \times 10^{10} M_\odot$, leading to a temporary phase of enhanced accretion flow [233, 234].

Among the most interesting strongly gravitating astrophysical systems that the state-of-the-art codes can begin to accurately simulate in the next few years are "wet merger"[20] black-hole binaries and the corresponding electromagnetic counterpart associated with the gravitational waveform. Such simulations require fully-nonlinear numerical relativity simulations with magnetohydrodynamics (i.e. in presence of matter and electromagnetic fields).

The main goal of this kind of simulation is to obtain the electromagnetic counterpart of the gravitational radiation triggered by the strong gravity scenario coupled via matter and

[20]The term "wet mergers" is usually reserved for environments where there is some sort of matter present, as opposed to "dry mergers" that are referred as mergers in vacuum (no matter present).

the so called "viscous dissipation"[21]. For that reason it is necessary to implement full General Relativistic MagnetoHydroDynamics (GRMHD) codes able to handle the electromagnetic interaction with matter in the strong gravity regime. Moreover this type of code is hard to implement, not only because the difficulties in the complexity of the problem to be tackled but also because of the technical challenges involved. One of the most well known issues is the divergence-free constraint coming from the magnetic non-existence of monopoles law. Several different techniques have been tried to overcome this issue, e.g. divergence cleaning, constraint damping, etc. On the other hand, having a code with such features will allow the study of some of the most spectacular astrophysics scenarios, e.g. the central engines at the AGN and their powerful astrophysical jets [53, 54].

1.6 Research Projects

For this PhD thesis several different projects were developed and executed. Basically each of the subsequent chapters describe the projects. Additionally we will emphasize the most important concepts described previously in this introductory chapter, linking each of these fundamental concepts from the theory with the corresponding research project:

- Event horizons (Sec. 1.5.1) were investigated and numerically computed for particular and interesting configurations.

- Gravitational recoils "kicks" of black holes, due to the asymmetric emission of gravitational radiation (Secs. 1.3.1 and 1.5.2), in presence of accretion disks were modeled and analyzed numerically via the implementation and simulations of hydrodynamics techniques.

Following we present a brief review and summary of the corresponding research projects.

[21]The term *viscosity* in this context is highly controversial, perhaps leading to some degree of confusion because it is actually more appropriate to denominate it as "shear" more than a "viscous dissipation" [235, 40].

1.6.1 Event Horizons and Topological Censorship

For the event horizon searches, we look for toroidal slices of the event horizon from an initially stationary ring singularity [22]. Our main goal was to evolve a continuum ring singularity, a discrete ring, and linear BH configurations. To this end, we construct initial data inspired by electrostatic methods ("method of images") and the superposition principle for Brill-Lindquist initial data. I implemented the initial data in a thorn within the `cactus` framework [236, 237, 238, 239, 240] and evolved the system using fixed mesh refinement (`carpet` [241, 242]) and unigrid (`PUGH`) drivers. This required two evolutions: a forward in time evolution (saving the full spacetime in a region large enough to contain the EH) and a subsequent backwards in time evolution to locate the EH. Here I used the final apparent horizon (AH) from the first evolution as an initial guess for the EH in the backwards evolution. Because the null generators diverge exponentially from the EH in a forward in time evolution, an initial guess close to the location of the true EH will exponentially converge to the EH in the backwards evolution.

We used the `EHFinder Cactus` thorn [243] to find EHs. In practice, we track the generators of the EH. Because generators that cross leave the EH, I needed to implement a scheme to locate when generators cross or form caustics. Once located, then those generators were removed from subsequent slices. With this "cleaning" algorithm, it was possible to determine the topology and structure of the spatial slices of the EH from several different configurations. Finally, the data was processed and visualized using `OpenDx` [244] and a custom visualization suite developed at RIT called `Spiegel` [1].

From the mathematical relativity point of view, this work involves an interesting analysis of the topology of the event horizons found. While topological censorship requires that the EH be simply connected, no such restriction in placed in the spatial slices. We were able to show that in the standard moving punctures gauge, there is no toroidal slice for BHs arranged on a ring. However, due to the way the common EH formed at a single timestep, we were able to show that a distortion of this slicing can produce toroidal slices. One can

[22] This project has been developed in collaboration with Prof. Yosef Zlochower (SMS/CCRG-RIT) and Prof. Carlos Lousto (SMS/CCRG-RIT).

even try modifying the lapse to demonstrate this numerically. We propose a reliable picture for the sequence of the EH topology for the continuum ring singularity, which turned out to be a tremendously demanding simulation for sufficiently large ring radii, inaccessible with the current technologies. Actually it is important to note that, unlike the case of discrete punctures, where the puncture singularities are only coordinate singularities, the singularities for these continuum ring and linear distributions are physical singularities. Interestingly, we found evidence that for the continuum ring configuration, rather than there being a toroidal slice, the singularity is not surrounded by an EH in the past which could be an indication of a naked singularity [245].

1.6.2 Newtonian Gas Dynamics around Kicked BHs

We developed a code using Smoothed Particle Hydrodynamics (SPH) techniques for studying "kicked" black-hole scenarios in the vicinity of disks [23]. The code is state-of-the-art for this type of simulation, guaranteeing not only excellent energy and angular momentum preservation but also combining novel techniques in order to deal with several numerical and technical details that usually are not considered.

For this project we implemented our own version of the Smooth Particle Hydrodynamic (SPH) techniques to evolve a 'kicked' black hole surrounded by an accretion disk. We also perform analytical studies of the "wet recoil" scenario, beginning with a study of the physical scales that define the kicked disk problem. Additionally we use a semi-analytic, 2-dimensional collisionless disk model to explore the dynamics of disks acted upon by gravitational attraction between disk matter and the BH only.

Using our SPH code, 3-dimensional collisional simulations were performed varying the recoiling angle. For generating the initial data, we construct semi-analytic models of accretion disks in hydrodynamic equilibrium to use as initial conditions before laying down particles using a Monte Carlo technique. To do so, we first assume that the orbital velocity is independent of the height within the disk and varies only with cylindrical radius. To get a disk with finite

[23] This project has been developed in collaboration with Prof. Joshua Faber (SMS/CCRG-RIT) and Prof. Jamie Lombardi (Allegheny College).

extent in the radial and vertical directions, we choose a non-Keplerian rotation profile. Here, we assume a power-law form, to yield a compactly bounded configuration. The precise method for generating the geometrical properties and their relation with the dynamics quantities will be widely discussed and presented in our publication and this thesis. Following this procedure we were able to produce a relaxed model, generating the initial profile of velocities in order to start the dynamical evolution.

In order to deal with the effects from the strong gravitational potential of the black hole for close particles, and to guarantee an almost perfect energy and angular momentum conservation, we implemented a "smoothed black hole potential" to account for the finite size of the particles. We ran the simulations on parallel CPUs, varying the recoil angle of the black hole with respect to the accretion disk. As results we obtained individual variables such as positions, velocities and accelerations of the SPH particles. Also global dynamic quantities such as energies, entropy, were computed live during the simulations. Results from these simulations, focusing on the hydrodynamic and thermodynamic evolution of the disk, are reported in this thesis in detail in Chapter 4.

We wrote and applied a set of routines to post-process and analyze the raw data coming from the simulations for computing relevant astrophysical quantities. We distinguished and identified between dynamically bounded and unbounded portions of the disk and quantified energies, angular momenta, and orientations of the disks. The different cases studied allow us to distinguish among properties correlated to the angles of recoil. Among the astrophysical interesting quantities computed are surface densities, luminosity (as the variation of the internal energy) and temperature profiles. We further discuss bounded/accreted material, and models for the optical properties of the disk (optical thin/thick), etc.

To the best of our knowledge, so far in the literature there is only one investigation that tackles these sorts of scenarios with the same technique described here [246] and we believe that the novel approach we used and the techniques we implemented will provide a unique perspective and with unprecedented result and insights in these situations. Two main results highlight this research: we found strong evidence correlating the kick angle and a depletion

of matter ("gap") in the inner region of the disk; also tidal tails were apparent with more oblique recoils. We also found associated peaks in luminosity for certain recoiling angles, which could lead to interesting counterpart signatures and represent a potential way to identify observational clues from "kicked black holes" [247].

1.6.3 Organization

The rest of this thesis is organized as follows: in Chapter 2, the basic concepts and formulations behind Numerical Relativity are reviewed, as well as the computational framework for implementing the computational simulations; in Chapter 3, the "Event Horizons for a Ring Singularity" research project is treated and studied in detail; in Chapter 4, "Gravitational Recoils of Black Holes surrounded by Accretion Disks" are investigated using Smoothed Particle Hydrodynamics simulations; finally in Chapter 5, we will summarize and compile the main results and projects from this thesis, and we will discuss future directions, proposals and remaining open questions.

Overview Last but not least, we would like to recall the cohesive picture underlying and connecting the projects investigated in this thesis. Each of these projects refers to a particular stage in the timeline of the picture of a black hole interaction scenario (e.g. a BHB merger). Beginning with well separated black holes, it is possible to study the "structure" of the event horizons (see Chapter 3) in a region close enough to the BH so the topological structure of the BH can be studied. Continuing with the timeline, as the BHB merges and radiates, it will get a kick that will affect the accretion disk (post-merger event, see Chapter 4), while the waveform would be observable as a gravitational signal, the merger will lead to a unique imprint in the surrounding matter. In summary, each of our research projects studies a particular stage (either localized or separated in time and space) in the evolution of black holes interactions (e.g. merger timeline).

Chapter 2

Numerical Relativity

In this Chapter we review the basic concepts of Numerical Relativity, starting with a brief review of the formalism of General Relativity. Some basic concepts were already introduced in Chapter 1, and will be revisited and expanded in this chapter.

Moreover, this Chapter itself, as well as most of the material presented in Chapter 1, are reviews of very well known topics in the field of Astrophysics, General Relativity and Numerical Relativity. In particular this Chapter, represents a summary and overview of the following references [123, 124, 5].

Conventions We use the usual conventions followed in Numerical Relativity literature, e.g. the use of Einstein summation convention of addition over repeated indices, Greek-indices for spacetime components (i.e. $\mu = 0, 1, 2, 3$), Latin-indices for spatial components (i.e. $i = 1, 2, 3$).

2.1 General Relativity Formalism

2.1.1 Mathematical Foundations of General Relativity

2.1.1.1 The Metric Tensor

General Relativity as mentioned in Sec.1.1, is a theory about the geometry of spacetime. One of the fundamental concepts in General Relativity is the 4-dimensional *spacetime*, which can be described mathematically by the combination of a 4-dimensional Lorentzian manifold M and a *metric* g: (M, g).

The metric, usually represented by a second rank tensor $g_{\mu\nu}$, is a symmetric bilinear map from $T_p \otimes T_p$ to $\mathbb{R}$, where T_p is the tangent space at the point p on the manifold M and $\otimes$ represents the usual Cartesian product. The inner product of two vectors is given by,

$$g_{\mu\nu} v^\mu w^\nu. \tag{II-1}$$

The metric also expresses the relation between the coordinates $x^\mu = (x^0, x^1, x^2, x^3)$ and physical distances. The invariant interval (distance) between two nearby events in the spacetime is given by,

$$ds^2 = g_{\mu\nu} dx^\mu \otimes dx^\nu. \tag{II-2}$$

The metric is not-positive definite, so zero-length curves and vectors are possible. These null directions are the characteristics of the theory.

In general the components of the metric tensor are given by the scalar product between the four basis vectors $\mathbf{e}_\mu$ that span the vector space tangent to the spacetime manifold,

$$\mathbf{e}_\mu \cdot \mathbf{e}_\nu = g_{\mu\nu}. \tag{II-3}$$

2.1.1.2 Covariant Derivative

It is important to recall that in the field of General Relativity we are dealing with a 4-dimensional curved spacetime. Therefore in order to define derivatives, we need to account for

the contribution of changes induce by the curvature of the spacetime. For instance, to know how a 4-vector changes we need to define an appropriate "derivative", namely the *covariant derivative*. For a contravariant 4-vector v^μ, the covariant derivative can be written as,

$$v^\mu_{;\nu} = \nabla_\nu v^\mu = \partial_\mu v^\nu + \Gamma^\mu_{\nu\sigma} v^\sigma, \tag{II-4}$$

where $\Gamma^\mu_{\nu\sigma}$ are *connection coefficients*, or in the case of coordinates bases, Christoffel symbols, associated to the spacetime metric $g_{\mu\nu}$. The connections coefficients measure the changes in the metric coefficients along the coordinate directions. In a coordinate basis they are related to partial derivatives of the metric,

$$\Gamma^\lambda_{\mu\nu} = \frac{1}{2} g^{\lambda\sigma}(\partial_\mu g_{\nu\sigma} + \partial_\nu g_{\sigma\mu} - \partial_\sigma g_{\mu\nu}). \tag{II-5}$$

The covariant derivative given by Eq.(II-4) for a contravariant 4-vector, can be generalized for covariant 4-vectors (1-forms in the language of differential geometry) and tensors, and has the form

$$\nabla_\sigma T^{\mu_1\mu_2\ldots\mu_k}_{\nu_1\nu_2\ldots\nu_l} = \partial_\sigma T^{\mu_1\mu_2\ldots\mu_k}_{\nu_1\nu_2\ldots\nu_l} + \Gamma^{\mu_1}_{\sigma\lambda} T^{\lambda\mu_2\ldots\mu_k}_{\nu_1\nu_2\ldots} + \Gamma^{\mu_2}_{\sigma\lambda} T^{\mu_1\lambda\ldots\mu_k}_{\nu_1\nu_2\ldots} + \ldots - \Gamma^{\lambda}_{\sigma\nu_1} T^{\mu_1\mu_2\ldots\mu_k}_{\lambda\nu_2\ldots} - \Gamma^{\lambda}_{\sigma\nu_2} T^{\mu_1\mu_2\ldots\mu_k}_{\nu_1\lambda\ldots} - \ldots \tag{II-6}$$

2.1.1.3 Lie derivative

The covariant derivative is associated with curvature, as it was explained before. There is a more primitive derivative, known as the *Lie derivative* which does not depend on curvature. The *Lie derivative* measures the change of a vector field, or more generally a tensor field, along the flow of another vector field. This change is coordinate invariant and therefore the Lie derivative is defined on any differentiable manifold. To obtain the Lie derivative one evaluates the vector at a point $q = \phi_\lambda(p)$, drags it back to a point p using ϕ^{-1}, and takes the difference with original vector at p in the limit when $\lambda \to 0$, i.e. the Lie derivative of a vector

field is given by,

$$\pounds_{\vec{v}}\vec{u} \triangleq \lim_{\lambda\to 0}\left[\frac{\phi_{-\lambda}^{-1}(\vec{u}_{|\phi_\lambda(p)}) - \vec{u}_{|p}}{\lambda}\right], \tag{II-7}$$

where ϕ is a diffeomorphism mapping from q to p. Clearly the Lie derivative depends on the vector field ($\vec{v}$) used for the dragging.

For instance, the Lie derivative can be written as

$$\pounds_{\vec{x}}\vec{v} = x^\nu \nabla_\nu v^\mu - v^\nu \nabla_\nu v^\mu, \tag{II-8}$$

which is independent of the connection $\Gamma^\mu_{\nu\sigma}$.

The Lie derivative of a scalar function f, is defined as,

$$(\mathcal{L}_X f)(p) \triangleq \frac{\mathrm{d}}{\mathrm{d}\,t} f(\gamma(t))\bigg|_{t=0},$$

where $\gamma(t)$ is a curve on M such that $\frac{\mathrm{d}}{\mathrm{d}\,t}\gamma(t) = X_{\gamma(t)}$ for the smooth vector field X on M with $p = \gamma(0)$.

The components of the Lie derivative, are given by

$$\pounds_{\vec{v}}\vec{u} = v^\beta \partial_\beta u^\alpha - u^\beta \partial_\beta v^\alpha. \tag{II-9}$$

It is associated with commutator of two vectors, given by,

$$[\vec{v},\vec{u}]^\alpha \triangleq v^\beta \partial_\beta u^\alpha - u^\beta \partial_\beta v^\alpha, \tag{II-10}$$

where

$$\pounds_{\vec{v}}\vec{u} = [\vec{v},\vec{u}]\,. \tag{II-11}$$

Furthermore, it is possible to extend the definition to all type of geometrical objects, such

as covectors or one-forms ($\tilde{\omega}$), tensors (T^{α}_{β}), and tensor densities ($\gamma^{w/2}T^{\{\cdots\mu\nu\cdots\}}$):

$$\pounds_{\vec{v}}\omega_{\alpha} = v^{\beta}\partial_{\beta}\omega_{\alpha} - \omega_{\beta}\partial_{\beta}v^{\alpha}, \tag{II-12}$$

$$\pounds_{\vec{v}}T^{\alpha}_{\beta} = v^{\mu}\partial_{\mu}T^{\alpha}_{\beta} - T^{\mu}_{\beta}\partial_{\mu}v^{\alpha} + T^{\alpha}_{\mu}\partial_{\beta}v^{\mu}, \tag{II-13}$$

$$\pounds_{\vec{\beta}} = \Big[\pounds_{\vec{\beta}}T\Big]_{w=0} + wT\partial_{i}\beta^{i}. \tag{II-14}$$

An interesting geometrical interpretation of the Lie derivative, assuming that the coordinate line is the integral curve of the vector field $\vec{v}$, i.e. $v^{\alpha} = \delta^{\alpha}_{\hat{e}_i}$, then $\pounds_{\vec{v}}T^{\alpha\beta\ldots}_{\mu\nu\ldots} = \partial_{\hat{e}_i}T^{\alpha\beta\ldots}_{\mu\nu\ldots}$. Therefore the Lie derivative represents a way to write partial derivatives along direction of a vector field independent of the coordinates.

2.1.1.4 Killing fields and Symmetries

An important application of the Lie derivative is associated with *symmetries* of a manifold. A manifold has a specified symmetry with respect to some vector field $\vec{\xi}$ if $\pounds_{\vec{\xi}}g = 0$, where g is the metric; i.e. $\xi^{\mu}\partial_{\mu}g_{\alpha\beta} + g_{\alpha\mu}\partial_{\beta}\xi^{\mu} + g_{\mu\beta}\partial_{\alpha}\xi\mu = 0$. This allows one to define a *Killing field*, which are vectors fields $\vec{\xi}$ obeying

$$\pounds_{\vec{\xi}}g = 0. \tag{II-15}$$

The existence of Killing fields implies the presence of symmetries in the manifold. This can be easily seen by considering coordinate lines adapted to the integral curve of $\vec{\xi}$, then if $\vec{\xi}$ (or correspondingly the coordinate line –$\hat{e_j}$–) is a Killing field, then $\partial_{\hat{e_j}}g_{\alpha\beta} = 0$ which implies that the components of the metric tensor are in fact independent of the coordinate x^{j}.

Timelike Killing vectors

- A metric that possesses a Killing vector that is timelike near infinity is called *stationary.*
- More restrictively, a metric is called *static* if it possesses a timelike Killing vector that is orthogonal to a family of hypersurfaces.

2.1.1.5 Parallel Transport

Given any metric $g_{\mu\nu}$, it is possible to define the Riemann curvature tensor (see Eq.(II-17)), which is directly associated with concept of *parallel transport*. The generalization of the concept of derivatives to covariant derivative, takes into account the fact that, being embedded in a curved manifold the changes to geometrical objects (4-vectors, 1-forms, tensors) along given paths have contributions due to the curvature. Mathematically, the parallel transport of a 4-vector v^μ along the path γ obeys,

$$T^\nu \nabla_\nu v^\mu = 0, \tag{II-16}$$

where T^ν is the tangent to the path γ; i.e. the covariant change in v^μ is zero along γ.

Parallel transport allows one to drag a vector along a curve keeping it as "unchanged" as possible.

2.1.1.6 Riemann Tensor

The Riemann tensor, can be represented as a combination of partial derivatives of the connections of the metric (at the end it will be a expression combining products of first derivatives and second derivatives of the metric), given by

$$R^\mu_{\nu\delta\gamma} = \Gamma^\mu_{\nu\gamma,\delta} - \Gamma^\mu_{\nu\delta,\gamma} + \Gamma^\mu_{\delta\sigma}\Gamma^\sigma_{\nu\gamma} - \Gamma^\mu_{\nu\sigma}\Gamma^\sigma_{\delta\gamma}. \tag{II-17}$$

It basically contains the information of how the spacetime manifold is geometrically described, e.g. it can be interpreted/defined as the parallel transport deficit in a closed path due to the curvature, or the non-commutativity behavior of second cross covariant derivatives of tensor fields, or the geodesic deviation of free falling particles. The Riemann tensor, is a rank four tensor, which can be expected to have n^4 independent components in an n-dimensional space. But because this tensor also obeys certain symmetry properties (antisymmetry in the first and last pair of indices: $R_{\rho\sigma\mu\nu} = -R_{\rho\sigma\nu\mu}$, $R_{\rho\sigma\mu\nu} = -R_{\sigma\rho\mu\nu}$; symmetry under interchange of first and last pair of indices: $R_{\rho\sigma\mu\nu} = R_{\mu\nu\rho\sigma}$; and vanishing antisymmetric part of the last three

indices: $R_{\rho[\sigma\mu\nu]} = 0$), these symmetries reduce the actual number of independent components to $\frac{1}{12}n^2(n^2-1)$. In four dimensions, therefore, the Riemann tensor has 20 independent components (in one dimension it has none). These twenty functions represent the 20 degrees of freedom in the second derivatives of the metric. This is also consistent with this tensor as an appropriate measure of curvature.

Of practical importance are the Ricci tensor $R_{\mu\nu}$ and the Einstein tensor $G_{\mu\nu}$, as it has been shown in Sec.1.1.1 and will be seen in Sec.2.1.4. The Ricci tensor is defined as a contraction of the Riemann tensor,

$$R_{\mu\nu} = R^{\lambda}{}_{\mu\lambda\nu}, \tag{II-18}$$

and the Einstein tensor is defined as

$$G_{\mu\nu} = R_{\mu\nu} - \frac{1}{2}Rg_{\mu\nu}, \tag{II-19}$$

where R is the Ricci scalar, given by the contraction of the Ricci tensor, $R = R^{\mu}_{\mu}$.

In order to contract indices from tensors, it is necessary to use the metric $g_{\mu\nu}$: the metric can be used to lower or raise indices (e.g. $v_\mu = g_{\mu\nu}v^\nu$); and following the Einstein convention of summation for repeated indices is possible to contract a tensor reducing its rank.

2.1.1.7 Geodesics

Another important application of the concepts of the covariant derivative and parallel transport has to do with the generalization of a straight line for curvilinear coordinates on curved manifolds. In Euclidean space, a straight line is a curve such that its tangent always remains parallel to itself. Using the same idea, by defining a *geodesic* as a curve that parallelly transports its own tangent vector, i.e. a curve whose tangent vector v^μ satisfies,

$$v^\beta \nabla_\beta v^\alpha = 0. \tag{II-20}$$

A geodesic (affine parametrized) is simply a curve that remains locally as straight as

possible. From Eq.(II-20), the equation for a geodesic can be rewritten as,

$$\frac{d^2x^\alpha}{d\lambda^2} + \Gamma^\alpha_{\beta\gamma}\frac{dx^\beta}{d\lambda}\frac{dx^\gamma}{d\lambda} = 0, \tag{II-21}$$

where λ is a parameter (affine) that allows to characterize (parametrize) the curve.

Geodesics are extremal curves of the spacetime, in the sense that its length,

$$l = \int \sqrt{g_{\mu\nu}\dot{x^\mu}\dot{x^\nu}}ds, \tag{II-22}$$

has the maximum possible length in time (for a timelike curve) or the minimum possible length in space (for a spacelike curve). This result can be shown by taking variations over Eq.(II-22), such that $\delta l = 0$.

2.1.2 Black Holes

Black Holes are particular solutions to the Einstein field equations (see Sec.2.1.4). A black hole is region of spacetime that cannot communicate with the outside universe. The boundary of this region is a 3-dimensional hypersurface in spacetime (a spatial 2-dim surface propagating in time) called an *event horizon* or surface of the black hole. Nothing can escape from the interior of a black hole, not even light. Spacetimes singularities form inside the black holes, as it is enclosed by the BH, the singularity is "causally disconnected" from the exterior universe. Einstein's equations can still describe the outside universe, but they supposedly break down inside the black hole due to the singularity.

The most general stationary black hole solution to Einstein's equations is the analytical Kerr-Newman solution. It is uniquely described by only three parameters: the mass M, the angular momentum J and the charge Q of the black hole. Special cases of this solution are the Kerr black hole ($Q = 0$), the Reissner-Nordström black hole ($J = 0$), and the Schwarzschild black hole ($J = 0$, $Q = 0$).

2.1.2.1 Schwarzschild Black Hole

In General Relativity, the assumption of both spherical symmetry and vacuum (i.e. $T^{\mu\nu} = 0$) implies that the metric is the Schwarzschild metric,

$$ds^2 = -\left(1 - \frac{2GM}{r}\right) dt^2 + \left(1 - \frac{2GM}{r}\right)^{-1} dr^2 + r^2(d\theta^2 + \sin^2\theta d\phi^2), \tag{II-23}$$

which is a static and spherically symmetric spacetime. This means that there are no dynamical spherical symmetric spacetimes (Birkhoff's Theorem).

An important feature regarding spherically symmetric metrics, is that any spherically symmetric vacuum metric possesses a timelike Killing vector, i.e. it is stationary.

The Schwarzschild metric has a physical singularity at the origin, $r = 0$; while it has a coordinate singularity at $r = 2GM$ in the given form of Eq.(II-23), which can be removed by an appropriate change of variables.

2.1.2.2 Charged Reissner-Nordström Black Hole

The Reissner-Nordström metric represents a closed form solution for electrically charged black holes. This sort of object is not extremely relevant in astrophysical scenarios, in nature a highly-charged black hole would be quickly neutralized (because the electromagnetic force is much stronger than the gravitational). The Reissner-Nordström metric is given by,

$$ds^2 = -\left(1 - \frac{2GM}{r} + \frac{GQ^2}{r^2}\right) dt^2 + \left(1 - \frac{2GM}{r} + \frac{GQ^2}{r^2}\right)^{-1} dr^2 + r^2(d\theta^2 + \sin^2\theta d\phi^2). \tag{II-24}$$

This spacetime is still spherically symmetry, although, the solution is no longer a vacuum spacetime since the nonzero electromagnetic field acts as a source of energy-momentum. The electromagnetic fields associated with this solution are,

$$\begin{aligned} E_r &= F_{rt} = \tfrac{Q}{r^2}, \\ B_r &= \tfrac{F_{\theta\phi}}{r^2 \sin\theta} = 0. \end{aligned} \tag{II-25}$$

The Reissner-Nordström metric has a physical singularity at $r = 0$.

2.1.2.3 Rotating Kerr Black Hole

The Kerr black hole solution is an axially symmetric solution that is also stationary. It has the form,

$$\begin{aligned} ds^2 &= -\left(1-\tfrac{2GMr}{\rho^2}\right)dt^2 - \tfrac{2GMar\sin^2\theta}{\rho^2}\left(dtd\phi + d\phi dt\right) \\ &\quad + \tfrac{\rho^2}{\Delta}dr^2 + \rho^2 d\theta^2 + \tfrac{\sin^2\theta}{\Delta}\left[(r^2+a^2) - a^2\Delta\sin^2\theta\right]d\phi^2, \end{aligned} \tag{II-26}$$

with $\Delta(r) = r^2 - 2GMr + a^2$ and $\rho^2(r,\theta) = r^2 + a^2\cos^2\theta$, where a is the angular momentum per unit mass, $a = J/M$.

The Kerr metric has a ring singularity, which in the case where the spin parameter a goes larger than M (extremal Kerr), the black hole losses its event horizon and the singularity is naked.

2.1.2.4 Rotating Charged Kerr-Newman Black Hole

The Kerr-Newman black hole represents the simplest stationary, axisymmetric, asymptotically flat solution of Einstein's equations in the presence of an electromagnetic field in four dimensions. It is sometimes referred to as an "electrovacuum" solution of Einstein's equations. It has the form

$$\begin{aligned} ds^2 &= -\left(1-\tfrac{2GMr-GQ^2}{\rho^2}\right)dt^2 - \tfrac{(2GM-GQ^2)ar\sin^2\theta}{\rho^2}\left(dtd\phi + d\phi dt\right) \\ &\quad + \tfrac{\rho^2}{\Delta}dr^2 + \rho^2 d\theta^2 + \tfrac{\sin^2\theta}{\Delta}\left[(r^2+a^2) - a^2\Delta\sin^2\theta\right]d\phi^2, \end{aligned} \tag{II-27}$$

where $\Delta(r) = r^2 - (2GMr - GQ^2) + a^2$ and $\rho^2(r,\theta) = r^2 + a^2\cos^2\theta$, and a is the angular momentum per unit mass, $a = J/M$.

The Kerr-Newman metric defines a black hole with an event horizon only when $a^2 + Q^2 \leq M^2$, otherwise it is naked.

2.1.2.5 Global Theorems

There are many interesting and surprising theorems related to black holes. In Chap.1 we mentioned the "No-Hair" theorem, in Chap.3 several "singularity theorems" are discussed. In Sec.2.1.2.1 we mention "Birkhoff's theorem". Furthermore, Hawking [248] has formulated a set

of "four laws of black hole mechanics" remarkably similar to the four laws of thermodynamics.

One important consequence resulting from the "second law of black hole dynamics" states that: for an isolated system, the sum of the surface areas of all black holes can never decrease.

For instance, considering the case of a Kerr black hole, the surface area is the area $\mathcal{A}$ of the horizon at a given time, is given by

$$\mathcal{A} = 8\pi M \left(M + (M^2 - a^2)^{1/2} \right), \tag{II-28}$$

which reduces to $\mathcal{A} = 4\pi(2M)^2$ when $a = 0$.

By defining the *irreducible mass* M_{irr} as,

$$M_{irr} = \sqrt{\frac{\mathcal{A}}{16\pi}}, \tag{II-29}$$

then

$$M^2 = M_{irr}^2 + \frac{J^2}{4M_{irr}^2}. \tag{II-30}$$

Thus, the mass of a Kerr black hole is composed of an irreducible contribution plus a rotational kinetic energy contribution.

2.1.3 Asymptotically Flatness

An *asymptotically flat spacetime* is a Lorentzian manifold in which, roughly speaking, the curvature vanishes at large distances from some central region, so that at large distances, the geometry becomes indistinguishable from the Minkowski spacetime. Asymptotically flat spacetimes can be thought of as an isolated system in General Relativity, although no physical system can truly be isolated from the rest of the universe, the concept can be considered as an approximation in order to study the structure of a particular system ignoring the influence of distant matter, curvature, or energy.

The previous definition of asymptotically flat spacetime, is a coordinate based definition, i.e. the definition can be formulated in such a way that given some restricted coordinate system $\{x^0, x^1, x^2, x^3\}$, the metric components in these coordinates behave in an appropriate

way at large coordinate values, i.e. $g^{\mu\nu} = \eta^{\mu\nu} + O(l/r)$ as $r \to \infty$, along either spatial or null directions. Although this definition is adequate in many respects, it is very difficult to work with it since the coordinate invariance of all statements must be carefully checked.

These difficulties have been solved by a formulation of the notion of asymptotic flatness which defines a spacetime to be asymptotically flat if an appropriate boundary representing "points at infinity" can be "added" to the spacetime in a suitable way. This type of definition is manifestly coordinate independent, and, by providing definite boundary points representing infinity, it eliminates most of the difficulties associated with taking limits to infinity.

Actually both concepts, asymptotically flatness and limits going to infinity, are important for extracting information from the spacetimes (e.g. when extracting gravitational waves).

One formal way to proceed is, starting with the metric given on a suitable coordinate system, consider a *conformal transformation* of the physical spacetime M to an unphysical, or conformal, spacetime $\bar{M}$ via

$$\bar{g}_{\mu\nu} = \Omega^2 g_{\mu\nu}, \tag{II-31}$$

where $\Omega^2(x) > 0$ is a smooth function that gets arbitrary small at large distances. Then we add points to $\bar{M}$ corresponding to $\Omega = 0$, such points are necessarily infinitely far away in physical units. These points are considered to be the boundary of spacetime and form the set called *conformal infinity*.

By doing this we have extended the physical space M into an unphysical space $\bar{M}$, such that M is contained in $\bar{M}$. Additionally it allows one to introduce some special points and locations in the extended unphysical space. In the first place, all spacelike curves that are infinitely extended in M intersect the boundary at the same point i_0 in $\bar{M}$, known as *spacelike infinity*. In the neighborhood of i_0 there is a region of the boundary corresponding to null curves that are infinitely extended either to the future or to the past, called *future null infinity* $\mathscr{I}^+$ and *past null infinity* $\mathscr{I}^-$ respectively (the symbol $\mathscr{I}$ is usually referred to as "scri").

In addition there are the points i^+/i^-, where timelike geodesics start/stop. A spacetime that allows this construction is asymptotically flat, which formalizes the definition of "far away" from sources.

Additionally, it allows for precise definition of event horizon: an event horizon $\mathcal{H}$ is given by $\dot{J}(\mathscr{I}^+) \cap M$, i.e. the boundary of all events visible to $\mathscr{I}^+$. Note that the symbol $\dot{J}$ represents the boundary of the causal past of $\mathscr{I}^+$. $\mathcal{H}$ is a 3-dim hypersurface with null generators that do not terminate at $\mathscr{I}^+$ but may begin at $\mathscr{I}^-$.

The *Causal past/future* of a point $p \in M$, is the set $J^+(p)/J^-(p)$ of all points that can be reached by a future/past directed causal curve starting at p; where a *causal curve* (or non-spacelike) is a curve in M where the tangent vector is nowhere spacelike. The boundary of $J(S)$, $\dot{J}(S)$, is necessarily a null hypersurface.

It is possible to represent the spacetime structure of a black hole by representing the lightcones (and thus the causal structure) of the spacetime with lines at 45° from vertical (as in the Minkowski spacetime diagrams of special relativity). This is made possible by the systematic distortion of spatial and temporal distances as one approaches the black hole.

Figure 2.1 represents a spherically symmetric spacetime with no black hole; it could be either empty flat space, or the spacetime containing a single stable sphere of matter. Each point represents a sphere of radius r where $4\pi r^2$ is the area. All of spatial infinity is condensed to a single point, i_0. All of future infinity is likewise represented by the point i^+, and all past infinity by i^-. Light paths that originate at some finite time will terminate on the future null infinity $\mathscr{I}^+$. The curved line stretching from past timelike infinity to future timelike infinity is a line of fixed radius r; e.g. the surface of a stable body sitting in space.

Figure 2.2 represents a spacetime in which a body has collapsed down to form a black hole. In this case, there will be some light paths that escape to infinity (i.e., to $\mathscr{I}^+$), but others will end at the central singularity (represented by the jagged line). The event horizon is the last light path that avoids the singularity and makes it out to infinity. The interior of the event horizon is the black hole. This way of picturing a black hole makes clear both that there is an interior to the black hole (which is missed by the Schwarzschild coordinates), and that once one enters a black hole, it is impossible to escape the central singularity without traveling faster than light (i.e., more than 45° from vertical).

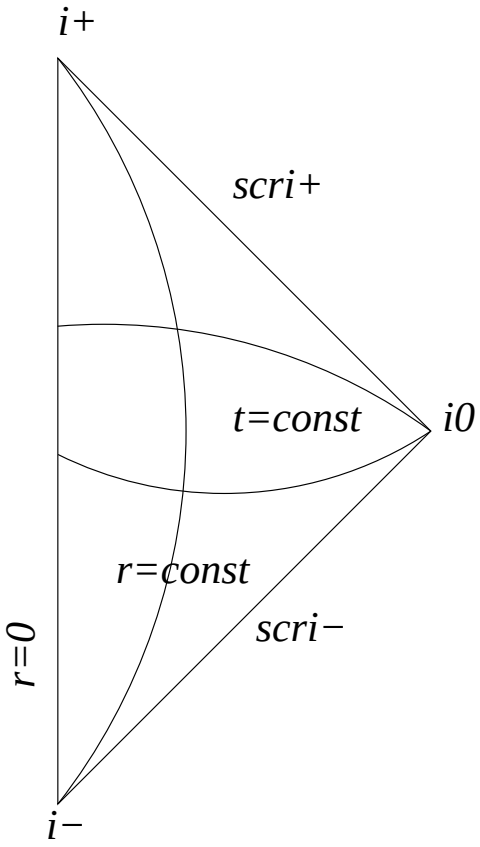

Figure 2.1: Conformal spacetime diagram for an empty flat spacetime (or a spherical symmetry without black holes).

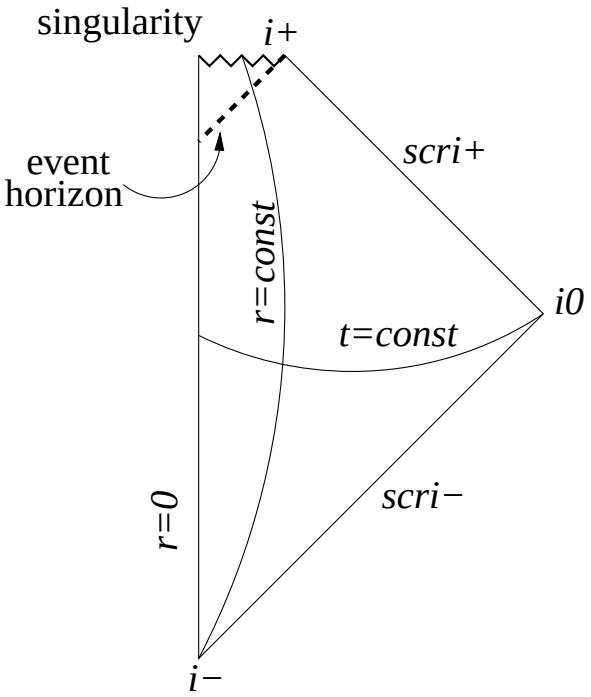

Figure 2.2: Conformal diagram for spacetime containing a black hole.

2.1.4 Einstein Field Equations

As described in Sec.1.1.1, Einstein's Equations relate the curvature of the spacetime with the stress-energy of matter and fields, through the relation

$$G_{\mu\nu} = \frac{8\pi G}{c^4} T_{\mu\nu}, \tag{II-32}$$

where $G_{\mu\nu}$ is the Einstein tensor, constructed from a nonlinear combination of first and second derivatives of the metric $g_{\mu\nu}$ ($G_{\mu\nu} = R_{\mu\nu} - \frac{1}{2} R g_{\mu\nu}$, where $R_{\mu\nu}$ is the Riemann tensor defined in Sec.1.1.1), and $T_{\mu\nu}$ is related to the energy and momentum of the matter and fields.

If the metric is known, then it is possible to determine how matter fields behave in the spacetime. The trick is that matter and energy affect the metric as well. That is $g_{\mu\nu}$ affects how $T_{\mu\nu}$ behaves and $T_{\mu\nu}$ affects $g_{\mu\nu}$ ("spacetime tells matter how to move, and matter tells spacetime how to curve"). Note that the Einstein equations relate the curvature associated with $g_{\mu\nu}$ to the stress energy, not the topology.

Two spacetimes (M_1, g_1) and (M_2, g_2) are equivalent if they can be mapped to each other by a diffeomorphism. Basically, this can be thought of as the coordinate freedom (gauge) in the theory. Therefore the Einstein Equations cannot give the metric uniquely, thus it is necessary to have supplementary conditions.

In their covariant form, the Einstein equations –Eq.(II-32)– are not hyperbolic. As mentioned before, the metric is not unique due to coordinate (gauge) freedom. Therefore, it is necessary to break covariance in order to put the equations into a hyperbolic form.

There have been several approaches to describe the evolution of the gravitational field as a *Cauchy problem* (i.e. providing the initial data and boundary conditions, in order to generate the evolution). Among the most well-known are: the «3+1» formalism, ADM or BSSN, the generalized harmonic formulation, as well as non-Cauchy formalisms, such as the characteristic formalism.

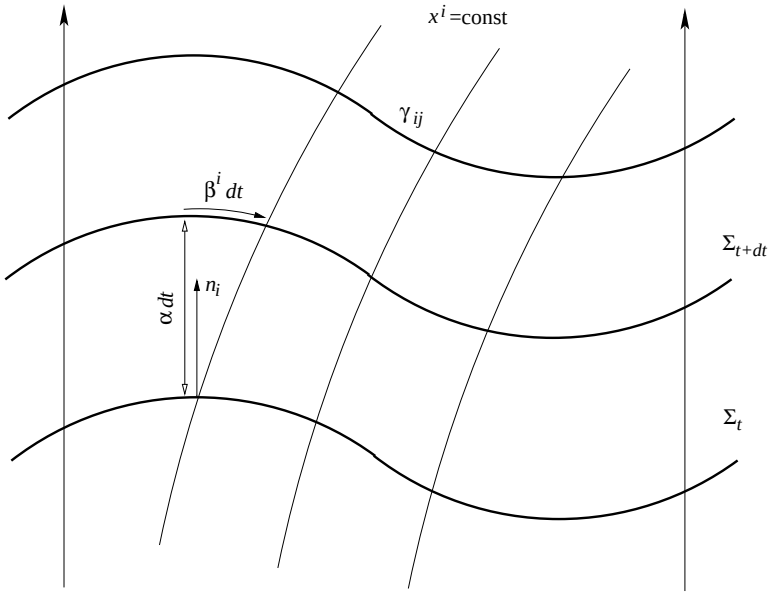

Figure 2.3: Graphical description of the «3+1» decomposition.

2.2 The 3+1 formalism

In order to perform evolutions, it is necessary to break the covariance of the Einstein equations by splitting the spacetime into a 3-dim spacelike hypersurface and a 1-dimensional time direction.

2.2.1 3+1 split of spacetime

For describing the Einstein equations as a Cauchy problem, the roles of space and time must be split in a clear way. The General Relativity formulation that emerges from this splitting is known as the *«3+1» formalism*. The first condition, is to assume that the spacetime of interest is *globally hyperbolic*, i.e. that it has a Cauchy surface [1]. Any globally hyperbolic spacetime can be completely foliated (i.e. sliced into 3-dim cuts) in such a way that each 3-dim slice is spacelike. Such 3-dim hypersurfaces are known as *foliations* Σ_t, and there is a induced 3-dim metric $\gamma_{ij}(t)$ on each surface Σ_t.

The geometry of the region of spacetime contained between two nearby slices can be

[1] Cauchy surface is a surface of the spacetime such that given initial conditions on this surface determines the future (and the past) uniquely. More precisely, a Cauchy surface is any subset of spacetime which is intersected by every non-spacelike, inextensible curve, i.e. any causal curve, exactly once.

determined by the following fields:

- The 3-dim metric γ_{ij}, $i,j = 1,2,3$ measures the *proper distance* within each 3-dim hypersurface, i.e. $dl^2 = \gamma_{ij}dx^i dx^j$.

- The *lapse function* $\alpha(t, x^i)$, measures *proper time* $d\tau$ between Σ hypersurfaces measured by observers moving along the normal to the hypersurface (so called normal or Eulerian observers), i.e. $d\tau = \alpha(t, x^i)dt$.

- The *shift vector* β^i, relates *coordinates* between consecutive hypersurfaces Σ_t and $\Sigma t + dt$ when moving along the normal direction, i.e. on the normal $x^i_{t+dt} = x^i_t - \beta^i(t, x^j)dt$. In other words, it represents the relative velocity β^i between the Eulerian observers and the lines of constant spatial coordinates.

This setup is shown in Fig. 2.3.

The way in which the spacetime is foliated, and also the way in which the spatial coordinate system propagates from one hypersurfaces to the next, is not unique. The lapse function α and the shift vector β^i are therefore freely specifiable functions that carry information about the choice of the coordinate system, consequently they are known as gauge functions.

2.2.1.1 3d/4d metric relation

In terms of the functions $\alpha, \beta^i, \gamma_{ij}$, the metric of the spacetime is be given by,

$$ds^2 = (-\alpha^2 + \beta_i\beta^i)dt^2 + 2\beta_i dt dx^i + \gamma_{ij}dx^i dx^j, \tag{II-33}$$

where β_i is given by $\beta_i = \gamma_{ij}\beta^j$. Equation (II-33) is known as the 3+1 split of the metric, in conventional matrix notation is given by

$$g_{\mu\nu} = \begin{bmatrix} -\alpha^2 + \beta_k\beta^k & \beta_i \\ \beta_j & \gamma_{ij} \end{bmatrix}, \qquad g^{\mu\nu} = \begin{bmatrix} \frac{-1}{\alpha^2} & \frac{\beta^i}{\alpha^2} \\ \frac{\beta^j}{\alpha^2} & \frac{\gamma^{ij} - \beta^i\beta^j}{\alpha^2} \end{bmatrix}.$$

Furthermore the 4-dim volume element [2] in the «3+1» variables is given by, $\sqrt{-g} = \alpha\sqrt{\gamma}$, where g and γ are the determinant of the 4-dim and 3-dim induced metrics respectively; i.e. the proper volume is given by, $\int \sqrt{-g} d^4x$.

2.2.1.2 Geometrical Interpretation of the 3+1 Decomposition

Considering the unit normal vector n^μ to spatial hypersurface Σ_t,

$$n^\mu = (1/\alpha, -\beta^i/\alpha), \qquad n_\mu = (-\alpha, 0), \tag{II-34}$$

then the 3-dim metric, can be written as,

$$\gamma_{\mu\nu} = g_{\mu\nu} + n_\mu n_\nu. \tag{II-35}$$

Thus, the spatial metric is none other than the *projection operator* onto the spatial hypersurfaces, i.e. $n^\mu \gamma_{\mu\nu} v^\nu = 0$ for any u^ν.

The lapse function, α, is given by

$$\alpha = \sqrt{-\nabla_\mu t \nabla^\mu t} = \sqrt{-\nabla_\mu t \nabla_\nu g^{\mu\nu}} = -g^{tt}, \tag{II-36}$$

where t is the "time" coordinate, and the unit normal vector to the hypersurface Σ_t, is given by,

$$n^\mu = -\alpha \nabla^\mu t, \tag{II-37}$$

where the minus sign indicates that $\vec{n}$ is pointing towards future times.

The shift vector describes how when moving from one hypersurface Σ_t to a nearby one Σ_{t+dt}, in the direction of the normal vector, the coordinate labels change, i.e. $x^i_{t+dt} = x^i_t - \beta^i dt$,

[2] The metric g defines a natural volume form, which can be used to integrate over spacetimes. In local coordinates x^μ of a manifold, the volume form can be written $\mathrm{vol}_g = \sqrt{|\det g|}\, dx^0 \wedge dx^1 \wedge dx^2 \wedge dx^3$ where $\det g$ is the determinant of the matrix of components of the metric tensor for the given coordinate system. To define an invariant volume element, it is necessary to multiply the volume element $d^4x = dx^0 dx^1 dx^2 dx^3$ by $\sqrt{-g}$. Under a coordinate transformation $\sqrt{-g} d^4x$ transform as expected, i.e. contains the appropriate Jacobian terms.

therefore

$$\beta^i = -\alpha(n^j \partial_j x^i). \tag{II-38}$$

It is possible to extend the definition of the shift vector to a 4-vector, $\beta^\mu = (0, \beta^i)$. This allows one to construct a time vector, $\vec{t}$: $t^\mu \triangleq \alpha n^\mu + \beta^\mu$; which is the tangent vector to the time lines, i.e. the lines of constant spatial coordinates.

According to the given definitions of the lapse, shift and normal vector, the following relations also hold: $t^\mu n_\mu = -\alpha$, which implies that $t^\mu \nabla_\mu t = 1$. Moreover, the shift is the projection of $\vec{t}$ onto the spatial hypersurface, $\beta_\mu \triangleq \gamma_{\mu\nu} t^\nu$.

2.2.2 Extrinsic Curvature

Given the introduction of the 3-dim spatial hypersurfaces to foliate the 4-dim spacetime, it is necessary to distinguish between the *intrinsic curvature* of the foliating hypersurfaces due to their internal geometry, and the *extrinsic curvature* associated with the way in which these hypersurfaces are embedded in the 4-dim spacetime. The intrinsic curvature is given by the 3-dim Riemann tensor defined in terms of the 3-metric γ_{ij}. The extrinsic curvature, takes into account the variations of the normal vector along the hypersurface. The extrinsic curvature tensor $K_{\alpha\beta}$ is a measure of the change of the normal vector under along Σ.

A useful element to define is the *projection operator* P^α_β onto the spatial hypersurface,

$$P^\alpha_\beta \triangleq \delta^\alpha_\beta + n^\alpha n_\beta, \tag{II-39}$$

which actually is the metric on the induced spatial metric, $P_{\alpha\beta} = \gamma_{\alpha\beta}$.

Using the projection operator, the extrinsic curvature tensor is defined as,

$$K_{\mu\nu} \triangleq -P^\alpha_\mu \nabla_\alpha n_\nu = -(\nabla_\mu n_\nu + n_\mu n^\alpha \nabla_\alpha n_\nu). \tag{II-40}$$

The extrinsic curvature tensor, as defined by Eq.(II-40), has important properties: it is purely spatial, i.e. $n^\mu K_{\mu\nu} = n^\nu K_{\mu\nu} = 0$, and is symmetric, i.e. $K_{\mu\nu} = K_{\nu\mu}$.

Additionally, it can be proven that the extrinsic curvature tensor can be written as the Lie

derivative of the spatial metric along the normal direction, $K_{\mu\nu} = -\frac{1}{2}\pounds_{\vec{n}}\gamma_{\mu\nu}$, just by directly applying the definition of the Lie derivative, $\pounds_{\vec{n}}\gamma_{\mu\nu} = n^\alpha\nabla_\alpha\gamma_{\mu\nu} + \gamma_{\mu\alpha}\nabla_\nu n^\alpha + \gamma_{\nu\alpha}\nabla_\mu n^\alpha$.

By relating the Lie derivative of the spatial metric in the time and shift directions, it is possible to construct an evolution equation for the spatial metric,

$$\left(\pounds_{\vec{t}} - \pounds_{\vec{\beta}}\right)\gamma_{\mu\nu} = -2\alpha K_{\mu\nu}. \tag{II-41}$$

By considering only the spatial components of Eq.(II-41) and recalling that in the adapted coordinate system $\pounds_{\vec{t}} = \partial_t$, then

$$\partial_t\gamma_{ij} - \pounds_{\vec{\beta}}\gamma_{ij} = -2\alpha K_{ij}, \tag{II-42}$$

which can be rewritten as,

$$\partial_t\gamma_{ij} = -2\alpha K_{ij} + D_i\beta_j + D_j\beta_i, \tag{II-43}$$

where D_i represents the 3-dim covariant derivative, that is, the one associated with the 3-metric γ_{ij}, which is the projection of the full 4-dim covariant derivative: $D_\mu \triangleq P^\alpha_\mu\nabla_\alpha$.

Either Eq.(II-42) or (II-43), give an evolution equation for the spatial metric. It is still necessary to find an evolution equation for the extrinsic curvature K_{ij}, i.e. how the hypersurfaces are embedded in the 4-dim spacetime. Additionally, the evolution equations of the spatial metric have been obtained without using the Einstein equations at all. It is precisely from the Einstein equations that the evolution equations for K_{ij} will arise. Therefore the evolution equations of the spatial metric are kinematic, while the dynamics of the system will be contained in the evolution equations for K_{ij}.

But for the system to be stable, these coordinates themselves need to obey PDEs that are coupled with the metric evolution. In order to perform evolutions, the variables to consider are: the induced spatial metric γ_{ij}, the extrinsic curvature K_{ij}, as well as the lapse α and the shift β^i.

2.2.3 Einstein Equations

The dynamics of the gravitational field are given by the Einstein field equations. In order to reformulate the Einstein theory in terms of a Cauchy problem, the Einstein equations need to be rewritten in the «3+1» formalism. For doing that, the Einstein equations can be divided into 2 groups by projecting them parallel and orthogonal to the 3-d hypersurface Σ_t. Or equivalently, contracting the Einstein equations with the normal vector $\vec{n}$ and the projection operator P^{α}_{β}. After doing this, the Einstein equations are split in two different sets:

- 4 equations without second time derivatives, which are "constraint" equations.
- 6 equations including time derivatives, the actual "evolution" equations.

More details about these derivations can be found in [123, 124].

2.2.4 Constraints

Considering the contractions with the normal vector, the starting point is to express the 4-dim Riemann curvature tensor $R^{\mu}_{\nu\lambda\sigma}$ in terms of the intrinsic 3-dim Riemann tensor of the hypersurface itself ${}^{(3)}R^{\mu}_{\nu\lambda\sigma}$ and the extrinsic curvature tensor $K_{\mu\nu}$. The full projection of the Riemann tensor onto the spatial hypersurface are given by the so-called *Gauss-Codazzi equations*,

$$P^{\delta}_{\alpha}P^{\kappa}_{\beta}P^{\lambda}_{\mu}P^{\sigma}_{\nu}R_{\delta\kappa\lambda\sigma} = {}^{(3)}R_{\alpha\beta\mu\nu} + K_{\alpha\mu}K_{\beta\nu} - K_{\alpha\nu}K_{\beta\mu}. \tag{II-44}$$

Similarly, the projection onto the hypersurface of the Riemann tensor contracted once with normal vector results in the *Codazzi-Mainardi* equations,

$$P^{\delta}_{\alpha}P^{\kappa}_{\beta}P^{\lambda}_{\mu}P^{\sigma}_{\nu}R_{\delta\kappa\lambda\sigma} = {}^{(3)}R_{\alpha\beta\mu\nu} + K_{\alpha\mu}K_{\beta\nu} - K_{\alpha\nu}K_{\beta\mu}. \tag{II-45}$$

The Gauss-Codazzi equations lead to the *Hamiltonian* or *energy constraint*,

$${}^{(3)}R + (\mathrm{tr}K)^2 - K_{\mu\nu}K^{\mu\nu} = 16\pi\rho, \tag{II-46}$$

where $\rho \triangleq n^{\mu}n^{\nu}T_{\mu\nu}$, is the local energy density measured by the Eulerian observers.

Meanwhile, the Codazzi-Mainardi equations, lead to the *momentum constraints*,

$$D_\mu \left(K^{\alpha\mu} - K\gamma^{\alpha\mu} \right) = 8\pi j^\alpha, \tag{II-47}$$

where $j^\alpha \triangleq -P^{\alpha\mu} n^\nu T_{\mu\nu}$, is the momentum density measured by the Eulerian observers.

In a coordinate system adapted to the foliation, the Hamiltonian and momentum constraints take the form,

$$\begin{cases} {}^{(3)}\!R + (\mathrm{tr}K)^2 - K_{ij}K^{ij} &= 16\pi\rho, \\ D_j \left(K^{ij} - K\gamma^{ij} \right) &= 8\pi j^i. \end{cases} \tag{II-48}$$

The constraint equations not only do not involve time derivatives, but they are also independent of the gauge functions α and β^i. This indicates that these relations are restricted to a given hypersurface. Furthermore, these constraints represent relations between the dynamical variables that should be satisfied at all times.

In general for constrained theories, and in particular for the «3+1» formalism, the existence of constraints imply that it is not possible to specify arbitrarily all 12 dynamical quantities $\{\gamma_{ij}, K_{ij}\}$ as initial conditions. The initial data must already satisfy the constraints, otherwise the solutions will not be valid.

2.2.5 The ADM Evolution Equations

The Hamiltonian and momentum constraints give four of ten independent equations arising from the Einstein field equations. In order to find the evolution equations, the Riemann tensor must be projected onto the hypersurface, i.e. $P_i^\mu P_j^\nu G_{\mu\nu}$, which yields

$$\begin{aligned} \partial_t K_{ij} = \quad & \beta^k \partial_k K_{ij} + K_{ki}\partial_j \beta^k + K_{kj}\partial_i \beta^k - D_i D_j \alpha \\ & + \alpha \left[{}^{(3)}\!R_{ij} + K K_{ij} - 2K_{ik}K_j^k \right] + 4\pi\alpha \left[\gamma_{ij} \left(S - \rho \right) - 2S_{ij} \right], \end{aligned} \tag{II-49}$$

where $S_{\mu\nu} \triangleq P_\mu^\alpha P_\nu^\beta T_{\alpha\beta}$ represents the spatial stress tensor measured by Eulerian observers ($S \triangleq S_\mu^\mu = \mathrm{tr}(S)$). These equations give the dynamical evolution of the six independent components of the extrinsic curvature K_{ij}.

Equations (II-42) for the evolution of the spatial metric, together with Eq.(II-49) for the evolution of the extrinsic curvature, translate the Einstein equations into a Cauchy problem. It is important to note that there are no evolution equations for the gauge functions α and β^i, as they represent the coordinate freedom and can therefore be chosen freely.

Equations (II-49), expressed in term of Lie derivatives,

$$\begin{aligned} \partial_t K_{ij} - \pounds_{\vec{\beta}} K_{ij} = & -D_i D_j \alpha + \alpha \left[{}^{(3)}R_{ij} + K K_{ij} - 2K_{ik} K^k_j \right] \\ & +4\pi\alpha \left[\gamma_{ij} \left(S - \rho \right) - 2S_{ij} \right], \end{aligned} \tag{II-50}$$

are known as the *Arnowitt-Deser-Misner (ADM) equations* [128]. These equations as written above, are known as "standard ADM" or "ADM equations á la York", which is not the original derived form [128], but instead a non-trivial rewriting due to York [249]. The difference between the ADM and York evolution equations comes from the fact that the ADM equations proceeds from the field equations written in terms of the Einstein tensor, whereas York's version was derived in terms of the Ricci tensor. The original ADM variables were the spatial metric γ_{ij} and its canonical conjugate momentum π_{ij}.

The ADM equations are not unique. For instance, the original formulation and York's formulation are physically equivalent, but mathematically different. They have a different space of solutions, that only coincide in the constraint hypersurface (this is not a hypersurface in the spacetime, rather a hypersurface in space of the solution of the evolution equations).

Another way to see that the «3+1» evolution equations are non-unique, is to note that it is always possible to add terms proportional to the constraints. The different systems of evolution equations will coincide in the physical solution, but might differ dramatically in their mathematical properties, in particular in the way that respond to small violations of the constraints (that in the numerical field is almost inevitable).

2.2.5.1 Propagation of Constraints

If the constraints are satisfied initially, thanks to Bianchi identities –Eq.(I-4)– the propagation of the constraints are guaranteed upon the evolution. It can be shown that by taking the

orthogonal and parallel projection of the Bianchi identities onto Σ_t, with initial data consistent with $\mathcal{H} = \mathcal{M}_\mu = 0$ (i.e. satisfying the constraint equations), and evolutions consistent with the remaining Einstein equations $\mathcal{E}_{\mu\nu} = 0$, that the Bianchi identities guarantee that on the next hypersurface Σ_{t+dt} the constraints will still vanish. Note that this equations can be written in the form,

$$\begin{cases} \mathcal{H} & \triangleq n^\alpha n^\beta G_{\alpha\beta} - 8\pi\rho, \\ \mathcal{M}_\mu & \triangleq -n^\alpha P^\beta_\mu G_{\alpha\beta} - 8\pi j_\mu, \\ \mathcal{E}_{\mu\nu} & \triangleq P^\alpha_\mu P^\beta_\nu G_{\alpha\beta} - 8\pi S_{\mu\nu}. \end{cases} \tag{II-51}$$

Interestingly, in York's version, the evolution equation are given by, $\mathcal{E}_{\mu\nu} - \gamma_{\mu\nu}\mathcal{H} = 0$.

According to [250], neither the ADM nor the BSSN systems are strongly hyperbolic, although some of them are weakly hyperbolic, which means that they may yet be well posed but only under very restrictive conditions for the terms of order lower than second in the equations. Even more, the second-order equations for the 3-metric that are implied by a large number of first-order reductions of the «3+1» Einstein equations whose evolution equations differ by the addition of different multiples of the Hamiltonian constraint are potentially ill-posed irrespective of whether the lapse is constant or densitized.

2.2.6 Numerical Evolutions: free vs constrained evolutions

As discussed above, the Einstein field equations can be split into evolution equations and constraint equations. Additionally, the Bianchi identities guarantee the constraint preservation upon the evolution. From the numerical simulation perspective, it is necessary to evolve the geometric quantities γ_{ij} and K_{ij} while keeping the constraints satisfied. With this in mind, it is necessary to obtain a set of discretized evolution and constraint equations. Unfortunately no such discretization scheme exists that allows for the discrete version of constraint equations to be satisfied during the evolution of the discrete evolution equations. This implies that, not all 10 Einstein equations will remain satisfied at the discretized level during a numerical simulation. The expectation is that a good numerical implementation will allow one to recover a solution of the full set of equations in the continuum limit.

In practice, one can choose which set of the 10 equations one would like to solve numerically. One approach is called: "free evolution", it starts with a solution of the constraints as initial data, and evolves in time solving all 12 evolution equations for γ_{ij} and K_{ij}. In the free evolution scheme, the constraints are only monitored their violations are considered a measure of the accuracy of the simulation. Alternatively, in the "constrained evolution" system, one chooses to solve some or all of the constraint equations at each time step for a specific subset of the components of the metric and extrinsic curvature, and evolve the remaining components using the evolution equations. There is a third alternative known as "constrained metric evolution", where some extra conditions on the metric are introduced (for instance conformal flatness) and impose this condition during the whole evolution, which usually simplifies the equations to be solved. However, imposing extra conditions on the metric is not in general compatible with Einstein equations.

2.2.7 Hamiltonian Formulation

It is possible to express General Relativity as a field theory formulation using a Hilbert Lagrangian. In order to do that, it can be shown that an appropriate choice of Lagrangian is $L = R$, where R is the Ricci scalar. Then using the action, $S = \int L dV$, $dV = \sqrt{g} d^4x$, where it is possible to obtain the Einstein field equations. The variations of the action with respect to the metric will give the conservation laws, while variations with respect to the fields will give the field equations. But the Lagrangian formulation of a field theory uses a covariant approach. The Lagrangian itself is a scalar function, and also the equations derived from the variational principle come out in fully covariant form. On the other hand a Hamiltonian formulation requires a clear distinction to be made between space and time, so it is therefore not covariant. In general there is no clear way to split space and time, however the basics of the «3+1» formulation can be used as a basis to construct a Hamiltonian formulation of the theory. The first step is to identify the configuration variables that identify the state of the system at any time. For this case, an interesting choice is the spatial metric γ_{ij}, the lapse function α, and the co-variant shift vector β_i: $\{\gamma_{ij}, \alpha, \beta_i\}$.

In the «3+1» language, the Ricci scalar can be written as,

$$R = {}^{(3)}R + K_{\mu\nu}K^{\mu\nu} - K^2 - 2\nabla_\lambda \left(n^\nu \nabla_\nu n^\lambda - n^\lambda \nabla_\nu n^\nu \right). \tag{II-52}$$

The last term in Eq.(II-52) is a total divergence, which upon integration, necessarily vanishes under variations. This is because the volume integral can be transformed into a surface integral applying Gauss' divergence theorem, and therefore this term will yield a boundary term to the action integral. Thus this term can be omitted from the Lagrangian, because variations on the boundary vanish. Therefore the Lagrangian of General Relativity in «3+1» language can be written as,

$$L = {}^{(3)}R + K_{\mu\nu}K^{\mu\nu} - K^2. \tag{II-53}$$

Lagrangian & Hamiltonian densities The Lagrangian density, is given by,

$$\mathcal{L} = \alpha\sqrt{\gamma} \left({}^{(3)}R + K_{\mu\nu}K^{\mu\nu} - K^2 \right). \tag{II-54}$$

Canonical momenta conjugate are defined as the derivatives of the Lagrangian density with respect to the velocity of the fields. For the spatial metric, the conjugate momenta are $\pi^{ij} \triangleq \frac{\partial \mathcal{L}}{\partial \dot{\gamma}_{ij}}$, and recalling that $\dot{\gamma_{ij}} = -2\alpha K_{ij} + \pounds_{\vec{\beta}}\gamma_{ij}$, then

$$\pi^{ij} = -\sqrt{\gamma} \left(K^{ij} - \gamma^{ij} K \right). \tag{II-55}$$

By taking the trace of Eq.(II-55), it is possible to invert the relation between π_{ij} and K_{ij},

$$K_{ij} = -\frac{1}{\sqrt{\gamma}} \left(\pi_{ij} - \frac{1}{2}\gamma_{ij}\pi \right). \tag{II-56}$$

The Lagrangian density is independent of any derivatives of the lapse and shift, therefore the conjugate momenta associated to these variables are zero.

The Hamiltonian density is defined as, $\mathscr{H} = \pi^{ij}\dot{\gamma_{ij}} - \mathcal{L}$, where

$$\mathscr{H} = \left[-\alpha\sqrt{\gamma}\left({}^{(3)}R + K^2 - K_{ij}K^{ij}\right) + 2\pi^{ij}D_i\beta_j\right], \tag{II-57}$$

which can be rewritten as,

$$\mathscr{H} = -2\sqrt{\gamma}\left[\alpha\mathcal{H} + \beta_i\mathcal{M}^i\right], \tag{II-58}$$

where $\mathcal{H}$ and $\mathcal{M}$ are given by Eqs.(II-51), without matter contribution.

The total Hamiltonian is defined as, $H \triangleq \int \mathscr{H} d^3x$. By taking variations of the Hamiltonian H with respect to the lapse α and the shift β^i one obtains the Hamiltonian and momentum constraints for vacuum $\mathcal{H} = 0$ and $\mathcal{M}^i = 0$. Thus, the lapse and shift behave as Lagrange multipliers of a constrained system.

Hamilton's evolution equations The evolution equations are given by the Hamilton's equations, $\dot{\gamma_{ij}} = \frac{\delta H}{\delta \pi^{ij}}$ and $\dot{\pi}^{ij} = -\frac{\delta H}{\delta \gamma_{ij}}$.

Giving the evolution equation for the spatial metric,

$$\dot{\gamma_{ij}} = \frac{2\alpha}{\sqrt{\gamma}}\left(\pi_{ij} - \frac{1}{2}\gamma_{ij}\pi\right) + \pounds_{\vec{\beta}}\gamma_{ij}, \tag{II-59}$$

and the ADM evolution equations for π_{ij}.

2.3 The NOK-BSSN Formulation

The BSSN formulation represents a reformulation of ADM that has proven to be robust in numerical evolution of a large variety of spacetimes. Recall that the ADM equations are not stable in long-terms numerical simulations, since the system is actually only weakly hyperbolic.

2.3.1 General Considerations: BSSN//NOK-BSSN//conformal Γ

Nakamura, Oohara and Kojima (1987) [145], based on a *conformal transformation*, improved the stability of the system. Later on, Baumgarte and Shapiro (1998) [147] compared the

proposed system to the ADM, showing that has superior stability properties.

This new formulation is referred as "BSSN" (Baumgarte, Shapiro, Shibata, Nakamura), although a more appropriate term will be "NOK-BSSN" or "conformal ADM" or "conformal Γ formulation" [145, 146, 147].

The first step is to introduce a conformal rescaling of the spatial metric, $\tilde{\gamma}_{ij} \triangleq \psi^{-4}\gamma_{ij}$, where ψ is a conformal factor that can in principle be chosen in different ways. For example, evolving black hole spacetimes with conformally flat initial data, it is possible to simply take ψ to be the initial singular conformal factor and restrict this conformal factor to remain fixed in time. This allows one to evolve only the non-singular part of the metric; and is known as the *fixed puncture* method. Alternatively, it is possible to take the conformal factor initially given by some arbitrarily chosen scalar function and then propose some convenient evolution equation for this scalar function.

2.3.2 Conformal factor & Conformal metric

By choosing the conformal factor, such that the conformal metric $\tilde{\gamma}_{ij}$ has unit determinant ($\tilde{\gamma} = 1$) one obtains

$$\psi^4 = \gamma^{1/3} \qquad \Rightarrow \qquad \psi = \gamma^{1/12}. \tag{II-60}$$

It is necessary that Eq.(II-60) remains satisfied during the evolution. By using the spatial metric evolution Eq.(II-42), the evolution equation for the determinant of the metric becomes,

$$\partial_t \psi = -\frac{1}{6}(\alpha K - \partial_i \beta^i) + \beta^i \partial_i \psi. \tag{II-61}$$

Usually the following variables are introduced, $\phi = \ln \psi = \frac{1}{12} \ln \gamma$; so that, $\tilde{\gamma}_{ij} = e^{-4\phi}\gamma_{ij}$ and

$$\partial_t \phi = -\frac{1}{6}(\alpha K - \partial_i \beta^i) + \beta^i \partial_i \phi. \tag{II-62}$$

Campanelli *et al.* [138], suggested that evolving $\chi = 1/\psi^4 = \exp(-4\phi)$ is a better alternative when considering black hole spacetimes for which ψ typically has a $1/r$ singularity (so that ϕ has a logarithmic singularity), while χ is a C^4 function at $r = 0$. For regular spacetimes, it

should make no difference evolving ϕ, ψ, or χ.

The NOK-BSSN formulation separates the extrinsic curvature into its trace K and its tracefree part $A_{ij} = K_{ij} - \frac{1}{3}\gamma_{ij}K$. In addition, one evolves a conformal rescaling version of A_{ij}, $\tilde{A}_{ij}$, which represents a conformal rescaling of the traceless extrinsic curvature, $\tilde{A}_{ij} = \psi^{-4}A_{ij} = e^{-4\phi}A_{ij}$.

2.3.3 Conformal Connection Functions

Three auxiliary variables known as *conformal connection functions* are defined as,

$$\tilde{\Gamma}^i \triangleq \tilde{\gamma}^{jk}\tilde{\Gamma}^i_{jk} = -\partial_j\tilde{\gamma}^{ij}, \tag{II-63}$$

where $\tilde{\Gamma}^i_{jk}$ are the Christoffel symbols of the conformal metric.

2.3.4 Evolution Equations

While the ADM description has 12 variables: $\{\gamma_{ij}, K_{ij}\}$; the NOK-BSSN description has 17 variables: $\{\phi, K, \tilde{\gamma}_{ij}, \tilde{A}_{ij}, \tilde{\Gamma}^i\}$.

The system of evolutions equations takes the form,

$$\begin{cases} \frac{d}{dt}\tilde{\gamma}_{ij} &= -2\alpha\tilde{A}_{ij}, \\ \frac{d}{dt}\phi &= -\frac{1}{6}\alpha K, \\ \frac{d}{dt}\tilde{A}_{ij} &= e^{-4\phi}\left\{-D_iD_j\alpha + \alpha R_{ij} + 4\pi\alpha\left[\gamma_{ij}\left(S-\rho\right) - 2S_{ij}\right]\right\}^{\mathrm{TF}} \\ & \quad +\alpha\left(K\tilde{A}_{ij} - 2\tilde{A}_{ik}\tilde{A}^k_j\right), \\ \frac{d}{dt}K &= -D_iD^i\alpha + \alpha\left(\tilde{A}ij\tilde{A}^{ij} + \frac{1}{3}K^2\right) + 4\pi\alpha\left(\rho + S\right), \end{cases} \tag{II-64}$$

where $d/dt \triangleq \partial_t - \pounds_{\vec{\beta}}$, and TF denotes the tracefree part of the expression inside the brackets. In the previous expression, indices of the conformal quantities should be raised and lowered with the conformal metric (e.g. $\tilde{A}^{ij} = e^{4\phi}A^{ij}$). There are certain subtle details about the evolution Eqs.(II-64), such as: the evolution equations for $\tilde{A}_{ij}$ and K implies covariant derivatives of the lapse function with respect to the physical metric γ_{ij}, which can be easily calculated by

using the relations between the Christoffel symbols are their corresponding conformal version. Also the evolution equations involve computing Lie derivatives with respect to $\vec{\beta}$ of *tensor densities* (i.e. tensors multiplied by powers of the determinant of the metric γ). If a given object is a tensor multiplied by $\gamma^{w/2}$, then this maps into a tensor density of weight w. The Lie derivative of a tensor density of weight w, can be expressed as, $\pounds_{\vec{\beta}} = \left[\pounds_{\vec{\beta}} T\right]_{w=0} + wT\partial_i\beta^i$; where the first term denotes the Lie derivative assuming $w = 0$, and the second is the additional contribution due to the density factor.

There are several motivations for changing to these variables: the conformal transformation and the separating out of the trace of the extrinsic curvature allow for a better control over the slicing conditions (in general related to the trace of K_{ij}); the introduction of the conformal connection variables $\tilde{\Gamma}^i$, considered as independent variables reduce some terms to the Laplace operator $\tilde{\gamma}^{lm}\partial_l\partial_m\tilde{\gamma}_{ij}$, and it makes the system strongly hyperbolic.

2.3.5 Final Set of Evolution Equations & Constraints

If $\tilde{\Gamma}^i$ are considered as independent variables, another extra evolution equation is required. The evolution equation for $\tilde{\Gamma}^i$, given $\partial_t\tilde{\Gamma}^i = -\partial_j\left(\pounds_{\vec{\beta}}\tilde{\gamma}^{ij}\right) - 2\left(\alpha\partial_j\tilde{A}^{ij} + \tilde{A}^{ij}\partial_j\alpha\right)$, then

$$\frac{d}{dt}\tilde{\Gamma}^i = -\tilde{\gamma}^{jk}\partial_j\partial_k\beta^i + \frac{1}{3}\tilde{\gamma}^{ij}\partial_j\partial_k\beta^k - 2\left(\alpha\partial_j\tilde{A}^{ij} + \tilde{A}^{ij}\partial_j\alpha\right). \tag{II-65}$$

But using the evolution equations given by Eqs.(II-64) and (II-65) used in numerical simulations, turns out to be unstable. In order to fix this problem, the momentum constraints need to be used; which in terms of the new variables introduced take the form,

$$\partial_j\tilde{A}^{ij} = -\tilde{\Gamma}^i_{jk}\tilde{A}^{jk} - 6\tilde{A}^{ij}\partial_j\phi + \frac{2}{3}\tilde{\gamma}^{ij}\partial_j K + 8\pi\tilde{j}^i, \tag{II-66}$$

where $\tilde{j}^i \triangleq e^{4\phi}j^i$; and using the evolution equation for $\tilde{\Gamma}^i$, one obtains,

$$\frac{d}{dt}\tilde{\Gamma}^i = -\tilde{\gamma}^{jk}\partial_j\partial_k\beta^i + \frac{1}{3}\tilde{\gamma}^{ij}\partial_j\partial_k\beta^k - 2\tilde{A}^{ij}\partial_j\alpha + 2\alpha\left(\tilde{\Gamma}^i_{jk}\tilde{A}^{jk} + 6\tilde{A}^{ij}\partial_j\phi - \frac{2}{3}\tilde{\gamma}^{ij}\partial_j K - 8\pi\tilde{j}^i\right). \tag{II-67}$$

The final system of evolution equations Eqs.(II-64) and, (II-67), $\left\{ \frac{d}{dt}\tilde{\gamma}_{ij}, \frac{d}{dt}\phi, \frac{d}{dt}\tilde{A}_{ij}, \frac{d}{dt}K, \frac{d}{dt}\tilde{\Gamma}^i \right\}$, in conjunction with an appropriate evolution system for the gauge variables, is stable.

A key element in the NOK-BSSN formulation is the use of momentum constraints to modify evolution equations. There are some additional tricks that have been used to improve this scheme, such as: force the trace of the conformal-traceless extrinsic curvature $\tilde{A}^{ij}$ to remain zero during evolution, and use independently evolved $\tilde{\Gamma}^i$ only in terms where derivatives appear.

2.4 Moving Puncture Approach

The *Moving Puncture* approach was developed by Campanelli *et al.* [138], and Baker *et al.* [141]. As we will discuss in Sec.2.8.2, this is the system of equations that the evolution code we used (`LazEv`) solves. It uses the BSSN formulation and *punctures*, which makes the system strong-hyperbolic equivalent. It implements modified gauges to allow punctures to move across the grid, and introduces new variables that regularize the puncture [138], and has the advantage of not require to use singularity excision.

The fixed puncture method allows one to handle infinities associated with puncture initial data, but it has a major disadvantage, by factoring out the infinities analytically and keeping them static it forces the punctures to remain at a fixed location. The idea of allowing the puncture to evolve, generated a true breakthrough in the black hole simulations field. It allowed the accurate simulation of binary black holes for multiple orbits [251], with the black holes moving through the grid instead of remaining glued in a fixed position as the static puncture evolution method required.

The moving-punctures BSSN field variables The moving puncture approach starts from the NOK-BSSN formulation. The dynamical conformal factor $\phi = \ln \psi$ has a logarithmic singularity which is directly evolved. The moving puncture approach uses the following variables, previously described on the NOK-BSSN formalism:

- Conformal 3-metric, $\tilde{\gamma}_{ij} = W^2 \gamma_{ij}$

- Conformal extrinsic curvature, $\tilde{A}_{ij} = W^2 \left(K_{ij} \frac{1}{3} \gamma_{ij} K \right)$
- Trace K of the extrinsic curvature
- $\tilde{\Gamma}^i = -\partial_j \tilde{\gamma}^{ij}$
- Conformal factor, $W = e^{-2\phi}$
- Gauge variables: α, β^i
- W is chosen such that, W vanishes at the singularity

Gauge Conditions The coordinates are chosen in such a way that they are singularity avoiding, otherwise we would need to use excision. The coordinates should not be too distorted, and the gridpoints should resolve the region of interest. In term of equations are ruled by,

$$\left(\partial_t - \beta^i \partial_i\right) \alpha = -2\alpha K, \tag{II-68a}$$

$$\partial_t \beta^i = \frac{3}{4} \tilde{\Gamma}^i - \eta \beta^i. \tag{II-68b}$$

Eq.(II-68a) is known as "1+log" slicing condition; Eq.(II-68b) is one of the family of the "Gamma driver" for the shift vector.

Evolution Equations

$$\begin{cases} \left(\partial_t - \pounds_{\vec{\beta}}\right) W = -\frac{1}{3} W \left(\partial_j \beta^j - \alpha K\right), \\ \left(\partial_t - \pounds_{\vec{\beta}}\right) K = -\gamma^{ij} D_i D_j \alpha + \alpha \left(\tilde{A}^i_j \tilde{A}^j_i + \frac{1}{3} K^2\right), \\ \left(\partial_t - \pounds_{\vec{\beta}}\right) \tilde{g}_{ij} = -2\alpha \tilde{A}_{ij}, \\ \left(\partial_t - \pounds_{\vec{\beta}}\right) \tilde{A}_{ij} = W^2 \left[-D_i D_j \alpha + \alpha R_{ij}\right]^{\mathrm{TF}} + \alpha \left(K \tilde{A}_{ij} - 2 \tilde{A}_{ik} \tilde{A}^k_j\right), \\ \left(\partial_t - \pounds_{\vec{\beta}}\right) \tilde{\Gamma}^i = \tilde{\gamma}^{jk} \partial_j \partial_k \beta^i + \frac{1}{3} \partial^i \partial_j \beta^j - 2 \tilde{A}^{ij} \partial_j \alpha \\ \qquad\qquad + 2\alpha \left(\tilde{\Gamma}^i_{jk} \tilde{A}^{jk} + 6 \tilde{A}^{ij} \partial_j \phi - \frac{2}{3} \tilde{\gamma}^{ij} \partial_j K\right). \end{cases} \tag{II-69}$$

Constraint Equations

$$\begin{cases} \mathcal{H} = R - \tilde{A}_{ij}\tilde{A}^{ij} + \frac{2}{3}K^2 &= 0, \\ \mathcal{C}^i = \partial_j \tilde{A}^{ij} + \tilde{\Gamma}^i_{jk}\tilde{A}^{jk} + 6\tilde{A}^{ij}\partial_j \alpha - \frac{2}{3}\tilde{\gamma}^{ij}\partial_j K &= 0. \end{cases} \tag{II-70}$$

The position of the puncture x^i_p can be tracked by integrating the equation of motion, $\frac{dx^i_p}{dt} = -\beta^i(x^i_p)$.

The shift is typically chosen to vanish initially, but the Gamma driver condition rapidly causes the shift to evolve in such a way that counteracts the longitudinal slice stretching effect, and for orbiting black holes it automatically acquires a tangential component that allows the punctures to orbit each other.

2.5 Initial Data

Initial data are the starting point for any numerical simulation. In the case of numerical relativity, Einstein's equations constrain our choices of these initial data.

As mentioned in Sec.2.1, there are several approaches to describe the evolution of the gravitational field as a Cauchy problem, i.e. a well posed evolution given by initial data and boundary conditions.

All of the methods begin with a snapshot of the gravitational fields on some hypersurface Σ_t, the *initial data*, and evolve these data to neighboring hypersurfaces Σ_{t+dt}. Due to the constraint equations, the initial data cannot be freely specified. Rather they are subject to certain constraints that must be satisfied. Because of the nonlinearity of Einstein's equations, there is no unique way of choosing which pieces of the initial data can be freely specified and which are constrained.

The construction of initial data requires solving the Hamiltonian and momentum constraints. The constraints form a system of four coupled elliptical partial differential equations, which are in general difficult to solve. Among the most common procedures are the conformal decomposition and the so-called conformal thin-sandwich approach.

Together,γ_{ij} and K_{ij} are the minimal set of initial data that must be specified for a Cauchy

evolution of Einstein's equations. The starting point is to use a conformal transformation of the 3-metric of the form,

$$\gamma_{ij} = \psi^4 \bar{\gamma}_{ij}, \tag{II-71}$$

where the conformal metric $\bar{\gamma}_{ij}$ is considered as given. All the "bar" quantities are the corresponding operators associated with $\bar{\gamma}_{ij}$ (for instance $\bar{\nabla}^2 = \bar{\gamma}^{ij}\bar{\nabla}_i\bar{\nabla}_j$ and $\bar{R}$ are the Laplace operator and Ricci scalar associated with $\bar{\gamma_{ij}}$).

The Hamiltonian and the momentum constraint, Eqs.(II-48), by adapting a coordinate system to the foliation and using the conformal transformation given by Eq.(II-71), can be explicitly rewritten as

$$\begin{cases} 8\bar{\nabla}^2\psi - \bar{R}\psi + \psi^5(K_{ij}K^{ij} - K^2) + 16\pi\psi^5\rho &= 0, \\ D_j\left(K^{ij} - K\psi^4\bar{\gamma}^{ij}\right) - 8\pi j^i &= 0. \end{cases} \tag{II-72}$$

The four constraint equations represent conditions that the 3-metric and extrinsic curvature must satisfy. But, they do not specify which components (or combination of components) are constrained and which are freely specifiable. The goal is to transform the equations into standard elliptic forms that can be solved given appropriate boundary conditions. Each different decomposition yields a unique set of elliptic equations to be solved and a unique set of freely specifiable parameters that must be fixed somehow. Seemingly similar sets of assumptions applied to different decompositions can lead to physically different initial conditions.

2.5.1 Black Hole Initial Data

Building initial data for numerical simulations in Numerical Relativity is a difficult and technical problem. There are many studies related to the generation of initial data [252, 124, 123], for the sake of simplicity we will just briefly summarize some useful final results.

The simplest cases for constructing Cauchy initial data assume an asymptotically flat spacetime and vacuum. It is possible to construct initial data for spacetimes with matter, although it is more complicated.

The simplest black-hole solution is the Schwarzschild solution. It represents a static space-

time containing a single black hole that connects two causally disconnected, asymptotically flat universes. There are actually many different coordinate representations of the Schwarzschild solution. The simplest representations are time-symmetric ($K_{ij} = 0$), and so exist on a "maximally embedded" spacelike hypersurface ($K = 0$). These choices fix the foliation Σ. Spherical symmetry fixes two of the three spatial gauge choices.

By choosing a time-symmetric initial-data hypersurface, i.e. $K_{ij} = 0$, which eliminates the need to solve the momentum constraints, and choosing the conformal 3-geometry to be given by a flat metric (in spherical coordinates in this case), the vacuum Hamiltonian constraint Eq.(II-72) becomes

$$\bar{\nabla}^2\psi = \frac{1}{8}\psi\bar{R}. \tag{II-73}$$

The assumption of conformal flatness (i.e. $\bar{\gamma}_{ij} = \eta_{ij}$) dramatically simplifies all calculations, since $\bar{\nabla}$ reduces to the flat covariant derivative (and in particular to partial derivatives in Cartesian coordinates) with $\bar{R} = 0$. Therefore, Eq.(II-73) can be simplified to

$$\bar{\nabla}^2\psi = 0, \tag{II-74}$$

i.e. the Laplacian equation for ψ.

Assuming an asymptotically flat physical 3-metric implies the boundary condition that $\psi(\tilde{r} \to \infty) = 1$. The simplest solution of this equation is

$$\psi = 1 + \frac{M}{2\tilde{r}}, \tag{II-75}$$

where the integration constant has been chosen to give a mass M at infinity.

For multiple black holes initial data solutions, due to the linearity of the Hamiltonian constraint, when $K_{ij} = 0$, it is possible to choose the solution to be a superposition of solutions with the form of Eq.(II-75), i.e.

$$\psi = 1 + \sum_{\sigma=1}^{N} \frac{\mu_\sigma}{2|x - C_\sigma|}, \tag{II-76}$$

where $|x - C_\sigma|$ is a coordinate distance from the point C_σ in the Euclidean conformal space, and μ_σ are constants related to the masses of the black holes.

As will be explained in Chap.3, we implemented solutions to Eq.(II-74) and superpositions given by Eq.(II-76), see Sec.3.3.1 for more details.

If the extrinsic curvature does not vanish (i.e. $K_{ij} \neq 0$), the equations are still solvable although the problem is a non-linear Poisson type which requires special techniques.

2.6 Horizons

In Sec.1.5.1 we introduced and defined the idea of horizons (event horizon, apparent horizon, trapped surfaces, etc.). Far from being just very interesting mathematical concepts and physically related to the singularities spacetime, these concepts are truly useful at the moment of extracting information from the numerical simulations. Locating black hole horizons is also crucial in approaches where singularities excision is used.

Excellent reviews and more detailed discussions in the topics presented in this section, can be found in [253, 243, 254].

2.6.1 Apparent Horizons

Apparent horizons can be located during a live simulation on each spatial hypersurface. They are good indicators of the presence of the black hole, and they can be used either to locate the black (e.g. when using excision techniques), and also to measure physical quantities associated with the black hole, such as mass and angular momentum.

A *marginally trapped surface* is a closed 2-surface in a slice whose congruence of future-pointing outgoing null geodesics has zero expansion. There may be several such surfaces, some nested inside others; an *apparent horizon* is an outermost marginally trapped surface. In terms of the usual «3+1» variables, an apparent horizon satisfies the equation

$$\Theta \equiv \nabla_i n^i + K_{ij} n^i n^j - K = 0, \tag{II-77}$$

where n^i is the outward-pointing unit normal to the apparent horizon, and ∇_i is the covariant derivative operator associated with the 3-metric γ_{ij} in the slice.

In order to find AHs numerically, we used the `AHFinderDirect` thorn [255, 256], that finds an apparent horizon by numerically solving Eq.(II-77). The thorn requires as input the usual 3-metric γ_{ij} and extrinsic curvature K_{ij} and produces as output the (x, y, z) coordinates of a large number of points on the apparent horizon, together with some auxiliary information like the apparent horizon area and centroid position, and the irreducible mass associated with the area (see Sec.2.6.3).

2.6.2 Events Horizons

The defining property of a black hole is the presence of an event horizon (EH): a black hole is defined as a region of spacetime from which no null or timelike curve geodesic can escape to infinity. The surface of the black hole acts as a one-way membrane through which light and mater can enter the black hole, but once inside, can never escape. It is the boundary in spacetime separating those events that can emit light rays that can propagate to infinity and those which cannot. More precisely, the EH is defined as the boundary of the causal past of future null infinity $\mathscr{I}^+$. It is a 2+1 dimensional null hypersurface in spacetime formed by those outward-outgoing, future-directed null geodesics that neither escape to infinity not fall toward the center of the black hole.

There are basically three techniques to find event horizons in numerical spacetimes: integrating geodesics, integrating a surface, and integrating a level-set of surfaces over a volume.

Integrating null geodesics A direct approach to finding EHs is based on locating null geodesics by solving

$$\frac{d^2x^\mu}{d\lambda^2} + \Gamma^\mu_{\nu\gamma}\frac{dx^\nu}{d\lambda}\frac{dx^\gamma}{d\lambda} = 0, \tag{II-78}$$

where λ is an affine parameter.

One can numerically integrate the null geodesic Eq.(II-78) forwards in time from a starting

position to determine which geodesics "escape".

For numerical work it is straightforward to rewrite the null geodesic equation Eq.(II-78) as a coupled system of two first-order equations, giving the time evolution of photon positions and 3-momenta in terms of the 3+1 geometry variables $\alpha, \beta^i, \gamma_{ij}$, and their spatial derivatives. These can then be time-integrated by standard numerical algorithms. However, in practice several factors complicate this algorithm. One complicating factor is that the numerical computations generally only span a finite region of spacetime, so it is not entirely obvious whether or not a given geodesic will eventually reach $\mathscr{I}^+$. However, if the final numerically-generated slice contains an apparent horizon, certain approximations can be use.

However, following geodesics forward in time is unstable in that slightly perturbed geodesics will diverge from the EH and either escape to infinity or fall into the singularity. Furthermore, a large number of geodesics with different directions must be sampled at each point and at each time step to determine if one of these succeeds in escaping to infinity.

Since outgoing null geodesics diverge from the event horizon when going forward in time, when going backward in time they will converge onto the event horizon. All recent EH finders use this observation, and follow null geodesics or null surfaces backward in time.

Integrating null surface As described before, the geodesic method works by simply integrating the geodesic equation. One weak point is that the geodesic method may be susceptible to tangential "drifting" of the geodesics. To avoid any sort of drifting, it has been proposed that one should evolve a complete null surface (rather than individual geodesics), backward in time.

The most general way to parametrize a 2-surface in a slice is to define a scalar "level-set function" F on some neighborhood of the surface, with the surface itself then being defined as the level set, $F = 0$ on the surface.

By parametrizing the event horizon with any level-set function F satisfying the basic level-set definition, then the condition for the surface F to be null is just

$$g^{\mu\nu}\partial_\mu F \partial_\nu F = 0. \tag{II-79}$$

Applying the «3+1» decomposition to this then gives a quadratic equation which can be solved to find the time evolution of the level-set function.

This equation does not contain any derivatives of the 4-metric (or equivalently the 3+1 geometry variables). This makes it much easier to integrate these latter equations accurately. This formulation of the event-horizon finding problem also completely eliminates the tangential-drifting.

2.6.2.1 `EHFinder` Thorn

In our research projects (see Chap.3), we used the integration of a null surface backwards in time method for finding event horizons, via the `EHFinder` thorn [243] within the `Cactus/ET` infrastructure.

The surface will be parametrized as the 0-value isosurface of a level set function. This ensures that it is possible to handle cases when the topology changes (when evolving backwards in time) from one common event horizon to two (or more) individual event horizons.

This method depends on the fact that, except in cases where the coordinates are adapted to outgoing null geodesics, an outgoing null surface started close to the EH, when evolved forward in time, diverges exponentially from the EH. Reversing the time evolution then means that an outgoing null surface will converge exponentially to the EH. The level set function, f, is evolved according to

$$\begin{aligned} \partial_t f &= \frac{-g^{ti}\partial_i f + \sqrt{(g^{ti}\partial_i f)^2 - g^{tt}g^{ij}\partial_i f \partial_j f}}{g^{tt}} \\ &= \beta^i \partial_i f - \sqrt{\alpha^2 \gamma^{ij} \partial_i f \partial_j f}, \end{aligned} \tag{II-80}$$

where in the second equation the lapse, shift and 3-metric has been substituted for the 4-metric.

One important point in this technique, is that according to how it is implemented it requires an initial guess for the back-tracking surface. In our cases we used two initial surfaces that bracket the last apparent horizons.

2.6.3 Applications: Irreducible Mass

The intersection of the event horizon with a t =constant spatial hypersurface Σ, i.e. the "snapshot" of the horizon at the instant of time associated with Σ, forms a closed, 2-dimensional surface, with proper surface area $\mathcal{A}$. The area theorem from Hawking [248] states that this surface area can never decrease in time, $\delta\mathcal{A} \geq 0$, as long as all matter satisfies the null energy condition. Therefore, in the collision and coalescence of two or more black holes, the surface area of the remnant black hole must be greater than the sum of the progenitors. The fact that the event horizon area cannot decrease motivates the definition of *irreducible mass*,

$$M_{irr} \triangleq \left(\frac{\mathcal{A}}{16\pi}\right)^{1/2}. \tag{II-81}$$

Note, even though is possible to extract energy and angular momentum from a rotating Kerr black hole, thus reducing the black hole's mass, one cannot reduce its area.

Given the irreducible mass M_{irr} and the angular momentum (spin) J of an isolated, stationary black hole, it is possible to compute it *Kerr mass* ($= M_{ADM}$) as,

$$M^2 = M_{irr}^2 + \frac{1}{4}\frac{J^2}{M_{irr}^2}, \tag{II-82}$$

or equivalently,

$$M_{irr}^2 = \frac{M^2}{2}\left(1 + \sqrt{1 - \frac{J^2}{M^4}}\right), \tag{II-83}$$

which by the way, shows that $M^2/M_{irr}^2 \leq 2$ for Kerr black holes, with the extreme Kerr limit when $J = M^2$.

2.6.4 Isolated and Dynamical Horizons

The formalism of isolated and dynamical horizon combines in many aspects the AH and EH applications as black hole diagnostics. Like the AHs, isolated and dynamical horizons are quasilocal and do not require global knowledge of the spacetime. Like EHs, but unlike AHs, isolated and dynamical horizons furnish insight into the evolution of a black hole.

In order to define an isolated horizon, it is necessary to define the notion of non-expanding horizon. A *non-expanding horizon*, is a null 3-dimensional hypersurface H, with topology $S^2 \times \mathbb{R}$, that is foliated by marginally trapped surfaces, sometimes called worldtube. It can be thought as the structure (worldtube) emerging from a sequence of AHs on neighboring spatial slices Σ, although this picture requires the assumption that the collection of AHs generates smooth sections of H. For example, in the case of a stationary black hole, the worldtube is formed by simply stacking the AHs at each spatial hypersurface. The worldtube could be either spacelike or null: if matter or radiation is falling into the horizon, then the black hole's irreducible mass is increasing with time, and H is spacelike. In which case H is called a *dynamical horizon*. If no matter or radiation is falling into the black hole, H becomes null and it is a non-expanding horizon.

An *isolated horizon* (IH) is a non-expanding horizon H with the additional requirement that its intrinsic geometry (induced from the 4-dimensional metric) is not evolving along the null generators [257]. The distinction between non-expanding horizons and IHs is rather technical, but it allows one to use a Hamiltonian formulation to define the mass and angular momentum for the horizon H. It turns out, that the explicit expressions for the mass and angular momentum are independent of the extra structure of an IH, and hold for non-expanding horizons as well.

For the definition of angular momentum, it is required that the surface S given by the intersection of the worldtube H with hypersurface Σ, to be axisymmetric, i.e. that there exists a *Killing vector field* $\vec{\varphi}$ on the horizon. If $\vec{s}$ is the unit outward pointing normal to S, then the Killing condition implies, $\pounds_{\vec{\varphi}} q_{ij} = 0$, where $q_{ij} \triangleq \gamma_{ij} - s_i s_j$ is the induced metric on the horizon.

Given the Killing field $\vec{\varphi}$, the magnitude of the angular momentum on the horizon can be written in «3+1» form as,

$$J_H = \frac{1}{8\pi} \oint_S \varphi^l s^m K_{lm} dA, \tag{II-84}$$

where K_{ij} the extrinsic curvature of the 3-dim spatial hypersurface Σ and dA the area element on S.

This is expression is essentially the same as the ADM angular momentum, with the only difference that the ADM angular momentum is computed at infinity while this one is calculated at the horizon.

Having found the angular momentum, the horizon mass M_H can be given by,

$$M_H^2 = \frac{A_H}{16\pi} + \frac{4\pi J_H^2}{A_H}, \tag{II-85}$$

where $A_H = \oint_S \sqrt{q} d^2x$ is the area of the surface S.

The definition of IH only applies to black holes that are stationary. In the dynamical case, the dynamical horizon formalism can be used to define fluxes and balance laws for mass and angular momentum on the horizon.

2.7 Finite Differencing

There are different ways to numerically solve partial differential equations (PDE); among the most used methods are: finite differencing, finite elements and spectral methods. Interestingly enough, numerical relativity mostly uses finite differencing and spectral methods.

This section will briefly review some the basic ideas behind these techniques. A thorough description and presentation can be found in [258].

2.7.1 Classification of Partial Differential Equations

The second-order partial differential equations can be generally classified into three categories:

- *elliptic* equations, such as the Poisson's equation: $\partial_x^2\phi + \partial_y^2\phi = \rho$, where ρ is a source term that may depend on the position or even on ϕ up to first-order derivatives;

- *parabolic* equations, such as the diffusion equation: $\partial_t\phi - \partial_x(\kappa\partial_x\phi) = \rho$, where κ is the diffusion coefficient;

- *hyperbolic* equations, such as the wave equation: $\partial_t^2\phi - v^2\partial_x^2\phi = \rho$, where v is the wave speed.

A very well-known technique to deal with higher-order PDEs is to reduce the equations via change of variables, to a first-order system. For instance the wave equation can be rewritten as,

$$\begin{cases} \partial_t \phi & = -f, \\ \partial_t f + v^2 \partial_x g & = -\rho, \\ \partial_t g + \partial_x f & = 0, \end{cases} \tag{II-86}$$

or in a more compact way,

$$\partial_t \mathbf{u} + \mathbf{A} \cdot \partial_x \mathbf{u} = \mathbf{S}, \tag{II-87}$$

where $\mathbf{u} = (\phi, f, g)$ is the solution vector, $\mathbf{S} = (-f, -\rho, 0)$ is the source vector, and $\mathbf{A}$ is the velocity matrix given by

$$\mathbf{A} = \begin{pmatrix} 0 & 0 & 0 \\ 0 & 0 & v^2 \\ 0 & 1 & 0 \end{pmatrix}.$$

Alternatively, given a general expression of a second-order partial differential equation,

$$A\partial_\xi^2 \phi + 2B\partial_\xi \partial_\eta \phi + C\partial_\eta^2 \phi = \tilde{\rho}, \tag{II-88}$$

where the coefficients A, B and C are real, differentiable, and do not vanish simultaneously, the source term $\tilde{\rho}$ may depend on ϕ but only up to first-order derivatives; then the classification of the PDEs can be given in terms of the coefficients A, B and C:

- if $AC - B^2 > 0$, then the equation is elliptic;
- if $AC - B^2 = 0$, then the equation is parabolic;
- if $AC - B^2 < 0$, then the equation is hyperbolic.

These different types of partial differential equations require different kind of boundary and/or initial conditions.

Boundary conditions can take various forms, for example: Dirichlet conditions (specify the values of the solution on the boundary), Neumann conditions (specify their gradients on the

boundary, or other combinations.

2.7.1.1 Hyperbolicity

Given a hyperbolic PDE (e.g. wave equation), in the first order form

$$\partial_t \mathbf{u} + \mathbf{A}^i \cdot \partial_i \mathbf{u} = \mathbf{S}, \tag{II-89}$$

where $\mathbf{u}$ is the solution vector ($\in \mathbb{R}^n$), $\mathbf{S} = \mathbf{S}(\mathbf{u})$ is a source vector ($\in \mathbb{R}^n$), and $\mathbf{A}$ is the velocity matrix ($\in \mathbb{R}^{n\times n}$). The classification is independent of the value of $\mathbf{S}$, for instance considering the homogeneous equation, i.e. $\mathbf{S} = 0$.

The problem is called *well-posed* if it is possible to define a norm $||...||$ such that the norm of the solution vector (for constant coefficients) satisfies,

$$||\mathbf{u}(t, x^i)|| \leq k e^{\alpha t} ||\mathbf{u}(0, x^i)||, \tag{II-90}$$

for all times $t \geq 0$; k and α are two constants that are independent of the initial data $\mathbf{u}(0, x^i)$. This implies that solutions of a well-posed problem cannot increase more rapidly than exponentially. The solution is bound by the initial data.

For defining the notion of hyperbolicity, it is necessary to study the properties of the *characteristic matrices* $\mathbf{A}^i$. Considering an arbitrary unit vector n_i, it is possible to construct the matrix, $\mathbf{P}(n_i) \triangleq \mathbf{A}^i n_i$, known as the *principal symbol* of the system. Based on the properties of $\mathbf{P}$, there are different notions of hyperbolicity:

- *Symmetric hyperbolic*, if $\mathbf{P}$ can be symmetrized in a way that is independent of n_i.
- *Strongly hyperbolic*, if $\mathbf{P}$ has real eigenvalues and a complete set of eigenvectors for all n_i.
- *Weakly hyperbolic*, if $\mathbf{P}$ has real eigenvalues but it does not have a complete set of eigenvectors for all n_i.

- *Strictly hyperbolic*, when the eigenvalues of $\mathbf{P}$ are not only real but are also distinct for all n_i.

For example, simple wave equations are symmetric hyperbolic. Symmetric hyperbolic systems are automatically strongly hyperbolic. Importantly, strongly hyperbolic equations are well-posed, while systems that are weakly hyperbolic are not necessarily.

2.7.2 Finite Difference Methods

In a finite difference approximation a function $f(t, x)$ is represented by values at a discrete set of points. The basic idea of the finite difference approximation is to substitute the continuous spacetime with a set of discrete points, i.e. a numerical or computational grid or mesh. The grid need not to be uniform. In general the geometry and symmetries of the problem will determine the grid.

Once the computational grid is established, the next step is to substitute the differential equations with a system of algebraic equations. This is done by approximating the differential operators by finite differences between the values of the functions at nearby points of the grid. These algebraic equations involve the values of the functions at each point of the grid and its nearest neighbors. The resulting system is a system of algebraic equations at each point in the grid that must be solved numerically.

Given a differential equation in the general form,

$$\mathcal{L}u = 0, \tag{II-91}$$

where u denotes a set of functions of the spacetime coordinates (t, x^i) and $\mathcal{L}$ is some differential operator acting on u. Let u_Δ represents the *discretized* approximation of u evaluated at the points of the computational grid, and $\mathcal{L}_\Delta$ the finite difference version of the differential operator. Δ can represent either Δx or Δt. The finite difference version of the differential equation then takes the form,

$$\mathcal{L}_\Delta u_\Delta = 0. \tag{II-92}$$

In particular a function $f(t,x)$, given a particular grid, all the points in the grid can be given by, $x_i = x_0 + \Delta x$ and $t^n = t^0 + n\Delta t$. The result of this discretized spacetime, propagates to the function $f(t,x)$,

$$f_i^n = f(t^n, x_i) + \text{truncation error.} \tag{II-93}$$

Assuming that $f(x)$ is differentiable to sufficiently high order and that it can be represented by a Taylor series, then

$$f_{i+1} = f(x_i + \Delta x) = f(x_i) + \Delta x(\partial_x f)_{x_i} + \frac{(\Delta x)^2}{2}(\partial_x^2 f)_{x_i} + \mathcal{O}(\Delta x^3). \tag{II-94}$$

Solving for $(\partial f)_{x_i} = (\partial_x f)_i$, then

$$(\partial_x f)_i = \frac{f_{i+1} - f_i}{\Delta x} + \mathcal{O}(\Delta x), \tag{II-95}$$

in the limit when $\Delta x \to 0$, Eq.(II-95) recovers the definition of the partial derivative.

Considering the Taylor expansion to the point x_{i-1},

$$f_{i-1} = f(x_i - \Delta x) = f(x_i) - \Delta x(\partial_x f)_{x_i} + \frac{(\Delta x)^2}{2}(\partial_x^2 f)_{x_i} + \mathcal{O}(\Delta x^3), \tag{II-96}$$

subtracting Eq.(II-94) from Eq.(II-96), one obtains

$$(\partial_x f)_i = \frac{f_{i+1} - f_{i-1}}{2\Delta x} + \mathcal{O}(\Delta x^2), \tag{II-97}$$

which represent the discretized version of the first derivative in second order in Δx, meaning the truncation error drops by a factor of four when the grid spacing is reduced by a factor two. Basically, by combining Taylor expansions in such a way that the leading order term cancels out, leading to a higher-order representation of the derivative (this cancellation works for uniform grid, when Δx is independent of x: this is why some numerical relativity applications of finite difference schemes work with uniform grids).

Higher-order derivatives can be constructed in a similar fashion, for instance,

$$(\partial_x^2 f)_i = \frac{f_{i+1} - 2f_i + f_{i-1}}{\Delta x^2} + \mathcal{O}(\Delta x^2). \tag{II-98}$$

Additionally it is possible to enhance this technique by constructing discretrizations at intermediate grid points $x_{i+1/2}$ and $x_{i-1/2}$.

Numerical relativity codes often use finite-difference representations that are higher than second order (for instance `LazEv` –Sec.2.8.2–, the evolution code developed by Campanelli *et al.* employed in our simulations, uses 8th order).

The derivation of higher-order stencils is analogous at the previous one: express derivatives of a function at a certain point as a linear combination of function values at the point and neighboring grid points; express the function as Taylor expansions; and finally combine the expressions in such a way that all term up to the desired order cancel out. For centered, second-order derivatives, it is only necessary to include the immediate nearest neighbors (i.e. points at $i-1$ and $i+1$), but higher-order expansions require larger number of points. For instance the expressions for fourth-order first- and second- derivatives are given by,

$$(\partial_x f)_i = \frac{1}{12(\Delta x)} \left(f_{i-2} - 8f_{i-1} + 8f_{i+1} - f_{i+2}\right) + \mathcal{O}(\Delta x^4), \tag{II-99}$$

$$(\partial_x^2 f)_i = \frac{1}{12(\Delta x)^2} \left(-f_{i-2} + 16f_{i-1} - 30f_i + 16f_{i+1} - f_{i+2}\right) + \mathcal{O}(\Delta x^4). \tag{II-100}$$

Additionally, changing the "discretization scheme", i.e. centered/forward/backward, can work as a strategy to improve the efficiency and accuracy.

Finally, by substituting the discrete expression for the derivatives into the PDE, one can solve for the future values of the function given the values in a past time.

2.7.3 Uniform Grids, Fixed Mesh Refinement, and Adaptive Mesh Refinement

A standard way of solving partial differential equations is the implementation of finite differences on a regular grid, which is usually known as *unigrid*. This grid may be broken up into several parts for parallelization purposes, but parallelization should be transparent to the physics part of the application.

The spacing of the grid points determines the local error, and hence the accuracy of the solution. The spacing also determines the number of calculations to be made to cover the domain of the problem, and thus the cost of the computation. Increasing the resolution in a unigrid application is somewhat expensive. For example, increasing the resolution by a factor of two requires a factor of eight more storage in three dimensions. Given a constant Courant factor, the calculation time will go up by a factor of sixteen. This behavior makes it easy to find problems that cannot be solved on contemporary supercomputers, no matter how big and fast those computers are.

Fixed Mesh Refinement (FMR) is a way of implementing a non-uniform resolution into a unigrid application with minimal changes to its structure. Instead of only one grid, there are several grids or grid patches with different resolutions. The coarsest grid usually encloses the whole simulation domain. Successively finer grids overlap the coarser grids at those locations where a higher resolutions is needed. The coarser grids provide boundary conditions to the finer grid through interpolation. Instead of updating only one grid, the application has to update all grids. The usual approach is to first take a step on the coarsest grid, and then recursively take several smaller steps on the finer grids. The Courant criterion requires that the step sizes on the finer grids be smaller than on the coarse grid. The boundary values for the finer grids are found through interpolation in space and time from the coarser grid. In the end, the information on the finer grids is injected into the coarser grids.

A more sophisticated method is to dynamically adapt the refined sub-grids into the coarser domain, known as Adaptive Mesh Refinement (AMR). In the adaptive mesh refinement technique, we start with a base coarse grid. As the solution proceeds we identify the regions

requiring more resolution by some parameter characterizing the solution, for instance the local truncation error. We superimpose finer subgrids only on these regions where the error estimate exceeds some tolerance. Finer and finer subgrids are added recursively until either a given maximum level of refinement levels is reached, or the local truncation error has dropped below the desired level.

Between these two extremes is guided mesh refinement, where the refinement levels are moved about the grid according some pre-established criterion (usually based on numerical experience). For example, placing high resolution in the vicinity of the black holes.

2.7.4 Other Approaches

2.7.4.1 Spectral Method

Spectral methods work by expanding the solutions as a finite linear combination of some appropriate basis functions. In this case, the variables to solve for are the coefficients of such an expansion.

When applicable, spectral methods have excellent error properties, with the so called "exponential convergence" being the fastest possible. Typical examples of spectral methods are: Fourier series methods for periodic geometry problems, polynomial spectral methods for finite and unbounded geometry problems, pseudospectral methods for highly nonlinear problems, and spectral iteration methods for fast solution of steady state problems.

The spectral method and the finite element method are closely related and build on the same ideas; the main difference between them is that the spectral method approximates the solution as linear combination of continuous functions that are generally nonzero over the domain of solution (usually sinusoidal or Chebyshev polynomials), while the finite element method approximates the solution as a linear combination of piecewise functions that are nonzero on small subdomains. Because of this, the spectral method takes on a global approach while the finite element method is a local approach. This is part of why the spectral method works best when the solution is smooth.

2.7.4.2 Method of Lines (MoL)

The basic idea of the *method of lines* is to finite difference the spatial derivatives only. MoL starts from a PDE, and proceeds by first discretizing the spatial derivatives only and leaving the time variable continuous. This leads to a coupled system of ordinary differential equations to which a numerical method for initial value ordinary equations can be applied.

For instance, instead of having $u_i^n = u(t^n, x_i)$ as for finite differences, MoL starts with only a spatial grid, $u_i(t) = u(t, x_i)$ remaining as a continuous function of time. Then the PDE for $u(t, x)$ becomes a set of ordinary differential equations for the grid values $u_i(t)$, e.g.

$$\left(\frac{du_i}{dt}\right)^n = F(u_i^n, u_n^{n\pm1}, ..., \Delta t, ...) + \mathcal{O}(\Delta t).$$

Finally a "time" grid needs to be introduced, labeled by n. The appealing feature of the MoL, is that any method for the integration of ODE can be used at this stage (e.g. Runge-Kutta).

2.8 Simulations Framework

2.8.1 Cactus

The `Cactus/ET` framework is a suite of tools aimed for the numerical relativity community [237, 242, 236, 238, 239, 240]. It has been developed as open-source environment with a modular infrastructure: the central core ("flesh") connects to applications modules ("thorns"). It provides support for: BSSN formulation (phi, W, 1+log, Gamma driver, up to 8th order); GRHydro (formerly based on `WhiskyCode`; Valencia formulation); BH/NS initial data (`TwoPunctures`, `Lorene`); Excision/Turduckening techniques; Method of Lines (MoL), Runge-Kutta; Adaptive Mesh Refinement (through `Carpet` driver), or also uniform grids (`PUGH` driver); Black hole horizon finders (AH and EH); Gravitational wave extraction; Parallelization: `MPI`, `OpenMP`; and other tools, such as: `HDF5` output, Visualization import, etc.

The pre-defined core thorns provide many basic utilities, such as: boundary conditions, I/O methods, reduction and interpolation operations, coordinate symmetries, parallel drivers,

elliptic solvers.

`Cactus` allows us to incorporate our own "thorns" in order to perform specific tasks, where the thorn/code can be written in `C`, `Fortran`, or even using wrappers. In the project where we investigated the ring singularity EHs searches (Chap.3), we developed our own thorns to define the initial data of the problem and perform the evolution of the system using the `Cactus` framework, with the assistance of many predefined thorns, e.g. `LazEv` (is the evolution algorithm), `Carpet` (allows to use fixed mesh refinement), `AHFinderDirect` (AH finder), `EHFinder` (EH finder), `TwoPunctures` (initial data).

2.8.2 LazEv

The `LazEv` General Relativistic evolution code makes use of finite-difference techniques to evolve the gravitational fields of strongly gravitating sources like BHs and other compact objects. The partial differential equations that make up the BSSN formulation (Baumgarte-Shapiro-Shibata-Nakamura; [145, 146, 147]) of Einstein's equations for the spacetime metric are solved using eighth-order finite differencing, with boundary conditions being applied in the asymptotic region away from the strong-field sources. Parallelization and data storage are handled by the `Cactus` toolkit [239, 240], which is well supported by the Einstein Toolkit community [240]. The code for the evolution routines, was generated using the `LazEv` computational framework, which was developed by Zlochower, Baker, Campanelli and Lousto [259]. It consists of a set of `Mathematica` scripts that converts tensorial equations into C code, and includes the ability to generate arbitrary-order finite differencing schemes, including both centered and upwind derivatives. Timestepping is handled using the Method of Lines, which allows for arbitrary-order timestepping, including a variety of Runge-Kutta schemes. Currently, most evolutions are performed using fourth-order Runge-Kutta stepping. Our vacuum code makes use of several in-house and publicly available `Cactus/Carpet/ET` analysis routines.

Chapter 3

Event Horizons for Nontrivial Black-Hole Topologies

3.1 Introduction

The recent dramatic breakthroughs in the numerical techniques to evolve black-hole-binary (BHB) spacetimes [139, 140, 141] led to rapid advancements in our understanding of black-hole physics. Notable among these advancements are developments in mathematical relativity, including systems of PDEs and gauge choices [260, 261, 262], the exploration of the validity of the cosmic censorship conjecture [263, 264, 265, 266, 267, 268], and the application of isolated horizon (IH) formulae [269, 270, 264, 265, 271, 272]. Recent studies include the algebraic classification of spacetime post-merger of BHBs [273, 274], investigations of the orbital mechanics of spinning BHBs [263, 264, 265, 103, 275, 276, 277], studies of the recoil from the merger of unequal mass BHBs [87, 88, 89], the remarkable discovery of unexpectedly large recoil velocities from the merger of certain spinning BHBs [90, 91, 92, 93, 94, 95, 96, 97, 98, 99, 100, 101, 102, 103, 104, 105, 106], investigations into the mapping between the BHB initial conditions (individual masses and spins) and the final state of the merged black hole [278, 279, 280, 281, 282, 283, 284, 109], and improvements in our understanding of the validity of approximate BHB orbital calculations using post-Newtonian (PN) methods [285,

286, 287, 288, 289, 290, 291, 292]. There were also notable advances in our understanding of the small mass ratio limit, as well as hybrid perturbative/numerical methods for evolving small mass ratio BHBs [293, 93, 294].

Even before the breakthrough there were important studies of the structure of event horizons for non-stationary spacetimes. An event horizons is a 3D null hypersurface in spacetime that forms the boundary of the region of causally connected to $\mathscr{I}^+$. The event horizon is actually that part of the null surface that is caustic free in the future. If two null generators cross, then prior to the crossing, the generators are not on the horizon, and a causal curve intersecting these generators can terminate on $\mathscr{I}^+$. To understand why this is, we note that the region of the null hypersurface containing this crossing is equivalent to a lightcone in the local Minkowski frame. Unlike the region of the interior of the light cone in the future of the intersection point, the region in the past of the intersection point of the light cone is causally connected to the region outside the light cone. In the case of the event horizon, points on the null generators prior to a caustic are causally connected to $\mathscr{I}^+$.

In Ref. [295] it was proven that, for asymptotically flat spacetimes satisfying the null energy condition, all causal (timelike or null) curves from $\mathscr{I}^-$ to $\mathscr{I}^+$ are deformable to a topologically trivial curve. An important consequence of this "topological censorship" theorem is that constant time slices of an event horizon must (at least in the distant future) be topologically spherical. Hawking proved [248, 186] (see [296, 297, 298] for generalizations of this theorem to higher dimensions) that spacelike slices of event horizons in asymptotically flat stationary spacetimes obeying the dominant energy condition have topology S^2. For non-stationary spacetimes, toroidal horizons are allowed, but the *holes* in these horizons would close up fast enough to prevent causal curves from traversing the holes. Interestingly, the existence of a single toroidal horizon slice implies that there is a 1-parameter family of toroidal horizon slices in the neighborhood of this particular horizon slice [297].

The first numerical studies of the event horizon topologies for non-stationary spacetimes involved the axisymmetric collapse of a rotating toroidal distribution of dust [299, 300] and theoretical studies of possible horizon topologies based ellipsoidal wavefronts in Minkowski

space [301]. However, as of yet, there have been no simulations published that have unequivocally shown event horizons with toroidal topologies from the mergers of multiple black holes (BHs) (see [243] for a possible example), and very few that have shown event horizons of any form (see [243, 253]). The main reason for this is that an event horizon is a global structure whose location is determined by the entire future of the spacetime (in practice, one only needs to evolve to the point where the final remnant BH equilibrates). Thus, in order to find an event horizon, one must first evolve the spacetime, obtain the full four-metric at all times in the future of the initial hypersurface, and then evolve the null generators normal to the last common apparent horizon (AH) backwards in time. This presents a significant storage challenge, and since much of the information about BHBs can be obtained from the AHs (using, for example, the IH formalism), such an event horizon search is seldom performed. In a typical BHB simulation, one is interested in the masses and spins of the individual BHs when they are far away and in the mass and spin of the remnant BH after it has equilibrated. In these two regimes, the IH formalism provides accurate measurements of the mass and spin of the BHs. However, near merger, where the AH and event horizon can differ significantly, the IH formalism will not produce accurate results. Moreover, the structure of the AHs will not match that of the event horizon. Thus, it is important to examine the event horizon structure in the vicinity of the merger in order to gain an understanding of how event horizons behave in highly dynamical spacetimes.

While topological censorship forbids an event horizon from remaining toroidal, it is interesting to see if purely vacuum configurations can have instantaneously toroidal slices. To partially address this question, we examine the dynamics of a spacetime with a ring-like singularity, rather than pointlike singularity. This configuration was first studied in [302], where it was found that an AH does not exist if the rings radius is sufficiently large, leading to the conjecture that this is a naked singularity (see also [303]). We find evidence to support this conjecture. Here we extend the analysis and show evidence that there is no common nonsingular event horizon for sufficiently large ring radii.

While our proposed configuration would not violate cosmic censorship because the singular-

ity does not develop in the future of a non-singular slice (i.e. all slices contain a singularity), questions concerning the validity of the cosmic censorship are also quite interesting. The authors of Ref. [304, 305] evolved a prolate spheroidal distribution of collisionless gas and found that generically, for large enough spheroids, a singular spindle forms on the long axis of the spheroid which is apparently naked, violating cosmic censorship. In a follow-up work in Ref. [306] they found vacuum configurations of linear black-hole distribution like the ones we use here also contain naked singularities for sufficiently long lines. In [307], the authors found that naked singularities can form in 5-dimensional black-string configurations.

For this project we use the following nomenclature. While the event horizon is a global 3-d hypersurface in a 4-d space, we are interested in spacelike slices of the horizon. That is if Σ_t is a one-parameter family of spacelike slices that foliates the spacetime and $\mathcal{H}$ is the event horizon, then we are interested in the object $\mathcal{H}_t = \Sigma_t \cap \mathcal{H}$ (which may be a disconnected set). In the sections below we refer to these spatial slices of the event horizon ($\mathcal{H}_t$) as "EHs". We note that for well separated BHs these "EHs" will also be AHs. In order to locate these distinct EHs we track the null generators using the `EHFinder Cactus` thorn [243], backwards in time, dropping those generators that have crossed, leaving only those generators still on the EH.

This chapter is organized as follows. In Sec. 3.3 we discuss the ring configuration and toroidal event horizons. In Sec. 3.3.1 we discuss the initial data for the numerical simulations. In Sec. 3.4 we discuss the numerical techniques. In Sec. 3.5 we discuss the EHs found for the discrete ring and discrete line cases, as well as the AHs found for the continuum ring. Finally, in Sec. 3.6 we discuss the implication of our numerical results and speculate about the nature of the EH for the continuum ring.

3.2 Topology theorems and their consequences

Singularities arising from nontrivial topology General Relativity allows *a-priori* the universe to have nontrivial topology, for example the wormholes in the structure of the Schwarzschild and Kerrr spacetimes. In principle this topology could be detected, e.g. wormholes could be traversed by observers or starlight. But from particular examples, it is known

that nontrivial topological structures tend to "pinch off" and form singularities. More precisely, if M is a spacetime obeying the null energy condition and S is an asymptotically flat non-simply connected Cauchy surface for M then the spacetime is singular [308, 309]; i.e., M is future null geodesically incomplete.

These examples and results indicate that nontrivial topology tends to induce gravitational collapse. According to the Cosmic Censorship Conjecture, the process of gravitational collapse leads to the formation of an event horizon which hides the singularities that develop from view. This suggests a notion of Topological Censorship in which nontrivial topology becomes hidden behind the event horizon, and the region exterior to all black holes (and white holes) will have simple topology. In [310] it was proven that the steady state spatial topology outside horizons is Euclidean (proved using minimal surface theory).

Topological Censorship Theorem The topological censorship theorem states that general relativity does not allow an observer to probe the topology of spacetime: any topological structure collapses too quickly to allow light to traverse it. More precisely, in a globally hyperbolic, asymptotically flat spacetime satisfying the null energy condition, every causal curve from past null infinity to future null infinity is fixed-endpoint homotopic to a curve in a topologically trivial neighborhood of infinity [295]. That is every causal curve extending from past null infinity to future null infinity can be continuously deformed to a curve near infinity. Roughly speaking, this says that an observer, whose trip begins and ends near infinity, and who thus remains outside all black holes, is unable to probe any nontrivial topological structures. The topological censorship theorem of [295] applies to asymptotically flat spacetimes, i.e., spacetimes which "look like" Minkowski space near infinity.

M is globally hyperbolic if and only if it admits a Cauchy hypersurface S (a hypersurface which is intersected exactly once by every inextendible causal curve). If M is globally hyperbolic then the topology of M is given by $\mathbb{R} \times S$. The topological censorship theorem is closely related to a basic result concerning the end structure of spacetime: A spacetime may have more than one null infinity, $\mathscr{I} = \cup_\alpha \mathscr{I}_\alpha = \cup_\alpha (\mathscr{I}^+_\alpha \cup \mathscr{I}^-_\alpha)$. An example is the maximally extended Schwarzschild spacetime (see Fig.3.1).

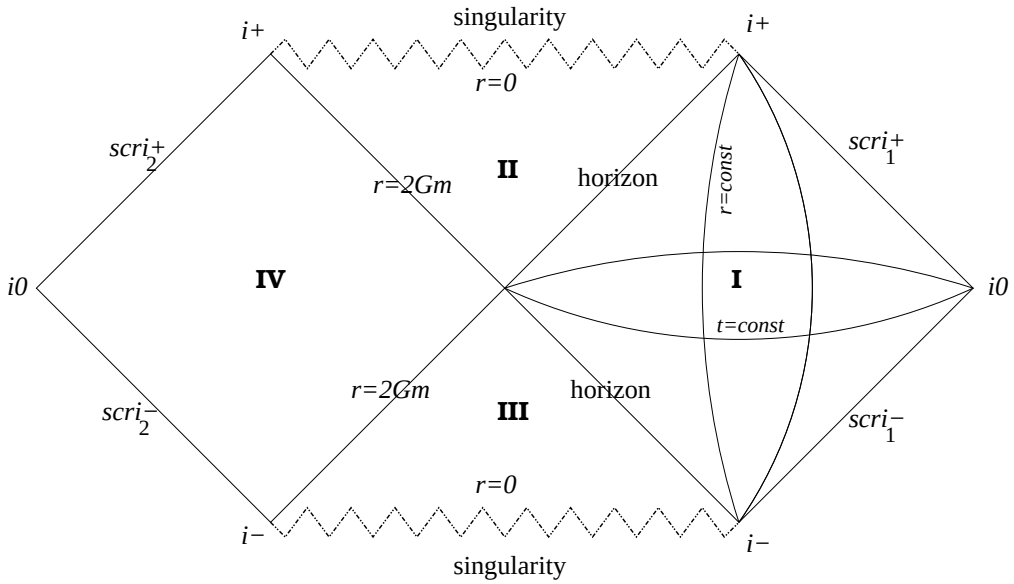

Figure 3.1: Conformal diagram for Schwarzschild spacetime: region I is the original Schwarzschild, region II is the black hole (once anything travels from region I into II, it can never return), region III is the time-reverse of region II (white hole), region IV is another asymptotically flat region of spacetime (a mirror image of region I, it can be thought to of as being connected to region I by a wormhole).

Strong form of the Cosmological Censorship The Topological Censorship is really a statement about the *domain of outer communications* (DOC). The DOC is a region outside all black holes and white holes, and is given by $J^-(\mathscr{I}^+) \cap J^+(\mathscr{I}^-)$.

In such terms, the topological censorship theorem could be stated as observers in the DOC do not detect any nontrivial topology. The strong form of the cosmological censorship then states that: observers in the DOC, **even superluminal ones**, do not detect any nontrivial topology.

There is a related theorem [311] that shows that given a spacetime (M, g_{ab}) is an asymptotically flat spacetime which obeys the averaged null energy condition, and supposing that the DOC is globally hyperbolic; then the DOC is simply connected, i.e. $\sqcap_1(DOC) = 0$.

3.2.1 Application to the topology of black holes

Topological Censorship provides an alternative proof of Hawking's black hole topology theorem, which states that black holes in asymptotically flat spacetimes have spherical topology.

The main advantages of this approach are that: it does not require the assumption of stationarity, and it is enough to use the weaker null energy condition.

3.2.1.1 Higher Genus Black Holes

Temporarily toroidal event horizons have been observed in numerical simulations [300, 243]. There have been also some "toy model" versions discussed in [300, 312].

The DOC is simply connected, even though the spatial slice $t = t_0$ is not (see Fig. 3.11). The Topological censorship theorem shows that eventually the black hole topology is spherical.

There is a Theorem [312, 313] that states: Let $(M; g_{ab})$ be an asymptotically locally AdS spacetime which obeys the averaged null energy condition, and suppose the DOC is globally hyperbolic (in the AdS sense). Then every curve (causal or otherwise) in the DOC with end points on $\mathscr{I}$ can be deformed to a curve lying in $\mathscr{I}$.

Then $\sqcap_1(DOC)$ can be no more complicated than $\sqcap_1(\mathscr{I})$, so $g_0 \leq g_\infty$; where, g_0 is the genus of black hole, and g_∞ represents the genus of surface at infinity.

In the Lorentzian setting, Topological Censorship shows that although conformal infinity may have multiple components, distinct components are not in causal contact.

3.2.1.2 Hoop Conjecture

The original Hoop Conjecture [314, 315] states that: "Horizons form when and only when a mass M gets compacted into a region whose circumference in every direction is $C \lesssim 4\pi GM/c^2 = 2\pi r_{Sch}$.

3.2.2 Higher-Dimensions and non-trivial Event Horizons

In 4-dimensional General Relativity, there are several theorems, as described previously, restricting the topology of the event horizon of a black hole. In the stationary case, black holes must have a spherical horizon, while a toroidal spatial topology is allowed only for a short time. Several works have focused on what happens to the topology of the event horizon when increasing the number of dimensions. For instance [316] considers spinning black holes inspired

by Loop Quantum Gravity and by alternative theories of gravity, finding that the spatial topology of the event horizon of these objects changes when the spin parameter exceeds a critical value. Such a possibility may be relevant in astrophysics, since in some models the accretion process can induce a topology transition in the horizon.

In particular event horizons deformations were studied in [317] using a perturbative approach. This work analyzed the geometry of the event horizon of a spacetime in which a small compact object plunges into a large Schwarzschild black hole.

More exotic scenarios have also been discussed, for instance when considering "black hole rings" in 4 and higher dimensions [318].

Most of the works studying the topologies of event horizons are based on the differentiability of the event horizon. Considering the whole structures of the event horizon, however, the event horizon cannot always be differentiable. In general, an event horizon is not smooth at its endpoints. In [319], the topologies of event horizons are investigated. By considering the existence of the endpoint of the event horizon, they found new possibilities for the topology of the event horizon. For instance, it was found that a toroidal event horizon of arbitrary genus is produced by two-dimensional endpoints if the set of endpoints form a 2-dimensional sheet. Similarly, if the endpoints set is a line, the time slicing can be distorted to give slices with an arbitrary numbers of BHs. Moreover, these aspects can be removed by an appropriate timeslicing.

3.3 Toroidal Event Horizons and Black Hole Rings

While topological censorship requires that the 3-d hypersurface corresponding to the event horizon is simply connected, there is no such restriction on 2-dimensional spatial slices of the event horizon. The question we wish to address in this work is, can a configuration of initially stationary (in the sense of having zero momentum, the spacetime itself is not stationary and does not possess a timelike Killing vector field) nonspinning black holes form a horizon with topologically toroidal slices, and if so, can we find these slices numerically? In order to investigate these questions, we examine configurations of BHs arranged in a ring configuration,

as well configurations with BHs arranged in a line. The idea behind using a ring is that if neighboring BHs are close enough together, and the ring is wide enough, then a common event horizon (if it exists) should have a toroidal topology (on the 3-dimensional slice). We can imagine constructing such a ring by keeping the total mass fixed, while increasing the number of BHs in the ring. We might expect that, for a sufficiently large number of BHs, a common event horizon will form. However, as we conjecture below based on our numerical simulations, this event horizon may only form in the limiting case where there is an infinite number of BHs with infinitesimal masses. The EH, while toroidal, may actually have zero width. Interestingly, we can construct initial data corresponding to this limiting distribution of BHs using the techniques of electrostatics. This configuration was studied in Ref. [302], as well as [303], where it was shown that a common AH does not exist if the ratio of the ring radius to mass is larger than $R/M \sim \frac{20}{3\pi} \approx 2.12$.

An AH must be simply connected [297], hence the absence of an AH indicates that the EH may not be simply connected. We note that it is possible, to construct unusual slicings where the EH is spherical but an AH does not exist. However, our initial data are based on a superposition of Brill-Lindquist BHs [320], which, at least for finite numbers of BHs, does not lead to these unusual slices. In [302], it was argued that the absence on an AH indicates that this singularity is naked.

3.3.1 Initial Data

We construct initial data by superimposing conformally-flat, initially stationary non-spinning, black-hole (BH) configurations. That is, we take as initial data $K_{ij} = 0$ and $\gamma_{ij} = \psi^4 \delta_{ij}$, where $\Delta\psi = 0$. For the case of discrete BHs, we use an ordinary superposition of Brill-Lindquist BHs [320], while for the case of the BH ring, we use the techniques of electrostatic to solve for the potential of a 1-dimensional ring of charge.

3.3.1.1 Continuous Ring

To construct initial data for the continuous BH ring we solve

$$\Psi(\vec{r}) = M \int_0^{2\pi} \frac{d\phi'}{\sqrt{r^2 - 2rR\cos(\phi - \phi') + z^2}}, \tag{III-1}$$

to obtain [302, 303]

$$\Psi = 1 + \frac{M}{2\pi}\left[\frac{2\mathrm{K}\left(\frac{-4\rho\rho_0}{z^2+(\rho-\rho_0)^2}\right)}{\sqrt{z^2+(\rho-\rho_0)^2}} + \frac{2\mathrm{K}\left(\frac{4\rho\rho_0}{z^2+(\rho+\rho_0)^2}\right)}{\sqrt{z^2+(\rho+\rho_0)^2}}\right], \tag{III-2}$$

where $K(x)$ is the complete elliptical integral of the first kind, with the convention used by Mathematica

$$K(x) = \int_0^{\pi/2} \frac{d\theta}{\sqrt{1 - k\sin^2\theta}}.$$

While initial data corresponding to arbitrary ring radii are easy to construct, actual evolutions of these data are numerically challenging for large radii, as explained below. Note that $\psi \sim \ln R$, where R is the coordinate distance to the ring, in the neighborhood of the ring singularity. Hence, the evolution variable $W = \psi^{-2}$ will have the form $W \sim 1/(\ln R)^2$, which is continuous, but not differentiable at $R = 0$.

3.3.1.2 Discrete Ring

To construct initial data for the discrete BH ring (i.e. a symmetric distribution of BHs on a ring) we superimposed N BHs, where the total mass of the ring is $1M$. Here ψ is given by

$$\begin{aligned} \psi &= 1 + \sum_{i=0}^{N-1} \frac{m_i}{|\vec{r} - \vec{r}_i|} \\ &= 1 + \sum_{i=0}^{N-1} \frac{m_i}{\sqrt{(x-x_i)^2 + (y-y_i)^2 + (z-z_i)^2}}, \end{aligned} \tag{III-3}$$

where $m_i = M/N$, $\vec{r}_i = [R\cos(i\alpha), R\sin(i\alpha), 0]$ is the coordinate location of BH i, R is the radius of the ring, and $\alpha = 2\pi/N$. In order to preserve reflection symmetry, N must be even.

For this configuration, the ADM mass of the spacetime is approximately $M_{\rm ADM} = Nm$ and hence the final merged BH should have a mass of $M \sim N\ m$, where N is the number of BHs and m is mass of each BH. Binding energy, which tends to zero as the configuration size goes to ∞, will reduce the ADM mass by a small amount (for example, the binding energy of a non-spinning BH binary near the ISCO is only about 2%), and gravitational radiation will further reduce the mass of the final black hole by a small percentage.

Our technique of using a discrete ring to model the horizon dynamics of a continuum ring distribution is a natural extension of the techniques developed in [306].

3.3.1.3 Line

In order to mimic the differential line element of the ring, we consider a finite line element constrained such that the average linear mass density of black holes per unit length of the line is the same as that of the ring. To construct this linear configuration of BHs, we consider a line of length L, and place N BHs on the line with a uniform separation ℓ. The outermost BHs are arranged a distance $\ell/2$ from the ends of the line. In this configuration, the mass density of the line is $m/\ell = M/L$, where $m = M/N$ (see Fig. 3.2). If L is the total length of the line and L_N is the separation between the two outer BHs, then $L = [N/(N-1)]L_N$ and the average linear density is $M/L = (N-1)m/L_N$. Hence

$$L_N = 2\pi R\frac{N-1}{N}, \tag{III-4}$$

where R is the radius of the ring.

Note this configuration was first studied in Ref. [306] to show that a common apparent horizon does not exist for lines larger than $L \sim 1.5M$, and to therefore argue that this configuration has a naked singularity.

Because $\mathcal{H}$ is a global entity, the legitimacy of using a linear mass distribution to model the behavior of the EH for a ring is not clear. As we argue below, the EH must be very close to the linear singularity when the line is sufficiently long, and hence its structure is, at least partially, dependent on the same singular behavior in the metric as the EH around the ring

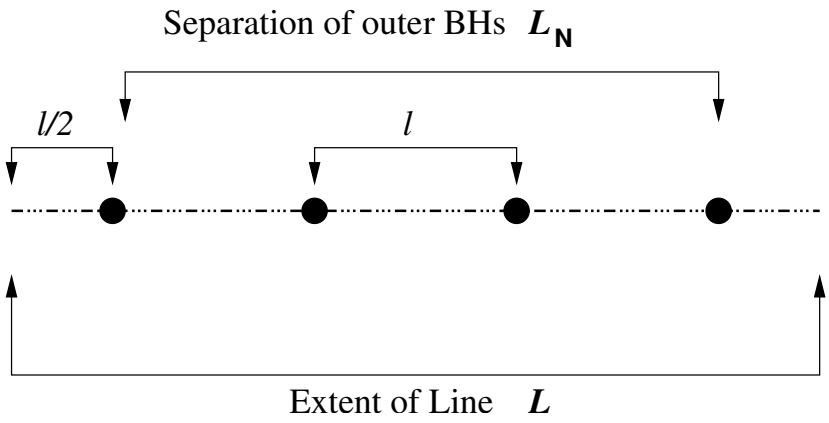

Figure 3.2: The setup for the linear distribution of BHs. l is the separation between neighboring BHs, L_N is the separation between the two outer BHs, while L is the length of the line. The line is formally a length l longer than the separation of the two outer BHs so that the linear density is the same in the neighborhood of each BH (we consider that the BH's mass is spread out over an interval of $\pm l/2$ around the BHs center.

singularity. In addition, the spacetime near the singularity rapidly approaches flat space in both configurations. So outgoing null generators far enough away from the singularity to see the differences in the metric are also likely to be far enough away to escape to infinity.

The study of the EH structure from a linear distribution is interesting in its own right, and if we can show that this distribution does not have a non-singular horizon in the distant past (which is supported by the work of [306]), this helps support the conjecture that any linear distribution, sufficiently extended in space, is surrounded by a singular horizon, or no horizon at all.

3.4 Numerical Techniques

We evolved these BH configuration using the LazEv [321] implementation of the moving puncture approach [140, 141]. We obtain accurate horizon parameters by evolving this system in conjunction with a modified 1+log lapse and a modified Gamma-driver shift condition [322, 140], and an initial lapse $\alpha(t=0) = 2/(1+\psi_{BL}^4)$, we also used $\alpha(t=0) = 1$ for the continuum

ring. The lapse and shift are evolved via

$$(\partial_t - \beta^i \partial_i)\alpha = -2\alpha K, \tag{III-5}$$

$$\partial_t \beta^a = 3/4(\tilde{\Gamma}^a - \tilde{\Gamma}^a(0). \tag{III-6}$$

When searching for EHs, we evolved these configuration using the unigrid `PUGH` driver [239]. After saving the metric at each timestep, we used the EHFinder thorn [243] to locate the event horizons. In this case, we used the PUGH driver because the publicly available version of EHFinder was not compatible with the Carpet AMR driver [237]. When evolving the continuum ring configuration, we used the Carpet diver because the resolutions required near the ring would have made a unigrid simulation prohibitively expensive. We used the AHFinderDirect [255] thorn to locate apparent horizons.

In order to make the unigrid runs more efficient, we mimicked fixed-mesh-refinement using a multi-transition FishEye transformation [323, 322, 321]. In addition to this, we also exploited 'octant symmetry' in most of our simulations, allowing us to increase the resolution.

Solving the Einstein Equations for a BH ring of arbitrary radius numerically is not feasible due to resolution constraints. To understand why this is, we can consider the case of a discrete ring of some large radius. As we add more BHs to the ring, the mass of each BH is reduced. The resolution required to evolve a BH is inversely proportional to its mass, hence in the continuum limit, we would need an infinitesimal gridspacing. On the other hand, if a spheroidal common apparent horizon is present, then we only need to resolve the region outside the AH. Thus, we can evolve ring configurations with small radii.

When searching for EHs using `EHFinder` [243] we first perform a standard forward in time evolution, outputting the full 4-d metric at every timestep, until the remnant BH is nearly spherical. We then perform a backwards in time evolution and track the null generators of the EH from the final AH backwards in time. As noted above, once two generators cross they leave the EH. Thus we need to remove these generators for all timesteps prior to their crossing. In practice, we do this by tracking the separation of each pair of generators, removing the pair if they get within a predetermined tolerance δ of each other. In practice we used $\delta \sim 10^{-4} - 10^{-5}$

(depending on the number of punctures). This tolerance is at least two or three orders of magnitude smaller than the spatial resolution used for evolving the system.

3.5 Results

3.5.1 Continuum Ring

For the continuum ring we evolved configurations with increasing ring radii using a set of fixed nested grids (FMR) with the `Carpet` mesh refinement driver.

We found that the resolution required to find the AH on the initial slice increases with the size of the ring (keeping the mass fixed). We were able to find AHs on the initial timeslice for rings with radii as large as $0.5M$. Based on axisymmetric simulations [302, 303], we know that AHs exist for rings of larger radii, but we were not able to find these initial AHs in our full 3d simulations due to a lack of spatial resolution. Even though we were unable to find an initial AHs numerically, we were still able to evolve ring configurations with radii as large as $1M$. On the other hand, an evolution of a ring with radius larger than $r \approx 1.2M$ was not possible even at high resolutions. Essentially, the logarithmic singularity in the metric disappears numerically due to the effects of finite differencing. That is, the evolution variable $W \sim 1/\log^2 R$, which is not differentiable. As is, this would not be a significant problem, but for large rings, the volume where W is close to zero is very small (see Fig. 3.4). Consequently W gets smoothed out in this region by finite-difference errors, and the central object quickly loses mass and disappears (and subsequent evolution show no evidence of collapse or an apparent horizon). For intermediate radii of $0.5 < r \leq 1.0M$, we were able to evolve the ring. In these cases, the ring collapsed and eventually a common AH was found.

We used a 3d-Cartesian coordinate grid with outer boundaries at $100M$, with 3 ghost and 3 buffer zones, 8 levels of refinements. We found that the apparent horizons for the ring singularity are oblate spheroids with minor axes through the perpendicular direction to the plane of the ring, i.e. coincident with the axis of the ring (Fig. 3.3). We found that for ring radii larger than $0.5M$, the ring failed to collapse and essentially evaporated numerically. By

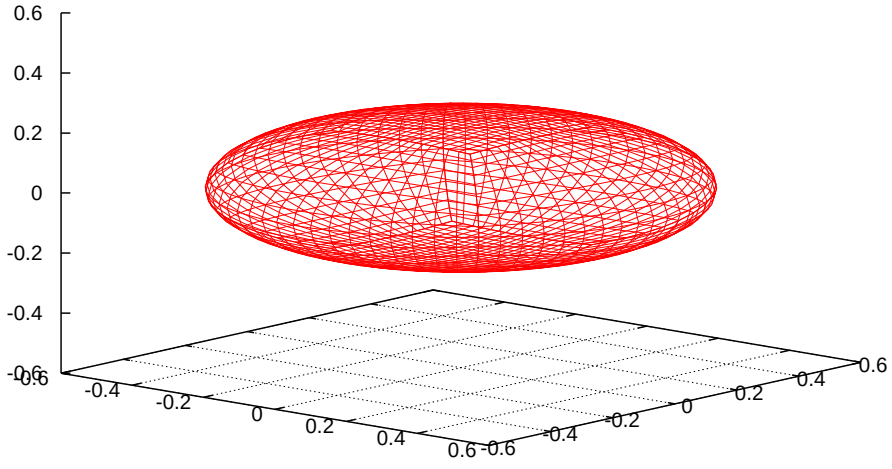

Figure 3.3: An early apparent horizon for a "continuum ring" singularity of radius 0.5 and unit mass. The AH is clearly an oblate spheroid with largest radius on the xy axis, corresponding to the plane of the ring singularity.

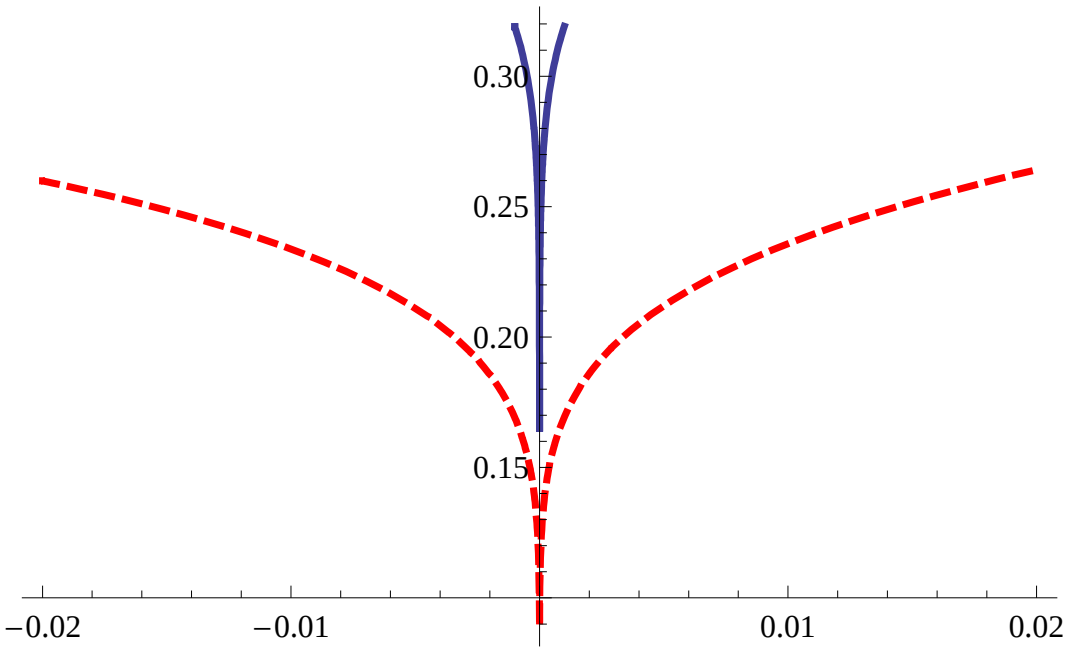

Figure 3.4: A plot of $W = 1/\psi^2$ versus $\tilde{\rho} = \rho - \rho_0$ on the xy plane for a ring of radius 1M (dashed) and 2M (solid). Note how much smaller the region $W < 0.3$ is for the larger ring radius. Based on the figure we estimate that an order 100 times the resolution is required to properly resolve the $r = 2M$ ring.

changing the initial lapse to $\alpha(t = 0) = 1$ we were able to evolve rings with radii as large as $\sim 1.0M$. However, this changed the AH at intermediate times from oblate to prolate. This would seem to indicate that $\alpha(t = 0) = 1$ leads to a distorted z coordinate during intermediate times. In all cases , the AH relaxed to a sphere at late times. We note that the AH area always increased from its initial value (or the value found at the first time the AH was detected). We did not search for EH for the continuum ring because we were unable to evolve rings of sufficient radius to have interesting EHs.

3.5.2 Discrete Ring

We evolved the discrete ring case in order to gain insight into the behavior of continuum rings with large radii (where numerical simulations are not feasible). The moving puncture approach has already been shown to work for large numbers of discrete punctures [324, 325, 326], and is therefore well suited for simulating the discrete case. The goal here was to see if, when

we increase the number of BHs in the ring, while keeping the ring mass and radius fixed, a common horizon forms. In practice, we evolved configurations with $N = 2, 4, 6, 8, 10, 20$ BHs.

For the cases of $N = 10$ and 20 BHs, the overhead of using a unigrid setup was too large. We performed some preliminary experiments calculating AHs using `Carpet` and FMR. However, we were not able to search for EHs. For these cases, we simulated rings with radii as large as $2.5M$. As expected, initially there were N distinct AHs, which then merged into a common AH,

For $N = 2, 4, 6, 8$, in order to find the EHs we used a unigrid setup (a requirement for the `EHFinder` thorn) with outer boundaries at a coordinate distance of $12.5M$, which corresponds to a physical distance of $45M$ due to the FishEye coordinates. Because the BH mass, and hence the required maximum gridspacing, scales as $1/N$, we used resolutions of $h = M/12$ and $h = M/16$ for $N = 2$, $h = M/24$ and $h = M/32$ for $N = 4$, and $h = M/48$ for $N = 6, 8$. In all the cases the Courant factor was set to 0.5. We varied the radius of the ring from $1.0M$ to $2.5M$.

In Fig. 3.5 we show the 8-BH discrete ring EH at the instant when the horizon transforms from 8 distinct objects to a single distorted horizon of topology S^2, as well as the horizon at one timestep later when there is only a single EH. As noted above, the EH is actually found by a backward in time evolution. From this perspective, we note how the central part of the horizon 'pancakes' to zero width during a single timestep. Also note that the central part of the horizon is concave, indicating that the generators near $(x, y) = 0$ will not cross first. Thus a "hole" will not form and the EH (in this slicing) will not have a toroidal topology. In Figs. 3.7 and 3.6 we show xy projections and xz cuts of the same 8 BH configuration, while in Fig .3.8 we show 3-d plots of the EHs (for $z \geq 0$). In Fig. 3.10 we show a sequence of $t = const$ slices of the EH, arranged vertically, to show the "octopus" like structure of this EH. Similar results for 4 and 6 BHs show that no central "hole" forms at any time.

Although we found no toroidal slice here, the caustic structure of the horizons indicates that a toroidal slice is possible. That is, the caustic forms a 2-d spacelike *plane*, and a minor distortion of the slicing should produce a new slice that is slightly more advanced in a small

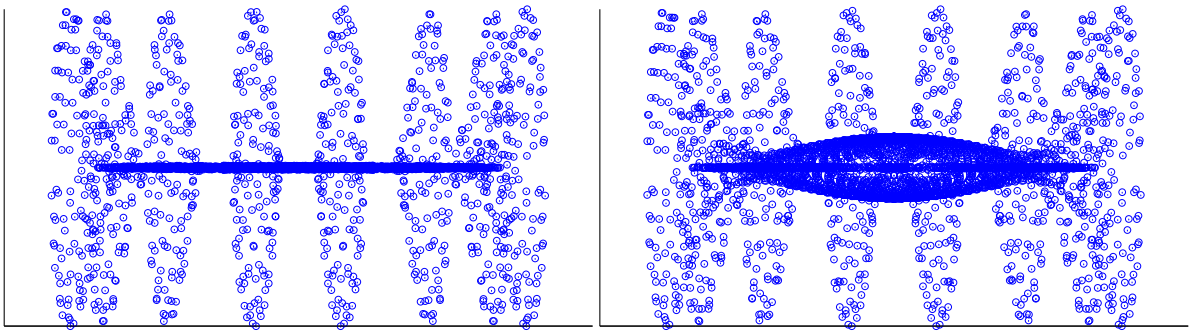

Figure 3.5: An edge-on view of the 'pancaking' of the central part of the EH for 8 BHs on a ring. The figure on the left shows the generators of the horizon at the timestep when the central generators just pass through the caustic and enter the horizons. The figure on the right shows the generators one timestep later. In the figure on the left, the central generators are just crossing (thus are not part of $\mathcal{H}$, while in the figure on the right an extended central object is visible. Note that the z axis is magnified by a factor of 10 compared to the x and y axes.

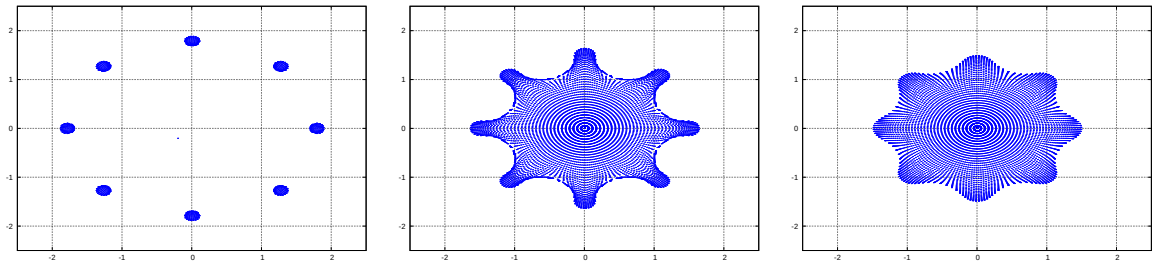

Figure 3.6: xy projections of the 8 BH ring configuration showing a time sequence with (left) 8 individual EHs, (center) a highly distorted common EH, (right) and a less distorted common EH.

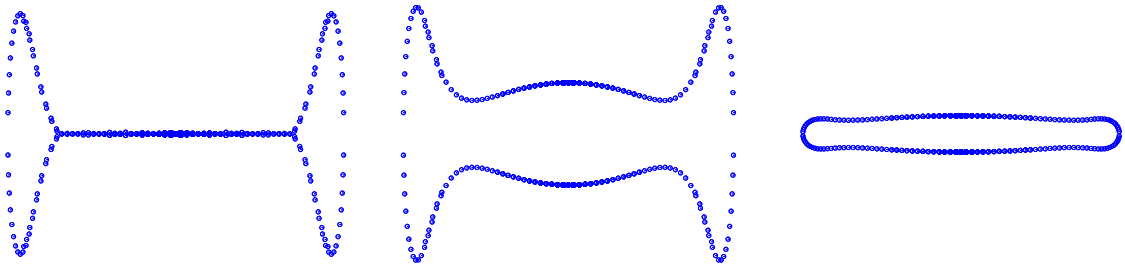

Figure 3.7: xz cuts of EH for the 8BH ring configuration at the instant in time when the common EH forms (left), two timesteps later (center, note the concave shape of the central region), and five timesteps after that (right). Note that the z axis in the two leftmost figures is magnified by a factor of 10 compared to the x axis, while the z scale is equal to the x scale in the last figure.

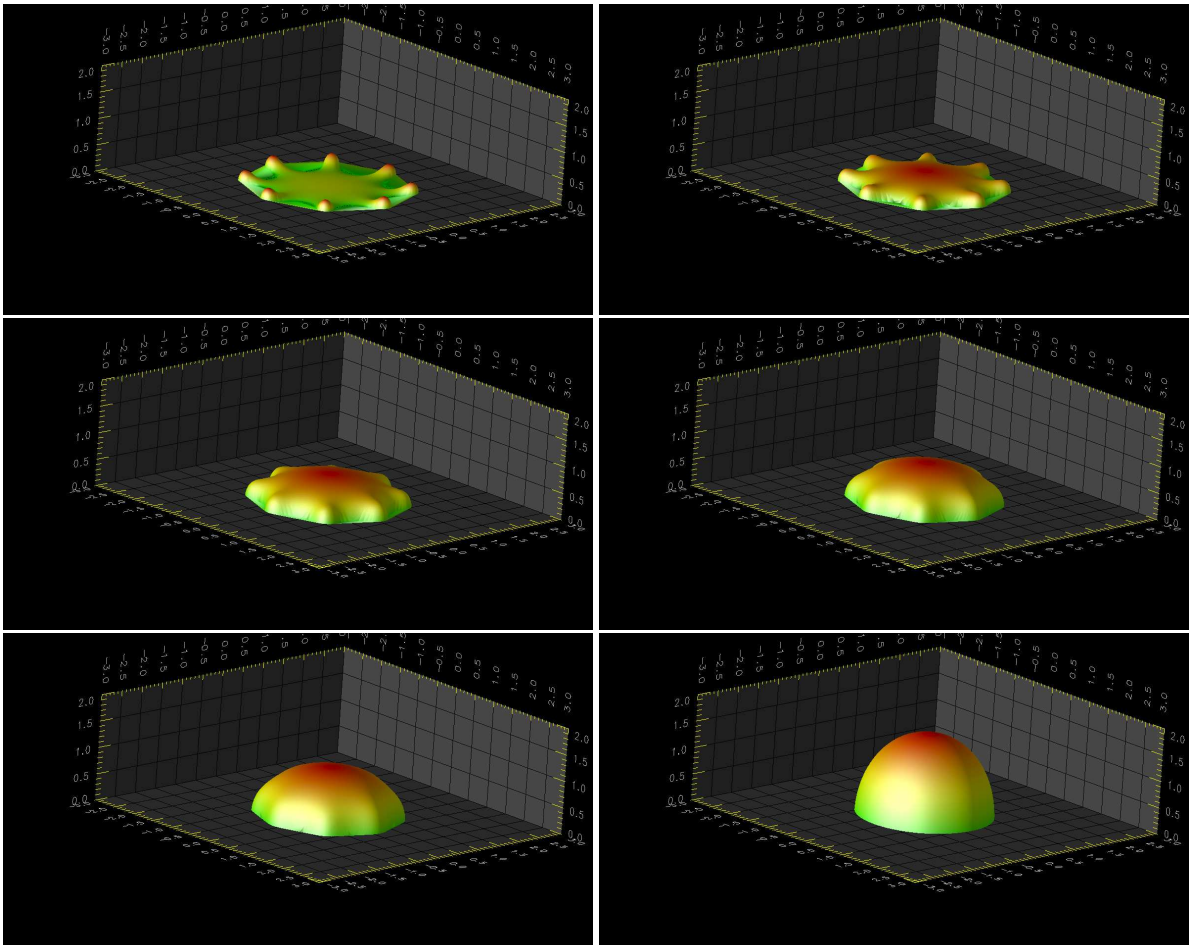

Figure 3.8: 3-d snapshots of the 8 BH ring configuration (only the top part of the horizon ($z \geq 0$ is shown). The sequence in time runs from left to right and top to bottom, beginning with the first common horizon and forward in time from then to when the horizon in nearly spherical. Note that the flat (green) sheet apparent between the horizon on the first and second slices is an artifact of the visualization and does not belong to the horizon. This provides another way to visualized the 'pancaking' process also visible in Figs. 3.5 and 3.7.

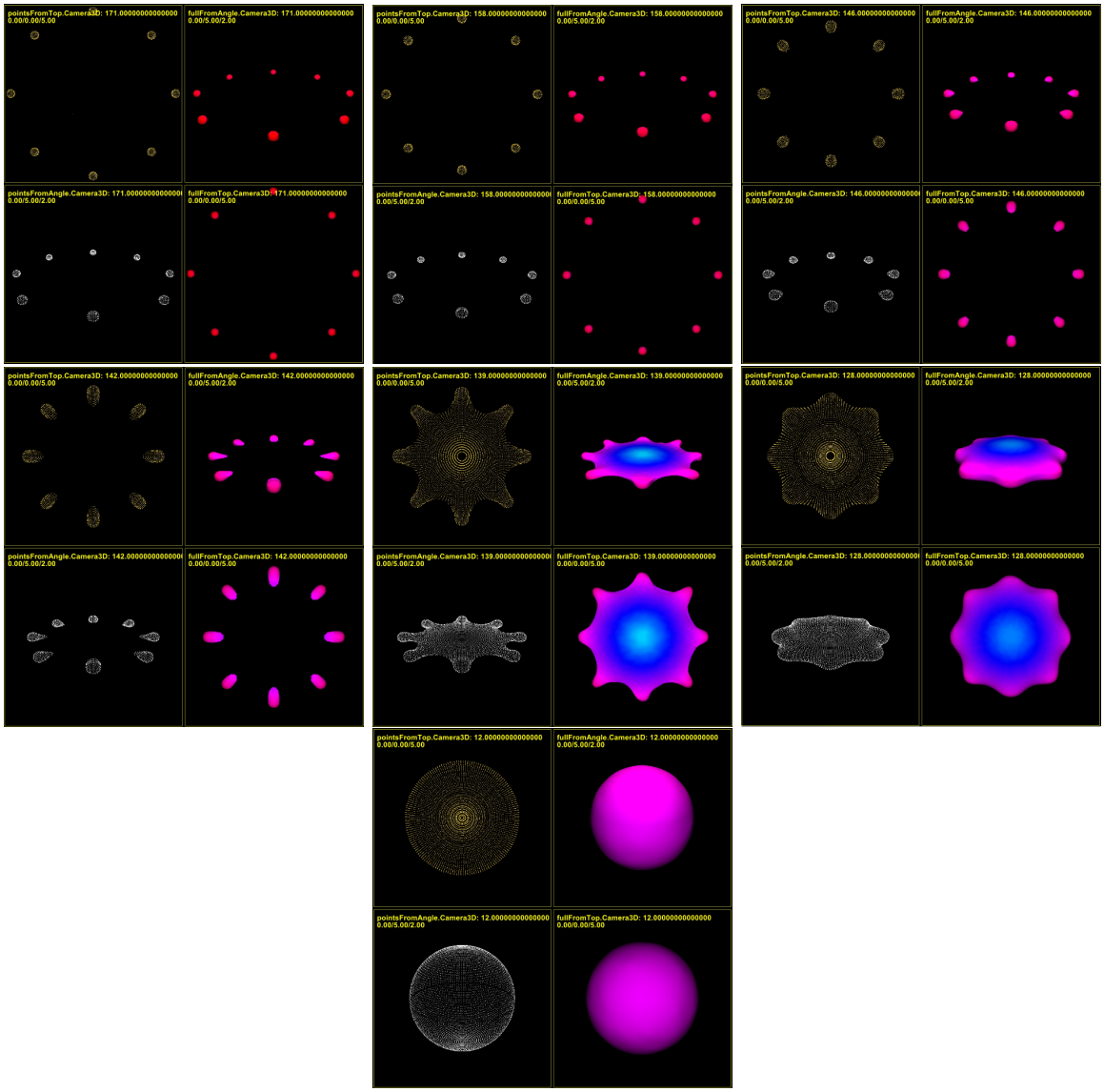

Figure 3.9: Another set of 3-d snapshots of the 8 BH ring configuration. In this case, the sequence in time runs from left to right and top to bottom. Each panel shows four different perspectives of the configuration for a given time. The EHs are represented with two different type of visualizations: in the left column of each panel, the original data of the generators are represented by dots, on the right column of each panel a surface connecting the generators is represented using a color scheme coding the distance to the center of the configuration. This provides one way to visualize the 'pancaking' process which occurs close to the moment when the common EH of the system emerges. The snapshots are from movies produced by Prof. Hans-Peter Bischof (CCRG-RIT) using `Spiegel` [1].

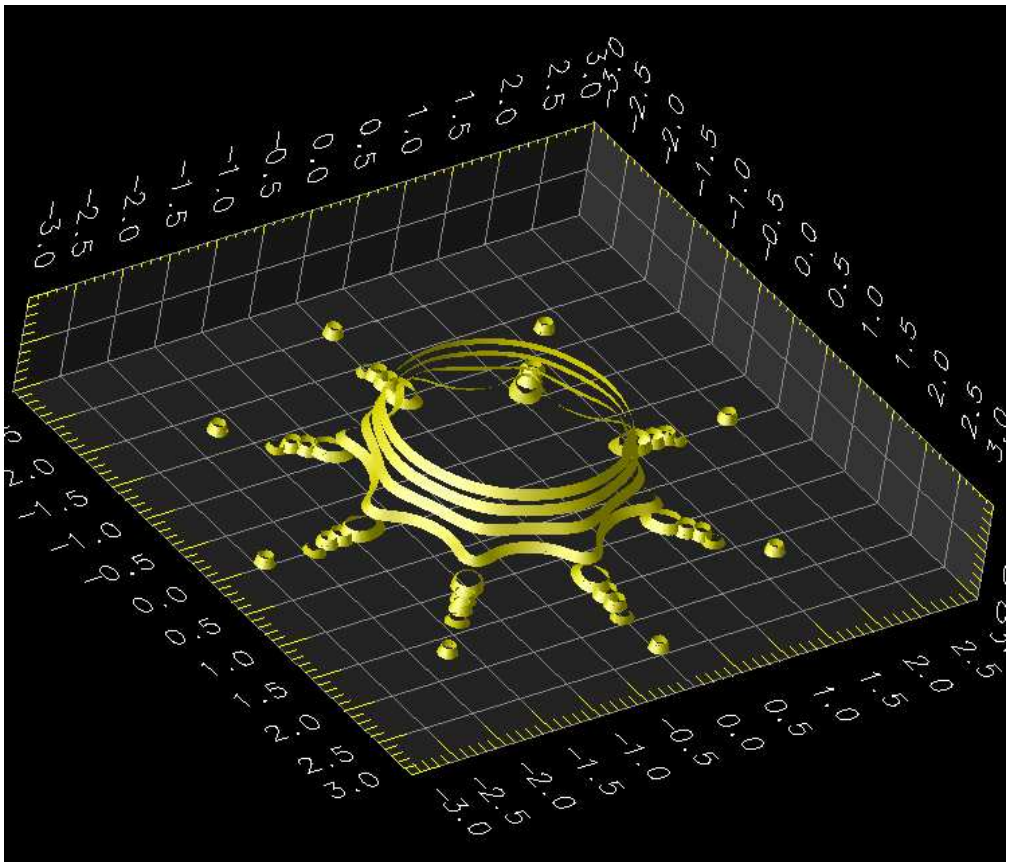

Figure 3.10: A sequence of $t = const$ slices of EH for the 8 BH ring configuration arranged vertically to show the "octopus" like structure of the EH

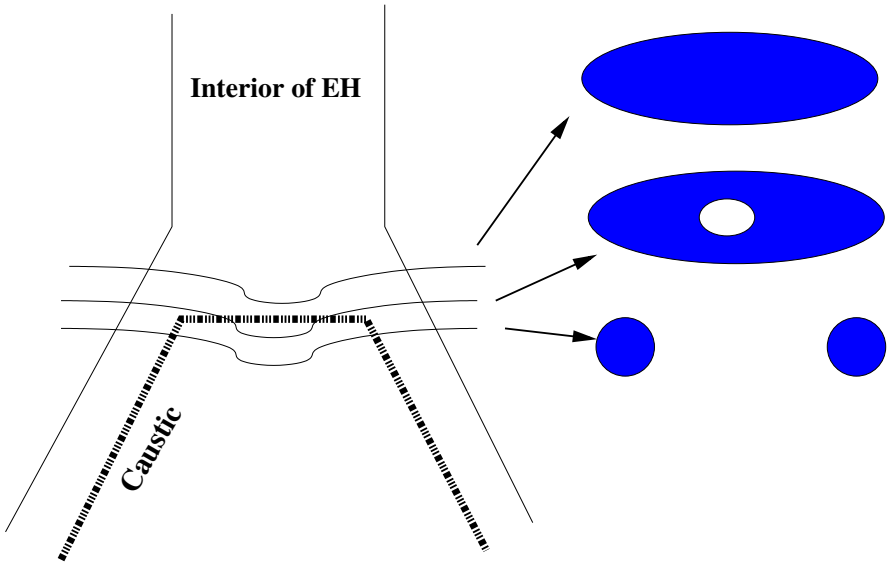

Figure 3.11: The caustic structure for the multiple black holes arranged on a ring. Only the tx plane is shown. From the figure, one can see that a toroidal horizon is possible if the slicing near the origin is retarded.

volume outside the origin than it is at the origin itself. For example, one could try to modify the right-hand-side of Eq. (III-5) by adding a term of the form $-f(t)\exp[-(r/\sigma)^2]$, which should retard the slicing around the origin,leading to a toroidal slice (see Fig. 3.11).

3.5.3 Linear BH

As a test of conjecture that a black hole ring is not surrounded by a finite-sized toroidal horizon (for sufficiently large ring radii), we simulated the case where a differential line element of the ring can be approximated by a finite line segment. In other words, in order for there to be a common EH in the discrete ring case (with sufficiently large ring radius) a single EH must surround two neighboring punctures as the number of punctures becomes very large. In which case, a small section of the ring will look like a linear distribution of BHs. The question then is, if we have a finite length linear distribution of BHs of fixed total mass, will a common horizon form if the number of punctures in the line is increased arbitrarily, while keeping the total mass of the line fixed. In order to keep the linear mass density constant as we change the number of BHs on the line (N), the length of the line element is given by Eq. (III-4).

There are two important objections to our modeling of the ring distribution with a linear distribution. First, because the metric on the initial slice is obtained by solving an elliptical equation, the notion that a linear mass distribution will mimic the relevant regions of the spacetime near a ring distribution requires some justification. Second, because the event horizon is a global structure, the global differences between the two spacetimes can cause the two event horizons to have very different property.

Our argument for using this linear distribution model goes as follows, as we move backwards in time and the ring gets larger, the event horizon must get progressively closer to the ring. This is due to the fact that the conformal factor ψ approaches 1 (and hence the metric rapidly approached Minkowski) progressively more rapidly as the ring radius is increased (see Fig. 3.4). Therefore $\mathcal{H}$ gets progressively closer to the ring as the ring radius is increased. Indeed, because the region where ψ differs significantly from 1 shrinks very rapidly as the ring radius increases, the horizon radius must tend to zero faster than the reciprocal of the ring radius. Otherwise the outgoing null generators would enter a region where the space was nearly Minkowski and, due to the rapid falloff of ψ would therefore be able to escape to infinity. Consequently, for a large enough ring, the horizon will lie in a region where the metric is dominated by the singular $\log R$ term in ψ and will look like the metric in the vicinity of a linear mass distribution. As noted above, due to the global nature of the event horizon, it is not clear how precise the correspondence is between the horizon structure of the line and the ring. Consequently our results for the linear distribution should only be considered suggestive of the behavior of the horizon around the ring.

With the aim of numerically testing the conjecture that no finite sized EH exists for the distant past in the continuum ring case, we ran simulations with different values of N. First we determined the minimal distance between two black holes to generate two isolated (non-connected) event horizons in their initial configuration. We found that for a system of 2 black holes with total mass $M = 1.0$, the minimal separation between the BHs is $\approx 0.9M$. Given this, we then proceeded to evolve configurations for $N = 4$ with a line length of $4.0M$ (which guarantees that no common EH exists initially). We then increased the number of BHs on

the line and measured the coordinate separation of the two central holes as a function of N. For this analysis, we rescaled this inter-BH separation by the reciprocal of the individual BH masses. That is, the separation will decrease as N increases naturally because there are more BHs on the line, but we are interested in whether or not the EHs will merge as N increases. If the EHs merge then the separation l of the EHs will approach $2r$, where r is the EH radius. If on the other hand l/r tends to a constant larger than 2, as was the case here, then no common EH will form. Since the BH masses, and therefore coordinate radii, are proportional to $1/N$, we rescale the distances by a factor of N.

In Fig. 3.12, we plot the intersection of $\mathcal{H}_t$ with the xy plane for the 10 BH line configuration for several different times. Interestingly, the two central BH merge first, followed by the two BHs neighboring the central ones, followed by the outermost ones. At one time there are three distinct EH formed by the two outermost EH on either side (2 objects) of the line and the 6 central objects (1 object).

In Figure 3.13 we show the EHs at $t \approx 0$ for the linear distribution with $N = 4, 6, 8$, and 10 BHs uniformly distributed over a line with length given by Eq. (III-4), i.e. lengths: $4.0, 4.444, 4.667, 4.8$. For these evolution we used resolutions of $M/16$, $M/32$, $M/40$, and $M/50$ for $N = 4$, $N = 6$, $N = 8$, and $N = 10$, respectively. Due to an instability in the EH search, we could not find EHs at exactly $t = 0$ in all cases. In Figs. 3.14 and 3.15 we show only the two innermost EHs.

According to these figures, there is a clear trend towards reducing the effective size of the event horizons while keeping their separations, relative to the individual BH radius, fixed when increasing N (see for instance Fig. 3.15). This suggests that for finite N there will be N distinct BHs rather than a common EH. Thus for the limiting case $N \to \infty$, the event horizons would seem to have at most point like width, giving in the most optimistic scenario a null-width connected ring.

This setup was examined using an axisymmetric code with up to 1000 BHs arranged on a line in Ref. [306]. In that paper it was found that no common AH exists for lines longer than $1.5M$. Here we have extended this argument (somewhat) to no common event horizon

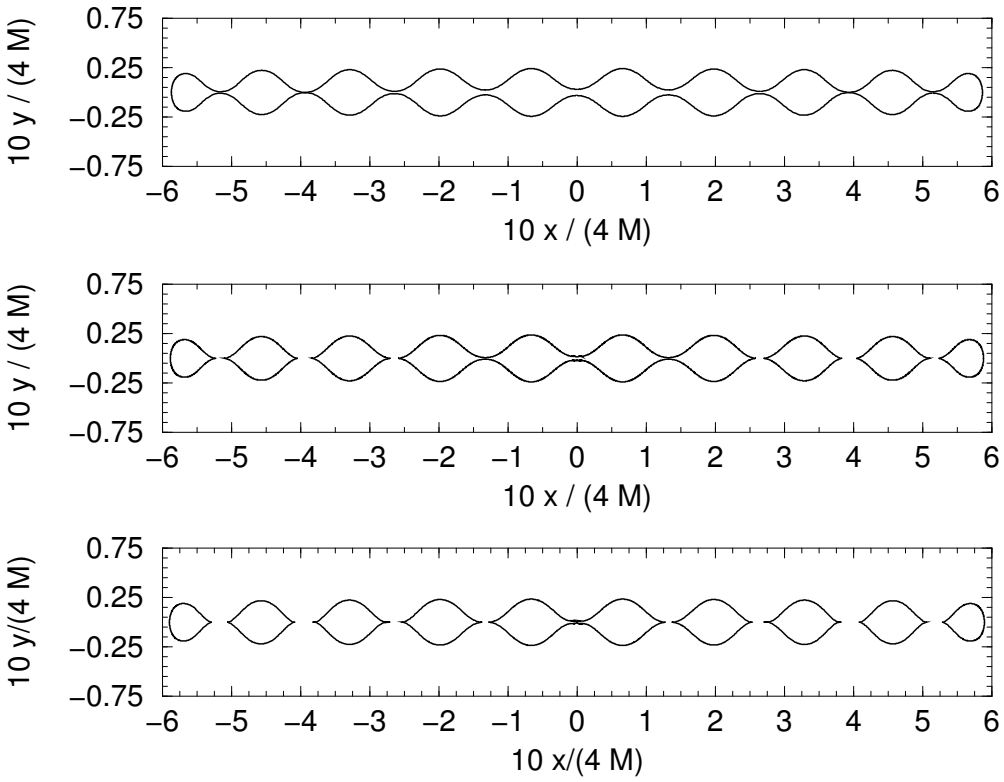

Figure 3.12: $t =$ const slices of the intersection of $\mathcal{H}$ and the xy plane for the 10 black hole line configuration. The figure on top shows the first common EH, the figure in the center shows an earlier slice with 7 distinct objects, while the figure on the bottom shows the EH when there are 9 distinct objects. Note that the two central BHs merge first.

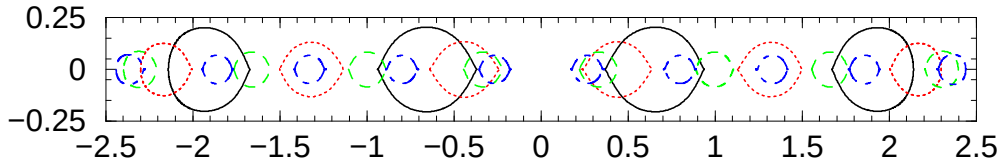

Figure 3.13: Sets of EHs near $t = 0$ for the linear distribution with $N = 4$ (solid), $N = 6$ (dotted), $N = 8$ (dashed), and $N = 10$ (dot-dashed) BHs. In this plot the coordinates have not been rescaled. Note that as N increases the two innermost horizons approach each other, but also simultaneously shrink in size.

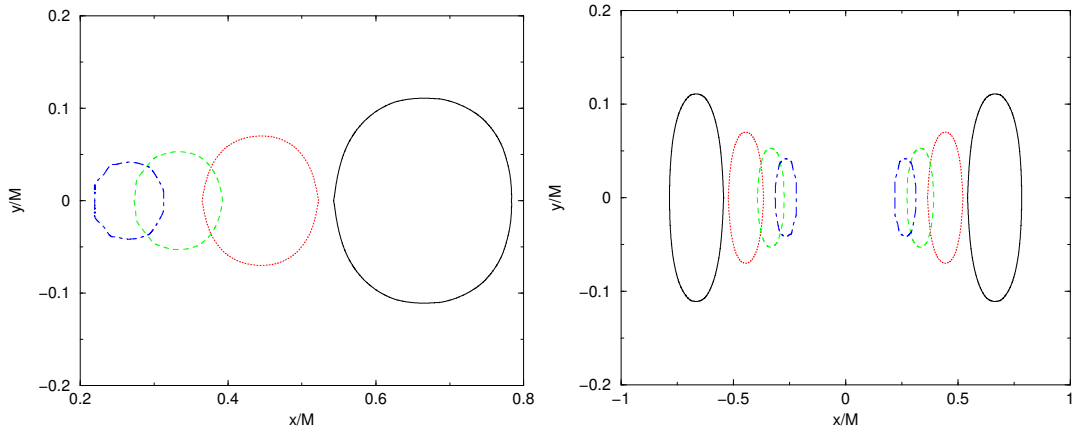

Figure 3.14: The two innermost EHs near $t = 0$ for the linear distribution with $N = 4$ (solid), $N = 6$ (dotted), $N = 8$ (dashed), and $N = 10$ (dot-dashed) BHs. In this plot the coordinates have not been rescaled. Note that as N increases the two innermost horizons approach each other, but also simultaneously shrink in size.

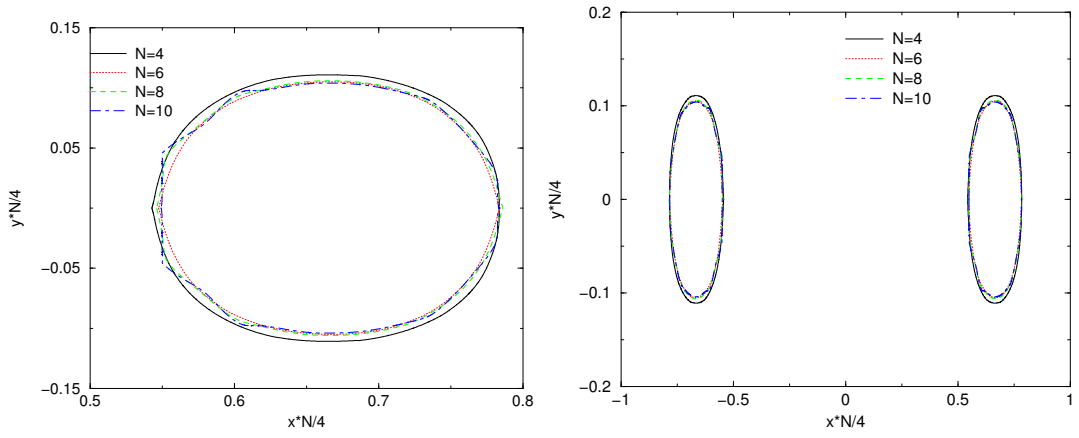

Figure 3.15: The two innermost EHs near $t = 0$ for the linear distribution with $N = 4$ (solid), $N = 6$ (dotted), $N = 8$ (dashed), and $N = 10$ (dot-dashed) BHs. Note that the distances have been scaled by $N/4$ and that the innermost horizons do not appear to approach each other as N increases.

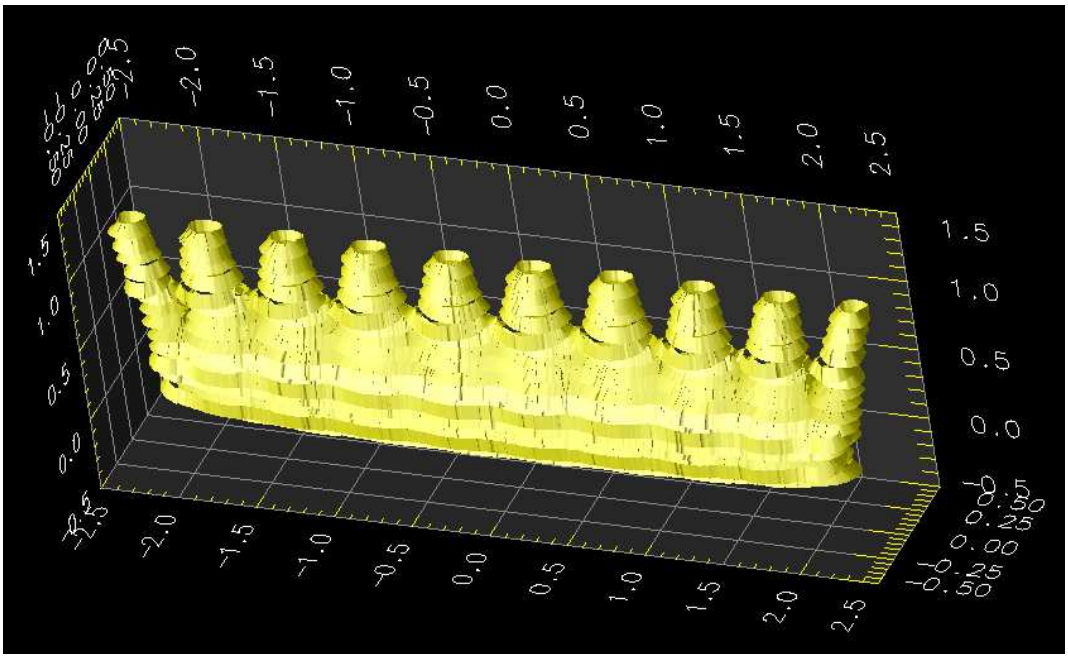

Figure 3.16: A sequence of $t = const$ slices of EH for the 10 BH line configuration arranged vertically to show the "coral" like structure of the EH

for lines larger than $4M$ (we did not do a systematic study to determine the minimum line length for the existence of a common event horizon as a function of the number of BHs).

3.6 Discussion

It is important to note that, unlike the case of discrete punctures, where the puncture singularities are only coordinate singularities, the singularities for these continuum linear distributions are physical singularities. We can show this by noting that the initial hypersurfaces are not geodesically complete. In the vicinity of a linear distribution, the conformal factor ψ will behave like $\psi \sim \log \rho$, where ρ is the coordinate distance to the line. Consequently, the physical distance of a point ρ away from the line is $\delta s \sim \rho \log^2 \rho$, which is finite. Next we note that the Kretschmann invariant $K = R_{\alpha\beta\gamma\delta} R^{\alpha\beta\gamma\delta}$ is singular and of the form $K \sim 1/[\rho^4 (\log \rho)^{10}]$.

We can strengthen the argument for a non-simply connected EH in the continuum ring configuration (for large enough radius). We expect that the ring singularity will undergo gravitational collapse to a point. That is, the ring radius in quasi-isotropic coordinates will

decrease with time. We therefore expect that the radius will get larger the farther back we move in time (one could also consider a family of initial data, where the mass of the ring is fixed to $1M$ but the radius is made arbitrarily large).

Suppose that there is an S^2 slice of $\mathcal{H}$ surrounding the ring at all times. The surface area of the horizon will become arbitrarily large (we note that metric in the neighborhood of the ring is only logarithmically singular, and approaches Minkowski rapidly with the distance from the ring. This means that the spacetime will be very nearly Minkowski, including in the center of the ring) in the distant past (see Fig. 3.17). Thus if the ring is surrounded by an S^2 horizon in the distant past, the spacetime will be asymptotically predictable (i.e. posses at least a partial Cauchy surface) and should evolve to a Schwarzschild BH with surface area at least as big as the surface of the horizon when the ring is arbitrarily large (i.e. for the very distant past). However, this is not possible because the ring's mass is fixed, and hence its the horizons area is bounded. Consequently, the EH, if it exists, cannot by S^2. We note that our tests with discrete ring configuration, and ring singularities with small radii, all indicate that the horizon area increases with time (as required). The increase in area is quite dramatic for the discrete ring. This is due to fact that the configuration does not radiate significantly, so the initial horizon masses are approximately equal to the total mass divided by the number of black holes. Hence the area of each horizon is proportional equal to $16\pi(M/N)^2$ and the total initial area is equal to $16\pi M^2/N$, or $1/N$ times the final horizon area. In the limit $N \to \infty$ this leads to an initial horizon with vanishing area.

We note that our results from the discrete ring configuration suggests that the EH, if it exists, may have vanishing width. If this is so, then null geodesics originating arbitrarily close to the singularity (and hence in regions of arbitrarily large curvature) are visible to null infinity $\mathscr{I}^+$, indicating the presence of a type of naked singularity, and the spacetime itself may not be asymptotically predictable (the presence of a naked singularity does not preclude that the spacetime is asymptotically predictable). While a horizon $\mathcal{H}_t$ with a stable toroidal topology does not appear to exist for the ring singularity, the caustic structure of $\mathcal{H}$ indicates that instantaneous toroidal slices are possible. Here the spacetime has no common EH at

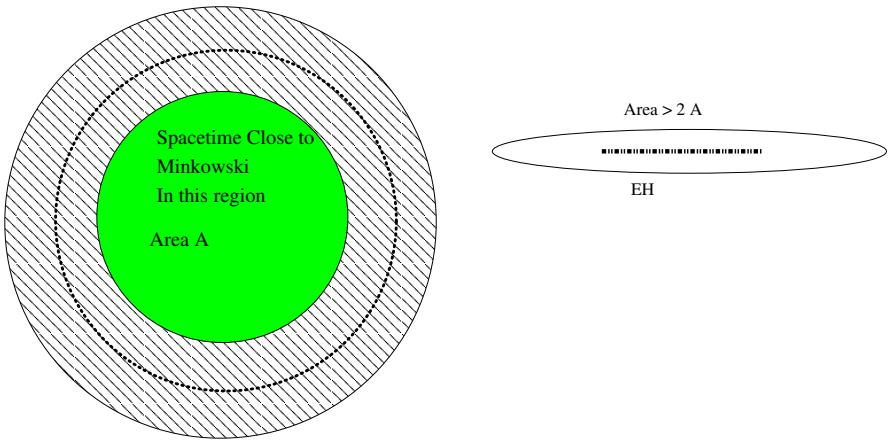

Figure 3.17: The conjectured S^2 horizon outside the ring singularity (dotted line) for a ring singularity with large radius. The shaded region is a region inside the ring but still far enough from the singularity that the metric is nearly flat. The surface area of this region is proportional to the square of the ring's radius, and hence get arbitrarily large. The horizon's area must be larger than twice this area. The plot on the left shows a cut on the xy plane, while the plot on the right shows a cut on the xz plane.

sufficiently early timeslices and only first appears at a timeslice Σ_h as an extended object with topology S^2. However, because $\mathcal{H} \cap \Sigma_h$ is an extended object, Σ_h can be distorted to an alternate slice $\tilde{\Sigma}_h$ such that $\tilde{\Sigma}_h \cap \mathcal{H}$ is not simply connected (e.g. by distorting the timeslice such that the center of the ring is slightly earlier in time than the neighboring points). See Fig. 3.11.

Although we started by looking for configurations with EHs with toroidal slices, we actually have a more interesting case of a ring singularity with an EH in the future of some slice Σ_0 and a possible naked singularity in the past of Σ_0. Although, in the slicing used here, the horizon appears to not have toroidal topology, we note that the slicing can be distorted to produce a toroidal horizon. This configuration appears to be a very interesting topic for further analytical investigations.

3.6.1 Naked singularities and cosmological censorship

It has been proposed that the cosmic censorship hypothesis could be observationally tested [327, 188, 328]; suggesting that black holes and naked singularities could be observationally

differentiated through their gravitational lensing characteristics. If the metric is known, the lens equation can be used to compute image positions, magnifications, and time delay, etc.

According to [328, 188], a black hole and a naked singularity of the same ADM mass and the same symmetry, acting as gravitational lenses (deflectors), give rise to different number of images of the same light source. Parities (orientations) of images are also different. Therefore, gravitational lensing can be an important astrophysical tool to observationally test the Cosmic Censorship conjecture.

Likewise, in [328, 188] the total magnification of images due to gravitational lensing by a naked singularity is studied and computed to be higher than the total magnification of images due to gravitational lensing by a black hole of the same ADM mass and the same symmetry.

Furthermore, [328, 188] claims that time delays of images due to gravitational lensing by a naked singularity are less than of those due to gravitational lensing by a black hole. Moreover, it is proposed that higher values of "nakedness" parameter give smaller time delays (for example: in Kerr metric, $(a/M)^2$ is termed as a "nakedness" parameter).

Likewise [328, 188] proposed also that naked singularities can give rise to images of negative time delays as well. This means that time taken by light to travel (in the gravitational field of a naked singularity) from a source to the observer could be less than the time taken for the light to travel (in Minkowski spacetime) from the same source to the observer.

Whether such predictions are correct and accurate or not is hard to say, but having studies and information that allows for concrete astrophysical measurements opens an interesting way to gain insights about these theoretical objects.

Chapter 4

Newtonian Gas Dynamics around kicked BHs

Numerical calculations of merging black hole binaries indicate that asymmetric emission of gravitational radiation can kick the merged black hole at up to thousands of km/s, and a number of systems have been observed recently whose properties are consistent with an active galactic nucleus containing a supermassive black hole moving with substantial velocity with respect to its broader accretion disk. Here we study the effect of an impulsive kick delivered to a black hole on the dynamical evolution of its accretion disk using a smoothed particle hydrodynamics code, focusing attention on the role played by the kick angle with respect to the orbital angular momentum vector of the pre-kicked disk. We find that for more vertical kicks, for which the angle between the kick and the normal vector to the disk $\theta \lesssim 30^\circ$, a gap remains present in the inner disk, in accordance with the prediction from an analytic collisionless Keplerian disk model, while for more oblique kicks with $\theta \gtrsim 45^\circ$, matter rapidly accretes toward the black hole. There is a systematic trend for higher potential luminosities for more oblique kick angles for a given black hole mass, disk mass and kick velocity, and we find large amplitude oscillations in time in the case of a kick oriented 60° from the vertical.

4.1 Review of gravitational kicks

In the past few years, a combination of surprising numerical studies and astronomical observations have indicated that asymmetric momentum losses in gravitational radiation from the mergers of binary black holes may produce "kicks" of up to several thousand km/s. For the mergers of supermassive black holes (SMBH) at the centers of galaxies, the kicks may be large enough to eject the remnant BH out of the galactic center if not out of the galaxy entirely. Kicked BHs may have already been observed indirectly as active galactic nuclei (AGN) with different components at different redshifts; broad-line regions that are thought to originate near the BH itself will remain bound to the kicked BH and acquire its new line-of-sight velocity, while narrowline systems that are produced further away will become unbound and remain behind.

While kicks from the mergers of unequal-mass, non-spinning BHs have long been predicted by post-Newtonian calculations [329], the ability to evolve black holes in fully general relativistic simulations has considerably expanded our view. Indeed, it is the merger of equal-mass, *spinning* BH that produce the largest kicks calculated to date, with maximum values of up to 5000km/s possible for configurations with carefully chosen alignments [91, 92, 95, 110]. Configurations with spins partially aligned with the orbital angular momentum seen to produce larger recoils (up to 1200km/s more) than those with spins lying in the orbital plane (the superkicks configuration). While speeds this large represent only a small fraction of the likely merging BH parameter space, Monte Carlo simulations of merging BHs with arbitrary spins of dimensionless magnitude $S/M^2 = 0.97$ find that the mean kick for BH systems with mass ratios uniformly distributed between 0 and 1 is 630km/s, with more than 20% of the kicks larger than 1000km/s [229]. Such kicks have the potential to unbind the remnant from smaller galaxies, or displace the BH and any bound gas for larger galaxies. In roughly half of all major mergers between comparable-mass SMBHs, the merged SMBH should remain displaced for 30 Myr outside the central torus of material that would power an AGN [330].

Somewhat more recently, several AGN have been observed to contain broadline emission systems that appear to have very different redshifts than the narrowline emission systems.

In the first of these, SDSSJ092712.65+294344.0, a blueshift of 2650km/s is observed for the broadline systems relative to narrow lines [111]. Although several different physical models have been proposed to account for the observations, including broadline emission from the smaller SMBH within a binary surrounded by a disk [214, 215], a pair of SMBHs at the respective centers of interacting galaxies [216], and even spatial coincidence [112], the kicked disk model remains entirely plausible. Since then, several more systems with similar velocity offsets between different AGN emission regions have been discovered, including SDSS J105041.35+345631.3 [3500km/s; [114]], CXOC J100043.1+020637 [1200km/s; [115]], and E1821+643 [2100 km/s; [116]].

Given a number of recent results that suggest that binary SMBH spins should align with the angular momentum of the accretion disk prior to merger, these large kick velocities are somewhat unexpected. Indeed, completely aligned spins can produce kicks of several hundred km/s [92, 90, 105] but not the "superkicks" with recoil velocities $\gtrsim 1000$km/s. Ref.[331] suggest that the accretion torques in gas-rich ("wet") mergers should suffice to align the SMBH spins with the accretion disk prior to merger. In [217], high resolution simulations of SMBH binaries whose orbits counter-rotate with regard to a surrounding disk indicate that they should undergo an angular momentum flip long before merger. With typical spin-orbit misalignments of no more than $10^\circ - 30^\circ$ depending on the parameters of the disk, in particular its temperature, they find that the recoil kick during mergers should have a median value of 70km/s, with superkicks an exceedingly rare event [332]. However recent results [110] from the RIT group indicates that the recoil for partially aligned binaries can be much larger, leading to higher probabilities of getting larger kicks.

While some of the observed candidate recoil velocities are so large that they fall well out into the tail of the kick velocity probability distribution function, it is difficult to constrain exactly how many systems indicate potential recoils given the challenges in clearly distinguishing multiple velocity components within a single AGN. Given this difficulty, we attempt here to study potential electromagnetic (EM) signatures that would originate from post-merger disks.

The qualitative details of pre-merger evolution have been studied by other groups, and a

relatively coherent picture emerges. In general, each SMBH may be surrounded by a circum-BH accretion disk extending out to a distance substantially smaller than the binary separation, since orbits near the outer edge are unstable to perturbations from the other SMBH. A circumbinary disk may be present as well, extending inward to a distance of roughly a few times that of the binary separation, with a gap appearing between the circumbinary disks and the inner disks. Previous hydrodynamical studies have shown that the inner edge of the circumbinary disk is driven into a high-eccentricity configuration that precesses slowly, while a 2-armed spiral density wave is formed extending out to larger radii [218]. Meanwhile, the inner disks will be fed by mass transfer from the circumbinary disk [219, 230], as the $m = 2$ azimuthal gravitational perturbation induces an elongation in the outer disk. For circular orbits, the mass transfer rate is relatively constant, while for elliptic binaries the mass transfer takes on a more periodic character. Finally, once the binary begins its gravitational radiation-driven plunge, the binary decouples form the outer disk, and mass transfer basically ceases.

Among the first predictions of the observational consequences of a post-kick accretion disk are those in [225], where it was found that off-center quasars could be observed for up to 10^7 years after a SMBH merger. In [226], it was reported that the inner edge of the circumbinary disk is likely to occur at roughly $1000M$, in typical relativistic units where $G = c = 1$, with the value only weakly dependent on the typical disk parameters like the assumed α-parameter. Based on semi-analytic models of the post-merger accretion disk, they find the potential for observable infrared emission lasting hundreds of thousands of years, leading to the prediction that several such sources might be present today, though they would be difficult to disentangle from other AGN sources. On much shorter timescales immediately prior to the merger, the dissipation of gravitational radiation energy through spacetime metric-induced shearing of the disk can also lead to enhanced emission in the optically thin components of the disk [227].

One of the first studies of post-kick disk dynamics was performed in [113], where they analyzed the approximate physical scales characterizing the post-merger disk and concluded that the total energy available to be dissipated by shocks is roughly $\frac{1}{2}M_b v_{\rm kick}^2$, where M_b is the mass of the portion of the disk that remained bound and $v_{\rm kick}$ is the SMBH kick velocity.

They estimated from a simple analytical model that an excess luminosity of $\sim 10^{46}$ erg/s would be observable for roughly 3000 years, with a characteristic observed temperature of $\sim 10^7$K assuming $v_{\rm kick} = 1000$km/s. This model is checked by means of a *collisionless* N-body simulation of a disk around a kicked SMBH, which found rough agreement with the analytical model and confirmed the prediction of a detectable soft X-ray emission that would last for a few thousand years after the initial kick.

Using a 2-d version of the `FLASH` code, the authors of [220] studied the response of a thin disk if the kick is directed in the equatorial plane. They find that the characteristic response is a one-armed spiral shock wave, capable of producing total luminosities up to $\sim 10\%$ of the Eddington luminosity on a timescale of months to years. The relativistic decrease of the total SMBH mass, attributable to the energy carried off in gravitational waves and roughly 5% of the original total, leads to a decrease in the luminosity of approximately 15% but does not provide a clear signature that can be disentangled from the other global processes occurring in the disk. Nevertheless, with future radio instruments such as the Square Kilometer Array, impulsive changes to a disk may be observable in the jet emission [333]. Even in the case where the BH kick is very small, the secular, as opposed to dynamical, filling of the inner region of the disk should produce an afterglow that could exceed the Eddington luminosity if the accretion rate is sufficiently large prior to the binary decoupling and merger [334].

The most direct comparison to the calculations we present here is found in [246]. Using an analytic treatment of disks with power-law density profiles, they construct a model for disk evolutions in which, immediately after the kick, fluid elements are assumed to circularize at radii determined by their specific angular momentum, with the resulting energy gain by shocks released as EM radiation. Their work establishes that the primary energy reservoir for kicked disks is potential energy that can be released by elliptical orbits, not the relative kinetic energy of the kick itself nor the impulse sent through the disk by instantaneous mass loss to gravitational radiation by the central SMBH during the merger. They also perform detailed 2-d Eulerian and 3-d SPH simulations of post-kick accretion disks, although there are some important differences between the latter simulations and our SPH studies, as we

discuss throughout the chapter below. Among these, they assume that disks are isothermal, with all shock heating immediately radiated away, whereas we evolve the energy equation and allow the fluid to heat. As such, their results and ours bracket the range of possible heating scenarios.

The 2-d calculations performed in [246] of razor-thin disks using the ZEUS code indicate that vertical kicks (that is, in the direction of the disk angular momentum vector) lead to modulated emission, unlike all other kick angles they consider. This result is confirmed by their 3-d SPH simulations. In-plane kicks develop a clear spiral-wave structure with accretion streams forming as the simulation progressed, but a smooth luminosity profile. Their 3-d SPH simulations with oblique (less vertical) kicks indicate essentially a 2-phase model for the observed EM emission. Immediately after the kick, the majority of the luminosity may be attributed to the innermost region of the disk dissipating the kinetic energy it acquired during the kick, while at later times, after roughly one standard timescale of the disk ($\hat{t} = 1$ in the notation of Eq.(IV-1)) below and thereafter, the dominant dissipation mode is potential energy from infalling material on elliptical orbits. Post-kick disks are found to be rather compact, extending out to roughly the "bound radius" ($\hat{r} = 1$ according to the notation of our Eq.(IV-2)) with steep density dropoffs at larger radii. Luminosities are generally highest for in-plane kicks, with roughly a factor of four difference in peak luminosity between largest peak luminosity (in-plane kick) and the smallest (vertical kick), with peaks occurring later for more oblique kicks. Relativistic BH mass decrease was found to be unimportant at large radii, and potentially important only in the vicinity of the BH (out to a few hundred Schwarzschild radii) where the effect of the kick is merely perturbative compared to the nearly relativistic Keplerian velocities.

Numerical relativity groups have also considered the hydrodynamics of matter around both binary SMBHs and kicked BHs, typically at much smaller size scales. In [335], flows of gas around a binary SMBH system are considered at scales roughly 10^5 smaller than typical Newtonian calculations, spanning scales roughly 1AU across, rather than ∼parsec scales. They find that EM emission is dominated by variability created by Doppler beaming of the SMBHs

as they shock the gas, leading to an EM signal that demonstrates the same periodicity as the gravitational wave signal, with corresponding peaks in the timing of the maximum emission for each. In a follow-up work, Bode and collaborators [336] predict that observable EM emission from near the SMBHs is much more likely to arise in a hot accretion flow, in which a flare would be seen coincident with the merger. In [337], the effect of a kicked BH moving through the equatorial plane of an accretion torus is considered using a fully general relativistic Eulerian hydrodynamics code. In their simulations, the newly-merged SMBH is surrounded by a torus extending out to 50M (50AU for a $10^8 M_\odot$ SMBH), and the overall timescale studied is approximately 10,000M (in relativistic units with $G = c = 1$), or about two months. They find that a kick in the direction of the equatorial plane of the torus produces the strongest shock in the system and therefore the strongest EM emission, consistent with studies that examine disks on substantially larger scales. By ray-tracing their simulations in a post-processing step [338], they confirm that simple Bremsstrahlung luminosity estimates yield a qualitatively accurate picture of the disk luminosity for high-energy radiation, while their torus is optically thick to low-energy emission.

Numerical calculations of vacuum EM fields surrounding an SMBH merger indicate that they could contribute to periodic emission [339, 340] but are likely to be too small in amplitude and at the wrong frequencies ($\sim 10^{-4}$Hz) to be observed directly [341]. Such mergers could produce observable levels of Poynting flux in jets [342], however, through a binary analogue of the Blandford-Znajek mechanism [343], which seems especially effective for spinning BHs [344]. Calculations of non-Keplerian accretion disks in general relativity indicate that the spiral wave structures seen in Newtonian simulations could exist in relativistic models with small disks when the BH kick is sufficiently small, but that larger kicks disrupt the spiral pattern, as could dissipative processes such as magnetic stress or radiative cooling [345]. The inferred emission due to synchrotron emission from a relativistic disk is considered by the Illinois group [346, 347], who find that emission could peak at a luminosity of $\sim 10^{46}$ erg/s, a few orders of magnitude brighter than the corresponding bremsstrahlung luminosity and potentially observable by either WFIRST or LSST.

The outline of this chapter is as follows: in Section 4.2, we introduce the physical scales that define the kicked disk problem, while in Sec. 4.3, we use a semi-analytic, 2-dimensional *collisionless* disk model to explore the dynamics of disks acted upon by gravitational attraction between disk matter and the BH only. In Sec. 4.4, we describe the SPH code used to perform 3-dimensional *collisional simulations*. Results from these simulations, focusing on the hydrodynamic and thermodynamic evolution of the disk, are reported in Sec. 4.5. Finally, in Sec. 4.6, we lay out consequences of our results and plans to extend them in the future.

4.2 Physical scales

Throughout this chapter, we use scaled units, denoted by hats, under the assumption that $G = M_{\rm BH} = v_{\rm kick} = 1$. A single unit of time, for example, is thus $GM_{\rm BH}v_{\rm kick}^{-3}$. Choosing reference values $M_{\rm BH} = 10^8 M_\odot$ and $v_{\rm kick} = 10^8$ cm/s, the resulting time and distance scales are defined as

$$t = 1.327\times10^{10}\left(\frac{M_{\rm BH}}{10^8 M_\odot}\right)\left(\frac{v_{\rm kick}}{10^8\ {\rm cm/s}}\right)^{-3}\hat{t}\ {\rm s} = 421\left(\frac{M_{\rm BH}}{10^8 M_\odot}\right)\left(\frac{v_{\rm kick}}{10^8\ {\rm cm/s}}\right)^{-3}\hat{t}\ {\rm yr} \quad \text{(IV-1)}$$

$$d = 1.327\times10^{18}\left(\frac{M_{\rm BH}}{10^8 M_\odot}\right)\left(\frac{v_{\rm kick}}{10^8\ {\rm cm/s}}\right)^{-2}\hat{d}\ {\rm cm} = 8.87\times10^{4}\left(\frac{M_{\rm BH}}{10^8 M_\odot}\right)\left(\frac{v_{\rm kick}}{10^8\ {\rm cm/s}}\right)^{-2}\hat{d}\ {\rm AU}$$

$$= 0.43\left(\frac{M_{\rm BH}}{10^8 M_\odot}\right)\left(\frac{v_{\rm kick}}{10^8\ {\rm cm/s}}\right)^{-2}\hat{d}\ {\rm pc}. \quad \text{(IV-2)}$$

Because the disk is evolved without self-gravity, the disk mass scale is formally independent of the BH mass that sets the rest of the physical scales.

For a disk of total mass $m_{\rm disk}$, we may define a set of quantities marked with tildes by choosing a reference value $m_{\rm disk} = 10^4 M_\odot$. The physical scales for energy, its time derivative,

volume density, and surface density are then given respectively by

$$\begin{aligned}
E &= 1.99\times10^{53}\left(\frac{m_{\rm disk}}{10^4\ M_\odot}\right)\left(\frac{v_{\rm kick}}{10^8\ {\rm cm/s}}\right)^2\tilde{E}\ {\rm erg}\\
\frac{dE}{dt} &= 1.50\times10^{43}\left(\frac{m_{\rm disk}}{10^4\ M_\odot}\right)\left(\frac{M_{\rm BH}}{10^8M_\odot}\right)^{-1}\left(\frac{v_{\rm kick}}{10^8\ {\rm cm/s}}\right)^5\frac{d\tilde{E}}{d\hat{t}}\ {\rm erg/s}\\
\rho &= 8.51\times10^{-18}\ \left(\frac{m_{\rm disk}}{10^4\ M_\odot}\right)\left(\frac{M_{\rm BH}}{10^8M_\odot}\right)^{-3}\left(\frac{v_{\rm kick}}{10^8\ {\rm cm/s}}\right)^6\tilde{\rho}\ {\rm g/cm^3}\\
&= 1.26\times10^{5}\ \left(\frac{m_{\rm disk}}{10^4\ M_\odot}\right)\left(\frac{M_{\rm BH}}{10^8M_\odot}\right)^{-3}\left(\frac{v_{\rm kick}}{10^8\ {\rm cm/s}}\right)^6\tilde{\rho}\ {\rm M_\odot/pc^3}\\
\Sigma &= 11.3\ \left(\frac{m_{\rm disk}}{10^4\ M_\odot}\right)\left(\frac{M_{\rm BH}}{10^8M_\odot}\right)^{-2}\left(\frac{v_{\rm kick}}{10^8\ {\rm cm/s}}\right)^4\tilde{\Sigma}\ {\rm g/cm^2}.
\end{aligned}$$

Assuming the fluid is a fully ionized ideal gas with mass fractions $X = 0.7$, $Y = 0.28$ (where X is the Hydrogen mass fraction and Y is the Helium mass fraction respectively), the mean molecular mass is $\mu = 2/(1 + 3X + 0.5Y) = 0.617$, and the characteristic temperature scales like

$$T = \frac{\mu m_p v_{\rm kick}^2}{k_B}\tilde{T} = 7.48\times10^7\left(\frac{v_{\rm kick}}{10^8\ {\rm cm/s}}\right)^2\tilde{T}\ {\rm K},$$

where m_p is the mass of a proton, and k_B is the Boltzmann constant. The optical depth for Thomson scattering, $\tau \equiv \kappa_e\Sigma$, where $\kappa_e \approx 0.2(1 + X) = 0.34\ {\rm cm^2/g}$ is appropriate for non-relativistic plasma, is given by

$$\tau \equiv \kappa_e\Sigma \approx 3.8\ \left(\frac{m_{\rm disk}}{10^4\ M_\odot}\right)\left(\frac{M_{\rm BH}}{10^8M_\odot}\right)^{-2}\left(\frac{v_{\rm kick}}{10^8\ {\rm cm/s}}\right)^4\tilde{\Sigma}. \qquad \text{(IV-3)}$$

4.2.1 Other Opacity Models

In cases where the disk mass is sufficiently small that the optical depth $\tau < 1$ (see. Eq.(IV-3)), the disk can be considered in the optically thin limit, assuming that the flux follows the blackbody form

$$F = \sigma T^4 \qquad \text{(IV-4)}$$

while for the optically thick case, $\tau > 1$, it is possible to assume a simple diffusion law

$$F = \frac{\sigma T^4}{\kappa \Sigma}$$

where we sum over the cylindrical radius oriented with respect to the angular momentum of the bound component of the disk.

4.2.1.1 Models with different regions of Temperatures distributions

By considering differential regions of temperature distributions it is possible to account for more precise and accurate computations of the optical depth and therefore the luminosity from the disk. A very interesting case taking into account the temperature distribution arises by assuming that the opacity can be described by a 3-part model: a low-Temperature model: assuming Hydrogen-emission, using $\kappa = 10^{-36}\rho^{1/3}T^{10}$ [348]; a medium-Temperature model: due to bound-free/free-free electron emission yields $10^{25}\rho T^{-7/2}$; a high-Temperature model: due to Thomson scattering, $\kappa = 0.34$.

For every SPH particle, we have a density ρ_i and a temperature $T_i = m_p/k_B P_i/\rho_i$,[1] and thus can classify its opacity regime. Even more, knowing the contribution to the surface density, it is possible to multiply $\Sigma \times \kappa$ to get a dimensionless number representing that particle's contribution to the optical depth.

Another possibility is to consider a 2-part model by grouping medium and high temperatures together: $\kappa = 10^{25}\rho T^{-7/2} + 0.34$. Some raw experimentation with a simplified model shows that factors like $10^{-36.5}$ (for low temperatures distribution, where T goes like T^{10}) and $10^{24.5}$ (for medium temperatures distribution, where T goes like $T^{-7/2}$) would give better

[1] In the temperature equation $T_i = m_p/k_B P_i/\rho_i$, m_p in the numerator should really be the mean molecular weight μ and not the proton mass m_p. Unfortunately, the calculation of μ depends on the ionization level of the gas. By assuming that the gas is hot enough to make it fully ionized, makes it easy: $\mu = 2m_p/(1 + 3X + 0.5Y)$ (see the computation described in 4.2.1). But if there are low temperature portions of the disk such approximation would not be valid. And then in high temperature regions the underlying equation of state $P = A\rho^{5/3}$ is not valid, because radiation pressure makes the adiabatic index drop below 5/3. It could be possible to partially account for radiation pressure by solving $P_i = \rho_i k_B T_i/\mu + aT_i^{4/3}$ for T_i, but this is not really self-consistent unless radiation transport is included, otherwise the usually computed P_i assumes no radiation pressure. Therefore, by using $T_i = \mu/k_B P_i/\rho_i$ with $\mu = 2m_p/(1 + 3X + 0.5Y)$ and recalling that there may be some regions of the disk in which this temperature approximation is crude but that it still gives the correct order of magnitude and is valid in most cases/places of interest.

approximations to the true opacity. Even with these smaller coefficients, the opacity is too large by a factor of ~ 10 for $\rho = 10^{-3}\mathrm{g/cm}^3$ and temperatures between 10^4 and 10^5 Kelvin. Unfortunately, there is probably no simplified model that will give good opacities for all densities and temperatures. Additionally, if one is willing to move away from physically motivated formulas in order simply to fit the data better, the temperature power in the low temperature region could be a fitting parameter. Other possibilities would include the use of pre-tabulated opacity tables, although these are extremely model-dependent. Whatever technique or criteria are used will affect the results and therefore the predictions, this particularly is an outstanding problem representing sometimes the ignorance from our models. In this way, considering models as the previously discussed, it is possible to calculate the optical depth not just for a reference model, but for any set of choices $M_{BH}, m_{disk}, v_{kick}$. Furthermore, these sorts of analyses do not scale (i.e. are not scale invariant), and having 3 physical scales will allow for determining some non-trivial behavior, covering a wider parameter space.

Unfortunately in our case the densities are roughly only $10^{-18}\mathrm{g/cm}^3$. In other words, there is no significant bound-free or free-free region for a plasma this tenuous. We get optical depths of nearly unity because the scale height of the disk is roughly $0.1 - 1$parsecs. Thus, these previously discussed clever models do not really apply, and we basically have Thomson opacity where the temperature is large enough to support a plasma and virtually no opacity otherwise. Therefore in the rest of this project we will assume the validity of Eq.(IV-3).

4.3 Collisionless disks

The simplest model for a disk around a merging SMBH binary consists of a 2-dimensional, infinitely thin disk with a perfectly Keplerian rotational profile. If we assume that Newtonian gravity applies, we have a nearly scale-free system, where only the mass of the SMBH binary contains units. In what follows, we work in dimensionless units such that $G = M_{\rm BH} = 1$, where $M_{\rm BH}$ is the total mass of the SMBH binary, assumed for the moment to be equal to the total mass of the merged SMBH that will be formed in the merger and immediately kicked with velocity $v_{\rm kick}$ at an angle θ relative to the angular momentum of the 2-d disk. We also

choose $v_{\rm kick} = 1$ to set the overall scaling for the remaining quantities we consider, denoting all quantities in these units by hats. The Keplerian rotational velocity, for instance, is given by $\hat{v}_0 = \hat{r}^{-1/2}$. Note that our unit system results in the speed of light *not* being set to unity, as we will discuss below. Note that our conventions are very similar to those found in [246], except for the definition of the kick angle: we define θ to be the angle away from vertical, whereas they define θ to be an the angle between the kick and the initial disk plane.

In what follows, we assume that the disk orbits in the $x-y$ plane, with angular momentum in the positive z-direction. We define ϕ to be the azimuthal angle in this plane, measured counterclockwise from the x axis. The BH kick falls in the $x-z$ plane, and we assume that the SMBH proceeds to move off with constant velocity, feeling no accelerations from either the disk or the galactic potential on the timescales of interest.

The relative velocity of points in the disk with respect to the newly kicked BH is given by

$$\begin{aligned} \hat{v}(r,\phi) &\equiv \hat{v}_0 - \hat{v}_{\rm k} = (-\sin\theta - \hat{r}^{-1/2}\sin\phi,\ \hat{r}^{-1/2}\cos\phi,\ -\cos\theta) \\ |\hat{v}(r,\phi)| &= \sqrt{1 + 2\hat{v}_0 \sin\theta\sin\phi + \hat{v}_0^2} = \left(1 + 2\hat{r}^{-1/2}\sin\theta\sin\phi + \hat{r}^{-1}\right)^{1/2}. \end{aligned}$$

Thus, the specific energy at each point in the disk, $\hat{E}(r,\phi) \equiv \hat{v}^2/2 - \hat{r}^{-1}$, is

$$\hat{E}(r,\phi) = \frac{1 + 2\hat{v}_0\sin\theta\sin\phi - \hat{v}_0^2}{2} = \frac{1 + 2\hat{r}^{-1/2}\sin\theta\sin\phi - \hat{r}^{-1}}{2}. \qquad \text{(IV-5)}$$

Accordingly , we can find the critical velocity $\hat{v}_b$ and thus radius $\hat{r}_b$ as a function of azimuthal angle ϕ inside of which the matter is bound to the kicked BH and unbound outside:

$$\begin{aligned} \hat{v}_{\rm b}(\phi) &= \sin\theta\sin\phi + \sqrt{1 + \sin^2\theta\sin^2\phi} \\ \hat{r}_b &= \hat{v}_{\rm b}^{-2} = \left(\sin\theta\sin\phi + \sqrt{1 + \sin^2\theta\sin^2\phi}\right)^{-2}. \end{aligned}$$

In Fig. 4.1, we show the boundary of the bound matter for kick angles of 0, 30, 60, 90 degrees away from vertical (an equivalent plot appears as Fig. 1 of [246]; the result itself is easily derived and well-known, and we include it here to establish notation and a reference point for

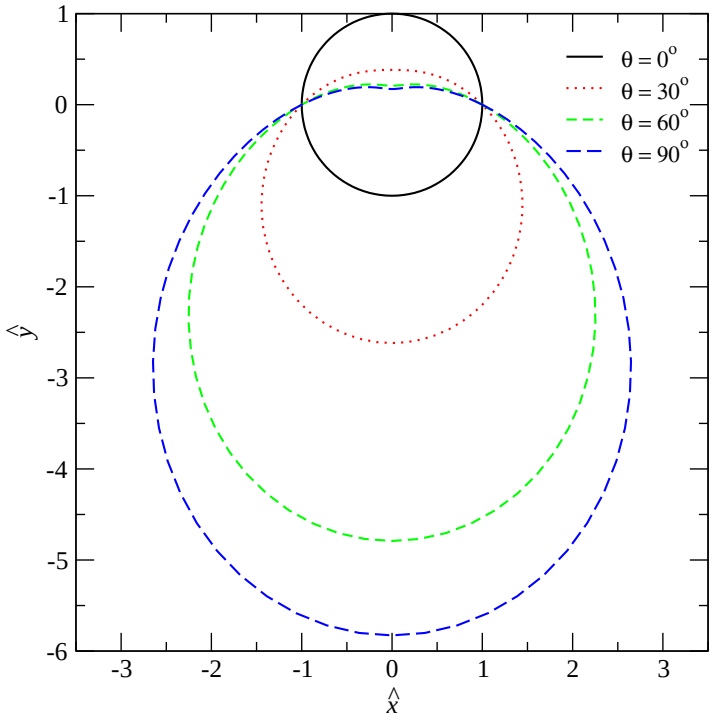

Figure 4.1: Boundary of the bound component of the disk as a function of the kick angle θ away from vertical, in hatted units where $G = M = v_{\rm kick} = 1$. For a vertical kick, the condition may be simply stated that matter is bound when the Keplerian velocity is greater than the kick velocity, and unbound otherwise.

further discussion).

For both bound and unbound particles, we may calculate the full trajectory of the particles assuming they remain collisionless by solving the two-body problem with respect to the kicked black hole. In Fig. 4.2, we show the eccentricity of particles at various radii for a selection of azimuthal angles in the disk, as a function of the kick angle. Note that, by symmetry, eccentricities for angles $90^\circ \leq \phi \leq 270^\circ$ are equivalent to those at $90^\circ - \phi$. While eccentricities increase nearly linearly with radius out to $\hat{r}_b(\phi)$ for particles located in the positive y-direction, the pattern is more complex for particles in the other half plane. In particular, there is a set

of points for which the resulting orbit around the kicked BH is circular, albeit in a different orbital plane than the original $x-y$ plane. Similarly, we show the periastron radius, $\hat{r}_p$, for the new orbits in Fig. 4.3, showing only longitude $\phi = -60°$ and $-90°$, for which the periastron as a function of initial radius is inevitably small. We note that values are systematically smallest for kick angles closest to the original disk plane ($\theta = 90°$), and, if we impose an inner edge on the original disk, there is a minimum periastron for all post-kick particles that decreases dramatically as the kick angle becomes more in-plane. This leads to a testable prediction for 3-d dynamical simulations: a "gap" should be present for more vertical kick angles, disappearing only once collisions in the inner region of the post-kick disk facilitate the angular momentum loss required to feed flow toward the SMBH. Because the time required to cross into the upper half-plane of the disk, at a distance similar to the initial radius, is generally of order the orbital period for kicks near the vertical, we expect that it should take several times the orbital period at the inner edge of a disk before any significant amount of matter is present near the SMBH. For in-plane kicks, the filling of the inner disk should be much more rapid.

4.3.1 Two-body dynamics for elliptical and hyperbolic orbits

The following subsection is a review of the Newtonian two-body problem, and may prove useful for understanding how the collisionless evolution code works. We will work in the reference frame of the BH, and assume that we know each particle's initial position $\vec{x}_0$ and velocity $\vec{v}_0$ relative to the BH. From these, we define the specific angular momentum vector, $\vec{l} = \vec{x}_0 \times \vec{v}_0$ with magnitude l. It is convenient to define the *eccentricity vector*,

$$\vec{e} \equiv \vec{v}_0 \times \vec{l} - \vec{x}_0/|\vec{x}_0|, \tag{IV-6}$$

which points toward the position of the pericenter and has magnitude equal to the orbital eccentricity. In the code, we normalize the vector, defining $\hat{e} = \vec{e}/|\vec{e}|$ and use this expression to determine the orbital eccentricity (e_x, e_y, e_z). Similarly, we complete the 3-d frame by defining a unit vector perpendicular to both the angular momentum and the eccentricity vector, $\vec{b} = \vec{l} \times \hat{e}/|\vec{l}| = (b_x, b_y, b_z)$. The particle's specific energy E_t is given by the standard

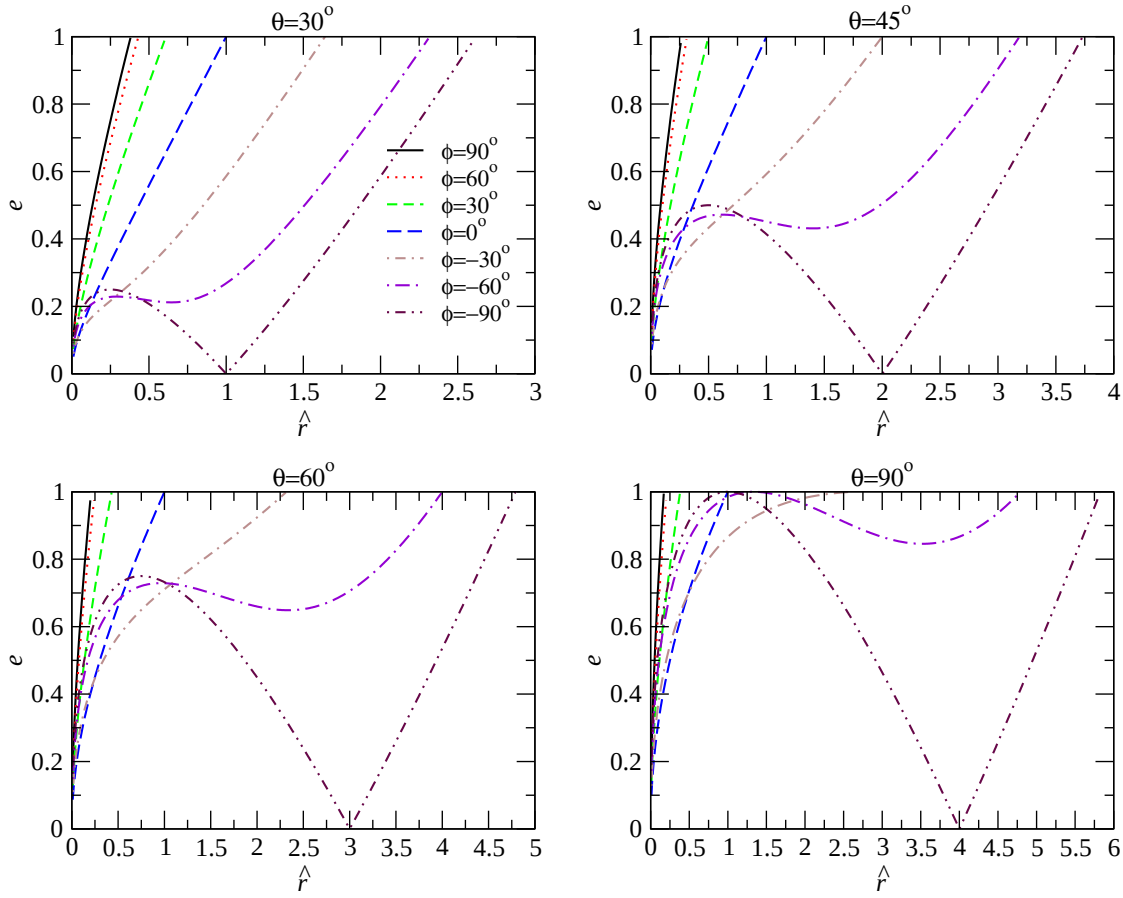

Figure 4.2: Particle eccentricities after the BH kick as a function of radius for a selection of azimuthal angles ϕ and kick angles θ.

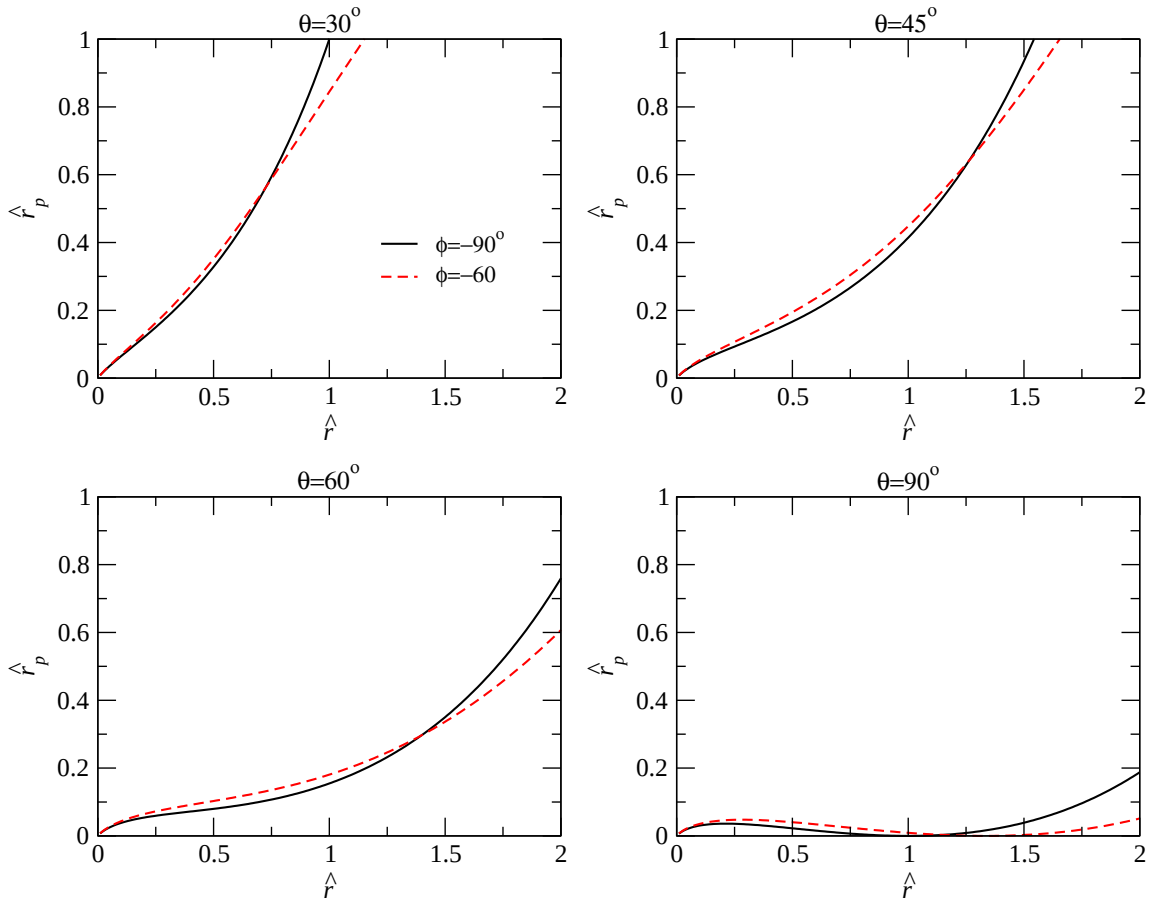

Figure 4.3: Particle periastron values after the BH kick as a function of radius for azimuthal angles $\phi = -60°,\ -90°$ and selected kick angles θ. Assuming the disk has an inner edge at $\hat{r} = \hat{r}_0$ prior to the kick, the minimum value of $\hat{r}_p$ decreases as θ increases from 0°, a vertical kick, to $\theta = 90°$, an in-plane kick, with particularly rapid changes for large values of θ.

expression, and we define bound particles as those that have negative energies, or equivalently, eccentricities larger than 1.

Regardless of whether a particle is bound or not, we may define the semi-major axis $a \equiv -E_t/2$ and orbital period $P = 2\pi|a|^{3/2}$, noting these are not physical quantities in the case of unbound hyperbolic trajectories, rather they are mathematical conveniences. To begin our determination of the path of the particle, we determine the initial *true anomaly* ν_0, i.e., the azimuthal angle of the particle with respect to the BH with pericenter defined as $\nu = 0$ through the relation

$$|\vec{x}_0| = \frac{a(1-e^2)}{1+e\cos\nu}; \tag{IV-7}$$

an expression that holds true for both elliptical and hyperbolic cases. To determine the quadrant of ν_0, we note that $\dot{r} > 0$ for $0 \leq \nu < \pi$, and vice versa.

For bound particles, we may define the pericenter and apocenter distances as $r_{a/p} \equiv a(1 \pm e)$. We determine the *eccentric anomaly* E from the relation

$$r = a(1 - e\cos E), \tag{IV-8}$$

and the *mean anomaly* M, from the expression $M = E - e\sin E$. The mean anomaly is the quantity whose growth is linear in time $M - M_0 = t/|a|^{3/2}$. For unbound particles, the eccentric and mean anomalies are given by

$$\begin{aligned} r &= a(1 - e\cosh E), \\ M &= e\sinh E - E. \end{aligned}$$

The formula above for the time dependence of the mean anomaly still applies in this case.

To evaluate the behavior of each particle in time, we evolve the mean anomaly, and then work backwards to find the eccentric and true anomalies. As neither the bound nor unbound expressions for the mean anomaly in terms of the eccentric anomaly is invertible, we use

Newton-Raphson to solve the relationship numerically. We also calculate $\dot{E}$:

$$\begin{aligned} \dot{E} &= a^{-3/2}/(1-e\cos E) \quad e<1 \\ \dot{E} &= |a|^{-3/2}/(e\cosh E-1) \quad e\geq 1. \end{aligned}$$

The true anomaly can be calculated analytically from the eccentric anomaly for either case:

$$\tan\left(\frac{\nu}{2}\right) = \sqrt{\frac{1+e}{1-e}}\tan\left(\frac{E}{2}\right),$$

or, equivalently[2]

$$\begin{aligned} \nu &= 2\mathbf{atan2}[\sqrt{1+e}\sin(E/2),\ \sqrt{1-e}\cos(E/2)] \quad e<1, \\ \cos\nu &= \frac{e-\cosh E}{e\cosh E-1} \quad e>1. \end{aligned}$$

where the latter expression[3] takes advantage of the fact that we know unbound particles are all receding from the BH, not approaching, for our particular situation. The distance from each particle to the BH r is given by $r=a(1-\cos E)$ for bound particles and $r=a(1-\cosh E)$ for unbound, and the radial velocity $\dot{r}$ by $\dot{r}=ae\dot{E}\sin(E)$ and $\dot{r}=-ae\dot{E}\sinh(E)$ for bound and unbound particles respectively. The simplest way to determine $\dot{\nu}$ is via conservation of angular momentum, $\dot{\nu}=l/r^2$.

Using these, we may evaluate the position $\vec{x}=(x,y,z)$ and velocity $\vec{v}=(v_x,v_y,v_z)$ through

[2]The two-argument function **atan2** is a variation of the arctangent function. For any real arguments x and y not both equal to zero, $\mathbf{atan2}(y,x)$ is the angle in radians between the positive x-axis of a plane and the point given by the coordinates (x,y) on it. The angle is positive for counter-clockwise angles (upper half-plane, $y>0$), and negative for clockwise angles (lower half-plane, $y<0$): $\mathbf{atan2}(y,x)=\begin{cases} \arctan\left(\frac{y}{x}\right) & x>0 \\ \pi+\arctan\left(\frac{y}{x}\right) & y\geq 0, x<0 \\ -\pi+\arctan\left(\frac{y}{x}\right) & y<0, x<0 \\ \frac{\pi}{2} & y<0, x=0 \\ -\frac{\pi}{2} & y<0, x=0 \\ \text{undefined} & y=0, x=0 \end{cases}$.

[3]`http://www.mps.mpg.de/homes/fraenz/systems/systems2art/node15.html`

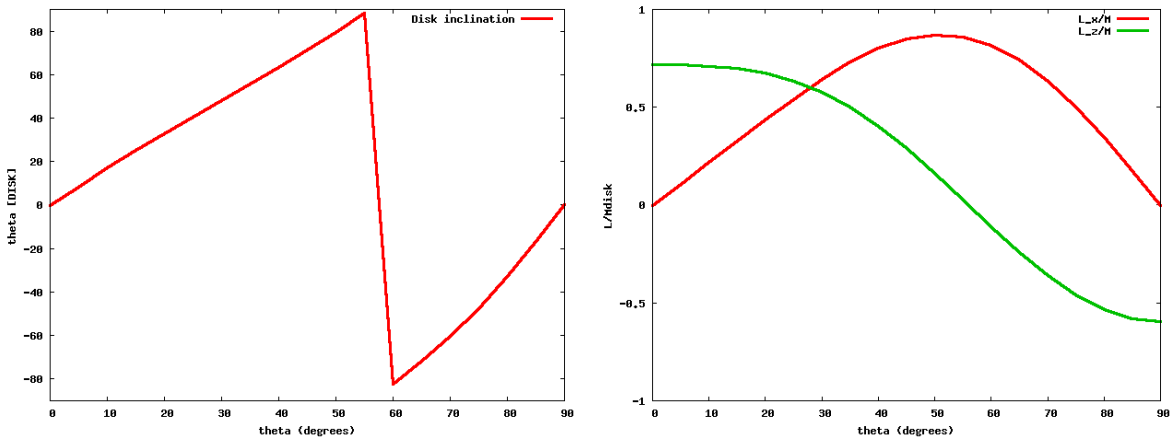

Figure 4.4: Left: Inclination angle i of the disk as a function of the kick angle. Right: Specific angular momenta components: $l_i = L_i/M_{bound}$, as a function of the kick angle.

use of the true anomaly and the various time derivatives present in the problem:

$$\begin{aligned} \vec{x} &= r(\hat{e}\cos\nu + \vec{b}\sin\nu), \\ \vec{v} &= \dot{r}(\hat{e}\cos\nu + \vec{b}\sin\nu) - r\dot{\nu}(\hat{e}\sin\nu - \vec{b}\cos\nu). \end{aligned}$$

4.3.2 Global properties of the disk

It is straightforward to identify the global properties of the bound component of the disk. While the disk's angular momentum is initially in the $+z$ direction, the net disk angular momentum after the kick points in the $-z$ direction after the kick for large values of θ, since the outer portion of the large prograde wing rotates backwards with respect to the BH after the kick (see Fig. 4.4). At an angle of roughly $\theta \sim 55 - 60°$, the net effect is that $L_z = 0$, since the $+z$ component of the angular momentum in the inner disk balances out the $-z$ component from the outer disk. Meanwhile, the asymmetry in the disk combined with the vertical component of the kick produces a rotation yielding a positive L_x component that peaks in magnitude at $\theta \sim 50°$. The disk inclination angle i is given by

$$\tan i = L_x/L_z. \tag{IV-9}$$

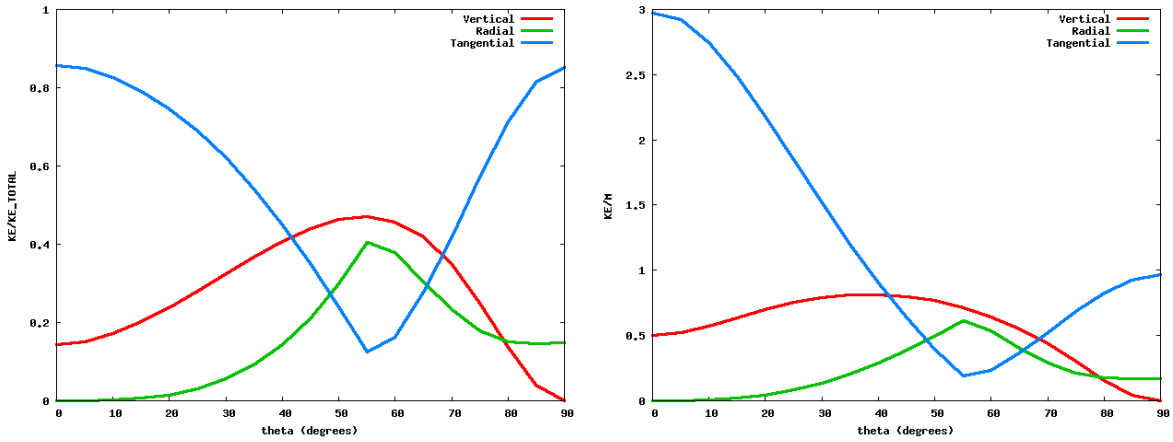

Figure 4.5: Left: Relative kinetic energy components of the bound part of the disk. Right: Specific kinetic energy components E/M as a function of the kick angle.

Similarly, we can investigate the kinetic energy of the particles in the disk, noting that these quantities are not conserved over time for elliptical orbits (see Fig. 4.5). Define vertical motion to be parallel to the net angular momentum of the disk, radial as motion toward or away from the BH, and tangential to be the component that contributes to the net angular momentum, and we can evaluate the relative contribution of each. Of particular interest is the vertical component, since the vertical energy in the disk will be most directly converted into heat. Generally speaking, the smaller the share of the tangential KE, the more heating the disk will undergo before it settles down into a more uniform rotation profile.

4.4 Smoothed Particle Hydrodynamics for kicked accretion disks

Smoothed Particle Hydrodynamics (SPH) is a very versatile and powerful technique that allows us to perform simulations of several kinds of fluids flows. It has been largely used in a wide range of fields, including but not limited to: astrophysics, ballistics, vulcanology, oceanology, oil spills and even development of games engines for representing fluids. It is a mesh-free Lagrangian method (where the coordinates move with the fluid), and the resolution of the method can easily be adjusted to variables such as the density. The (SPH) method works by dividing the fluid into a set of 'discrete elements': *particles*. These particles have a spatial distance (known as the "smoothing length" h), over which their properties are "smoothed" by

a *kernel function*. This means that any *physical quantity* of any particle can be obtained by summing the relevant properties of all the particles which lie within the range of the kernel. Usually this smoothing length is considered approximately constant, and in many cases this is a good approximation but in other more extreme cases this assumption must be removed. By doing this, new equations of motion must be obtained considering extra terms accounting for the variations of the smoothing length: so called '*grad-h*' correction factors. These generalized equations allow the preservation of energy as well as momenta during the evolution. Given the nature of the scenarios we were interested in modeling, we need to upgrade the modified version of our SPH code to incorporate the equations of motion consistently with a dynamical smoothing length. This guarantees that the code is conservative regarding energy and angular momentum.

We developed a code using Smoothed Particle Hydrodynamics (SPH) techniques for studying "kicked" black holes scenarios in the vicinity of disks. The code is a state-of-the-art, 3-dimensional colisionall SPH code, particularly developed for simulating this scenarios, guaranteeing not only excellent energy and angular momentum preservation but also combining novel techniques in order to deal with several numerical and technical details that usually are not considered.

We performed 3-dimensional collisional SPH simulations of accretion disks under the influence of a recoiling black hole.

In order to deal with the effects from the strong gravitational potential of the black hole for close particles, and to guarantee an almost perfect energy and angular momentum conservation, we implemented a "smoothed black hole potential" to account for the finite size of the particles. We ran the simulations on parallel CPUs, varying the recoil angle of the black hole with respect to the accretion disk.

In the following sections, we describe the initial data generation, the evolution equations, the time integration technique, and the thermodynamics and surface density computations.

4.4.1 Initial data

Following the methods outlined in Refs.[349, 350] and similar works, we construct semi-analytic models of accretion disks in hydrodynamic equilibrium to use as initial conditions before laying down particles using a Monte Carlo technique. To do so, we first assume a that the orbital velocity is independent of the height within the disk and varies only with cylindrical radius. Integrating the force equation for a system in stationary equilibrium,

$$-\frac{\nabla P}{\rho}+\nabla\left(\frac{GM}{r}\right)=-\frac{l(r_c)^2}{r_c^3}\hat{\mathbf{r}}_{\mathbf{c}}, \tag{IV-10}$$

and assuming the pressure $P=k\rho^{\gamma}$, where γ is the adiabatic index of the fluid, M the mass of the central BH, r and r_c are the spherical and cylindrical radii, $\hat{\mathbf{r}}_{\mathbf{c}}$ is the unit vector associated with the cylindrical radius, and $l(r_c)$ is the chosen radial specific angular momentum profile, we find

$$\eta\equiv\frac{\gamma}{\gamma-1}\frac{P}{\rho}=\frac{GM}{r}+\int\frac{l(r_c)^2}{r_c^3}dr_c-K, \tag{IV-11}$$

where K is an integration constant. For the Keplerian profile $l(r_c)=\sqrt{GMr_c}$, the integral on the right hand side of Eq.(IV-11) evaluates to $-GM/r_c$, and the disk can exist only in the $z=0$ plane (where $r=r_c$).

To get a disk with finite extent in the radial and vertical directions, we choose a non-Keplerian rotation profile. Here, we assume a power-law form, noting that it must satisfy $l(r)\propto r^{\kappa}$ with $\kappa<0.5$ to yield a compactly bounded configuration. We define rotation parameters through the relation

$$\int\frac{l(r_c)^2}{r_c^3}dr_c=-cr_c^{\alpha}, \tag{IV-12}$$

and find that the top edge of the disk, where $\eta=0$, yields the condition that

$$z(r_c)=\sqrt{\left(\frac{GM}{cr_c^{\alpha}+K}\right)^2-r_c^2}. \tag{IV-13}$$

Assuming (hatted) units such that $G=M=1$, the inner and outer edges of the disk for

a sub-Keplerian rotation profile ($\kappa < 0.5$ and thus $\alpha < -1$) are given by the two real roots of the equation $\hat{z}(\hat{r}) = 0$, or

$$\hat{c}\hat{r}^{\alpha+1} + \hat{K}\hat{r} = 1. \tag{IV-14}$$

To fix the inner and outer radii at $\hat{r}_i$ and $\hat{r}_0$ respectively, we determine $\hat{c}(\alpha)$ and $\hat{K}(\alpha)$ as follows. Defining $\hat{R}_i = \hat{r}_i^{\alpha+1}$ and $\hat{R}_o = \hat{r}_o^{\alpha+1}$, we find

$$\begin{aligned} \hat{c} &= \frac{\hat{r}_o - \hat{r}_i}{\hat{R}_i\hat{r}_o - \hat{R}_0\hat{r}_i} \\ \hat{K} &= \frac{\hat{R}_i - \hat{R}_o}{\hat{R}_i\hat{r}_o - \hat{R}_o\hat{r}_i}. \end{aligned}$$

For the case $\alpha = -2$, corresponding to a constant $l(r_c)$, the solution is easy to state explicitly: noting that $\hat{R}_o = 1/\hat{r}_o$ and $\hat{R}_i = 1/\hat{r}_i$, we find

$$\begin{aligned} \hat{c} &= \frac{\hat{r}_o - \hat{r}_i}{\hat{r}_o/\hat{r}_i - \hat{r}_i/\hat{r}_o} = \frac{\hat{r}_i\hat{r}_o}{\hat{r}_o + \hat{r}_i} \\ \hat{K} &= \frac{1/\hat{r}_i - 1/\hat{r}_o}{\hat{r}_o/\hat{r}_i - \hat{r}_i/\hat{r}_o} = \frac{1}{\hat{r}_o + \hat{r}_i}. \end{aligned}$$

In general, the easiest method to achieve a specific disk height $\hat{z}_{max}$ is to vary α and check numerically where the disk reaches its maximum height, iterating until the correct value is achieved. Relatively thin disks for which the radial extent is significantly greater than the vertical tend to be nearly Keplerian, with $\alpha = -1 - \epsilon_\alpha$, where the ϵ_α is positive and $\ll 1$.

For all the runs shown below, we chose initial parameters $\hat{r}_i = 0.1$, $\hat{r}_o = 2.0$, and $\hat{z}_{max} = 0.2$ for our initial disk, resulting in an SPH discretization and rotation curve we show in Fig. 4.6. This corresponds to a choice of parameters $\hat{c} = 0.9584$, $\alpha = -1.017$, and $\hat{K} = 2.651 \times 10^{-2}$. If we specify a value for the adiabatic index γ, we are left with a free parameter in the adiabatic constant $k \equiv P/\rho^\gamma$. Varying k has the effect of rescaling the density (see Eq.(IV-11)), and thus allows us to adjust the overall disk mass while leaving a uniform specific entropy.

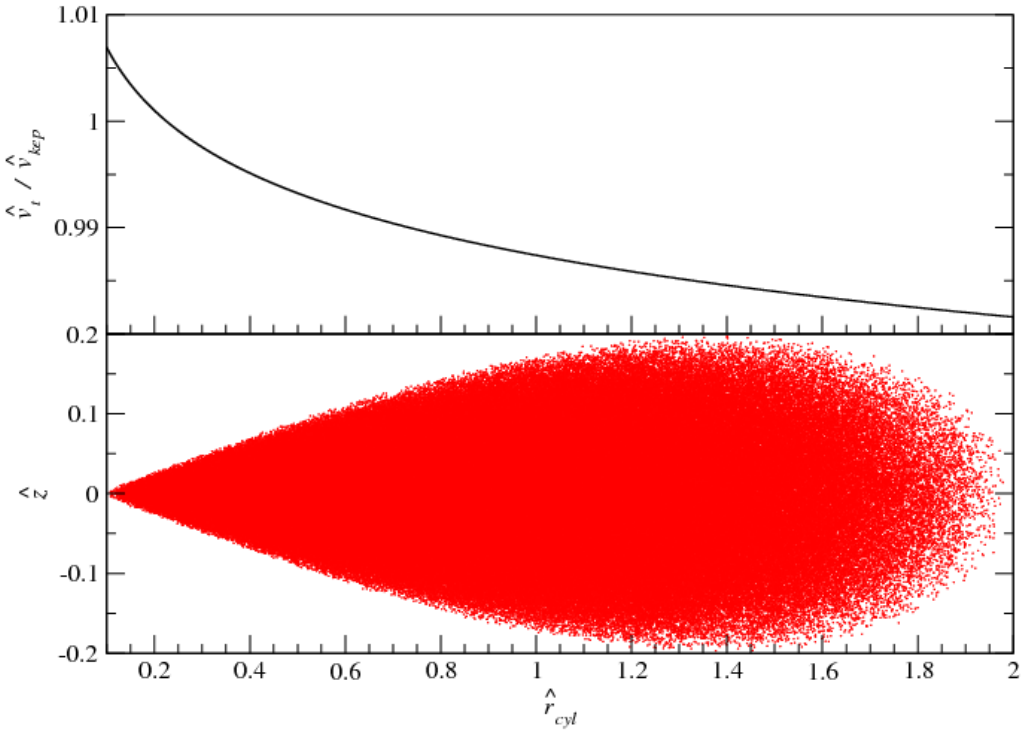

Figure 4.6: Top: The rotational profile of the disk, expressed as a ratio of the actual tangential velocity to the Keplerian velocity, shown as a function of radius. Bottom: Initial disk configuration, projected onto the $\hat{r}_c - \hat{z}$ plane. It has an inner radius $\hat{r}_i = 0.1$, outer radius $\hat{r}_o = 2.0$, and maximum height $\hat{z}_{max} = 0.2$. Finite disks require super-Keplerian rotation in the inner regions and sub-Keplerian rotation outside so that the centripetal acceleration balances the additional pressure force component. The density maximum occurs at $\hat{r} = 0.23$, where $\hat{v}_t = \hat{v}_{kep}$.

4.4.2 Evolution equations

The code used to perform our calculations combines the parallelization found in the `StarCrash` SPH code with a number of refinements described in Refs.[351] and [352], which we summarize here. Among these, we implement variable smoothing lengths for all of our particles following the formalism described in [353] and [354], which can be derived consistently from a particle-based Lagrangian. Defining a particle-based parameter

$$\Omega_i = 1 - \frac{\partial h_i}{\partial \rho_i} \sum_j m_j \frac{\partial W_{ij}(h_i)}{\partial h_i},$$

our acceleration equation is $\dot{\mathbf{v}}_i = \dot{\mathbf{v}}_i^{(\mathrm{SPH})} + \dot{\mathbf{v}}_i^{(\mathrm{grav})}$ with

$$\dot{\mathbf{v}}_i^{(\mathrm{SPH})} = -\sum_j m_j \left[\left(\frac{P_i}{\Omega_i \rho_i^2} + \frac{\Pi_{ij}}{2} \right) \nabla_i W_{ij}(h_i) + \left(\frac{P_j}{\Omega_j \rho_j^2} + \frac{\Pi_{ji}}{2} \right) \nabla_i W_{ij}(h_j) \right], \qquad \text{(IV-15)}$$

while our evolution equation for the entropic variable A_i is

$$\frac{d\,A_i}{d\,t} = \frac{\gamma - 1}{\rho_i^{\gamma-1}} \sum_j m_j \frac{\Pi_{ij}}{2} (\mathbf{v}_i - \mathbf{v}_j) \cdot \nabla_i W_{ij}(h_i)\,. \qquad \text{(IV-16)}$$

In the above, $W_{ij}(h_i)$ is the normalized second-order accurate kernel function introduced in [355], used widely throughout the SPH community, and h_i, ρ_i, m_i, and P_i are the SPH particle smoothing lengths, densities, masses, and pressures, respectively. The artificial viscosity term Π_{ij} is discussed below. We assume a smoothing length-density relation of the form

$$h_i = \left(\frac{1}{h_{max}} + b_i \rho_i^{1/3} \right)^{-1}, \qquad \text{(IV-17)}$$

where $h_{max} = 50$. The b_i values are chosen so that each particle should have ~ 200 neighbors given the initial density profile of the disk and are updated to maintain this condition during relaxation. Once the dynamical phase of the evolution begins, we hold b_i fixed and solve implicitly at each time step for the proper smoothing length and density that satisfy Eq.(IV-17).

Because the self-gravity of the disk is ignored here, the only gravitational force acting on the particles comes from the black hole. We assume instantaneous Newtonian gravitation, neglecting retardation effects from the moving black hole since our characteristic speeds are small fractions of the speed of light. Although we treat the black hole as a pure point mass without any *intrinsic* softening, the gravitational force on any SPH particle within two smoothing lengths of the black hole is softened according to the mass distribution of that SPH particle itself, as described by its smoothing kernel. To do so, we follow the formalism proposed in [356], using a variational approach to derive equations of motion that properly account for variable smoothing lengths. In particular, we start by writing the gravitational part of the Lagrangian as

$$L_{\rm grav} = -\sum_i m_i \Phi_i = -GM_{\rm BH} \sum_i m_i \varphi_i(h_i). \tag{IV-18}$$

The last equal sign in Eq.(IV-18) defines the gravitational potential Φ_i of particle i. Here $\varphi_i(h_i)$ refers to $\varphi(r_i, h_i)$ where $r_i = |\mathbf{r}_i|$ is the distance of particle i from the BH and

$$\varphi(r,h) = \begin{cases} \left(-\frac{7}{5} + \frac{2}{3}q^2 - \frac{3}{10}q^4 + \frac{1}{10}q^5\right)/h, & 0 \le q < 1; \\ \left(-\frac{8}{5} + \frac{1}{15q} + \frac{4}{3}q^2 - q^3 + \frac{3}{10}q^4 - \frac{1}{30}q^5\right)/h, & 1 \le q < 2; \\ -1/r & q \ge 2 \end{cases} , \tag{IV-19}$$

with $q = r/h$, is the gravitational potential associated with the usual SPH smoothing kernel (e.g. [356]).

Following the approach of §3 of [356], but with our Lagrangian, we find

$$\dot{\mathbf{v}}_i^{(\rm grav)} = -GM_{\rm BH}\nabla_i\varphi_i(h_i) - GM_{\rm BH}\sum_j m_j \left[\frac{1}{\Omega_i}\frac{\partial\varphi_i}{\partial h_i}\frac{\partial h_i}{\partial \rho_i}\nabla_i W_{ij}(h_i) + \frac{1}{\Omega_j}\frac{\partial\varphi_j}{\partial h_j}\frac{\partial h_j}{\partial \rho_j}\nabla_i W_{ij}(h_j)\right]. \tag{IV-20}$$

The first term on the right hand side of Eq.(IV-20) is the usual softened gravitational acceleration, while the remaining terms allow for variable smoothing lengths and preserve energy conservation. We note that one of these correction terms vanishes when the kernel of the relevant SPH particle does not overlap with the BH, because, given Eq.(IV-19), $\partial\varphi/\partial h = 0$ whenever $r > 2h$. Summing Eqs.(IV-15) and (IV-20), the total acceleration of particle i is

given by

$$\dot{\mathbf{v}}_i = -GM_{\rm BH}\nabla_i\varphi_i(h_i) - \sum_j m_j \left[\Upsilon_{ij}\nabla_i W_{ij}(h_i) + \Upsilon_{ji}\nabla_i W_{ij}(h_j)\right] , \tag{IV-21}$$

where

$$\Upsilon_{ij} = \frac{P_i}{\Omega_i\rho_i^2} + \frac{\Pi_{ij}}{2} + \frac{GM_{\rm BH}}{\Omega_i}\frac{\partial\varphi_i}{\partial h_i}\frac{\partial h_i}{\partial\rho_i} \tag{IV-22}$$

and where, given Eq.(IV-17), we use $\partial h_i/\partial\rho_i = -b_i h_i^2/(3\rho_i^{2/3})$.

The artificial viscosity (AV) has the form,

$$\Pi_{ij} = \left(\frac{P_i}{\rho_i^2} + \frac{P_j}{\rho_j^2}\right)\left(-\alpha\mu_{ij} + \beta\mu_{ij}^2\right) f_i \,, \tag{IV-23}$$

with $\alpha = \beta = 1$. Here,

$$\mu_{ij} = \begin{cases} \frac{(\mathbf{v}_i - \mathbf{v}_j)\cdot(\mathbf{r}_i - \mathbf{r}_j)}{h_{ij}\left(|\mathbf{r}_i - \mathbf{r}_j|^2/h_{ij}^2 + \eta^2\right)} \,, & \text{if}(\mathbf{v}_i - \mathbf{v}_j)\cdot(\mathbf{r}_i - \mathbf{r}_j) < 0 \,; \\ 0 \,, & \text{if}(\mathbf{v}_i - \mathbf{v}_j)\cdot(\mathbf{r}_i - \mathbf{r}_j) \geq 0 \,, \end{cases} \tag{IV-24}$$

with $\eta^2 = 10^{-2}$, and the Balsara switch f_i for particle i is defined by

$$f_i = \frac{|\nabla\cdot\mathbf{v}|_i}{|\nabla\cdot\mathbf{v}|_i + |\nabla\times\mathbf{v}|_i + \eta' c_i/h_i} \,, \tag{IV-25}$$

with $\eta' = 10^{-5}$ preventing numerical divergences [357]. The function f_i approaches unity in regions of strong compression ($|\nabla\cdot\mathbf{v}|_i >> |\nabla\times\mathbf{v}|_i$) and vanishes in regions of large vorticity ($|\nabla\times\mathbf{v}|_i >> |\nabla\cdot\mathbf{v}|_i$). Consequently, our evolution equations have the advantage that the artificial viscosity is suppressed in shear layers. We note that the artificial viscosity term is not symmetric under interchange of the indices i and j (that is, $\Pi_{ij} \neq \Pi_{ji}$), because the switch f_i is not symmetrized in Eq.(IV-23). Such an approach reduces the number of arrays shared among parallel processes. As the term in square brackets in Eq.(IV-21) is antisymmetric under the interchange of particles i and j, momentum is clearly conserved in every interaction pair. Similarly, it is straightforward to show total energy is conserved by our evolution equations: $\sum_i m_i(\mathbf{v}_i\cdot\dot{\mathbf{v}}_i + d\Phi_i/dt + du_i/dt) = 0$, where the specific internal energy $u_i = A_i\rho_i^{\gamma-1}/(\gamma-1)$.

4.4.3 Integration in Time

The evolution equations are integrated using a second-order explicit leap-frog scheme. For stability, the timestep must satisfy a Courant-like condition. Specifically, we calculate the timestep as

$$\Delta t = \mathrm{Min}_i \left(\Delta t_{1,i}, \Delta t_{2,i} \right). \tag{IV-26}$$

For each SPH particle i, we use

$$\Delta t_{1,i} = C_{N,1} \frac{h_i}{\mathrm{Max}_j \left(\Upsilon_{ij} \rho_i \right)^{1/2}} \tag{IV-27}$$

and

$$\Delta t_{2,i} = C_{N,2} \left(\frac{h_i}{|\dot{\mathbf{v}}_i|} \right)^{1/2}. \tag{IV-28}$$

For the simulations performed in this project, the Courant factors were $C_{N,1} = 0.4$ and $C_{N,2} = 0.05$. The Max_j function in Eq.(IV-27) refers to the maximum of the value of its expression for all SPH particles j that are neighbors with i. The denominator of Eq.(IV-27) is an approximate upper limit to the signal propagation speed near particle i.

4.4.4 Thermodynamics

For a monoatomic ideal gas, we can calculate the SPH internal energy via

$$E_{\mathrm{INT}} = \sum_i \frac{1}{\gamma - 1} m_i A_i \rho_i^{\gamma - 1} = \frac{3}{2} \sum_i m_i A_i \rho_i^{2/3}.$$

Furthermore, the temperature is related to the specific internal energy $u_i = \frac{3}{2} A_i \rho_i^{2/3}$ via the ideal gas law $E_{\mathrm{INT}} = \frac{3}{2} k_B T$, and is therefore given by

$$T_i = \frac{2}{3 k_B} \mu m_p u_i = \frac{\mu m_p}{k_B} A_i \rho_i^{2/3} = \frac{\mu m_p}{k_B} \frac{P_i}{\rho_i}, \tag{IV-29}$$

where m_p is the mass of a proton and $\mu = 0.617$ is the mean molecular weight, assuming that the disk is a plasma with mass fractions $X = 0.7,\ Y = 0.28$.

4.4.5 SPH expression for the surface density

We adopt a kernel function

$$W(r,h) = \frac{1}{\pi h^3}\begin{cases} 1-\frac{3}{2}\left(\frac{r}{h}\right)^2+\frac{3}{4}\left(\frac{r}{h}\right)^3, & 0\le\frac{r}{h}<1 \\ \frac{1}{4}\left(2-\frac{r}{h}\right)^3, & 1\le\frac{r}{h}<2 \\ 0, & \frac{r}{h}\ge 2 \end{cases} = \begin{cases} W_{out}, & 0\le\frac{r}{h}<2 \\ 0, & \frac{r}{h}\ge 2 \end{cases} + \begin{cases} W_{in}, & 0\le\frac{r}{h}<1 \\ 0, & \frac{r}{h}\ge 1 \end{cases},$$

where we have defined

$$\begin{aligned} W_{out} &= \frac{1}{4\pi h^3}\left(2-\frac{r}{h}\right)^3 = \frac{1}{\pi h^3}\left[2-3\frac{r}{h}+\frac{3}{2}\left(\frac{r}{h}\right)^2-\frac{1}{4}\left(\frac{r}{h}\right)^3\right] \\ W_{in} &= \frac{1}{\pi h^3}\left(\frac{r}{h}-1\right)^3 = \frac{1}{\pi h^3}\left[-1+3\frac{r}{h}-3\left(\frac{r}{h}\right)^2+\left(\frac{r}{h}\right)^3\right]. \end{aligned}$$

The function W_{out} is just the kernel function in the outer regions of the compact support ($1 \le r/h < 2$), while W_{in} is the difference between the kernel function in the inner and outer domains. The distance r from the center of an SPH particle to the points on a line passing vertically with horizontal offset ρ from that center is given by $r = \sqrt{Z^2+\rho^2}$, where Z is the vertical offset. Thus, we may define $z_{\rm out} = \sqrt{4h^2-\rho^2}$, and if $\rho < h$, the quantity $z_{\rm in} = \sqrt{h^2-\rho^2}$, to define the integration bounds for the kernel-based surface density

$$\Sigma = \sum_i m_i \int_{z_{\rm in}}^{z_{\rm out}} W(r,h_i)dZ. \qquad \text{(IV-30)}$$

In particular, aparticle i that passes close enough to the line being integrated, such that the outer part of its kernel intersects the line (so $h_i < \rho < 2h_i$), will contribute

$$\Sigma_{\rm out,i} = \frac{m_i}{\pi h_i^2}\left[2i_0\left(\frac{z_{out}}{h_i}\right)-3i_1\left(\frac{z_{out}}{h_i}\right)+\frac{3}{2}i_2\left(\frac{z_{out}}{h_i}\right)-\frac{1}{4}i_3\left(\frac{z_{out}}{h_i}\right)\right] \qquad \text{(IV-31)}$$

to the surface density. While if $\rho < h_i$ then particle i contributes

$$\Sigma_{\rm in,i} = \Sigma_{\rm out,i} + \frac{m_i}{\pi h_i^2}\left[-i_0\left(\frac{z_{in}}{h_i}\right) + 3i_1\left(\frac{z_{in}}{h_i}\right) - 3i_2\left(\frac{z_{in}}{h_i}\right) + i_3\left(\frac{z_{in}}{h_i}\right)\right] \quad \text{(IV-32)}$$

to the surface density.

Here we make use of the vertical symmetry of the kernel function to define the following integrals:

$$\begin{aligned}
I_0(z) = hi_0\left(\frac{z}{h}\right) &= \int_{-z}^{z} dZ = 2z, \\
I_1(z) = h^2 i_1\left(\frac{z}{h}\right) &= \int_{-z}^{z} r(Z)\, dZ = \int_{-z}^{z} \sqrt{Z^2+\rho^2}\, dZ \\
&= \frac{1}{2}\left(Z\sqrt{Z^2+\rho^2} + \rho^2 \ln\left[Z + \sqrt{Z^2+\rho^2}\right]\right)\Bigg|_{-z}^{z} \\
&= z\sqrt{z^2+\rho^2} + \rho^2 \ln\left(\frac{z+\sqrt{z^2+\rho^2}}{\rho}\right), \\
I_2(z) = h^3 i_2\left(\frac{z}{h}\right) &= \int_{-z}^{z} r^2 dZ = \int_{-z}^{z} (Z^2+\rho^2) dZ = \frac{2z}{3}(z^2+3\rho^2), \\
I_3(z) = h^4 i_3\left(\frac{z}{h}\right) &= \int_{-z}^{z} r^3 dZ = \int_{-z}^{z} (Z^2+\rho^2)^{3/2} dZ \\
&= \frac{1}{4}\left(z\sqrt{z^2+\rho^2}\left[2z^2+5\rho^2\right] + 3\rho^4 \ln\left[\frac{z+\sqrt{z^2+\rho^2}}{\rho}\right]\right).
\end{aligned}$$

4.4.6 Code Units: Rescaling

This section describes some documentation regarding the way in which the value of the parameters in the code are related to the real physical values. It can be thought as the connection between the `code units` and the "scaled units" described in Sec. 4.2.

If one chooses $G = 1$ but arbitrary values $M_{\rm BH} = M_{code}$, $m_{\rm disk} = m_{code}$ and $v_{\rm kick} = v_{code}$, we can convert all quantities to the hat/tilde form above through the following transformations:

$$
\begin{aligned}
\hat{d} &= \frac{v_{code}^2}{M_{code}} d_{code} \\
\hat{t} &= \frac{v_{code}^3}{M_{code}} t_{code} \\
\tilde{E} &= \frac{1}{m_{code} v_{code}^2} E_{code} \\
\tilde{\rho} &= \frac{M_{code}^3}{m_{code} v_{code}^6} \rho_{code} \\
\tilde{\Sigma} &= \frac{M_{code}^2}{m_{code} v_{code}^4} \Sigma_{code} \\
\tilde{P} &= \frac{M_{code}^3}{m_{code} v_{code}^8} P_{code}
\end{aligned}
$$

$$
\begin{aligned}
\tilde{A} &= \frac{m_{code}^{\gamma-1} v_{code}^{6\gamma-8}}{M_{code}^{3(\gamma-1)}} A_{code} \\
&= \frac{m_{code}^{2/3} v_{code}^2}{M_{code}^2} A_{code} \qquad (\gamma = 5/3 \text{ only})
\end{aligned}
$$

4.5 SPH simulations

To study the effect of the SMBH kick angle on the resulting disk evolution, we perform runs where the kick angles away from vertical are 15°, 30°, 45°, and 60°. We also perform a number of test calculations to optimize various SPH-related parameters including the number of neighbors and the Courant factors (see Sec. 4.4), along with numerical convergence tests to guarantee the validity of our simulations and determine the parameters for our fiducial production runs.

Our production runs are summarized in Table 4.1 below. The bound mass at the end of the simulation, $\tilde{M}_b$, is defined by Eq.(IV-35). The angular momentum vector $\vec{L}_b$ of the bound matter is in the original coordinates, with the initial angular momentum of the disk in the z-direction. The $\vec{L}_b$ vector defines the z'-direction used to construct cylindrical coordinates in the plots below. The tilt angle of the kicked disk is defined by the condition $\theta_{tilt} \equiv \arccos(\vec{L}_{z;b}/|L_b|)$. The approximate maximum luminosity of the disk may be estimated from

$\left(\frac{dE_{int}}{dt}\right)_{max}$, though we note that we allow for the SPH particles to shock heat.

Each run uses $N = 5 \times 10^5$ equal-mass SPH particles, and the number of neighbors is chosen to be 200 initially. All runs are started from the same relaxed disk configuration. To construct it, we lay down particles uniformly in space and use the local density as the basis for a Monte Carlo rejection technique. This configuration is relaxed for a time interval $\hat{t} = 160$, during which we apply a drag force

$$a_{drag} = (v - v_R)/t_{rel}, \tag{IV-33}$$

with $\hat{t}_{rel} = 0.8$ as the chosen relaxation timescale and v_R the exact rotation law satisfying Eq.(IV-12) above, with $v_R = l(r_c)/r_c$.

Kick angle (°)	Bound mass	$\lvert\tilde{L}_b\rvert$	$\vec{L}_b$	Tilt angle (°)	Max. Luminosity
15	0.73	0.543	(0.135,0.009,0.526)	14.3	0.016
30	0.65	0.444	(0.166, 0.011, 0.412)	21.9	0.024
45	0.60	0.359	(0.146, 0.010, 0.327)	24.2	0.039
60	0.57	0.296	(0.107, 0.006, 0.276)	21.3	0.073
None	0.9999	0.830	[a]	[a]	0.015/0.004 [b]

[a] For the unkicked disk, $|\tilde{L}^x|$, $|\tilde{L}^y| < 10^{-6}$, and thus $\theta_{tilt} < 10^{-6}$ as well.
[b] For the unkicked run, there is a brief burst of internal energy generation when the dynamical effects are turned on, yielding an internal energy generation rate $d\tilde{E}_{\rm INT}/d\hat{t} = 0.015$, but thereafter the maximum steady state luminosity is $d\tilde{E}_{\rm INT}/d\hat{t} = 0.004$.

Table 4.1: Summary of the runs performed.

Once the initial disk is relaxed, it is allowed to evolve dynamically until $\hat{t}_{kick} = 0.8$ before a kick is applied, except for a single unkicked control case we evolve to ensure that the physical effects we attribute to the kick are not merely an inevitable consequence of the dynamical evolution. In the discussion that follows, we define the time since the kick $\hat{t}_*$ as

$$\hat{t}_* \equiv \hat{t} - \hat{t}_{kick}. \tag{IV-34}$$

As shown in the bottom panel of Fig. 4.7, energy conservation is remarkably good for each

of the runs, with total variation of no more than 0.03% in the total energy after the kick in any of the runs. Achieving this level of conservation is a consequence of two important components of the evolution scheme: the softened BH potential, described in Eq.(IV-19), and the use of a Lagrangian-based variational scheme for evolving the smoothing length described in Sec. 4.4.2. The former, which may be justified given the finite spatial extent of an SPH particle, prevents particles on highly eccentric orbits that approach very closely to the BH from attaining spurious energy during the periapse passage. The latter, also used in [246], is required to allow for variable smoothing lengths without the energy varying on the same timescale as the smoothing lengths themselves.

As can be seen in Fig. 4.7, the overall level of internal energy generation within the unkicked disk is approximately 30% that of the most vertical kick configuration we consider (15° away from vertical), and roughly six times less that of the 60° kick simulation. We infer that while some of the heating we observe is an inevitable consequence of the disk evolution, the majority may be attributed to the kick and its aftermath, especially for cases where the kick is closer to the original disk plane. Similarly, the changes in the kinetic and potential energy seem to be almost entirely a result of the kick.

By the end of our simulations, the kicked accretion disks have nearly reached a steady-state, as indicated by Fig. 4.7 (for global quantities) and Fig. 4.8 (for bound matter). In general, the more oblique the kick, the more the resulting disk generates thermal energy, and, correspondingly, the deeper the potential energy well characterizing the disk. While the *total* kinetic energy is nearly uniform among all the kick angles we consider, we note that the bound mass is smaller for more in-plane kicks given the initial configuration we chose, and thus the specific kinetic energy of the disk increases with the obliqueness of the kick.

Fig. 4.8 shows the kinetic energy and relative mass of the bound portion of the disk after the kick for the different kick angles we considered, as well as for the unkicked model. Clearly for the unkicked case, all the disk remains bound to the black hole, while for the different kick angles virtually all of the unbinding occurs at the moment of the kick. The exact bound fractions are determined by our choice of initial disk configuration; our bound disk masses are

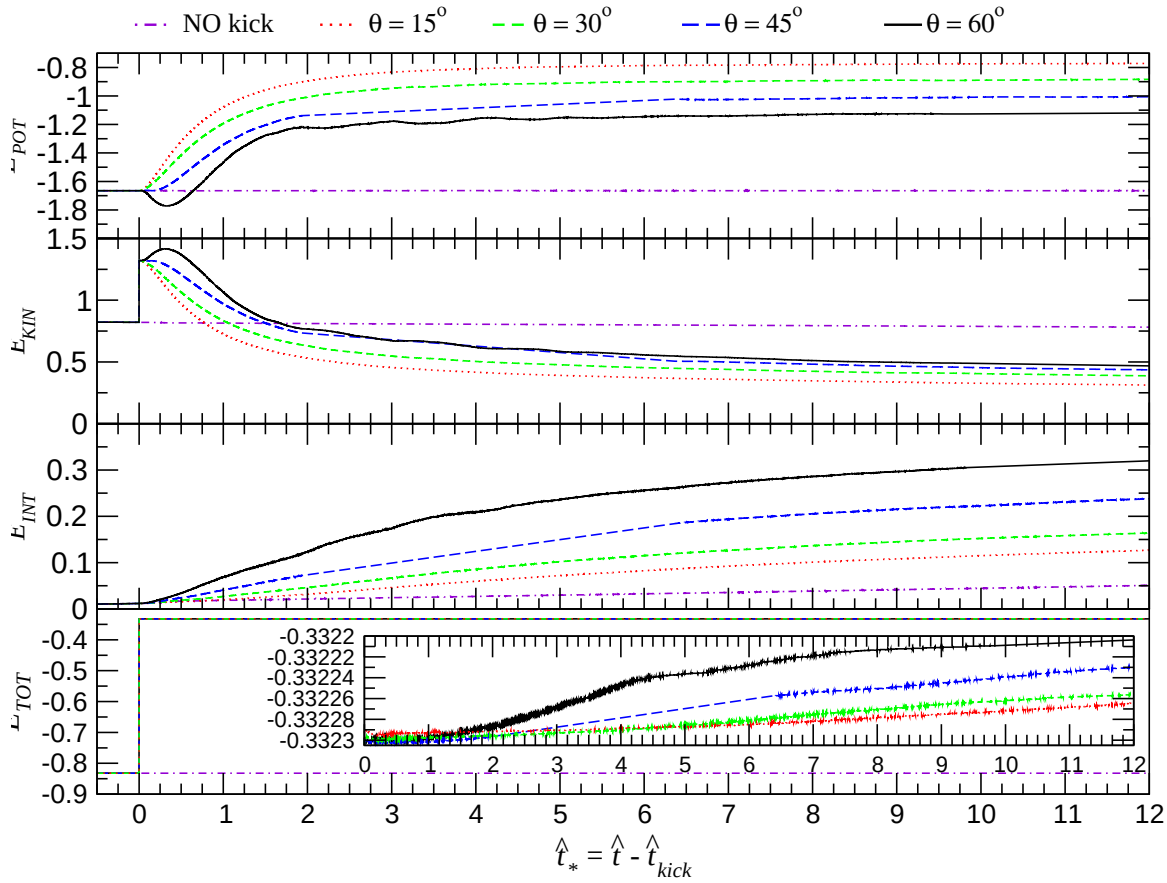

Figure 4.7: Evolution of the total potential energy (top panel), kinetic energy (second panel), internal energy (third panel), and total energy (bottom panel) for each of the runs. The kick occurs at $\hat{t}_* = 0$ (see Eq.(IV-34)). Each panel shows the unkicked control run (violet dotted-dashed line), and kicked cases of 15°(red dotted line), 30°(green dashed line), 45°(blue long-dashed line), and 60°(solid black line) away from vertical. Energy preservation is almost perfect, with a total variation of no more than $\leq 0.03\%$ for any run, as shown in the inset plot in the bottom panel.

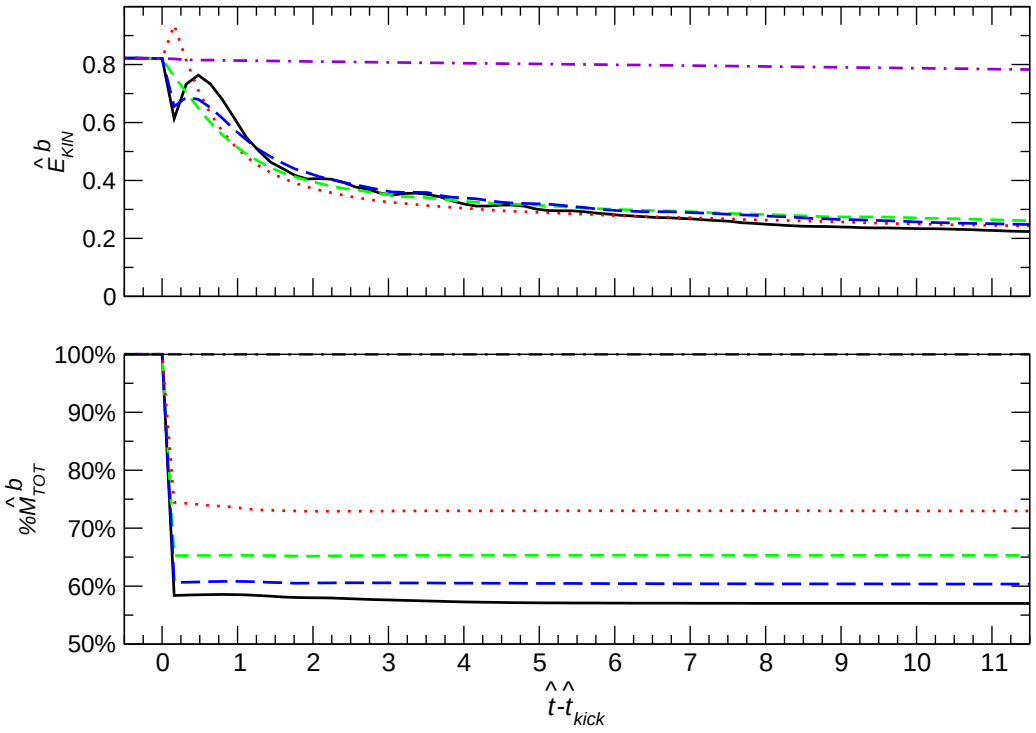

Figure 4.8: Evolution of the kinetic energy (top panel) and mass (bottom panel), relative to that of the initial disk, of the particles that remain bound to the SMBH. Conventions are as in Fig. 4.7, and the binding energy prescription is given by Eq.(IV-35).

particularly sensitive to the angle subtended by the bound region of the disk (See Fig. 4.1) at radii corresponding to the maximum surface density. Note that our definition of binding is the criterion

$$E_{\rm POT,i} + E_{\rm KIN,i} + E_{\rm INT,i} = m_i \left(\Phi_i + \frac{|v_i|^2}{2} + \frac{3A_i\rho_i^{2/3}}{2} \right) < 0, \qquad \text{(IV-35)}$$

since the internal energy of an SPH particle on an otherwise bound trajectory would eventually lead to adiabatic expansion and unbinding of the constituent gas. Disk heating does lead to some additional unbinding of material in most runs, ranging from no additional mass loss at all up to 1.5% of the total mass, most of which occurs shortly after the kick.

Shortly after the kick, at times $0 \leq \hat{t}_* \lesssim 1$, the net change in the disk's kinetic and potential energies is strongly dependent on the kick angle, as can be seen in Fig. 4.8. This is a purely geometric result that can be described in terms of our simple collisionless model (See Sec. 4.3): For a vertical kick, the entire mass of the disk is receding away from the BH immediately after the kick, and this remains nearly true for kicks near vertical. For more oblique kicks, where the bound component of the disk is drawn primarily from the part of the disk whose rotational velocity is aligned with the kick itself, a substantial part of the mass finds itself on orbits approaching the BH immediately after the kick before collisions and shocks begin to circularize the new orbits. Thus, for the oblique cases, we see an instantaneous decrease in the kinetic energy owing to the kick itself, followed by a rapid increase of larger magnitude as matter falls toward the BH. For more vertical cases, the effect is reversed, and we see an instantaneous jump in kinetic energy followed by a gradual turnaround and decrease. In both cases, the potential energy evolves accordingly, becoming more negative for the oblique cases relative to the vertical cases.

In Fig.4.9 we show the three "kinetic energy components" previously discussed for the collisionless disk (see Fig.4.5). To generate this figure, we rotated to the "bound projected coordinates" described below in Eq.(IV-36). For the tangential component, we actually kept track of the prograde and retrograde totals separately.

Fig.4.10 shows the mass and angular momentum (components and total angular momentum) of the bound portion of the disk as a function of the recoiling angle.

In Fig.4.11 both the angular momentum and the three "kinetic energy components" (as shown in Fig.4.9) are shown for the NO kick, 15, 30, 45, and 60 degrees kick.

The internal energy generated by kicks appears to increase non-linearly with kick angle: a larger recoiling angle generates more variation of the internal energy, with $\Delta E_{int}(\theta_k)$ being an increasing function. This is different from the behavior of the other energies. I did some preliminary experiments trying to fit some simple 1st, 2nd and 3rd order polynomials (Fig. 4.12). Interestingly the second order fittings look very nice with very interesting features and similar behaviors for in-plane kicks ($\theta_k = 90°$).

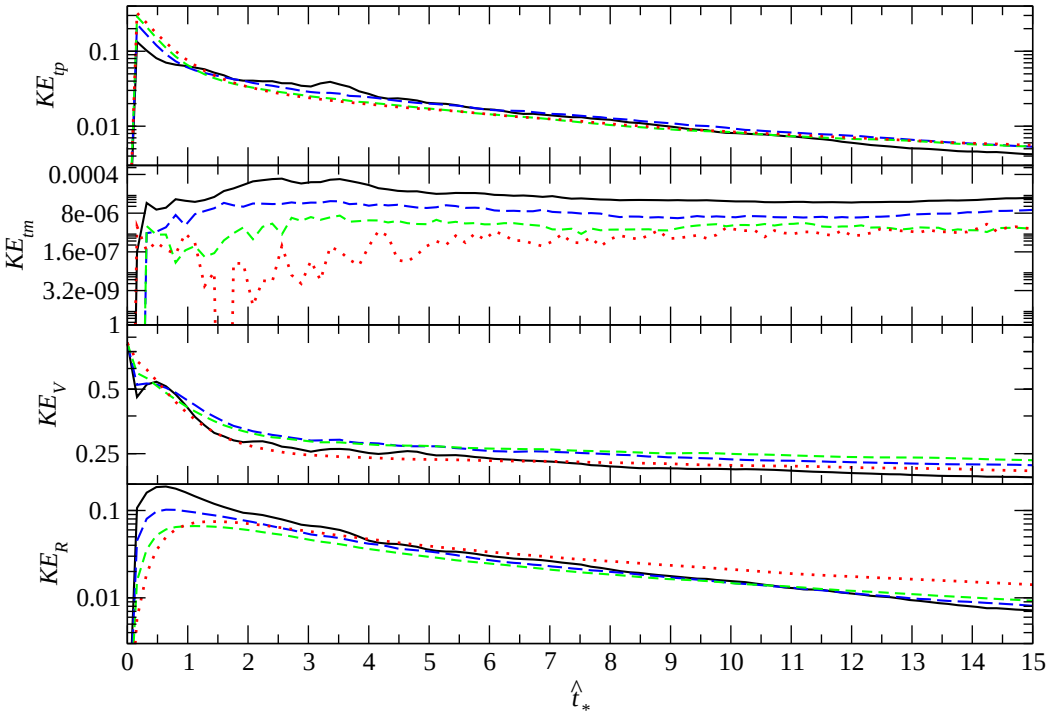

Figure 4.9: Evolution of the three "kinetic energy components". In the first panel (from top to bottom) we show the tangential prograde component, in the second panel the tangential retrograde component, in the third panel we show the vertical component, and in the fourth panel we show the radial component of the kinetic energy. The curves follow the conventions of Fig. 4.7.

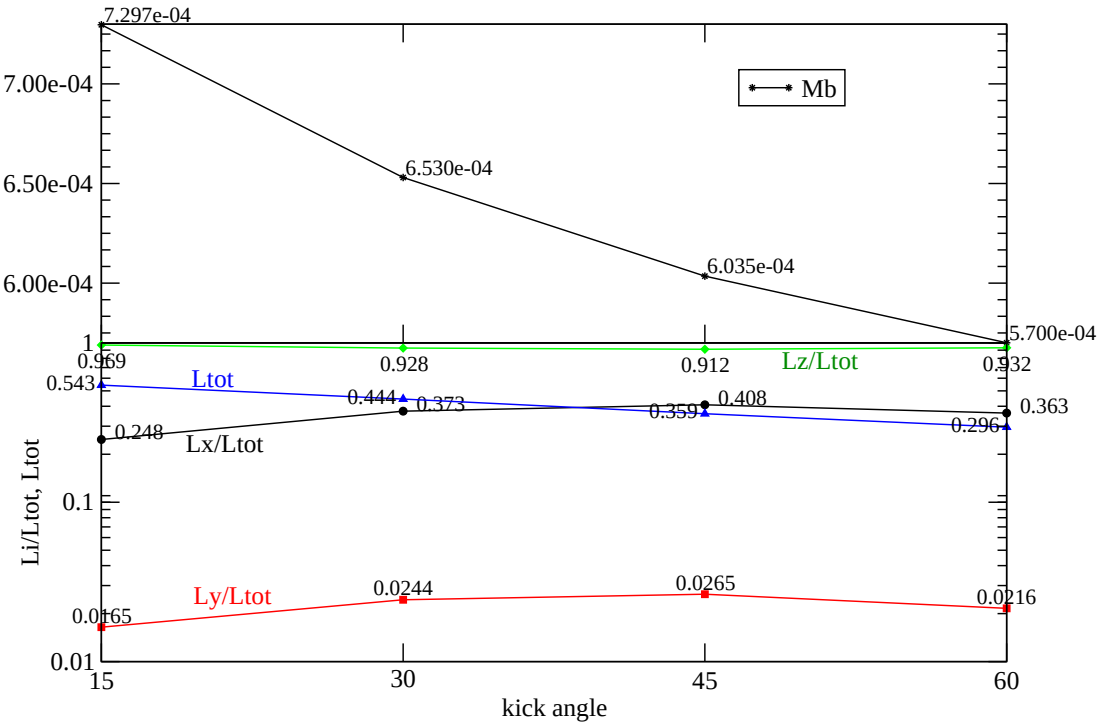

Figure 4.10: Bound angular momentum as a function of the recoiling angle. In the upper panel we show the bound mass, and in the lower we show the components of the angular momentum for the bound portion of the disk relative to the total angular momentum, as well as the total angular momentum of the bound portion of the disk.

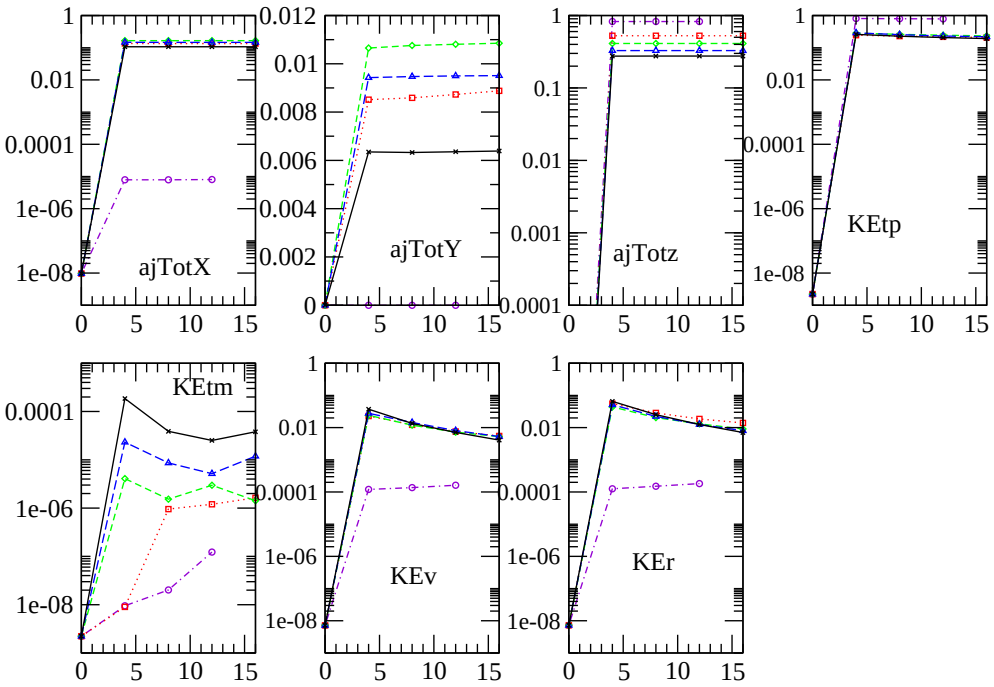

Figure 4.11: Evolution of the angular momentum and "kinetic energy components" for the NO kick, 15, 30, 45, and 60 degrees kick. The curves follow the conventions of Fig. 4.7.

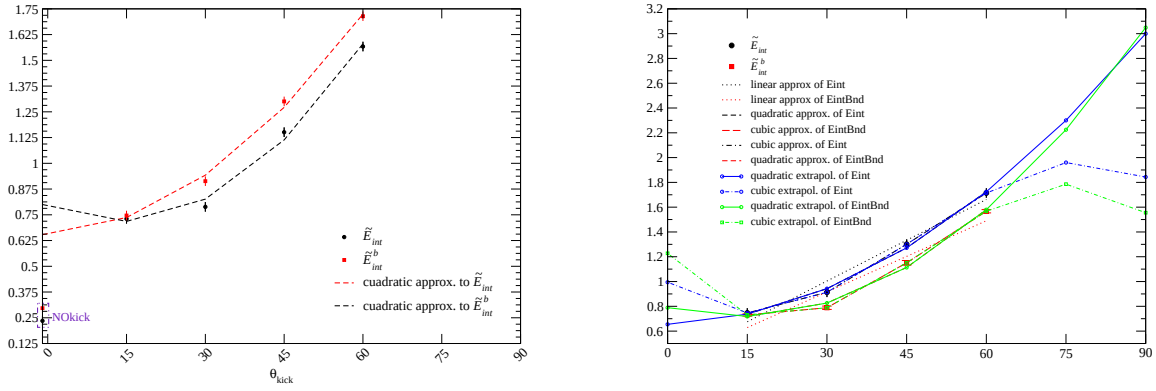

Figure 4.12: Internal Energy fitting using 1st, 2nd and 3rd order curves.

It is well-understood from previous calculations that the post-merger disk will be substantially tilted with respect to the initial equatorial plane, so we chose a simple prescription to define the post-kick disk plane. Considering only the bound particles, as defined by Eq.(IV-35), we calculate the angular momentum of the bound component of the disk with respect to the black hole, yielding the results shown in Table 4.1. Labeling this as the z-prime direction $\hat{z}'$, we define $\hat{x}'$ to be the original x-direction with the parallel projection of $\hat{z}'$ subtracted away, and the $\hat{y}'$-direction to be the cross product of the other two new coordinate directions:

$$\hat{z}' = \frac{\vec{L}_{bound}}{|\vec{L}_{bound}|}; \quad \hat{x}' = \frac{\hat{x} - (\hat{x}\cdot\hat{z}')\hat{z}'}{|\hat{x} - (\hat{x}\cdot\hat{z}')\hat{z}'|}; \quad \hat{y}' = \hat{z}'\times\hat{x}'. \tag{IV-36}$$

In all of the plots that follow, radii are assumed to represent cylindrical radii in the primed coordinate system.

To confirm the validity of the "gap-filling" model we discussed in Sec. 4.3, we show the SPH densities of the particles in the inner disk as a function of the cylindrical radius in Figs. 4.13 and 4.14. Turning first to the unkicked control model in the top panel of Fig.4.13, we see that there is relatively little density evolution except at the innermost edge of the disk, where viscous dissipation of angular momentum leads to an accretion of particles toward the SMBH. A density peak does form at the center, but with smaller densities than the kicked runs at any given radius $\hat{r} \lesssim 0.1$ during the duration of our simulations.

Considering the kicked runs next, we observe that the filling of the gap proceeds as predicted above. A wave of particles at relatively high densities ($\tilde{\rho} \sim 1 - 10$) is observed moving inward at $\hat{t}_* = 4$ for the two most oblique kick angles we considered, namely $\theta = 45°$ and $60°$, particularly the latter. No such densities profiles are ever found except in the immediate vicinity of the BH ($\hat{r} \lesssim 0.05$) for the more vertical kicks ($\theta = 15°$ and $30°$). Part of this effect is a simple matter of the larger post-kick periastron radii in the more vertical cases (see Fig. 4.3). Also, since the entire inner region of the disk remains bound in these cases, it forms an "inner ring" that will block any infalling matter from reaching radii $\hat{r} \lesssim 0.1 - 0.2$. For the more oblique cases, not only does some matter accrete promptly, but a gap is formed in the inner region corresponding to the initially retrograde portion of the disk (see Fig. 4.1) that

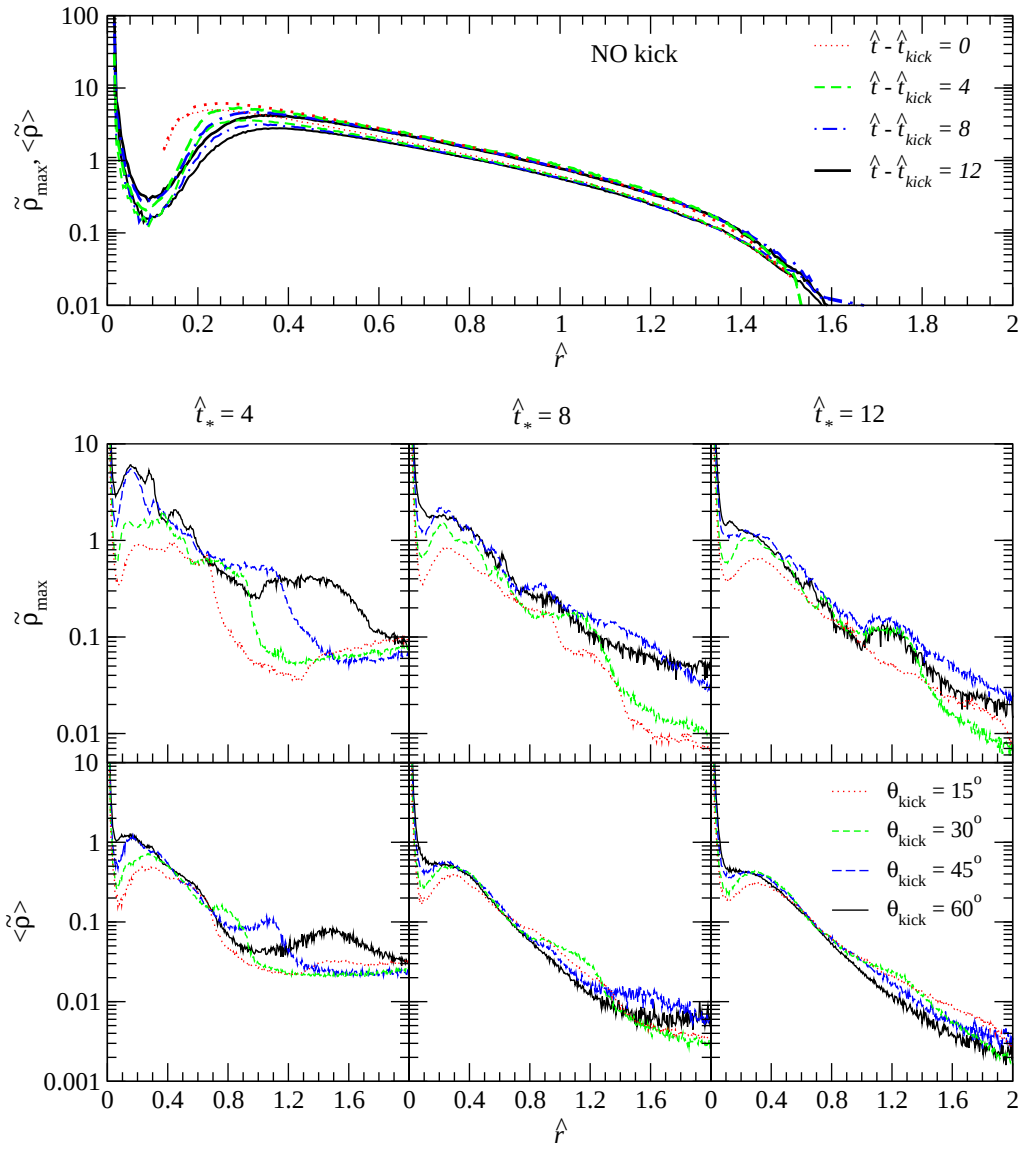

Figure 4.13: SPH particle-based density profile for the unkicked run (top panel), showing the maximum (thick lines) and average SPH densities (thin lines) for particles binned with respect to cylindrical radius at $\hat{t}_* = 0$ (red dotted lines), $\hat{t}_* = 4$ (green dashed lines), $\hat{t}_* = 8$ (blue dot-dashed lines), and $\hat{t}_* = 12$ (black solid lines) . Note that the $\hat{t}_* = 0$ configuration presents the common pre-kick state for all of our runs. There is a significantly very different density profile evolution in the kicked models (bottom panels). From left to right we show the evolution of our kicked models at $\hat{t}_* = 4$ (left), $\hat{t}_* = 8$ (center), and $\hat{t}_* = 12$ (right), with the maximum SPH density shown in the upper panels and the average SPH density in the lower panels. The curves follow the conventions of Fig. 4.7.

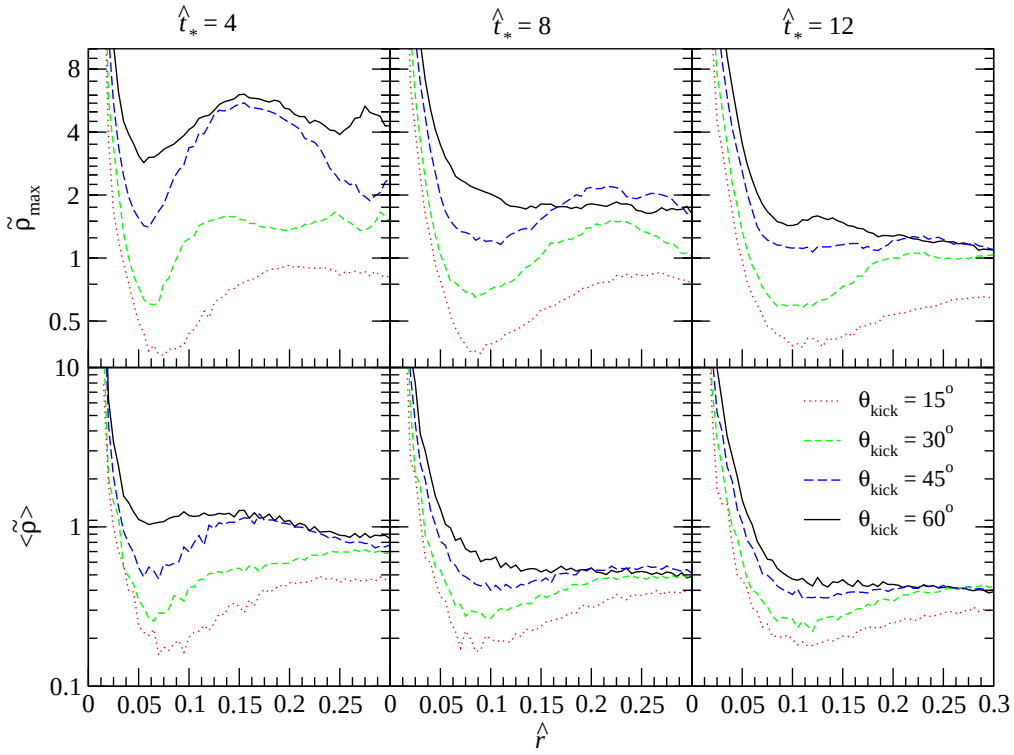

Figure 4.14: SPH particle-based densities for the innermost part of the accretion disks. All conventions follow those in Fig. 4.7 and the bottom panel of Fig. 4.13.

allows material to be channeled more easily toward radii $\hat{r} \lesssim 0.1$. This resulting density enhancement surrounding the BH is quite persistent; at $\hat{t}_* = 12$, which represents several orbital timescales for the innermost edge of the disk, there is a factor of five difference in the density at $\hat{r} \leq 0.1$ between the 60° and 15° runs. We note that there is some "crystallization" and pattern formation of the particles located closest to the BH, which is inevitable when a small number of SPH particles are located near the edge of a density distribution, but that we still are able to resolve a smooth density field there.

For the most oblique model, there is a clear oscillation in the maximum density at early times, which is highlighted in Fig. 4.14, showing the densities for the innermost region of the accretion disk. These features are an indication of the spiral density waves present in the disk and leave a clear imprint on the resulting thermodynamic evolution and emission properties we predict, as we discuss in more detail below. The general behavior of these density pulses, which move inward with time, is to increase the central density of the disk, as we can see by the closing of the gap between the densities for the 45° and 60° runs between $\hat{t}_* = 8$ and $\hat{t}_* = 12$. For the more vertically kicked runs, where spiral waves are much weaker, there is very little sign of rapid accretion of material to the center.

In setting up the runs shown here, it became evident that the BH softening potential we apply, Eq.(IV-19), can play an important role in suppressing spurious energy fluctuations. Indeed, when we ran simulations without introducing a BH softening potential, we found that the innermost particles around the BH would clump together, similarly to the so-called pairing instability of SPH [358] but with more than two particles per clump. These clumps would form quasi-stationary "bubbles," where mutual pressure interactions kept any particle from approaching within about a smoothing length of the black hole. This result was robust against several different choices of the SPH smoothing kernel definition and evolution schemes for the smoothing length in time. When outside interactions were finally able to "pop" the bubble, and other particles were able to flow inward to smaller radii, the measured kinetic and potential energies were seen to jump by substantial amounts due to the potential energy gains of a handful of particles even though the total energy remained flat.

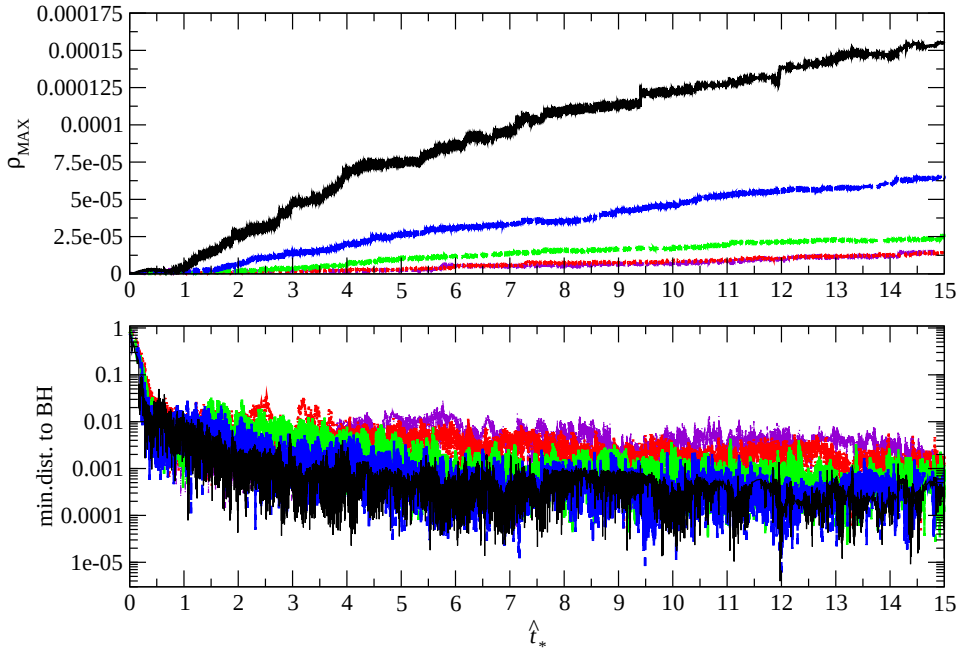

Figure 4.15: Maximum density and minimal distance (in log-scale) to the BH as a function of time for each simulation. The plot shows no kick, 15, 30, 45 and 60 degrees kick with same labels as previous figures. The color of the plots follows the convention of Fig.4.7.

For a slightly different view of the accretion disks, we show the azimuthally averaged radial surface density profiles $\tilde{\Sigma}(\hat{r})$ in Fig. 4.16. We see that the surface densities are markedly different in the inner region, with the oblique kicks leading to persistently higher surface densities by at least a factor of five compared to more vertical kicks for $\hat{r} \lesssim 0.2$ throughout the course of the simulation. In the outer regions of the bound disk, the surface density trend is reversed but much less dramatic: the more vertical kicks have slightly larger surface densities at a given radius than the oblique kicks, but the variation is never more than a factor of two once the disk begins to relax again at $\hat{t}_* \gtrsim 4$. The ratio of the initial surface density to the postkick surface density is relatively constant over a wide range of radii, from $0.4 \lesssim \hat{r} \lesssim 1.5$, but the postkick disk extends much further, since the same angular momentum exchange processes that funnel matter toward the BH at the inner edge of the disk also help to circularize it to larger radii at the outer edge of the bound region.

Our results also allow us to make some rough conclusions about the opacities of our disks, though we note we do not include any radiation transport effects nor radiative cooling in our simulations. Because the disks are hot and diffuse throughout, we expect the Thomson opacity for an ionized plasma to be a reasonable approximation. Whether or not the disk is optically thick ($\tau >> 1$) depends not only on the surface density but also on the values of the disk mass $m_{\rm disk}$, the BH mass $M_{\rm BH}$, and the kick velocity $v_{\rm kick}$ (see Eq.(IV-3)). For our reference model ($m_{\rm disk} = 10^4 M_\odot$, $M_{\rm BH} = 10^8 M_\odot$, and $v_{\rm kick} = 10^8$cm/s), the optical depth is slightly larger than unity throughout the pre-kick disk and slightly below throughout the post-kick disk, in which $\Sigma_{post}(r)/\Sigma_{pre}(r) \approx 0.2 - 0.4$ for most of the area of the disk, $0.4 \lesssim \hat{r} \lesssim 1.5$. If the initial disk had a substantially smaller surface density, our model would predict that the post-kick disk would remain so as well, except in the very central region near the BH. Meanwhile, an optically thick initial disk should produce a slightly less thick disk after the kick, extending outward to nearly the edge of the bound component.

While the azimuthal averages provide a clear picture of the global behavior of the disk, they do mask some of the more local phenomenon that develop after the kick. In Figs. 4.17 and 4.18 we show colormaps of the surface density at larger and smaller scales, respectively,

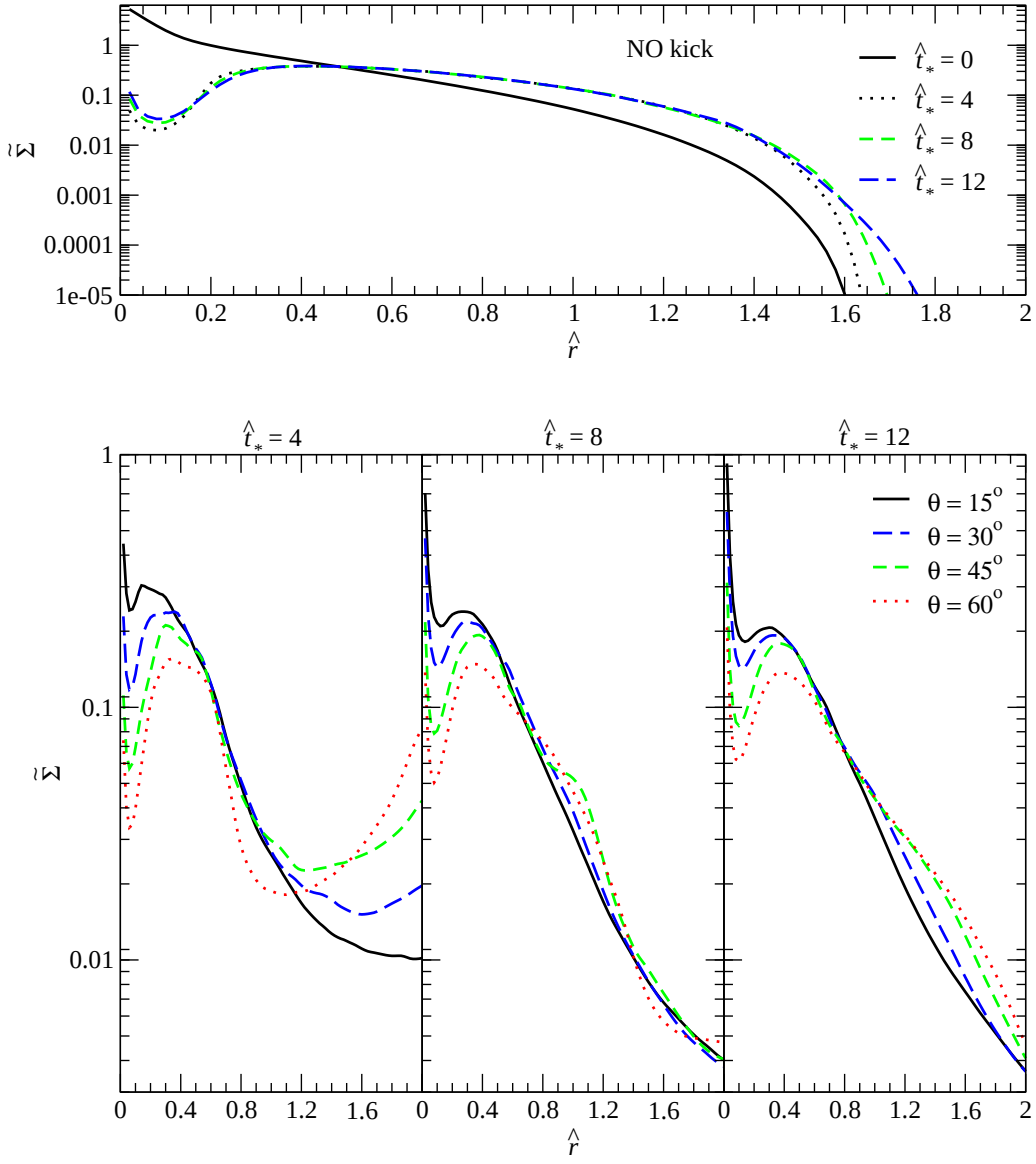

Figure 4.16: Radial profiles (averaged over azimuthal angle) of the surface densities (in log scale) for the initial disk model and the no-kick model (top panel) and for kick angles of 15, 30, 45 and 60 degrees; at $\hat{t}_* = 4, 8, 12$ (lower panels).

with different color mappings between the two to allow for maximum contrast. The large scale maps show the global expansion of the disk, though some care is required to interpret the results for the more oblique kicks. Most of the material that remains bound after the kick falls inward quickly to form the circularized inner disk extending out to $\hat{r} \lesssim 2.0$. The lower arc that appears clearly for the 45° and 60° on the left (smaller x'-values) of the inner disk (and more subtly so for the 30° case) represents the unbound upper portion of the original disk (see Fig. 4.1), with the density enhancements primarily a 2-dimensional projection effect. The material lies below (i.e., at lower z'-values) that the bound component of the disk, except for the marginally unbound material where the stream connects to the inner disk. The upper arc visible clearly in the more oblique cases represents the marginally bound component of the disk from the upper edge of the original disk. This stream of material initially moves way from the BH after the kick while remaining level vertically with the inner disk before accreting toward the inner disk following a roughly ballistic trajectory. When it collides with the inner disk, it shock heats and circularizes, with an accretion rate that decreases gradually over time. In each of our runs, the shock fronts are never particularly sharp, certainly less so than the adiabatic 2-d thin-disk calculations in [220], which are themselves much more spread out than isothermal calculations in which there is no shock heating. Instead, because we allow the gas to heat as it shocks, the spiral patterns rapidly blur, leading to more extended density enhancements. The non-axisymmetry is strongest during the early phases of the simulation, and gradually fades as the disks relax and collisions circularize the fluid, so that by $\hat{t}_* = 12$ we see only minor deviations from axisymmetry, particularly near the outer edge of the bound region where infalling matter is still playing a role.

In the smaller-scale surface density plots, Fig. 4.18, the role of the "gap" at $\hat{t}_* = 4$ is immediately apparent. For the 60° kick, the center of the disk has already filled in, though the surface density is strongly non-axisymmetric even at very small radii. Significantly more matter is located at small separations for the 45° kick simulation, but a hollow is clearly visible around the BH. For the more vertical kicks, the gap is clearly present and very little matter is evident to begin filling it. By $\hat{t}_* = 8$, this influx of matter leads to a very sharp increase

in the central density for the more oblique kicks that is not present in the more vertical ones. Finally, by $\hat{t}_* = 12$, the disk exhibits a much greater degree of axisymmetry, with only the most oblique kick case, in which the bound component of the disk is drawn almost entirely from one side of the pre-kick accretion disk (see Fig. 4.1), still retaining a marked angular dependence pattern.

In addition to the simulations and data analysis, we generated movies [4] for visualizing the effect of the kick on the disk. Snapshots from the movies of the projections in the coordinates planes, are displayed in Figs 4.19 and 4.20.

In the first panel of Fig. 4.21, we show the temperature evolution of the SPH particles for the unkicked run, finding that there is very little thermal evolution present, with only a slight degree of heating/cooling present in the disk, visible as a widening of the temperature histogram over time.

Turning to the approximate temperature profile of the disk, when considering the spatial distribution of the temperature profiles, there are some clear differences after $\hat{t} \approx 1.8$ time units. Interestingly these profiles changes mostly in their spatial distribution profile, apparently making the kicked disk hotter than the non-kicked disk. The shape difference has to occur, since one disk is kicked and the other not. The difference in the inner disks seems particularly critical for our results, because even though there is not a lot of particles, they contain a tremendous amount of energy.

Figs. 4.21, 4.22 and 4.23 show temperature histograms for the control unkicked model, and kick angles of 15°, 30°, 45° and 60°. The plots in Fig. 4.22 are arranged by kick angle, each with a sequence of 4-5 histograms for different times.

The temperatures evolution are quite different between the cases of NO-kick and kicks. For the NO-kick scenario the temperature peak does not change appreciably, and roughly keeps the same distribution slightly decreasing the number of particles at the temperature peak ($\approx 2\times10^4$ particles) and slightly increasing the tail of the distribution and higher temperatures. In the kick scenarios the distribution appears to be broken into two peaks: low temperatures with higher number of particles and high temperatures with lower number of particles. The peak in

[4]The movies are available at http://lanl.arxiv.org/abs/1107.1711 as ancillary files.

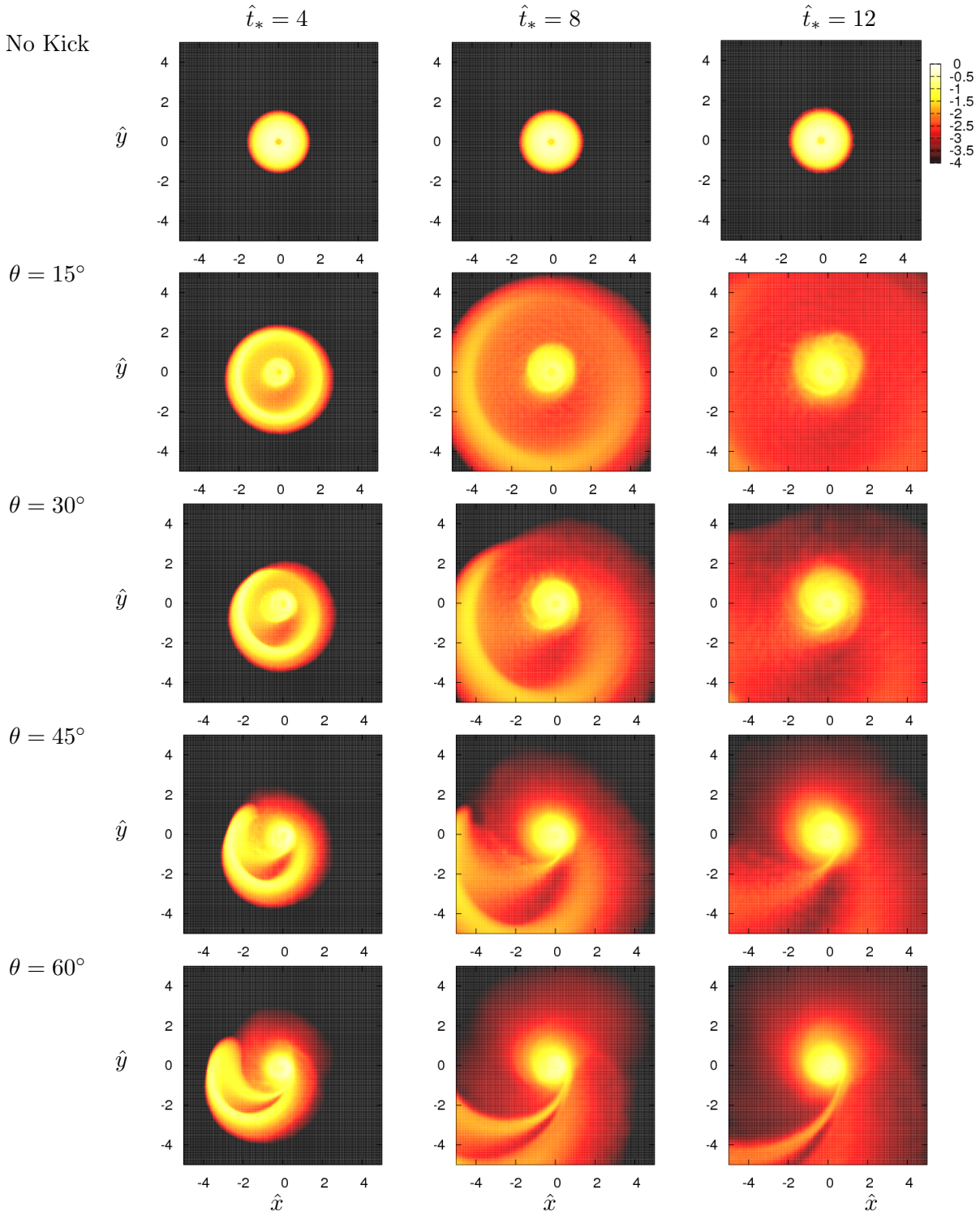

Figure 4.17: Projected surface densities (in log scale) for No-kick, and kick angles of 15, 30, 45 and 60 degrees (rows from top to bottom respectively); at $\hat{t}_* = 4, 8, 12$.

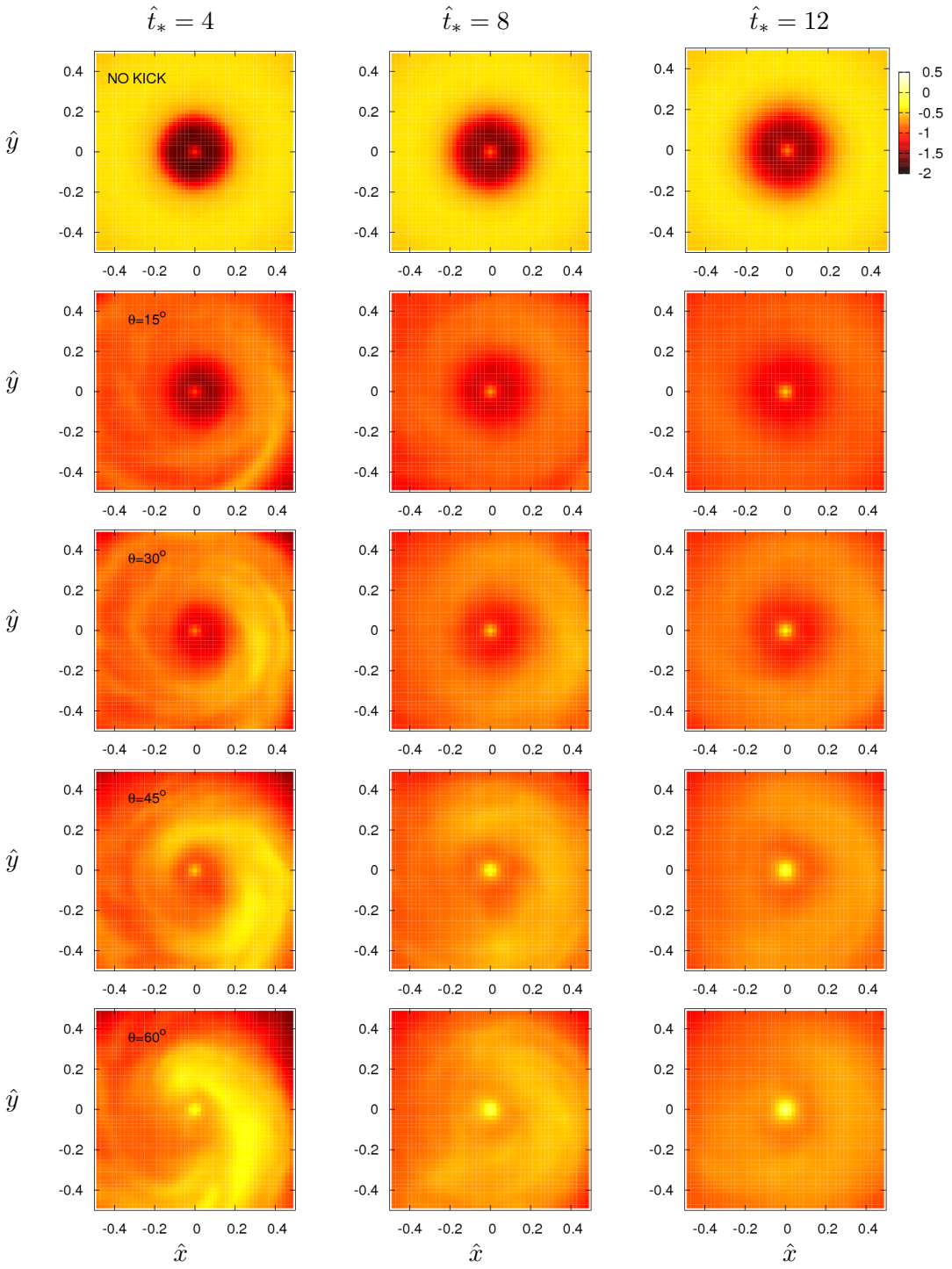

Figure 4.18: Projected surface densities (in log scale) for No-kick, and kick angles of 15, 30, 45 and 60 degrees (rows from top to bottom respectively); at $\hat{t}_* = 4, 8, 12$.

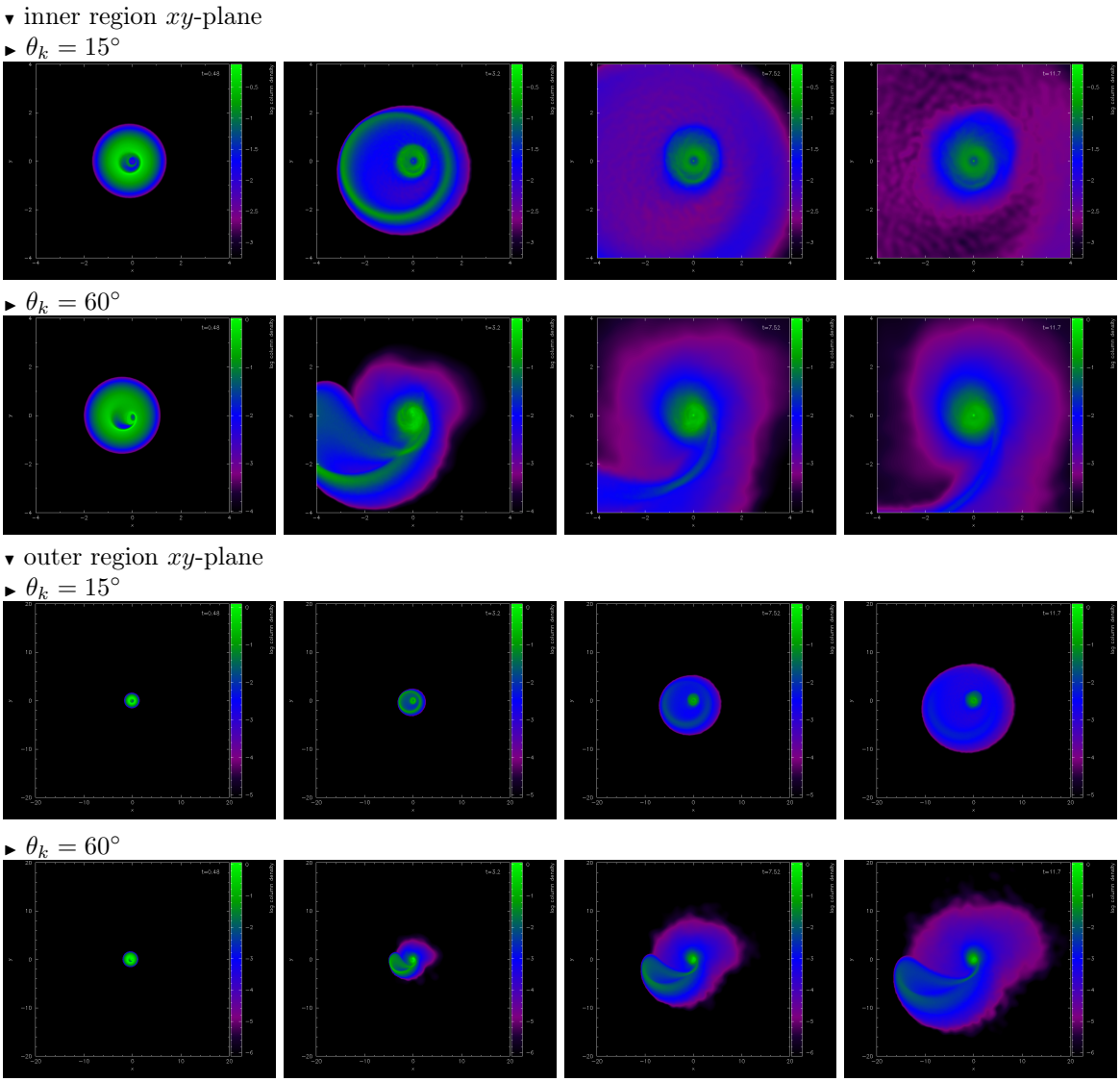

Figure 4.19: Density projections in the xy-plane, each column represents successive times $\hat{t}_* \approx 0.48, 3.2, 7.5, 11.7$. The first and third row show the projected densities for a kick angle of 15°. The second and fourth row show the projected densities for a kick angle of 60°.

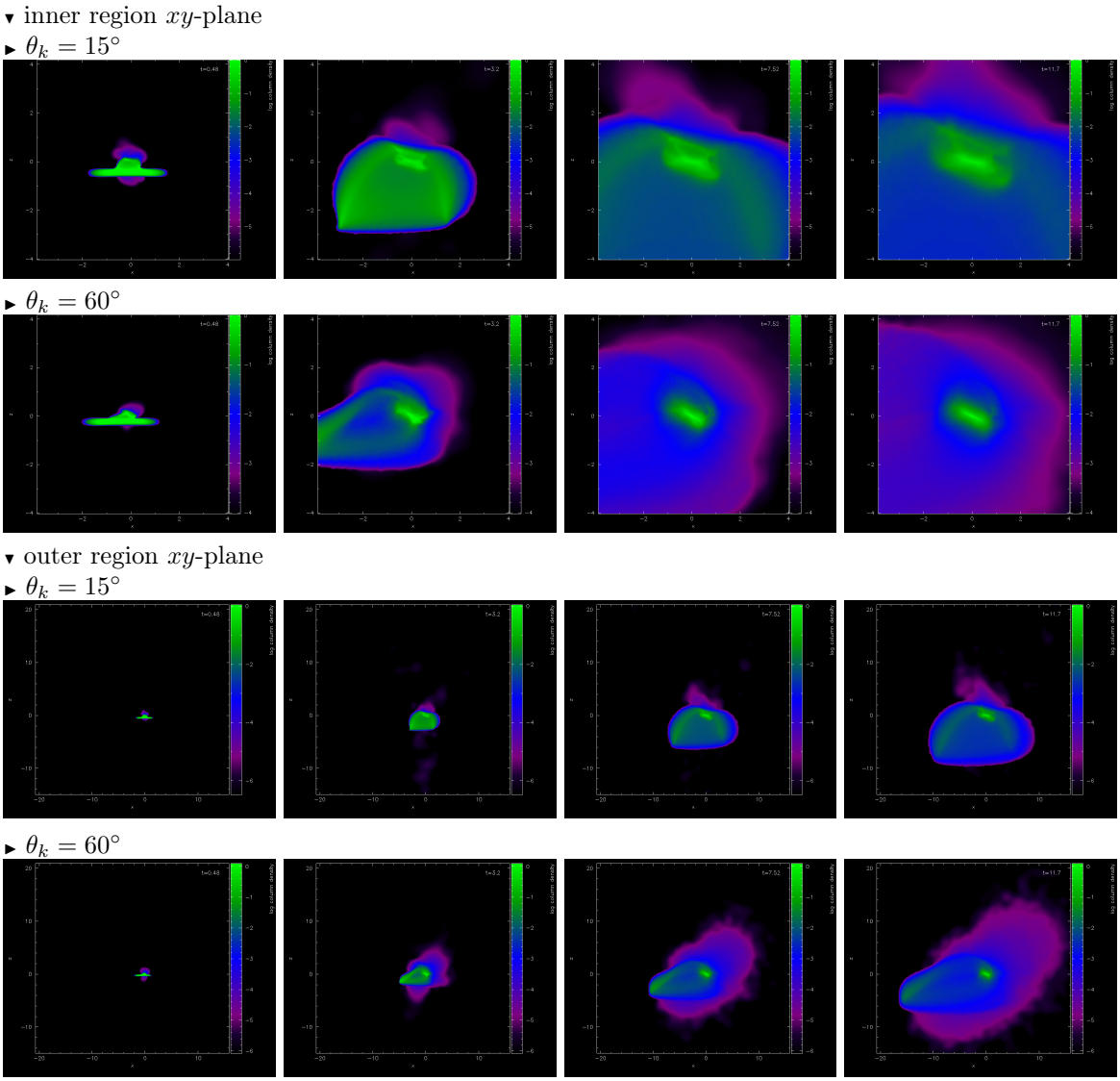

Figure 4.20: Density projections in the xz-place, each columns represents successive times $\hat{t}_* \approx 0.48, 3.2, 7.5, 11.7$. The first and third row show the projected densities for a kick angle of 15°. The second and fourth row show the projected densities for a kick angle of 60°. One of our main results shows apparently an interesting difference in the accretion dynamics according regarding the kick angle: more oblique recoiling kicks could destroy an inner 'gap' in the circumbinary disk reported and used in previous works in the field.

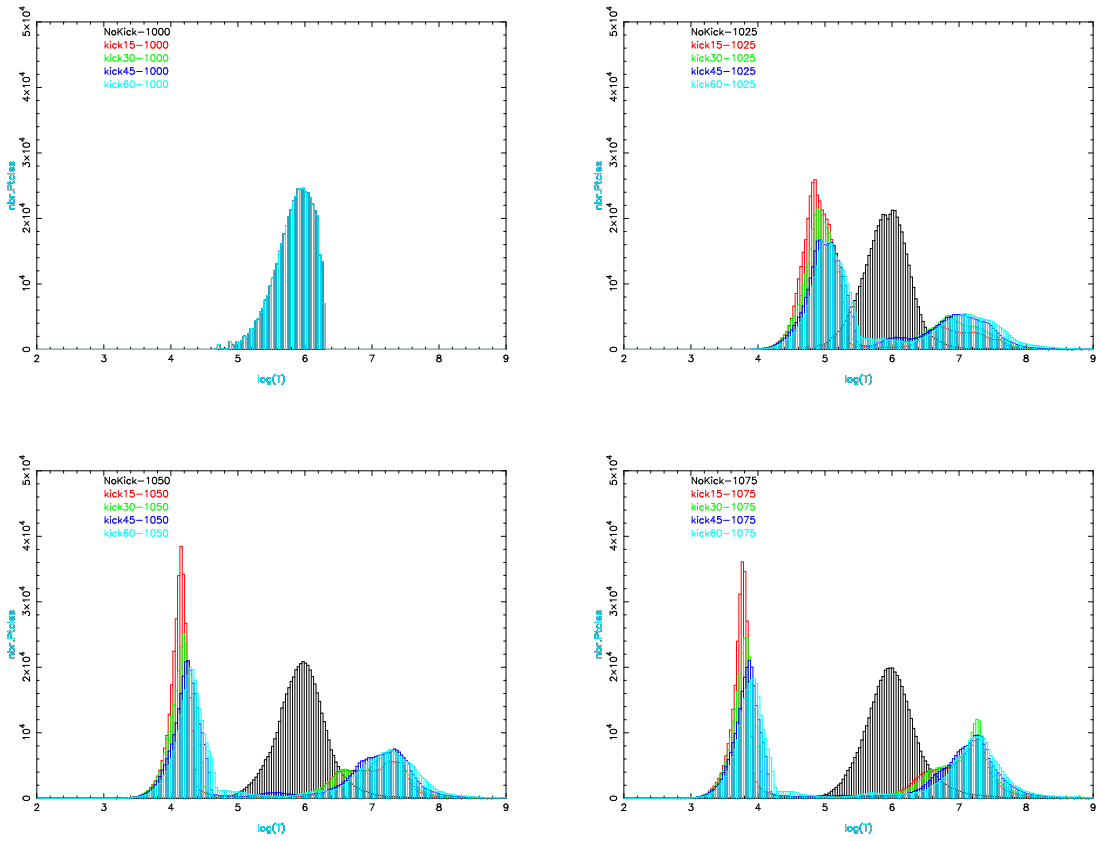

Figure 4.21: Temperature distributions (in log scale) for for $\hat{t}_* = 0$ (top left), 4 (top right), 8 (bottom left), and 12 (bottom right).

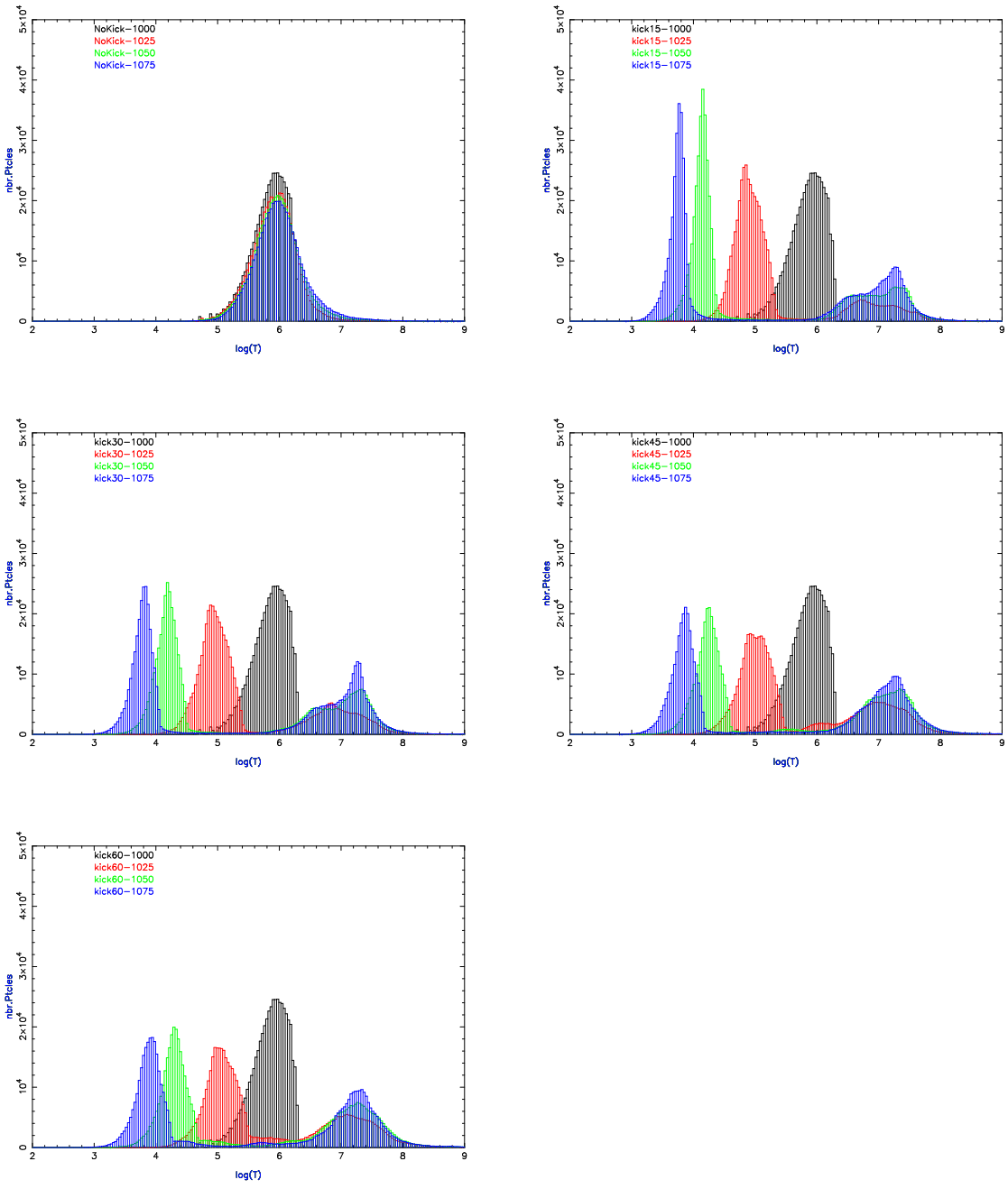

Figure 4.22: Evolution of the temperature distributions (in log scale) for: no-kick (top left), kick angle of 15° (top right), kick angle of 30° (middle left), kick angle of 45° (middle right), and kick angle of 60° (bottom).

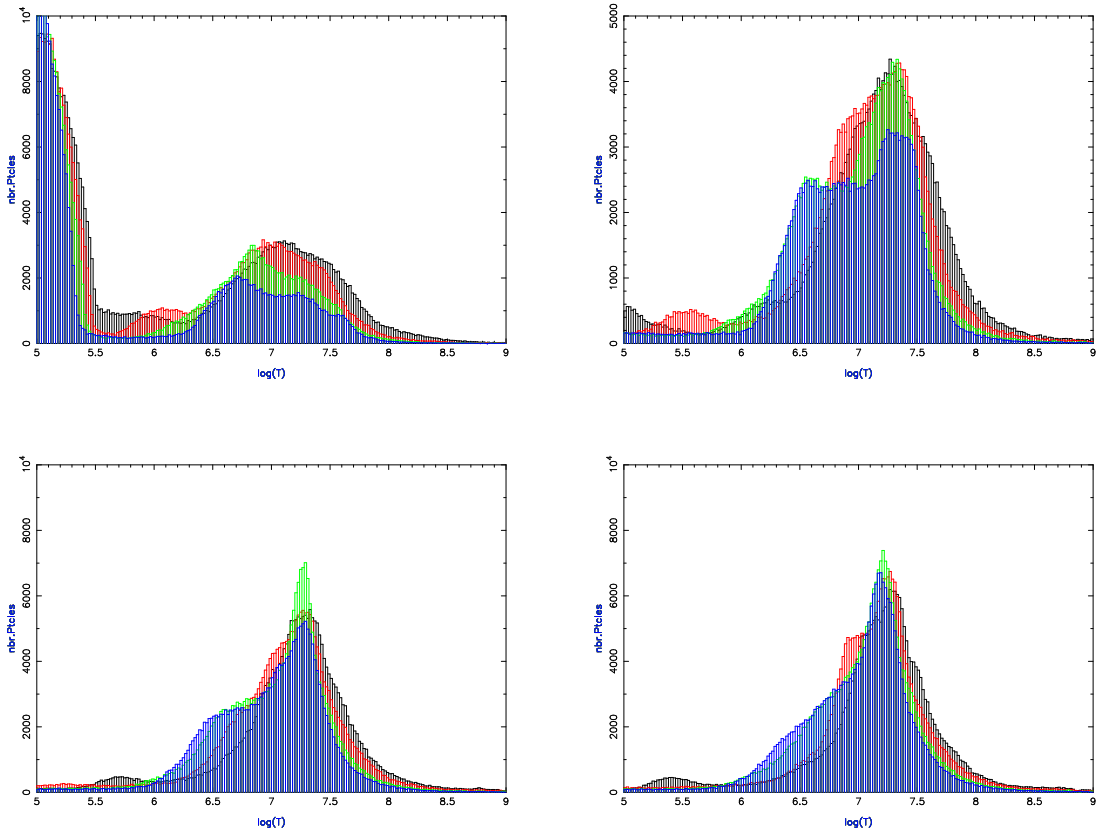

Figure 4.23: High Temperature peak distributions (in log scale) for $\hat{t} \approx 4, 8, 12, 16$ (from left to right and top to bottom). (Color online: black (60°), red (45°), green (30°), and blue (15°).)

the lower temperatures changes with time ($T(\hat{t} \sim t_{\rm kick}) = 10^6$ –pre-kick–), reducing its value as t increases. This peak presents a maximum of population of particles, around $\hat{t}_* \approx 7.2$, while the number of particles depends of the kick angle. However the values of the peak in the temperature is a function of time: $T(\hat{t}_* \sim -0.8) = 10^6$ –pre-kick–, $T(\hat{t}_* \approx 3.2) = 10^{4.9-5}$, $T(\hat{t}_* \sim 7.2, \text{max.pop.}) = 10^{4.1-4.3}$, $T(\hat{t}_* \sim 11.2) = 10^{3.8-4}$, $T(\hat{t}_* \sim 15.2) = 10^{3.4-3.6}$, and varies only slightly with kick angle. The range of values in the exponents are due to variations with the kick angle: smaller kick seems to lead to lower temperatures but higher populations (i.e. a larger number of particles). This population level (for the 'cold' peak) can reach 1.5-2 times higher levels for smaller kick angles ($\theta_k = 15°$, $\approx 3-4\times10^4$) than larger kick angles ($\theta_k = 60°$, $\approx 2 \times 10^4$). The peak on the high temperatures on the other hand, is quite stable in time ($T \sim 10^{7.1}$) although the population level is increasing with time, reaching larger numbers of particles at later times ($\sim 10^4$ approx. for all kick angles).

The "cold peak" is due to the unbound region as it adiabatically cools and therefore has no change in entropy. Since A_i remains fixed in the absence of shock heating, we find $T \sim P/\rho \sim A\rho^{2/3}$, and as the unbound region expands without shocking, the temperature decreases. This basically represents a proxy for the density. The hot peak is our bound region, and clearly shows that kicking the disk leaves a thermodynamic imprint in the gas.

In Fig. 4.23, the "hot peaks" ($T \sim 10^5 - 10^9$) are shown for the different kicked models at four different times ($\hat{t} \approx 4, 8, 12, 16$). There is a clear trend to accumulate larger numbers of particles for higher kick angles starting from early times. Although this tendency is weakened after $\hat{t} \approx 16$, when all distribution appear very similar for the high temperatures region (this is not true for the inner region of the disks at lower temperatures). Soon after the kick occurs ($\hat{t} \sim 4$, upper left panel in Fig. 4.23), a hot peak distribution formis which is very similar for all kicks angles. A short time later ($\hat{t} \sim 8$, upper right panel in Fig. 4.23), the models for $\theta_k = 15°$ and $30°$ show a similar feature around $T \sim 10^{6.5}$ with a local maximum of 2000 particles. On the other hand, all the models show a maximum around $T \sim 10^{7.25}$. Interestingly enough, these ranges of temperatures should produce X-rays in the energy range detectable by Chandra and XMM. For $\theta_k = 15°$, this maximum is smaller in population than for the

remaining cases: around 3200 particles; while for $\theta_k = 30°, 45°$, and $60°$, the population level is about 4400 particles. The local maxima at this early stages for $\theta_k = 15°$ and $30°$, will be smoothly redistributed with the rest of the particles, although a remnant of this early feature can be seen at later times. At later times ($\hat{t} \sim 8$, lower left panel in Fig. 4.23), an interesting feature for $\theta_k = 30°$ is still present showing the highest value in particle distribution (≈ 7000, at least a 1000 particles larger than the other cases) for the hot peak region of temperatures. For later times ($\hat{t} \sim 16$, lower right panel in Fig. 4.23), the peak for $\theta_k = 30°$ is still larger than the rest of the kicked models by a hundred particles. If our models are correct, this can represent an unique feature of the kicks at $30°$.

Turning to the thermal evolution of the disks, we see in the first panel of Fig. 4.24 the radially averaged thermal profile of our adiabatic initial model, for which $T \propto \rho^{2/3}$. We find substantial heating very quickly in the center of the disk, with strong shocking throughout the region $\hat{r} \lesssim 1$. The strong shock heating extends out through the majority of the bound component of the disk, except for the outermost regions, at early times. Indeed, the sudden dropoffs in the temperature profiles corresponding to the more vertical kicks ($15°$ and $30°$) at $\hat{t}_* = 4$ occur toward the outer part of the bound region of the disk, not the unbound part of the disk. This is in accordance with our previous discussion, as the outer reaches of the bound components for the more vertical kicks are initially sent outward in their orbits, and take longer to collide with other fluid streams and shock. Over time, the temperature profile smooths out, and by $\hat{t}_* = 12$ we have essentially a single temperature profile, peaked in the center and then falling off more slowly at larger radii, that characterizes all of our kicked disk simulations.

Based on the surface density and temperature profiles of our simulations (Figs. 4.16 and 4.24), it becomes clear that the differences in the global energies of the disks as a function of the kick angle are not the result of radically different temperature profiles, nor significantly different densities throughout the bulk of the disk, but rather from density differences in the innermost region of the disk. It is at small radii that all three energies take on their largest magnitudes, and the factor of $5 - 10$ difference in the surface densities at these radii

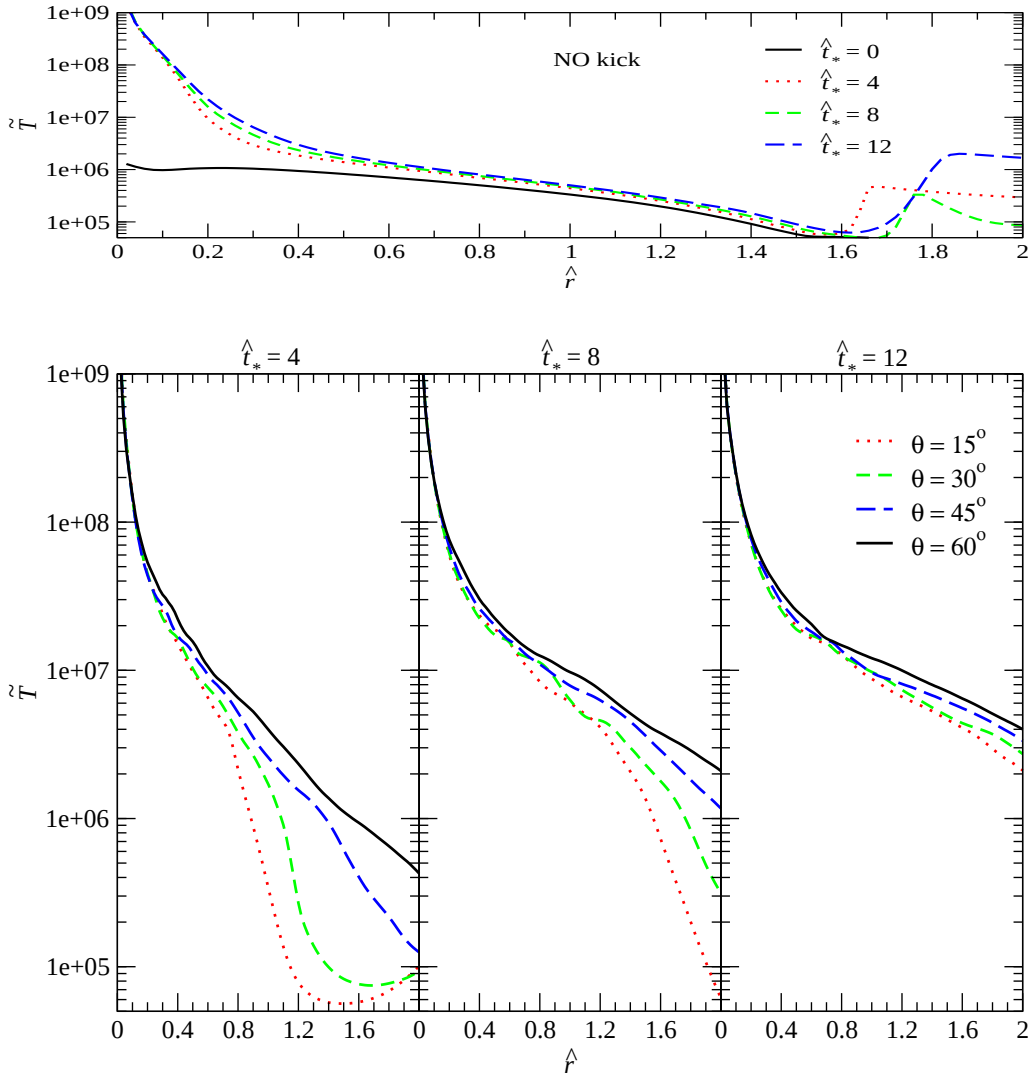

Figure 4.24: Radial profiles (averaged over azimuthal angle) of temperatures (in log scale) for the no-kick model (top panel), and kick angles of 15, 30, 45 and 60 degrees; at $\hat{t}_* = 0, 4, 8, 12$ (from left to right).

represent a significant fraction of the total energy, though not the total mass. Perhaps the clearest prediction from our simulations is that we expect oblique kicks to produce much more energetic signatures and substantially higher measured accretion rates for timescales of thousands of years for systems similar to our reference model and almost an order of magnitude larger for systems with kicks of roughly 500km/s.

If we estimate the luminosity of the disk by assuming that the internal energy gains would be immediately radiated away but not affect the dynamics in any other way (recall that our disks are allowed to shock heat without radiative cooling applied), we can convert the internal energy profiles from Fig. 4.7 into a luminosity by assuming that $\left(\frac{dE}{dt}\right)_{rad} = \frac{dE_{INT}}{dt}$. The results are shown in Fig. 4.25, where we differenced over intervals of 500 or 1000 timesteps to minimize spurious noise. In all cases, we see an immediate but purely numerical luminosity peak when we end relaxation and begin the dynamical evolution. For the unkicked disk, we see only a very small, nearly constant luminosity over time. For the more vertical kicks, we find a small rise in luminosity followed by a gradual decline, but with very little temporal structure. For the more oblique kicks, we see both significantly larger luminosities as well as quasiperiodic emission spikes, especially for the 60° case, in which there are persistent oscillation amplitudes of tens of percent with a period of slightly longer than $\hat{t} = 1$. Given the density patterns we observed, it seems clear that we are observing periodic shocking due to intersecting flows followed by accretion events as dense regions within the inner disk fall toward the BH while heating up significantly. The timescale roughly corresponds to the orbital timescale at the inner edge of the disk, with the strong $m = 1$ mode dependence of the fluid density (i.e., a single-arm spiral pattern) leading to increased shocking when the pattern wraps a full time around the BH.

We note that our angular convention is reversed from that of [246]; we refer to a vertical kick as $\theta = 0°$ and an in-plane kick as 90°, while they do the reverse. Thus, we find it interesting that while we see much more modulated emission produced in simulations with oblique kicks, they found substantial oscillations for the vertical kick, and essentially no oscillations at intermediate angles. Our luminosities also peak at larger times than their simulations indicated (see their Fig. 20). Among the possible explanations, it seems likeliest that the different

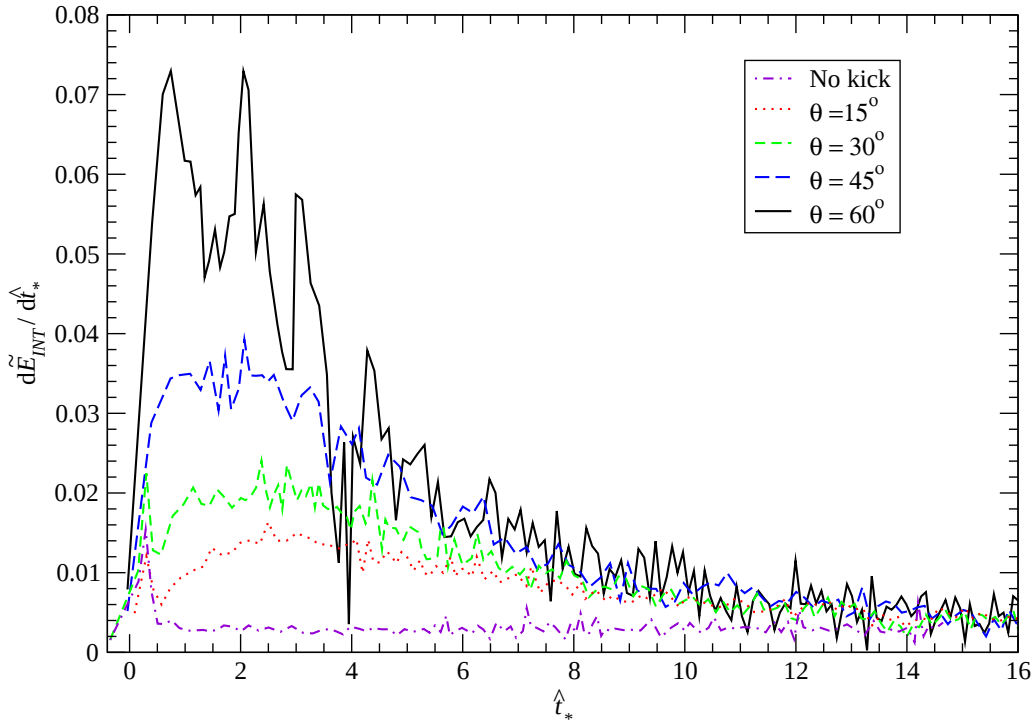

Figure 4.25: Potential disk luminosities from our disk models, calculated as the time derivative of the internal energy as shown in Fig. 4.7. To smooth the data and minimize SPH discretization noise, we difference over intervals of 500 (No kick, 15° and 30°) or 1000 timesteps (45° and 60°). Besides the expected increase on average luminosity as the kick becomes more oblique, we also see substantial oscillations in luminosity for the more oblique kicks, especially the 60° case.

initial disk configurations play a role, as we assumed an equilibrium model while theirs followed a power-law profile. The issue of adiabatic versus isothermal simulations also deserves mentioning, though spiral shocks are often stronger in isothermal models [220]. Finally, we note that SPH results can be very sensitive to how the BH is treated dynamically. We found a variety of spurious effects when we used an unsoftened BH potential, and it is possible that the respective implementations of the BH potential (theirs is unspecified) differ.

Although our initial disk model differs from that of [246], it still provides an opportunity to check our results alongside the "circularization" model proposed there, in which one calculates the approximate available energy for a fluid element within the disk by using its post-kick specific angular momentum l to infer a circularization radius $r_c = L^2/GM$ and energy $-GM/(2r_c)$, and subtracting this away from the fluid element's initial energy after the kick (see their Eqs. 6 – 10). Rather than construct the energy estimate by a surface integral over the disk, we compute it particle-by-particle from the common disk configuration present immediately before the kick. We also establish a minimum circularization radius $r_{min} = 2h_i$, representing the width of the particle's kernel function, since otherwise a handful of particles with extremely small angular momenta will dominate the overall predicted energy budget. Our results are shown in Table 4.2, where the columns list, respectively, the predicted "circularization energy" $\tilde{E}_c$, the actual internal energy $\tilde{E}_{\rm INT}$ at $\hat{t}_* = 12$, and the difference between the internal energy of a kicked model and our unkicked reference model $\tilde{E}_{{\rm INT};kick} \equiv \tilde{E}_{\rm INT} - \tilde{E}_{{\rm INT};nokick}$ at $\hat{t}_* = 12$, for each of the kicked runs. We see that while the overall values are relatively close, indicating that the circularization model yields a good approximation for the order of magnitude of the energy that could be emitted by the disk, this very simple model does not yield quantitatively accurate predictions with respect to the kick angle dependence. Thus, while the formula is certainly useful for establishing the approximate disk luminosity given a reasonable timescale for emission, we do not see strong evidence that it can be extrapolated to angles that lie very close to the disk plane, for which the predicted energy rises like a power law in the out-of-plane angle ($90^\circ - \theta_k$ in our notation) to extremely large values (see Figs. 4 and 21 of [246]).

Kick angle (°)	Circularization energy	Internal energy at $\hat{t}_* = 12$	Internal energy, corrected for kick
15	0.10	0.12	0.07
30	0.09	0.16	0.11
45	0.16	0.24	0.19
60	0.43	0.32	0.27

Table 4.2: Estimated energies available to the disk.

4.6 Discussion and future work

In this project, we studied the response of a quasi-equilibrium accretion disk around a SMBH that undergoes an impulsive kick, presumably because of a binary merger and the corresponding asymmetric emission of linear momentum in gravitational waves. While there are a number of sources that have been identified as candidate kicked disks with recoil velocities so large that they would be in the far tails of the kick velocity distribution, our results here are scale-free with regard to the kick, and may be applied to a broad swath of potential kicked systems. Indeed, while for our assumed reference model with $M_{\rm BH} = 10^8 M_\odot$, $m_{disk} = 10^4 M_\odot$, and $v_{\rm kick} = 1000$ km/s we find characteristic timescales of roughly 1000 years and disk luminosities and temperatures of up to 10^{42}erg/s and 10^{8-9}K, respectively, the results should work for a wide range of masses and kick velocities. There is a trade-off, to be had, of course, especially given the dependence of many of the quantities we investigate on the kick velocity. Indeed, cutting the kick velocity by half and leaving the masses of the BH and disk unchanged increases the timescales we consider by a factor of eight while cutting the energies and temperatures by a factor of four and thus the luminosities by 32, indicating that there should be a definite observational bias toward the larger kicks.

The code we introduce uses 3-dimensional SPH techniques, and is modified to incorporate a Lagrangian ("grad-h") prescription that allows energy to be conserved to high precision over the course of all our runs. We also introduce a Lagrangian-based black hole smoothing potential, which proves critical in allowing us to avoid numerical issues associated with point-like potentials. One of the most important purely numerical conclusions of this work is that black holes must be handled extremely carefully in SPH, since they can introduce particle

clustering instabilities that are both conservative but highly unphysical.

In order to examine the phase space of post-kick disks, we varied the kick angle of the SMBH with respect to the initial disk orientation, which has a large effect on the resulting evolution. More oblique kicks, i.e., those most oriented toward the equatorial plane of the original disk, produce substantially higher peak luminosities for a given BH and disk mass and kick velocity, with roughly a factor of four gain between kicks oriented 15° away from vertical and those oriented at 60° from vertical. Assuming an astrophysical context in which the disk is aligned with the SMBH binary orbit prior to merger [331], it is unlikely that more oblique kicks will actually yield more luminous events, however. Kick velocities are systematically higher for more vertical kicks [229], and given the v_{kick}^5 dependence of the luminosity, the brightest kicked disks are likely to be those with the highest speed kicks, with the kick angle playing a secondary role.

We find more rapid luminosity peaks appearing for more oblique kicks, which is the opposite result from a previous set of simulations that considered power-law density profile disks [246]. Based on our 60° calculation, we attribute this to the rapid filling of the innermost region of the disk by material kicked into high eccentricity orbits with extremely small periastron distances (see Figs. 4.2 and 4.3), which flows inward from the inner edge of the pre-merger disk; we note that this pattern differs from that found in Fig. 15 of [246], though we do not have a clear suggestion as to the nature of the discrepancy. Clearly, one of the important conclusions of this work and others is that flows of material toward the SMBH after the kick can release tremendous amounts of energy and potentially generate very high disk temperatures, but need to be modeled very carefully to derive reasonable light curves and spectra, pushing the limits of current numerical simulations. However, as discussed in Sec.4.5, the temperatures obtained imply luminous X-ray emission in Chandra and XMM range of sensitivity. Moreover, the luminosities and temperatures obtained in our simulations are in concordance with the Xray-inferred luminosities and temperatures for objects considered as "kick" candidates [359, 113, 360, 361].

The surface density oscillations and the resulting quasi-periodic emission we observe in

time for the most oblique kicks will make an interesting topic for further research. Based on our "gap-filling" model it seems clear the dynamics of the inner disk play an important role in the dynamical evolution and EM emission from the disk, and it would be highly useful to extend the same simulations on both sides of the kick to explore the full history of a circumbinary/post-kick disk. In particular, it will be important to accurately resolve the inner edge of the circumbinary disk, where the tidal field of the binary should have swept out a gap [226], and to understand how infalling material from that region interacts with the more tenuous tidal streams of matter in the process of accreting onto the SMBH prior to their merger [218, 219, 230]. It will also be useful to incorporate a more thorough treatment of the radiative evolution of the disk, since a proper treatment of radiative cooling and disk opacities will break the scale-invariance of the results and allow for much more accurate predictions of observable phenomena.

Chapter 5

Conclusions

5.1 Overview, Discussion & Further Extensions

In this thesis we study different elements of merging black-hole-binary spacetimes.

The research projects developed within this PhD thesis involve the fields of numerical relativity, theoretical modeling of astrophysics scenarios, and implementation of different computational techniques. The projects, codes, and techniques were devoted to Numerical Relativity, as well as classical formulations, although the final aim would be to extend and generalize these classical codes to General Relativity.

Furthermore, each of the projects within this thesis models different epochs during a BHB merger. In the first stage, where the BHs merge, we study how the individual EHs are distorted and a common EH emerges. At the same time gravitational radiation is emitted and in certain cases such emission may be asymmetric enough resulting in a gravitational recoil of the remnant BH (a 'kick'). Finally the accretion disk around the kicked remnant heats up, producing an electromagnetic signature that is potentially observable and diagnostic of the "kick".

The EH searches allow us to gain insights about the structure of the spacetime. In our project, we started by looking at a plausible scenario for finding toroidal slices of the event horizon, although we found that the most likely possibility is that there is a naked singularity, rather than a stable torus.

Studies like this, even when potentially abstract, are extremely useful for understanding the consequences of the theory of General Relativity, which is a geometrical theory, where topology is a key ingredient.

Remarkably the topology of $\mathcal{H} \cap \Sigma_t$ depends on the foliation of the spacetime, and such foliation can be distorted to obtain structure or even to change the genus of the intersected 3-dim surface in certain cases.

Another possibility would be to study a "rotating ring singularity", or in its discrete version a set of punctures (BHs) arranged over the ring, with a boost in the tangential direction. Such a configuration would have a ring singularity with angular momentum, like Kerr, but be manifestly non-Kerr and may yield interesting topological properties. Such a configuration would more closely match the configuration of [300], but with pure vacuum initial data rather than dust.

We found that in the numerical studies of EHs it would be interesting, for instance, to have ways to quantify the curvature on the EH itself, and which type of transition phase the EH undergoes when merging BHs (1st order, 2nd order, etc.). It may also be useful to find the Penrose diagram of the ring singularity.

It is remarkable that so far, any practical search for event horizons, one needs to perform two evolutions: a forward in time evolution (saving the full space time in a region large enough to contain the EH) and a subsequent backwards in time evolution to locate the EH. Although this is not really surprising because of the global nature of the EH. Here we used the final apparent horizon from the first evolution as an initial guess for the EH in the backwards evolution. Because the null generators diverge exponentially from the EH in a forward in time evolution, an initial guess close to the location of the true EH will exponentially converge to the EH in the backwards evolution.

This project was really exciting because it lies close to very interesting topics, such as cosmic censorship, naked singularities, topological structure of the spacetime, etc. Furthermore it deals with several technical challenges in computational techniques.

Moreover, very interesting results arriving from high energy physics and extensions and

generalizations of GR to higher dimensions, suggest that ring-type singularities may offer solutions with interesting features, such as critical self-similarity, instabilities similar to the instabilities apparent in the Navier-Stokes evolution of turbulent fluids [362], and in higher dimensions, more complicated singularity structures, such as bi-rings, black strings [307], etc.

A very interesting extension of this project, that will be useful for further studies of more dynamical and general situations, is to extend the event horizon searcher to work in simulations using adaptive mesh refinements (AMR) techniques. So far, the `EHFinder` thorn from the `Cactus/EinstenToolkit` infrastructure works only with unigrid (`PUGH` driver). Having a EH finder that allows one to locate the EH in an adaptive grid will enable EH searches in more technically challenging simulations (e.g. realistic BHB simulations).

A simple way to implement this would be to evolve the corresponding spacetime with AMR, and output the data on a grid that contains both BHs. Another method would be to interpolate to a uniform grid during evolution, and to output this uniform grid. This can be done by the thorn `CactusNumerical/InterpToArray` code. After the main simulation is finished, the remaining task is to read this grid array into the grid functions that are used by `EHFinder`.

Another possibility is to propagate geodesic backwards in time, although it has been argued that this method may not work in a stable fashion, recent results indicate that this method is, in fact, accurate [253].

For studying recoiling black holes in presence of an accretion disk, we implemented our own version of the Smooth Particle Hydrodynamic (SPH) techniques to evolve a 'kicked' black hole surrounded by an accretion disk [247]. We also perform analytical studies about the "wet recoil" scenario, beginning with a study of the physical scales that define the kicked disk problem. Additionally we use a semi-analytic, 2-dimensional collisionless disk model to explore the dynamics of disks acted upon by gravitational attraction between disk matter and the BH only.

Using our SPH code, 3-dimensional collisional simulations were performed varying the recoiling angle.

In order to deal with the effects from the strong gravitational potential of the black hole for nearby particles and guarantee an almost perfect energy and angular momentum conservation, we implemented a "smoothed black hole potential" to account for the finite size of the particles.

Our simulations, even though purely Newtonian, are valid descriptions of the dynamics for large enough length scales.

The different cases studied allow us to distinguish among properties correlated with the recoiling angles. Among the astrophysical interesting quantities computed are surface densities, luminosity (as the variation of the internal energy) and temperature profiles. We further discuss bounded/accreted material, and models for the optical properties of the disk (optical thin/thick), etc. Movies were also generated, showing the dynamical disk evolution.

To the best of our knowledge, thus far in the literature there is only one other work that tackles this kind of scenarios using these techniques [246] and we believe that the approach we used and the techniques we implemented are unique and will provide a unique perspective and insights into these situations. Two main results highlight this research: we found strong evidence correlating the kick angle and a depletion of matter ("gap") in the inner region, and we found strong tidal tails for more oblique recoils through the disk. We also found associated peaks in luminosity for certain recoiling angles, which could lead to interesting counterpart signatures and represent a potential way to identify observational clues from "kicked black holes".

It was only recently that we realized [363] that our model and the one studied by [246], are different, not only in the initial data, disk model studied, and thermodynamics evolution, but also in the evolution algorithm. Unlike in [246], we were able to resolve the inner part of the disk and the central region, by dealing with the central recoiled BH in such a way that we treated the BH like a Newtonian point particle for far away particles and with a smoothed potential for particles closer than a smoothing length. In this way our code is conservative and avoids spurious effects due to the finite size of the SPH-particles. In the SPH calculations of [246] the BH was a "sink particle" [364]. The potential was a simple $1/r$ law for $r > r_{acc}$, r_{acc} being a simulation parameter, that was set to be equal to the inner disc edge. This constitutes

a significant difference from our model, where we were actually able to resolve the inner regions close to the BH. While our results differ from the ones on [246], we believe that reason for this is that in [246] they do not resolve the central inner region of the disk. We have proposed and analyzed a plausible and reliable for the post-kick scenario. We were able to resolve the inner region, where most of the heating is coming from, resulting in the periodic luminosity for the larger kicks, without previous precedents in the literature.

Furthermore, because of the importance of these conclusions, we have being looking at convergence studies increasing the number of particles up to one million. Our preliminary results show that the periodicity in the peaks of the luminosity are robust and convergent; emphasizing the realistic aspects of these features.

The versatility and high accuracy, as well as the efficiency, of the SPH techniques offer the possibility to develop codes to model several interesting astrophysical scenarios.

Among the projects we expect to pursue are:

- a direct extension of the recoiled BH SPH code will be to apply it to other astrophysics scenarios, e.g. systems with multiple disks or multiple BHs with circumbinary disks;
- the implementation of a parallel hybrid CPU-GPU based SPH code that will allow for more efficient and accurate codes;
- a generalization of the SPH technique to include either Special Relativity and General Relativity (via a background metric).

Regarding the first possibility, given the remaining uncertainties in using theoretical models of SMBHs in dynamical configurations, such a code will be suitable to study a pair of models for which there is clear evidence of binary SMBH interactions. The clearest example of a SMBH binary surrounded by a circumbinary disk is NGC 6240, for which X-ray measurements indicate a binary nucleus with a separation of 1000pc [365, 366, 367], or even other examples of dual AGN [368, 369, 370]. These systems are clear indications of recent galaxy mergers, in which the SMBHs are now relatively close. While the observed separations are larger than what we plan to simulate, they are a clear indication that SMBHs definitely reach dynamically

interesting separations. Similarly, OJ287, the periodic blazar (described in Sec.1.5.2), indicates a SMBH binary separation of 0.06pc, if indeed the modulation observed in the object is caused by the secondary passing through the primary's disk. Clearly, these observational candidates could potentially place constraint on our modeling.

To study the evolution of circumbinary disks, we will construct relaxed models for accretion disks surrounding the binary, and determine how the binary eccentricity, mass ratio, and orientation affect the evolution of the disk and the mass transfer through the inner edge onto the binary itself, including a detailed estimate of the mass accretion rate toward each SMBH. We will incorporate radiative cooling into our evolutions in the optically thin limit, as well as relativistic corrections as matter falls toward the BHs.

Using our SPH code, we will study the property of circumbinary SMBH disks prior to merger, expanding the parameter space beyond that previously considered using hydrodynamical calculations [219, 230]. This will include simulating SMBH binaries that are *misaligned* with respect to the wider accretion disk, since it remains entirely undetermined whether or not accretion torques will be sufficient to align the inner binary with the angular momentum direction of the much larger disk. This should have important effects on the inner regions of the disk, inducing warping or radial oscillations in the inner disk. These in turn should change the character of the accretion flows onto the inner binary, particularly if the SMBHs have different masses or an orbit with a non-trivial ellipticity.

Having already developed the basic technology for evolving recoiling BH in presence of accretion disks, we are now in the position of trying more complex scenarios such as the one present in the case of the OJ287 blazar. This SPH code will be implemented using a hybrid platform: hydrodynamical computations will be carried out using multiple CPUs and parallelization through MPI, while gravity interactions will be performed using GPUs (via `CuN-Body` library). The implementation of these variants, take the code to a higher level of accuracy and efficiency, enhancing its performance by speeding it up by 1 to 2 orders of magnitude.

Having an hybrid SPH code will allow us to study cases such as possible models for the

outburst of the stellar object V838 Monocerotis [371]. Actually, we have already set up several simulations modeling this case, with a SPH code that was implemented using such a hybrid platform.

Last but not least, another really interesting project is the development of a SPH code that will take into account relativistic effects. The first step, will be the implementation of Special Relativity equations for SPH evolution equations [372, 373, 374]. Additionally the implementation of post-Newtonian approximations in the code may result in interesting additional features and new effects that could play important roles. A final stage for this project, will be to include a "background metric" with the SPH technique [375]. The "background metric" could be provided from analytical models or other simulations, such as BHB mergers. This implementation of a "background metric" could lead to the closest "GR+SPH" code ever done. Even though a "GR+SPH" code would never be as precise and accurate as a full GRMHD code, it will be an excellent tool for comparison, and will be sufficiently reliable for certain scenarios depending on the scales in the problem.

Finally, it could be interesting for several astrophysical scenarios to include "viscosity" in the SPH techniques in order to take into account heating due to shear. Even though our SPH code already includes artificial viscosity, a "real" (physical) viscosity can be included into the SPH equations to consider related effects. Additionally cooling mechanisms and radiation transport are dynamically important and we want to implement them in our code.

Another byproduct of these studies would be to provide a more realistic scenario of a circumbinary disk around near merging binary black holes for more detailed magneto-hydrodynamic simulations in the realm of numerical relativity.

Last but not least, continuing with the stages of the merger scenario, we are in the process of developing several ongoing follow-up projects. As mentioned before, during a BHB merger the emission of gravitational waves makes these events the most "luminous" in the universe. One project we are interested in pursuing is an accuracy study of gravitational waveforms, where we are interested in locating, characterizing, and mitigating sources of errors in the waveform for a wide range of configurations. For example, we have found that using timesteps

near the CFL limits produce disproportionally large errors in the phase of the waveform due to mass loss in the early orbital stage. These errors drop dramatically if we simply halve the ratio $c = dt/h$. Among the parameters we are studying are: dissipation coefficient, order of finite differencing, finite differencing operator, and spatial and temporal resolution. In this project we are interested in locating and eliminating lower-order errors that only become apparent at high resolutions. Additionally we implemented a dynamical time coordinate transformation, in order to simulate an adaptive time refinement ("temporal FishEye" coordinate transformation). This allows us to modify the timesteps throughout the simulations, allowing for larger timesteps when the dynamics are slow, and smaller timesteps as the dynamics speed up near merger. The Gravitational Wave Accuracy study project is likely to be of importance for many reasons. It is crucial to generate highly accurate and precise waveforms in order to produce appropriate templates for detection pursues. Furthermore improving the efficiency also will help to enhance the gravitational wave templates and cover a wider region of parameter spaces. Our initial goal in this project has been expanded to include a multi-dimensional parameter space, that will allow to provide better and more concrete prescriptions. However, covering a larger multi-dimensional parameter space implies a huge factor in the timeline for this project. Some of the simulations need to run for 1 month or more due to the intensive resources needed.

Another experiment we have done, involves the simulation of axisymmetric perturbations on accretion disk around black holes. This project uses fully nonlinear GR for the spacetime and a fully relativistic hydrodynamical treatment of the gas. As a very simple model for understanding the weak interaction between gravitational waves and matter, we performed full GR-hydro simulations studying the effects of axisymmetric curvature perturbations (with arbitrary alignments with respect to the disk) on accretion disks around black holes. This model, represents a simple scenario to test some controversial ideas about electromagnetic counterparts from gravitational wave interaction with matter [40]. We were looking for possible effects on the accretion disk to see if the luminosity profile of the disk is effected by the perturbations. We would then try to invert the relation to see if we can find signals in the EM profile that are closely associated with particular forms of the perturbation. We began

by studying an axisymmetric pulse-type solution (Brill wave), which requires the usage of an elliptic solver. We modified an original implementation for generating the corresponding initial data for an axisymmetric solution in order to make it more efficient and compatible with current memory allocation schemes. We also implemented a "rotation" of this perturbation, which allows us to set up the symmetry axis of the disk and perturbation in such a way that there is an arbitrary angle between them.

Bibliography

[1] Tim Peterson Hans-Peter Bischof, Edward Dale. Spiegel - a visualization framework for large and small scale systems. *Proceedings of the 2006 International Conference of Modeling Simulation and Visualization Methods*, pages 199–205, 2006. (document), 1.6.1, 3.9

[2] C. W. Misner, K. S. Thorne, and J. A. Wheeler. *Gravitation*. W. H. Freeman, San Francisco, 1973. ISBN-10: 0716703440 | ISBN-13: 978-0716703440. 1.1, 1.2

[3] S. Weinberg. *Gravitation and Cosmology: Principles and Applications of the General Theory of Relativity*. John Wiley and Sons, New York, 1972. ISBN-10: 0471925675 | ISBN-13: 978-0471925675. 1.1

[4] R. M. Wald. *General Relativity*. The University of Chicago Press, Chicago, 1984. ISBN-10: 0226870332 | ISBN-13: 978-0226870335. 1.1

[5] S. M. Carroll. *An Introduction to General Relativity: Spacetime and Geometry*. Benjamin Cummings, San Francisco, 2003. ISBN-10: 0805387323 | ISBN-13: 978-0805387322. 1.1, 1.5.1.2, 2

[6] Steven Weinberg. The cosmological constant problem. *Rev. Mod. Phys.*, 61:1–23, 1989. 2

[7] Sean M. Carroll. The cosmological constant. *Living Reviews in Relativity*, 4(1), 2001. 2, 1.3

[8] Marco Spaans. A topological extension of general relativity. *Nuclear Physics B*, 492(1-2):526 – 542, 1997. 5

[9] M. Tegmark. Letter to the Editor: On the dimensionality of spacetime. *Classical and Quantum Gravity*, 14:L69–L75, April 1997. 6

[10] M. MacCallum C. Hoenselaers H. Stephani, D. Kramer and E. Herlt. *Exact Solutions to Einsteins Field Equations Second ed.* Cambridge University Press, 2003. ISBN-13: 9780521461368 | ISBN-10: 0521461367. 1.1.1

[11] B. Schutz. *A First Course in General Relativity.* Cambridge University Press, 1985. ISBN-10: 0521887054 | ISBN-13: 978-0521887052. 1.2

[12] A.P. Lightman. *Problem book in relativity and gravitation.* Princeton University Press, 1975. ISBN-10: 069108162X | ISBN-13: 978-0691081625. 1.2

[13] B. Abbott et al. LIGO: The Laser Interferometer Gravitational-Wave Observatory. *Rept. Prog. Phys.*, 72:076901, 2009. 1.2

[14] A. A. Abramovici, W. Althouse, R. P. Drever, Y. Gursel, S. Kawamura, F. Raab, D. Shoemaker, L. Sievers, R. Spero, K. S. Thorne, R. Vogt, R. Weiss, S. Whitcomb, and M. Zuker. Ligo: The laser interferometer gravitational-wave observatory. *Science*, 256:325–333, 1992. 1.2

[15] K. S. Thorne. Ligo, virgo, and the international network of laser–interferometer gravitational–wave detectors. In M. Sasaki, editor, *Proceedings of the Eighth Nishinomiya-Yukawa Symposium on Relativistic Cosmology*, Japan, 1994. Universal Academy Press. 1.2

[16] F. Acernese et al. The virgo status. *Class. Quant. Grav.*, 23:S635–S642, 2006. 1.2

[17] LIGO - http://www.ligo.org/. 1.2

[18] VIRGO - http://www.virgo.infn.it/. 1.2

[19] GEO600 - http://www.geo600.org/. 1.2

[20] J. Abadie et al. Search for gravitational waves from binary black hole inspiral, merger and ringdown. *Phys.Rev.*, D83:122005, 2011. 1.2

[21] B. Abbott et al. First joint search for gravitational-wave bursts in LIGO and GEO600 data. *Class.Quant.Grav.*, 25:245008, 2008. 1.2

[22] B. Abbott et al. Coherent searches for periodic gravitational waves from unknown isolated sources and Scorpius X-1: Results from the second LIGO science run. *Phys.Rev.*, D76:082001, 2007. 1.2

[23] B. Abbott, R. Abbott, R. Adhikari, A. Ageev, J. Agresti, P. Ajith, B. Allen, J. Allen, R. Amin, S. B. Anderson, and et al. Joint LIGO and TAMA300 search for gravitational waves from inspiralling neutron star binaries. *Phys.Rev.D*, 73(10):102002–+, May 2006. 1.2

[24] L. Baggio, M. Bignotto, M. Bonaldi, M. Cerdonio, M. De Rosa, P. Falferi, S. Fattori, P. Fortini, G. Giusfredi, M. Inguscio, and et al. A joint search for gravitational wave bursts with AURIGA and LIGO. *Classical and Quantum Gravity*, 25(9):095004–+, May 2008. 1.2

[25] J. M. Weisberg and J. H. Taylor. The Relativistic Binary Pulsar B1913+16: Thirty Years of Observations and Analysis. In F. A. Rasio & I. H. Stairs, editor, *Binary Radio Pulsars*, volume 328 of *Astronomical Society of the Pacific Conference Series*, pages 25–+, July 2005. 1.2

[26] J. H. Taylor, A. Wolszczan, T. Damour, and J. M. Weisberg. Experimental constraints on strong-field relativistic gravity. *Nature*, 355:132–136, January 1992. 1.2

[27] J. H. Taylor, L. A. Fowler, and P. M. McCulloch. Measurements of general relativistic effects in the binary pulsar PSR 1913+16. *Nature*, 277:437–440, February 1979. 1.2

[28] G. S. Bisnovatyi-Kogan. Binary and recycled pulsars: 30 years after observational discovery. *Phys. Usp.*, 49:53–61, 2006. 1.2

[29] Clifford M. Will. The confrontation between general relativity and experiment. *Living Rev. Rel.*, 9:3, 2005. 1.2

[30] Gilles Esposito-Farese. Binary pulsar tests of strong field gravity and gravitational radiation damping. pages 647–666, 2004. 1.2

[31] N. D. R. Bhat, M. Bailes, and J. P. W. Verbiest. Gravitational-radiation losses from the pulsar white-dwarf binary PSR J1141 6545. *Phys.Rev.D*, 77(12):124017–+, June 2008. 1.2

[32] J. M. Weisberg, J. H. Taylor, and L. A. Fowler. Gravitational waves from an orbiting pulsar. *Scientific American*, 245:74–82, October 1981. 1.2

[33] John G. Baker, Manuela Campanelli, Frans Pretorius, and Yosef Zlochower. Comparisons of binary black hole merger waveforms. *Class. Quant. Grav.*, 24:S25–S31, 2007. 1.2

[34] Manuela Campanelli et al. Advances in Simulations of Generic Black-Hole Binaries. *Class. Quant. Grav.*, 27:084034, 2010. 1.2

[35] Laura Cadonati, Shourov Chatterji, Sebastian Fischetti, Gianluca Guidi, Satyanarayan R.P. Mohapatra, et al. Un-modeled search for black hole binary systems in the NINJA project. *Class.Quant.Grav.*, 26:204005, 2009. 1.2

[36] Benjamin Aylott et al. Status of NINJA: the Numerical INJection Analysis project. *Class. Quant. Grav.*, 26:114008, 2009. 1.2

[37] Alexander Stroeer and Jordan Camp. Ninja data analysis with a detection pipeline based on the Hilbert-Huang Transform. *Class. Quant. Grav.*, 26:114012, 2009. 1.2

[38] Lucia Santamaria, Badri Krishnan, and John T. Whelan. Searching for numerically-simulated signals of black hole binaries with a phenomenological template family. *Class. Quant. Grav.*, 26:114010, 2009. 1.2

[39] Benjamin Aylott et al. Testing gravitational-wave searches with numerical relativity waveforms: Results from the first Numerical INJection Analysis (NINJA) project. *Class. Quant. Grav.*, 26:165008, 2009. 1.2

[40] B. Kocsis and A. Loeb. Brightening of an accretion disk due to viscous dissipation of gravitational waves during the coalescence of supermassive black holes. *Physical Review Letters*, 101(4):041101–+, July 2008. 1.2, 21, 5.1

[41] V. Springel, S. D. M. White, A. Jenkins, C. S. Frenk, N. Yoshida, L. Gao, J. Navarro, R. Thacker, D. Croton, J. Helly, J. A. Peacock, S. Cole, P. Thomas, H. Couchman, A. Evrard, J. Colberg, and F. Pearce. Simulations of the formation, evolution and clustering of galaxies and quasars. *Nature*, 435:629–636, June 2005. 1.3

[42] M. Boylan-Kolchin, V. Springel, S. D. M. White, A. Jenkins, and G. Lemson. Resolving cosmic structure formation with the Millennium-II Simulation. *MNRAS*, 398:1150–1164, September 2009. 1.3

[43] Martin Goliath and George F. R. Ellis. Homogeneous cosmologies with cosmological constant. *Phys. Rev.*, D60:023502, 1999. 1.3

[44] Charles W. Misner. The Isotropy of the universe. *Astrophys. J.*, 151:431–457, 1968. 1.3

[45] C. B. Collins and S. W. Hawking. Why is the Universe isotropic? *Astrophys. J.*, 180:317–334, 1973. 1.3

[46] J. Kristian and R. K. Sachs. Observations in cosmology. *Astrophys. J.*, 143:379–399, 1966. 1.3

[47] G. Lemaitre. The expanding universe. *Gen. Rel. Grav.*, 29:641–680, 1997. 1.3

[48] H. P. Robertson. Relativistic Cosmology. *Rev. Mod. Phys.*, 5:62–90, 1933. 1.3

[49] G. F. R. Ellis. Topology and cosmology. *Gen. Rel. Grav.*, 2:7–21, 1971. 1.3

[50] J. M. Stewart. Perturbations of Friedmann-Robertson-Walker cosmological models. *Class. Quant. Grav.*, 7:1169–1180, 1990. 1.3

[51] G. F. R. Ellis and H. van Elst. Cosmological Models (Cargèse lectures 1998). In M. Lachièze-Rey, editor, *NATO ASIC Proc. 541: Theoretical and Observational Cosmology*, pages 1–116, 1999. 1.3

[52] David S. De Young. Astrophysical jets. *Science*, 252(5004):389–396, 1991. 1.3

[53] C. Palenzuela, L. Lehner, and S. L. Liebling. Dual Jets from Binary Black Holes. *Science*, 329:927–930, August 2010. 1.3, 1.5.2

[54] D. Neilsen, L. Lehner, C. Palenzuela, E. W. Hirschmann, S. L. Liebling, P. M. Motl, and T. Garrett. Boosting jet power in black hole spacetimes. *ArXiv e-prints*, December 2010. arXiv:astro-ph.HE/1012.5661. 1.3, 1.5.2

[55] R. Antonucci. Unified models for active galactic nuclei and quasars. *Annual Review of Astronomy and Astrophysics*, 31:473–521, 1993. 1.3

[56] C. M. Urry and P. Padovani. Unified Schemes for Radio-Loud Active Galactic Nuclei. *Publications of the Astronomical Society of the Pacific*, 107:803–+, September 1995. 1.3

[57] H. A. Bethe. Supernovae. *Physics Today*, 43:24–27, September 1990. 1.3

[58] C. L. Fryer. Mass Limits For Black Hole Formation. *Astrophys. J.*, 522:413–418, September 1999. 1.3

[59] S. Woosley and T. Janka. The physics of core-collapse supernovae. *Nature Physics*, 1:147–154, December 2005. 1.3

[60] A. Burrows, E. Livne, L. Dessart, C. D. Ott, and J. Murphy. A New Mechanism for Core-Collapse Supernova Explosions. *Astrophys. J.*, 640:878–890, April 2006. 1.3

[61] C. D Ott. Topical Review: The gravitational-wave signature of core-collapse supernovae. *Classical and Quantum Gravity*, 26(6):063001–+, March 2009. 1.3

[62] C. D. Ott, E. Schnetter, A. Burrows, E. Livne, E. O'Connor, and F. Löffler. Computational models of stellar collapse and core-collapse supernovae. *Journal of Physics Conference Series*, 180(1):012022–+, July 2009. 1.3

[63] E. O'Connor and C. D. Ott. Black Hole Formation in Failing Core-Collapse Supernovae. *Astrophys. J.*, 730:70–+, April 2011. 1.3

[64] M. J Hadley. Classical Dark Matter. *ArXiv General Relativity and Quantum Cosmology e-prints*, January 2007. arXiv:gr-qc/0701100. 1.3

[65] D. Clowe, M. Bradač, A. H. Gonzalez, M. Markevitch, S. W. Randall, C. Jones, and D. Zaritsky. A Direct Empirical Proof of the Existence of Dark Matter. *Astroph. J. Lett.*, 648:L109–L113, September 2006. 1.3

[66] G. Bertone and D. Merritt. Dark Matter Dynamics and Indirect Detection. *Modern Physics Letters A*, 20:1021–1036, 2005. 1.3

[67] G. Bertone, D. Hooper, and J. Silk. Particle dark matter: evidence, candidates and constraints. *Phys. Rept.*, 405:279–390, January 2005. 1.3

[68] L. V. E. Koopmans and T. Treu. The Structure and Dynamics of Luminous and Dark Matter in the Early-Type Lens Galaxy of 0047-281 at z = 0.485. *Astrophys. J.*, 583:606–615, February 2003. 1.3

[69] A. K. Drukier, K. Freese, and D. N. Spergel. Detecting cold dark-matter candidates. *Phys. Rev. D*, 33(12):3495–3508, Jun 1986. 1.3

[70] U. Seljak. Gravitational Lensing Effect on Cosmic Microwave Background Anisotropies: A Power Spectrum Approach. *Astrophys. J.*, 463:1–+, May 1996. 1.3

[71] G. Jungman, M. Kamionkowski, A. Kosowsky, and D. N. Spergel. Cosmological-parameter determination with microwave background maps. *Phys. Rev. D*, 54:1332–1344, July 1996. 1.3

[72] C. Carbone, C. Baccigalupi, M. Bartelmann, S. Matarrese, and V. Springel. Lensed CMB temperature and polarization maps from the Millennium Simulation. *MNRAS*, 396:668–679, June 2009. 1.3

[73] J. R. Brownstein and J. W. Moffat. The Bullet Cluster 1E0657-558 evidence shows modified gravity in the absence of dark matter. *MNRAS*, 382:29–47, November 2007. 1.3

[74] Jacob D. Bekenstein. Relativistic gravitation theory for the modified newtonian dynamics paradigm. *Phys. Rev. D*, 70(8):083509, Oct 2004. 9

[75] J. D. Bekenstein and R. H. Sanders. A Primer to Relativistic MOND Theory. In G. A. Mamon, F. Combes, C. Deffayet, & B. Fort, editor, *EAS Publications Series*, volume 20 of *EAS Publications Series*, pages 225–230, 2006. 9

[76] H. S. Zhao and B. Famaey. Refining the MOND Interpolating Function and TeVeS Lagrangian. *Astrophys. J. Lett.*, 638:L9–L12, February 2006. 9

[77] G. F. R. Ellis and A. R. King. Was the big bang a whimper? *Commun. Math. Phys.*, 38:119–156, 1974. 1.3

[78] Alan H. Guth. The Inflationary Universe: A Possible Solution to the Horizon and Flatness Problems. *Phys. Rev.*, D23:347–356, 1981. 1.3

[79] G. F. R. Ellis and William R. Stoeger, S. J. Horizons in Inflationary Universes. *Class. Quant. Grav.*, 5:207–220, 1988. 1.3

[80] A. K. Raychaudhuri and B. Modak. Cosmological Inflation with Arbitrary Initial Conditions. *Class. Quant. Grav.*, 5:225–232, 1988. 1.3

[81] N. Turok and P. J. Steinhardt. Beyond Inflation: A Cyclic Universe Scenario. *Physica Scripta Volume T*, 117:76–85, January 2005. 1.3

[82] P.J. Steinhardt and N. Turok. *Endless universe: beyond the Big Bang.* Doubleday, 2007. ISBN 9780385509640. 1.3

[83] F. Khan, A. Just, and D. Merritt. Efficient Merger of Binary Supermassive Black Holes in Merging Galaxies. *ArXiv e-prints*, March 2011. arXiv:astro-ph.CO/1103.0272. 1.3

[84] G. Lodato, S. Nayakshin, A. R. King, and J. E. Pringle. Black hole mergers: can gas discs solve the 'final parsec' problem? *MNRAS*, 398:1392–1402, September 2009. 1.3

[85] M. Milosavljević and D. Merritt. The Final Parsec Problem. In J. M. Centrella, editor, *The Astrophysics of Gravitational Wave Sources*, volume 686 of *American Institute of Physics Conference Series*, pages 201–210, October 2003. 1.3

[86] F. Herrmann, I. Hinder, D. Shoemaker, and P. Laguna. Binary black holes and recoil velocities. *AIP Conf. Proc.*, 873:89–93, 2006. 1.3.1

[87] F. Herrmann, D. Shoemaker, and P. Laguna. Unequal-mass binary black hole inspirals. *AIP Conf.*, 873:89–93, 2006. 1.3.1, 3.1

[88] John G. Baker et al. Getting a kick out of numerical relativity. *Astrophys. J.*, 653:L93–L96, 2006. 1.3.1, 3.1

[89] Jose A. González, Ulrich Sperhake, Bernd Brugmann, Mark Hannam, and Sascha Husa. Total recoil: the maximum kick from nonspinning black-hole binary inspiral. *Phys. Rev. Lett.*, 98:091101, 2007. 1.3.1, 3.1

[90] Frank Herrmann, Ian Hinder, Deirdre Shoemaker, Pablo Laguna, and Richard A. Matzner. Gravitational recoil from spinning binary black hole mergers. *Astrophys. J.*, 661:430–436, 2007. 1.3.1, 3.1, 4.1

[91] Manuela Campanelli, Carlos O. Lousto, Yosef Zlochower, and David Merritt. Large merger recoils and spin flips from generic black-hole binaries. *Astrophys. J.*, 659:L5–L8, 2007. 1.3.1, 1.5.2, 3.1, 4.1

[92] Manuela Campanelli, Carlos O. Lousto, Yosef Zlochower, and David Merritt. Maximum gravitational recoil. *Phys. Rev. Lett.*, 98:231102, 2007. 1.3.1, 3.1, 4.1

[93] Carlos O. Lousto and Yosef Zlochower. Modeling gravitational recoil from precessing highly- spinning unequal-mass black-hole binaries. *Phys. Rev. D*, 79:064018, 2009. 1.3.1, 3.1

[94] Denis Pollney et al. Recoil velocities from equal-mass binary black-hole mergers: a systematic investigation of spin-orbit aligned configurations. *Phys. Rev.*, D76:124002, 2007. 1.3.1, 3.1

[95] J. A. González, M. D. Hannam, U. Sperhake, B. Brugmann, and S. Husa. Supermassive kicks for spinning black holes. *Phys. Rev. Lett.*, 98:231101, 2007. 1.3.1, 3.1, 4.1

[96] Bernd Brugmann, Jose A. Gonzalez, Mark Hannam, Sascha Husa, and Ulrich Sperhake. Exploring black hole superkicks. *Phys. Rev.*, D77:124047, 2008. 1.3.1, 3.1

[97] Dae-Il Choi et al. Recoiling from a kick in the head-on collision of spinning black holes. *Phys. Rev.*, D76:104026, 2007. 1.3.1, 3.1

[98] John G. Baker et al. Modeling kicks from the merger of non-precessing black-hole binaries. *Astrophys. J.*, 668:1140–1144, 2007. 1.3.1, 3.1

[99] Jeremy D. Schnittman et al. Anatomy of the binary black hole recoil: A multipolar analysis. *Phys. Rev.*, D77:044031, 2008. 1.3.1, 3.1

[100] John G. Baker et al. Modeling kicks from the merger of generic black-hole binaries. *Astrophys. J.*, 682:L29, 2008. 1.3.1, 3.1

[101] James Healy et al. Superkicks in Hyperbolic Encounters of Binary Black Holes. *Phys. Rev. Lett.*, 102:041101, 2009. 1.3.1, 3.1

[102] Frank Herrmann, Ian Hinder, Deirdre Shoemaker, and Pablo Laguna. Unequal mass binary black hole plunges and gravitational recoil. *Class. Quant. Grav.*, 24:S33–S42, 2007. 1.3.1, 3.1

[103] Frank Herrmann, Ian Hinder, Deirdre M. Shoemaker, Pablo Laguna, and Richard A. Matzner. Binary Black Holes: Spin Dynamics and Gravitational Recoil. *Phys. Rev.*, D76:084032, 2007. 1.3.1, 3.1

[104] Wolfgang Tichy and Pedro Marronetti. Binary black hole mergers: Large kicks for generic spin orientations. *Phys. Rev.*, D76:061502, 2007. 1.3.1, 3.1

[105] Michael Koppitz et al. Getting a kick from equal-mass binary black hole mergers. *Phys. Rev. Lett.*, 99:041102, 2007. 1.3.1, 3.1, 4.1

[106] Sarah H. Miller and R. A. Matzner. Multipole Analysis of Kicks in Collision of Binary Black Holes. *Gen. Rel. Grav.*, 41:525–539, 2009. 1.3.1, 3.1

[107] C. O. Lousto and Y. Zlochower. Modeling maximum astrophysical gravitational recoil velocities. *Phys.Rev.D*, 83(2):024003–+, January 2011. 1.3.1

[108] Y. Zlochower, M. Campanelli, and C. O. Lousto. Modeling gravitational recoil from black-hole binaries using numerical relativity. *Classical and Quantum Gravity*, 28(11):114015–+, June 2011. 1.3.1

[109] Carlos O. Lousto, Manuela Campanelli, and Yosef Zlochower. Remnant Masses, Spins and Recoils from the Merger of Generic Black-Hole Binaries. *Class. Quant. Grav.*, 27:114006, 2010. 1.3.1, 1.5.2, 3.1

[110] Carlos O. Lousto and Yosef Zlochower. Hangup Kicks: Still Larger Recoils by Partial Spin/Orbit Alignment of Black-Hole Binaries. 2011. arXiv:gr-qc/1108.2009. 1.3.1, 4.1

[111] S. Komossa, H. Zhou, and H. Lu. A recoiling supermassive black hole in the quasar SDSSJ092712.65+294344.0? *Astrophys. J. Lett.*, 678:L81, 2008. 1.3.1, 1.5.2, 4.1

[112] G.A. Shields, E.W. Bonning, and S. Salviander. Comment on the Black Hole Recoil Candidate Quasar SDSS J092712.65+294344.0. *Astrophys.J.*, 696:1367–1373, 2009. 1.3.1, 1.5.2, 4.1

[113] G. A. Shields and E. W. Bonning. Powerful flares from recoiling black holes in quasars. *Astrophys. J.*, 682:758–766, August 2008. 1.3.1, 1.5.2, 4.1, 4.6

[114] G.A. Shields, D.J. Rosario, K.L. Smith, E.W. Bonning, S. Salviander, et al. The Quasar SDSS J105041.35+345631.3: Black Hole Recoil or Extreme Double-Peaked Emitter? *Astrophys.J.*, 707:936–941, 2009. 1.3.1, 1.5.2, 4.1

[115] F. Civano, M. Elvis, G. Lanzuisi, K. Jahnke, G. Zamorani, et al. A Runaway Black Hole in COSMOS: Gravitational Wave or Slingshot Recoil? *Astrophys.J.*, 717:209–222, 2010. 1.3.1, 1.5.2, 4.1

[116] Andrew Robinson, Stuart Young, David J. Axon, Preeti Kharb, and James E. Smith. Spectropolarimetric evidence for a kicked supermassive black hole in the Quasar E1821+643. *Astrophys. J. Lett.*, 717:L122, 2010. 1.3.1, 1.5.2, 4.1

[117] Mark J. Henriksen and Eric R. Tittley. Chandra observations of the A3266 galaxy cluster merger. *Astrophys.J.*, 577:701–709, 2002. 1.3.1, 1.5.2

[118] L.A. Nolan, T.J. Ponman, Andrew M. Read, and Francois Schweizer. XMM-Newton observations of the late-stage merger - remnant galaxies NGC 3921 and NGC 7252. *Mon.Not.Roy.Astron.Soc.*, 353:221, 2004. 1.3.1, 1.5.2

[119] B. C. Whitmore, R. Chandar, F. Schweizer, B. Rothberg, C. Leitherer, M. Rieke, G. Rieke, W. P. Blair, S. Mengel, and A. Alonso-Herrero. The Antennae Galaxies (NGC 4038/4039) Revisited: Advanced Camera for Surveys and NICMOS Observations of a Prototypical Merger. *Astroph.J.*, 140:75–109, July 2010. 1.3.1, 1.5.2

[120] Bradley C. Whitmore and Francois Schweizer. Hubble space telescope observations of young star clusters in NGC-4038/4039, 'the antennae' galaxies. *Astron.J.*, 109:960–980, 1995. 1.3.1, 1.5.2

[121] L. Blecha, T. J. Cox, A. Loeb, and L. Hernquist. Recoiling black holes in merging galaxies: relationship to active galactic nucleus lifetimes, starbursts and the M_{BH}-σ_* relation. *MNRAS*, 412:2154–2182, April 2011. 1.3.1

[122] L. Blecha, T. J. Cox, A. Loeb, and L. Hernquist. Recoiling Black Holes in Merging Galaxies: Relationship to AGN Lifetimes and Merger Remnant Properties. *ArXiv e-prints*, September 2011. 1.3.1

[123] S. L. Shapiro T. W. Baumgarte. *Numerical Relativity: Solving Einstein's Equations on the Computer*. Cambridge University Press, United Kingdom, Cambridge, 2010. ISBN-10: 052151407X; ISBN-13: 978-0521514071. 1.4, 2, 2.2.3, 2.5.1

[124] M. Alcubierre. *Introduction to 3+1 Numerical Relativity*. Oxford Science Publications, Great Britain, 2008. ISBN-10: 0199205671; ISBN-13: 978-0199205677. 1.4, 2, 2.2.3, 2.5.1

[125] C. Bona and C. Palenzuela-Luque. *Elements of numerical relativity: from Einstein's equations to Black Hole simulations*. Lecture notes in physics. Springer, 2005. ISBN 9783540257790. 1.4

[126] C.R. Evans, L.S. Finn, and D.W. Hobill. *Frontiers in numerical relativity*. Cambridge University Press, 1989. ISBN 9780521366663. 1.4

[127] J. M. Centrella. *Dynamical spacetimes and numerical relativity: proceedings of a workshop held at Drexel University, October 7-11, 1985*. Cambridge University Press, 1986. ISBN 9780521328609. 1.4

[128] R. Arnowitt, S. Deser, and C. W. Misner. The dynamics of general relativity. In L. Witten, editor, *Gravitation: An Introduction to Current Research*, pages 227–265. John Wiley, New York, 1962. 1.4, 2.2.5

[129] Susan G. Hahn and Richard W. Lindquist. The two-body problem in geometrodynamics. *Annals of Physics*, 29(2):304 – 331, 1964. 1.4

[130] A. Cadez. *Colliding Black Holes*. PhD thesis, The University of North Carolina at Chapel Hill, 1971. 1.4

[131] L. Smarr, A. Cadez, Bryce S. DeWitt, and K. Eppley. Collision of Two Black Holes: Theoretical Framework. *Phys.Rev.*, D14:2443–2452, 1976. 1.4

[132] Larry Smarr. Space-times generated by computers: Black holes with gravitational radiation. *Annals of the New York Academy of Sciences*, 302(1):569–604, 1977. 1.4

[133] L. L. Smarr. *The structure of general relativity with a numerical illustration: The collision of two black holes*. PhD thesis, Texas Univ., Austin., 1975. 1.4

[134] M. Alcubierre and B. Brügmann. Simple excision of a black hole in 3+1 numerical relativity. *Phys. Rev. D*, 63(10):104006–+, May 2001. 1.4

[135] F. Pretorius. Evolution of Binary Black-Hole Spacetimes. *Physical Review Letters*, 95(12):121101–+, September 2005. 1.4

[136] S. Brandt and B. Brügmann. A Simple Construction of Initial Data for Multiple Black Holes. *Physical Review Letters*, 78:3606–3609, May 1997. 1.4

[137] John G. Baker, Joan Centrella, Dae-Il Choi, Michael Koppitz, and James van Meter. Gravitational-wave extraction from an inspiraling configuration of merging black holes. *Phys. Rev. Lett.*, 96(11):111102, Mar 2006. 1.4

[138] M. Campanelli, C. O. Lousto, P. Marronetti, and Y. Zlochower. Accurate evolutions of orbiting black-hole binaries without excision. *Phys. Rev. Lett.*, 96(11):111101, Mar 2006. 1.4, 2.3.2, 2.4

[139] Frans Pretorius. Evolution of binary black hole spacetimes. *Phys. Rev. Lett.*, 95:121101, 2005. 1.4, 3.1

[140] Manuela Campanelli, C. O. Lousto, P. Marronetti, and Y. Zlochower. Accurate evolutions of orbiting black-hole binaries without excision. *Phys. Rev. Lett.*, 96:111101, 2006. 1.4, 3.1, 3.4

[141] John G. Baker, Joan Centrella, Dae-Il Choi, Michael Koppitz, and James van Meter. Gravitational wave extraction from an inspiraling configuration of merging black holes. *Phys. Rev. Lett.*, 96:111102, 2006. 1.4, 2.4, 3.1, 3.4

[142] James W. York. Conformally invariant orthogonal decomposition of symmetric tensors on riemannian manifolds and the initial-value problem of general relativity. *J. Math. Phys.*, 14(4):456–464, 1973. 1.4

[143] Larry Smarr and James W. York, Jr. Kinematical conditions in the construction of space-time. *Phys. Rev.*, D17:2529–2551, 1978. 1.4

[144] J. W. York, Jr. Kinematics and dynamics of general relativity. In L. L. Smarr, editor, *Sources of Gravitational Radiation*, pages 83–126, 1979. 1.4

[145] T. Nakamura, K. Oohara, and Y. Kojima. General Relativistic Collapse to Black Holes and Gravitational Waves from Black Holes. *Progress of Theoretical Physics Supplement*, 90:1–218, 1987. 1.4, 2.3.1, 2.8.2

[146] M. Shibata and T. Nakamura. Evolution of three-dimensional gravitational waves: Harmonic slicing case. *Phys. Rev. D*, 52:5428–5444, November 1995. 1.4, 2.3.1, 2.8.2

[147] T. W. Baumgarte and S. L. Shapiro. Numerical integration of Einstein's field equations. *Phys.Rev.D*, 59(2):024007–+, January 1999. 1.4, 2.3.1, 2.8.2

[148] H.-J. Yo, T. W. Baumgarte, and S. L. Shapiro. Improved numerical stability of stationary black hole evolution calculations. *Phys.Rev.D*, 66(8):084026–+, October 2002. 1.4

[149] H.-a. Shinkai and G. Yoneda. Hyperbolic formulations and numerical relativity: experiments using Ashtekar's connection variables. *Classical and Quantum Gravity*, 17:4799–4822, December 2000. 11

[150] J. M. Bardeen, O. Sarbach, and L. T. Buchman. Tetrad formalism for numerical relativity on conformally compactified constant mean curvature hypersurfaces. *Phys.Rev.D*, 83(10):104045–+, May 2011. 11

[151] C. S. Reynolds. Astrophysics: Bringing black holes into focus. *Nature*, 455:39–40, September 2008. 1.5

[152] R. Schödel, T. Ott, R. Genzel, R. Hofmann, M. Lehnert, A. Eckart, N. Mouawad, T. Alexander, M. J. Reid, R. Lenzen, M. Hartung, F. Lacombe, D. Rouan, E. Gendron, G. Rousset, A.-M. Lagrange, W. Brandner, N. Ageorges, C. Lidman, A. F. M. Moorwood, J. Spyromilio, N. Hubin, and K. M. Menten. A star in a 15.2-year orbit around the

supermassive black hole at the centre of the Milky Way. *Nature*, 419:694–696, October 2002. 1.5

[153] S. D. Townley. Designation of Variable Stars. *Publications of the Astronomical Society of the Pacific*, 27:209–+, December 1915. 1.5

[154] E. Treister, K. Schawinski, M. Volonteri, P. Natarajan, and E. Gawiser. Black hole growth in the early Universe is self-regulated and largely hidden from view. *Nature*, 474:356–358, June 2011. 1.5

[155] N. A. Inogamov and R. A. Sunyaev. Supermassive Black Hole in an Elliptical Galaxy: Accretion of a Hot Gas with a Low but Finite Angular Momentum. *Astron. Lett.*, 36:835, 2010. 1.5

[156] Steven W. Allen, R.J.H. Dunn, A.C. Fabian, G.B. Taylor, and C.S. Reynolds. The relation between accretion rate and jet power in x-ray luminous elliptical galaxies. *Mon.Not.Roy.Astron.Soc.*, 372:21–30, 2006. 1.5

[157] C. S. Reynolds, A. J. Young, M. C. Begelman, and A. C. Fabian. X-Ray Iron Line Reverberation from Black Hole Accretion Disks. *Astroph.J.*, 514:164–179, March 1999. 1.5

[158] Christopher S. Reynolds, Laura W. Brenneman, Jorn Wilms, and Mary Elizabeth Kaiser. Iron line spectroscopy of NGC 4593 with XMM-Newton: Where is the black hole accretion disk? *Mon.Not.Roy.Astron.Soc.*, 352:205, 2004. 1.5

[159] Laura W. Brenneman and Christopher S. Reynolds. Relativistic Broadening of Iron Emission Lines in a Sample of AGN. *Astrophys. J.*, 702:1367–1386, 2009. 1.5

[160] S. W. Hawking and R. Penrose. The Singularities of gravitational collapse and cosmology. *Proc. Roy. Soc. Lond.*, A314:529–548, 1970. 1.5

[161] R. Penrose. Gravitational collapse and space-time singularities. *Phys. Rev. Lett.*, 14:57–59, 1965. 1.5

[162] S. Chandrsekhar. *The Mathematical Theory of Black Holes*. Clarendon Press, New York, 1983. ISBN-10: 0198503709 | ISBN-13: 978-0198503705. 1.5

[163] S. Chandrasekhar. The highly collapsed configurations of a stellar mass (second paper). *MNRAS*, 95:207–, 1935. 1.5

[164] S. Chandrasekhar. The highly collapsed configurations of a stellar mass. *MNRAS*, 91:456–466, March 1931. 1.5

[165] Robert C. Myers and M. J. Perry. Black Holes in Higher Dimensional Space-Times. *Ann. Phys.*, 172:304, 1986. 1.5

[166] N. Arkani-Hamed, S. Dimopoulos, and G. Dvali. Phenomenology, astrophysics, and cosmology of theories with submillimeter dimensions and TeV scale quantum gravity. *Phys. Rev. D*, 59(8):086004–+, April 1999. 1.5

[167] S. Dimopoulos and G. Landsberg. Black Holes at the Large Hadron Collider. *Physical Review Letters*, 87(16):161602–+, October 2001. 1.5

[168] S. B. Giddings and S. Thomas. High energy colliders as black hole factories: The end of short distance physics. *Phys. Rev.D*, 65(5):056010–+, March 2002. 1.5

[169] G. Kane and S. Watson. Dark Matter and Lhc:. what is the Connection? *Modern Physics Letters A*, 23:2103–2123, 2008. 1.5

[170] R. Emparan and H. S. Reall. Black holes in higher dimensions. *Living Reviews in Relativity*, 11(6), 2008. 1.5

[171] P. H. Frampton. Looking for Intermediate-Mass Black Holes. *Nuclear Physics B Proceedings Supplements*, 200:176–178, March 2010. 1.5

[172] T. J. Maccarone, A. Kundu, S. E. Zepf, and K. L. Rhode. A black hole in a globular cluster. *Nature*, 445:183–185, January 2007. 1.5

[173] A. Patruno, S. Portegies Zwart, J. Dewi, and C. Hopman. The ultraluminous X-ray source in M82: an intermediate-mass black hole with a giant companion. *MNRAS*, 370:L6–L9, July 2006. 1.5

[174] G. Lavagetto, L. Burderi, F. D'Antona, T. di Salvo, R. Iaria, and N. R. Robba. The role of general relativity in the evolution of low-mass X-ray binaries. *MNRAS*, 359:734–740, May 2005. 16

[175] M. Mapelli, B. Moore, L. Giordano, L. Mayer, M. Colpi, E. Ripamonti, and S. Callegari. Intermediate-mass black holes and ultraluminous X-ray sources in the Cartwheel ring galaxy. *MNRAS*, 383:230–246, January 2008. 16

[176] C. Hopman and S. Portegies Zwart. Gravitational waves from remnants of ultraluminous X-ray sources. *MNRAS*, 363:L56–L60, October 2005. 1.5

[177] K. Gültekin, D. O. Richstone, K. Gebhardt, T. R. Lauer, S. Tremaine, M. C. Aller, R. Bender, A. Dressler, S. M. Faber, A. V. Filippenko, R. Green, L. C. Ho, J. Kormendy, J. Magorrian, J. Pinkney, and C. Siopis. The M-σ and M-L Relations in Galactic Bulges, and Determinations of Their Intrinsic Scatter. *Astroph. J.*, 698:198–221, June 2009. 17

[178] J. Silk and M. J. Rees. Quasars and galaxy formation. *Astronomy and Astrophysics*, 331:L1–L4, March 1998. 1.5

[179] L. Ferrarese and D. Merritt. A Fundamental Relation between Supermassive Black Holes and Their Host Galaxies. *Astrophys. J. Lett.*, 539:L9–L12, August 2000. 1.5

[180] K. Gebhardt, R. Bender, G. Bower, A. Dressler, S. M. Faber, A. V. Filippenko, R. Green, C. Grillmair, L. C. Ho, J. Kormendy, T. R. Lauer, J. Magorrian, J. Pinkney, D. Richstone, and S. Tremaine. A Relationship between Nuclear Black Hole Mass and Galaxy Velocity Dispersion. *Astrophys. J. Lett.*, 539:L13–L16, August 2000. 1.5

[181] R. Gambini and J. Pullin. Black Holes in Loop Quantum Gravity: The Complete Space-Time. *Physical Review Letters*, 101(16):161301–+, October 2008. 1.5

[182] S. W. Hawking. Information loss in black holes. *Phys. Rev. D*, 72(8):084013–+, October 2005. 1.5

[183] Jacob D. Bekenstein. Nonexistence of baryon number for static black holes. *Phys. Rev.*, D5:1239–1246, 1972. 1.5.1

[184] P. T. Chrusciel. "No Hair" Theorems – Folklore, Conjectures, Results. *ArXiv General Relativity and Quantum Cosmology e-prints*, February 1994. arXiv:gr-qc/9402032. 1.5.1

[185] Markus Heusler. Stationary black holes: Uniqueness and beyond. *Living Rev. Rel.*, 1:6, 1998. 1.5.1

[186] S. W. Hawking and G. F. R. Ellis. *The Large Scale Structure of Spacetime*. Cambridge University Press, Cambridge, England, 1973. ISBN-10: 0521099064 | ISBN-13: 978-0521099066. 1.5.1, 3.1

[187] R.M. Wald and V. Iyer. Trapped surfaces in the schwarzschild geometry and cosmic censorship. *Phys. Rev. D*, 44:R3719–R3722, 1991. 1.5.1

[188] K. S. Virbhadra and G. F. R. Ellis. Gravitational lensing by naked singularities. *Phys.Rev.*, D65:103004, 2002. 1.5.1.2, 3.6.1

[189] V.A. Belinskii and I.M. Khalatnikov. General solution of the gravitational equations with a physical singularity. *Sov. Phys. JETP*, 30:1174–1180, 1969. 1.5.1.2

[190] V.A. Belinskii and I.M. Khalatnikov. General solution of the gravitational equations with a physical oscillatory singularity. *Sov. Phys. JETP*, 32:169–172, 1971. 1.5.1.2

[191] V.A. Belinskii, I.M. Khalatnikov, and E.M. Lifshitz. A general solution of the einstein equations with a time singularity. *Adv. Phys.*, 31:639–667, 1982. 1.5.1.2

[192] T. Nakamura, S.L. Shapiro, and S.A. Teukolsky. Naked singularities and the hoop conjecture: An analytic exploration. *Phys. Rev. D*, 38:2972–2978, 1988. 1.5.1.2

[193] Martin Bojowald. Loop quantum cosmology. *Living Reviews in Relativity*, 11(4), 2008. 1.5.1.2

[194] R. Goswami, P. S. Joshi, and P. Singh. Quantum Evaporation of a Naked Singularity. *Physical Review Letters*, 96(3):031302–+, January 2006. 1.5.1.2

[195] R. Goswami and P. S. Joshi. Spherical gravitational collapse in N dimensions. *Phys. Rev. D*, 76(8):084026–+, October 2007. 1.5.1.2

[196] D. M. Eardley and L. Smarr. Time functions in numerical relativity: Marginally bound dust collapse. *Phys. Rev. D*, 19(8):2239–2259, Apr 1979. 1.5.1.2

[197] A. Królak. Nature of singularities in gravitational collapse. *Progress of Theoretical Physics Supplement*, 136:45–56, 1999. 1.5.1.2

[198] Beverly K. Berger. Numerical approaches to spacetime singularities. *Living Reviews in Relativity*, 5(1), 2002. 1.5.1.2

[199] A.M. Abrahams, K.H. Heiderich, S.L. Shapiro, and S.A. Teukolsky. Vacuum initial data, singularities, and cosmic censorship. *Phys. Rev. D*, 46:2452–2463, 1992. 1.5.1.2

[200] P.R. Brady and J.D. Smith. Black hole singularities: A numerical approach. *Phys. Rev. Lett.*, 75:1256–1259, 1995. 1.5.1.2

[201] S. L. Shapiro and S. A. Teukolsky. Black Holes, Star Clusters, and Naked Singularities: Numerical Solution of Einstein's Equations. *Royal Society of London Philosophical Transactions Series A*, 340:365–390, September 1992. 1.5.1.2

[202] R. Penrose. *Singularities of spacetime*, pages 217–243. 1978. 1.5.1.2

[203] T. P. Singh. Singularities and Cosmic Censorship. *Journal of Astrophysics and Astronomy*, 18:335–+, December 1997. 1.5.1.2

[204] R. M. Wald. Gravitational Collapse and Cosmic Censorship. *ArXiv General Relativity and Quantum Cosmology e-prints*, October 1997. arXiv:gr-qc/9710068. 1.5.1.2

[205] R. Penrose. The Question of Cosmic Censorship. In R. M. Wald, editor, *Black Holes and Relativistic Stars*, pages 103–+, 1998. 1.5.1.2

[206] R. Penrose. The Question of Cosmic Censorship. *Journal of Astrophysics and Astronomy*, 20:233–+, September 1999. 1.5.1.2

[207] M. Tegmark. Cosmic censorship. *Nature*, 415:375–+, January 2002. 1.5.1.2

[208] C. J. S. Clarke. Review Article: A title of cosmic censorship. *Classical and Quantum Gravity*, 11:1375–1386, June 1994. 1.5.1.2

[209] Robert M. Wald. "weak" cosmic censorship. *PSA: Proceedings of the Biennial Meeting of the Philosophy of Science Association*, 1992:pp. 181–190, 1992. 1.5.1.2

[210] Pong Soo Jang. Note on cosmic censorship. *Phys. Rev. D*, 20(4):834–838, Aug 1979. 1.5.1.2

[211] D. Lynden-Bell. Galactic Nuclei as Collapsed Old Quasars. *Nature*, 223:690–694, August 1969. 1.5.2

[212] Hagai Netzer. Quasars and active galactic nuclei. 1992. Vol.VI/3 Landolt-Bornstein, 'Astron. Astrophys.'. 1.5.2

[213] K. M. Dasyra et al. A view of the narrow-line region in the infrared: active galactic nuclei with resolved fine-structure lines in the Spitzer archive. *Astrophys. J.*, 740:94, 2011. 1.5.2

[214] M. Dotti, C. Montuori, R. Decarli, M. Volonteri, M. Colpi, et al. SDSSJ092712.65+294344.0: a candidate massive black hole binary. *Mon.Not.Roy.Astron.Soc.*, 398:L73–L77, 2009. 1.5.2, 4.1

[215] Tamara Bogdanovic, Michael Eracleous, and Steinn Sigurdsson. SDSS J092712.65+294344.0: Recoiling Black Hole or A Sub- parsec Binary Candidate? *Astrophys. J.*, 697:288–292, 2009. 1.5.2, 4.1

[216] Timothy M. Heckman, Julian H. Krolik, Sean M. Moran, Jeremy Schnittman, and Suvi Gezari. SDSSJ092712.65+294344.0: NGC 1275 at z=0.7? *Astrophys. J.*, 695:363–367, 2009. 1.5.2, 4.1

[217] M. Dotti, M. Ruszkowski, L. Paredi, M. Colpi, M. Volonteri, et al. Dual black holes in merger remnants. I: linking accretion to dynamics. *Mon.Not.Roy.Astron.Soc.*, 396:1640–1646, 2009. 1.5.2, 4.1

[218] Andrew I. Macfadyen and Milos Milosavljevic. An Eccentric Circumbinary Accretion Disk and the Detection of Binary Massive Black Holes. *Astrophys.J.*, 672:83–93, 2008. 1.5.2, 4.1, 4.6

[219] K. Hayasaki, S. Mineshige, and H. Sudou. Binary Black Hole Accretion Flows in Merged Galactic Nuclei. *Pub. Astron. Soc. Japan*, 59:427–441, April 2007. 1.5.2, 4.1, 4.6, 5.1

[220] Lia R. Corrales, Zoltan Haiman, and Andrew MacFadyen. Hydrodynamical Response of a Circumbinary Gas Disk to Black Hole Recoil and Mass Loss. 2009. arXiv:astro-ph.HE/0910.0014. 1.5.2, 4.1, 4.5, 4.5

[221] D. Batcheldor, A. Robinson, D.J. Axon, E.S. Perlman, and D. Merritt. A Displaced Supermassive Black Hole in M87. *Astrophys.J.*, 717:L6–10, 2010. 1.5.2

[222] H. Spinrad. *Galaxy formation and evolution*. Springer-Praxis books in astrophysics and astronomy. Springer, 2005. 1.5.2

[223] F. Antonini and D. Merritt. Dynamical Friction around Supermassive Black Holes. *ArXiv e-prints*, August 2011. 1.5.2

[224] W. Y. Chau. Orbital angular momentum loss via gravitational radiation and mass-transfer rates in close binary systems. *Astroph.J.*, 219:1038–1042, February 1978. 1.5.2

[225] Abraham Loeb. Observable Signatures of a Black Hole Ejected by Gravitational Radiation Recoil in a Galaxy Merger. *Phys. Rev. Lett.*, 99:041103, 2007. 1.5.2, 4.1

[226] Jeremy D. Schnittman and Julian H. Krolik. The Infrared Afterglow of Supermassive Black Hole Mergers. *Astrophys, J.*, 684:835–844, September 2008. 1.5.2, 4.1, 4.6

[227] Bence Kocsis and Abraham Loeb. Brightening of an Accretion Disk Due to Viscous Dissipation of Gravitational Waves During the Coalescence of Supermassive Black Holes. *Phys.Rev.Lett.*, 101:041101, 2008. 1.5.2, 4.1

[228] S. Collin and J.-M. Huré. Size-mass-luminosity relations in AGN and the role of the accretion disc. *Astronomy and Astrophysics*, 372:50–58, June 2001. 1.5.2

[229] Carlos O. Lousto, Hiroyuki Nakano, Yosef Zlochower, and Manuela Campanelli. Statistical studies of Spinning Black-Hole Binaries. *Phys.Rev.*, D81:084023, 2010. 1.5.2, 4.1, 4.6

[230] Kimitake Hayasaki, Shin Mineshige, and Luis C. Ho. A supermassive binary black hole with triple disks. *Astrophys. J.*, 682:1134–1140, August 2008. 1.5.2, 4.1, 4.6, 5.1

[231] M. J. Valtonen, H. J. Lehto, K. Nilsson, J. Heidt, L. O. Takalo, A. Sillanpää, C. Villforth, M. Kidger, G. Poyner, T. Pursimo, S. Zola, J.-H. Wu, X. Zhou, K. Sadakane, M. Drozdz, D. Koziel, D. Marchev, W. Ogloza, C. Porowski, M. Siwak, G. Stachowski, M. Winiarski, V.-P. Hentunen, M. Nissinen, A. Liakos, and S. Dogru. A massive binary black-hole system in OJ287 and a test of general relativity. *Nature*, 452:851–853, April 2008. 1.5.2

[232] M.J. Valtonen, S. Mikkola, H.J. Lehto, A. Gopakumar, R. Hudec, et al. Testing black hole no-hair theorem with OJ287. 2011. arXiv:astro-ph.CO/1108.5861. 1.5.2

[233] M. J. Valtonen, S. Mikkola, D. Merritt, A. Gopakumar, H. J. Lehto, T. Hyvönen, H. Rampadarath, R. Saunders, M. Basta, and R. Hudec. Measuring the Spin of the Primary Black Hole in OJ287. *Astroph. J.*, 709:725–732, February 2010. 1.5.2

[234] M. J. Valtonen, S. Mikkola, H. J. Lehto, T. Hyvönen, K. Nilsson, D. Merritt, A. Gopakumar, H. Rampadarath, R. Hudec, M. Basta, and R. Saunders. Measuring black hole spin in OJ287. *Celestial Mechanics and Dynamical Astronomy*, 106:235–243, March 2010. 1.5.2

[235] J. H. Krolik. Estimating the prompt electromagnetic luminosity of a black hole merger. *Astrophys. J.*, 709:774–779, February 2010. 21

[236] E. Schnetter, C. D. Ott, G. Allen, P. Diener, T. Goodale, T. Radke, E. Seidel, and J. Shalf. Cactus Framework: Black Holes to Gamma Ray Bursts. *ArXiv e-prints*, July 2007. arXiv:cs.DC/0707.1607. 1.6.1, 2.8.1

[237] Erik Schnetter, Scott H. Hawley, and Ian Hawke. Evolutions in 3D numerical relativity using fixed mesh refinement. *Class. Quant. Grav.*, 21:1465–1488, 2004. 1.6.1, 2.8.1, 3.4

[238] G. Allen, T. Goodale, F. Löffler, D. Rideout, E. Schnetter, and E. L. Seidel. Component Specification in the Cactus Framework: The Cactus Configuration Language. *ArXiv e-prints*, September 2010. arXiv:cs.DC/1009.1341. 1.6.1, 2.8.1

[239] Cactus Computational Toolkit home page: `http://www.cactuscode.org`. 1.6.1, 2.8.1, 2.8.2, 3.4

[240] Einstein Toolkit home page: `http://einsteintoolkit.org`. 1.6.1, 2.8.1, 2.8.2

[241] Fixed Mesh Refinement with Carpet: `http://www.tat.physik.uni-tuebingen.de/~schnette/carpet/`. 1.6.1

[242] Erik Schnetter, Scott H. Hawley, and Ian Hawke. Evolutions in 3D numerical relativity using fixed mesh refinement. *Class. Quantum Grav.*, 21(6):1465–1488, 21 March 2004. 1.6.1, 2.8.1

[243] Peter Diener. A new general purpose event horizon finder for 3d numerical spacetimes. *Class. Quant. Grav.*, 20:4901–4918, 2003. 1.6.1, 2.6, 2.6.2.1, 3.1, 3.2.1.1, 3.4

[244] Open DX Home Page `http://www.opendx.org`. 1.6.1

[245] M. Ponce, C. Lousto, and Y. Zlochower. Seeking for toroidal event horizons from initially stationary BH configurations. *Classical and Quantum Gravity*, 28(14):145027–+, July 2011. 1.6.1

[246] Elena M. Rossi, G. Lodato, P.J. Armitage, J.E. Pringle, and A.R. King. Black hole mergers: the first light. *Mon. Not. R. Astron. Soc.*, 401:2021–2035, January 2010. 1.6.2, 4.1, 4.3, 4.3, 4.5, 4.5, 4.6, 5.1

[247] M. Ponce, J. A. Faber, and J. C. Lombardi, Jr. Accretion disks around kicked black holes: Post-kick Dynamics. *ArXiv e-prints*, July 2011. arXiv:astro-ph.CO/1107.1711. 1.6.2, 5.1

[248] S. W. Hawking. Black holes in general relativity. *Commun. Math. Phys.*, 25:152–166, 1972. 2.1.2.5, 2.6.3, 3.1

[249] J. W. York, Jr. Conformal "Thin-Sandwich" Data for the Initial-Value Problem of General Relativity. *Physical Review Letters*, 82:1350–1353, February 1999. 2.2.5

[250] Simonetta Frittelli. Potential for ill-posedness in several 2nd-order formulations of the Einstein equations. *Phys.Rev.*, D70:044029, 2004. 2.2.5.1

[251] M. Campanelli, C. O. Lousto, and Y. Zlochower. Last orbit of binary black holes. *Phys. Rev. D*, 73(6):061501–+, March 2006. 2.4

[252] Gregory B. Cook. Initial data for numerical relativity. *Living Reviews in Relativity*, 3(5), 2000. 2.5.1

[253] Michael I. Cohen, Harald P. Pfeiffer, and Mark A. Scheel. Revisiting Event Horizon Finders. *Class. Quant. Grav.*, 26:035005, 2009. 2.6, 3.1, 5.1

[254] Jonathan Thornburg. Event and Apparent Horizon Finders for $3 + 1$ Numerical Relativity. *Living Rev. Rel.*, 10:3, 2007. 2.6

[255] Jonathan Thornburg. A fast apparent-horizon finder for 3-dimensional Cartesian grids in numerical relativity. *Class. Quantum Grav.*, 21(2):743–766, 21 January 2004. 2.6.1, 3.4

[256] Jonathan Thornburg. Finding apparent horizons in numerical relativity. *Physical Review D*, 54(8):4899–4918, October 15 1996. 2.6.1

[257] A Ashtekar and B Krishnan. Isolated and dynamical horizons and their applications. *Living Reviews in Relativity*, 7(10), 2004. 2.6.4

[258] R.L. Burden and J.D. Faires. *Numerical analysis*. Thomson Brooks/Cole, 2005. ISBN 9780534392000. 2.7

[259] Y. Zlochower, J. G. Baker, M. Campanelli, and C. O. Lousto. Accurate black hole evolutions by fourth-order numerical relativity. *Phys.Rev.D*, 72(2):024021–+, July 2005. 2.8.2

[260] Lee Lindblom, Mark A. Scheel, Lawrence E. Kidder, Robert Owen, and Oliver Rinne. A new generalized harmonic evolution system. *Class. Quant. Grav.*, 23:S447–S462, 2006. 3.1

[261] Carsten Gundlach and Jose M. Martin-Garcia. Well-posedness of formulations of the einstein equations with dynamical lapse and shift conditions. *Phys. Rev.*, D74:024016, 2006. 3.1

[262] James R. van Meter, John G. Baker, Michael Koppitz, and Dae-Il Choi. How to move a black hole without excision: gauge conditions for the numerical evolution of a moving puncture. *Phys. Rev.*, D73:124011, 2006. 3.1

[263] Manuela Campanelli, C. O. Lousto, and Y. Zlochower. Spinning-black-hole binaries: The orbital hang up. *Phys. Rev. D*, 74:041501(R), 2006. 3.1

[264] Manuela Campanelli, C. O. Lousto, and Yosef Zlochower. Spin-orbit interactions in black-hole binaries. *Phys. Rev. D*, 74:084023, 2006. 3.1

[265] Manuela Campanelli, Carlos O. Lousto, Yosef Zlochower, Badri Krishnan, and David Merritt. Spin flips and precession in black-hole-binary mergers. *Phys. Rev.*, D75:064030, 2007. 3.1

[266] Luciano Rezzolla et al. The final spin from the coalescence of aligned-spin black- hole binaries. *Astrophys. J.*, 674:L29–L32, 2008. 3.1

[267] Ulrich Sperhake et al. Eccentric binary black-hole mergers: The transition from inspiral to plunge in general relativity. *Phys. Rev.*, D78:064069, 2008. 3.1

[268] Sergio Dain, Carlos O. Lousto, and Yosef Zlochower. Extra-Large Remnant Recoil Velocities and Spins from Near- Extremal-Bowen-York-Spin Black-Hole Binaries. *Phys. Rev.*, D78:024039, 2008. 3.1

[269] Olaf Dreyer, Badri Krishnan, Deirdre Shoemaker, and Erik Schnetter. Introduction to isolated horizons in numerical relativity. *Phys. Rev.*, D67:024018, 2003. 3.1

[270] Erik Schnetter, Badri Krishnan, and Florian Beyer. Introduction to dynamical horizons in numerical relativity. *Phys. Rev.*, D74:024028, 2006. 3.1

[271] Gregory B. Cook and Bernard F. Whiting. Approximate killing vectors on s^2. *Phys. Rev.*, D76:041501, 2007. 3.1

[272] Badri Krishnan, Carlos O. Lousto, and Yosef Zlochower. Quasi-Local Linear Momentum in Black-Hole Binaries. *Phys. Rev.*, D76:081501, 2007. 3.1

[273] Manuela Campanelli, Carlos O. Lousto, and Yosef Zlochower. Algebraic Classification of Numerical Spacetimes and Black-Hole-Binary Remnants. *Phys. Rev.*, D79:084012, 2009. 3.1

[274] Robert Owen. Degeneracy measures for the algebraic classification of numerical spacetimes. *Phys. Rev.*, D81:124042, 2010. 3.1

[275] Pedro Marronetti et al. Binary black holes on a budget: Simulations using workstations. *Class. Quant. Grav.*, 24:S43–S58, 2007. 3.1

[276] Pedro Marronetti, Wolfgang Tichy, Bernd Brugmann, Jose Gonzalez, and Ulrich Sperhake. High-spin binary black hole mergers. *Phys. Rev.*, D77:064010, 2008. 3.1

[277] Emanuele Berti et al. Inspiral, merger and ringdown of unequal mass black hole binaries: A multipolar analysis. *Phys. Rev.*, D76:064034, 2007. 3.1

[278] Latham Boyle, Michael Kesden, and Samaya Nissanke. Binary black hole merger: symmetry and the spin expansion. *Phys. Rev. Lett.*, 100:151101, 2008. 3.1

[279] Latham Boyle and Michael Kesden. The spin expansion for binary black hole merger: new predictions and future directions. *Phys. Rev.*, D78:024017, 2008. 3.1

[280] Alessandra Buonanno, Lawrence E. Kidder, and Luis Lehner. Estimating the final spin of a binary black hole coalescence. *Phys. Rev.*, D77:026004, 2008. 3.1

[281] Wolfgang Tichy and Pedro Marronetti. The final mass and spin of black hole mergers. *Phys. Rev.*, D78:081501, 2008. 3.1

[282] Michael Kesden. Can binary mergers produce maximally spinning black holes? *Phys. Rev.*, D78:084030, 2008. 3.1

[283] Enrico Barausse and Luciano Rezzolla. Predicting the direction of the final spin from the coalescence of two black holes. *Astrophys. J. Lett.*, 704:L40–L44, 2009. 3.1

[284] Luciano Rezzolla. Modelling the final state from binary black-hole coalescences. *Class. Quant. Grav.*, 26:094023, 2009. 3.1

[285] Alessandra Buonanno, Gregory B. Cook, and Frans Pretorius. Inspiral, merger and ring-down of equal-mass black-hole binaries. *Phys. Rev.*, D75:124018, 2007. 3.1

[286] John G. Baker, James R. van Meter, Sean T. McWilliams, Joan Centrella, and Bernard J. Kelly. Consistency of post-Newtonian waveforms with numerical relativity. *Phys. Rev. Lett.*, 99:181101, 2007. 3.1

[287] Yi Pan et al. A data-analysis driven comparison of analytic and numerical coalescing binary waveforms: Nonspinning case. *Phys. Rev.*, D77:024014, 2008. 3.1

[288] Alessandra Buonanno et al. Toward faithful templates for non-spinning binary black holes using the effective-one-body approach. *Phys. Rev.*, D76:104049, 2007. 3.1

[289] Mark Hannam, Sascha Husa, Ulrich Sperhake, Bernd Brugmann, and Jose A. Gonzalez. Where post-Newtonian and numerical-relativity waveforms meet. *Phys. Rev.*, D77:044020, 2008. 3.1

[290] Mark Hannam, Sascha Husa, Bernd Bruegmann, and Achamveedu Gopakumar. Comparison between numerical-relativity and post-Newtonian waveforms from spinning binaries: the orbital hang-up case. *Phys. Rev.*, D78:104007, 2008. 3.1

[291] Achamveedu Gopakumar, Mark Hannam, Sascha Husa, and Bernd Bruegmann. Comparison between numerical relativity and a new class of post-Newtonian gravitational-wave phase evolutions: the non-spinning equal-mass case. *Phys. Rev.*, D78:064026, 2008. 3.1

[292] Ian Hinder, Frank Herrmann, Pablo Laguna, and Deirdre Shoemaker. Comparisons of eccentric binary black hole simulations with post-Newtonian models. *Phys. Rev.*, D82:024033, 2010. 3.1

[293] Jose A. Gonzalez, Ulrich Sperhake, and Bernd Brugmann. Black-hole binary simulations: the mass ratio 10:1. *Phys. Rev.*, D79:124006, 2009. 3.1

[294] Carlos O. Lousto, Hiroyuki Nakano, Yosef Zlochower, and Manuela Campanelli. Intermediate Mass Ratio Black Hole Binaries: Numerical Relativity meets Perturbation Theory. *Phys. Rev. Lett.*, 104:211101, 2010. 3.1

[295] John L. Friedman, Kristin Schleich, and Donald M. Witt. Topological censorship. *Phys. Rev. Lett.*, 71:1486–1489, 1993. 3.1, 3.2

[296] Gregory J. Galloway and Richard Schoen. A generalization of Hawking's black hole topology theorem to higher dimensions. *Commun. Math. Phys.*, 266:571–576, 2006. 3.1

[297] Gregory J. Galloway. Rigidity of outer horizons and the topology of black holes. 2006. arXiv:gr-qc/0608118. 3.1, 3.3

[298] Istvan Racz. A simple proof of the recent generalisations of Hawking's black hole topology theorem. *Class. Quant. Grav.*, 25:162001, 2008. 3.1

[299] Scott A. Hughes et al. Finding black holes in numerical space-times. *Phys. Rev.*, D49:4004–4015, 1994. 3.1

[300] S. L. Shapiro, S. A. Teukolsky, and J. Winicour. Toroidal black holes and topological censorship. *Phys. Rev.*, D52:6982–6987, 1995. 3.1, 3.2.1.1, 5.1

[301] Sascha Husa and Jeffrey Winicour. The asymmetric merger of black holes. *Phys. Rev.*, D60:084019, 1999. 3.1

[302] Jacek Wojtkiewicz. Naked singularities in initial surfaces. *Phys. Rev. D*, 41(6):1867–1874, Mar 1990. 3.1, 3.3, 3.3.1.1, 3.5.1

[303] Gabriela Jaramillo and Carlos O. Lousto. Study of multi black hole and ring singularity apparent horizons. 2010. arXiv:gr-qc/1008.2001. 3.1, 3.3, 3.3.1.1, 3.5.1

[304] Stuart L. Shapiro and Saul A. Teukolsky. Formation of naked singularities: The violation of cosmic censorship. *Phys. Rev. Lett.*, 66:994–997, 1991. 3.1

[305] Stuart L. Shapiro and Saul A. Teukolsky. Gravitational collapse of rotating spheroids and the formation of naked singularities. *Phys. Rev. D*, 45(6):2006–2012, Mar 1992. 3.1

[306] A. M. Abrahams, K. R. Heiderich, S. L. Shapiro, and S. A. Teukolsky. Vacuum initial data, singularities, and cosmic censorship. *Phys. Rev.*, D46:2452–2463, 1992. 3.1, 3.3.1.2, 3.3.1.3, 3.5.3

[307] Luis Lehner and Frans Pretorius. Black Strings, Low Viscosity Fluids, and Violation of Cosmic Censorship. *Phys. Rev. Lett.*, 105:101102, 2010. hep-th/1006.5960. 3.1, 5.1

[308] D. Gannon. Singularities in nonsimply connected space-times. *J. Math. Phys.*, 16(12):2364–2367, 1975. 3.2

[309] C. W. Lee. A restriction on the topology of cauchy surfaces in general relativity. *Communications in Mathematical Physics*, 51:157–162, 1976. 10.1007/BF01609346. 3.2

[310] G. J. Galloway. On the topology of black holes. *Communications in Mathematical Physics*, 151:53–66, January 1993. 3.2

[311] S. F. Browdy and G. J. Galloway. Topological censorship and the topology of black holes. *Journal of Mathematical Physics*, 36:4952–4961, September 1995. 3.2

[312] G. J. Galloway, K. Schleich, D. M. Witt, and E. Woolgar. Topological censorship and higher genus black holes. *Phys.Rev.D*, 60(10):104039–+, November 1999. 3.2.1.1

[313] G.J. Galloway, K. Schleich, D. Witt, and E. Woolgar. The AdS / CFT correspondence conjecture and topological censorship. *Phys.Lett.*, B505:255–262, 2001. 3.2.1.1

[314] J.A. Wheeler and J.R. Klauder. *Magic without magic: John Archibald Wheeler: a collection of essays in honor of his sixtieth birthday.* W. H. Freeman, 1972. ISBN 9780716703372. 3.2.1.2

[315] Kip S. Thorne. Black holes and time warps: Einstein's outrageous legacy. 1994. Book, W.W. Norton & Co., New York: 341-342, 2004. 3.2.1.2

[316] C. Bambi and L. Modesto. Can an astrophysical black hole have a topologically non-trivial event horizon? *ArXiv e-prints*, July 2011. arXiv:gr-qc/1107.4337. 3.2.2

[317] R. Hamerly and Y. Chen. Event Horizon Deformations in Extreme Mass-Ratio Black Hole Mergers. *ArXiv e-prints*, July 2010. arXiv:gr-qc/1007.5387. 3.2.2

[318] N. Iizuka and M. Shigemori. Are there four-dimensional small black rings? *Phys.Rev.D*, 77(4):044044–+, February 2008. 3.2.2

[319] M. Siino. Topology of event horizons. *Phys.Rev.D*, 58(10):104016–+, November 1998. 3.2.2

[320] D. Brill and R. Lindquist. Interaction energy in geometrostatics. *Phys. Rev.*, 131(1):471–476, 1963. 3.3, 3.3.1

[321] Y. Zlochower, J. G. Baker, Manuela Campanelli, and C. O. Lousto. Accurate black hole evolutions by fourth-order numerical relativity. *Phys. Rev.*, D72:024021, 2005. 3.4, 3.4

[322] Miguel Alcubierre, Bernd Brügmann, Peter Diener, Michael Koppitz, Denis Pollney, Edward Seidel, and Ryoji Takahashi. Gauge conditions for long-term numerical black hole evolutions without excision. *Phys. Rev.*, D67:084023, 2003. 3.4, 3.4

[323] John Baker, Manuela Campanelli, and Carlos O. Lousto. The Lazarus project: A pragmatic approach to binary black hole evolutions. *Phys. Rev. D*, 65:044001, 2002. 3.4

[324] Manuela Campanelli, Carlos O. Lousto, and Yosef Zlochower. Close encounters of three black holes. *Phys. Rev.*, D77:101501(R), 2008. 3.5.2

[325] Carlos O. Lousto and Yosef Zlochower. Foundations of multiple black hole evolutions. *Phys. Rev.*, D77:024034, 2008. 3.5.2

[326] Pablo Galaviz, Bernd Brugmann, and Zhoujian Cao. Numerical evolution of multiple black holes with accurate initial data. *Phys. Rev.*, D82:024005, 2010. 3.5.2

[327] K.S. Virbhadra, D. Narasimha, and S.M. Chitre. Role of the scalar field in gravitational lensing. *Astron.Astrophys.*, 337:1–8, 1998. 3.6.1

[328] K.S. Virbhadra and C.R. Keeton. Time delay and magnification centroid due to gravitational lensing by black holes and naked singularities. *Phys.Rev.*, D77:124014, 2008. 3.6.1

[329] M.J. Fitchett and Steven L. Detweiler. Linear momentum and gravitational-waves - circular orbits around a schwarzschild black-hole. *Mon.Not.Roy.Astron.Soc.*, 211:933–942, 1984. 4.1

[330] S. Komossa and David Merritt. Gravitational Wave Recoil Oscillations of Black Holes: Implications for Unified Models of Active Galactic Nuclei. *Astrophys. J. Lett.*, 689:l89, 2008. 4.1

[331] Tamara Bogdanovic, Christopher S. Reynolds, and M. Coleman Miller. Alignment of the spins of supermassive black holes prior to coalescence. *Astrophys. J. Lett.*, 661:L147, 2007. 4.1, 4.6

[332] M. Dotti, M. Volonteri, A. Perego, M. Colpi, M. Ruszkowski, et al. Dual black holes in merger remnants. II: spin evolution and gravitational recoil. *Mon.Not.Roy.Astron.Soc.*, 402:682–690, 2010. 4.1

[333] Sean M. O'Neill, M.Coleman Miller, Tamara Bogdanovic, Christopher S. Reynolds, and Jeremy Schnittman. Reaction of Accretion Disks to Abrupt Mass Loss During Binary Black Hole Merger. *Astrophys.J.*, 700:859–871, 2009. 4.1

[334] Stuart L. Shapiro. Filling the disk hollow following binary black hole merger: The transient accretion afterglow. *Phys.Rev.*, D81:024019, 2010. 4.1

[335] Tanja Bode, Roland Haas, Tamara Bogdanovic, Pablo Laguna, and Deirdre Shoemaker. Relativistic Mergers of Supermassive Black Holes and their Electromagnetic Signatures. *Astrophys.J.*, 715:1117–1131, 2010. 4.1

[336] Tanja Bode, Tamara Bogdanovic, Roland Haas, James Healy, Pablo Laguna, et al. Mergers of Supermassive Black Holes in Astrophysical Environments. 2011. arXiv:gr-qc/1101.4684. 4.1

[337] Miguel Megevand, Matthew Anderson, Juhan Frank, Eric W. Hirschmann, Luis Lehner, et al. Perturbed disks get shocked. Binary black hole merger effects on accretion disks. *Phys.Rev.*, D80:024012, 2009. 4.1

[338] Matthew Anderson, Luis Lehner, Miguel Megevand, and David Neilsen. Post-merger electromagnetic emissions from disks perturbed by binary black holes. *Phys.Rev.*, D81:044004, 2010. 4.1

[339] Carlos Palenzuela, Matthew Anderson, Luis Lehner, Steven L. Liebling, and David Neilsen. Stirring, not shaking: binary black holes' effects on electromagnetic fields. *Phys.Rev.Lett.*, 103:081101, 2009. 4.1

[340] Carlos Palenzuela, Luis Lehner, and Shin Yoshida. Understanding possible electromagnetic counterparts to loud gravitational wave events: Binary black hole effects on electromagnetic fields. *Phys.Rev.*, D81:084007, 2010. 4.1

[341] Philipp Mosta, Carlos Palenzuela, Luciano Rezzolla, Luis Lehner, Shin'ichirou Yoshida, et al. Vacuum Electromagnetic Counterparts of Binary Black-Hole Mergers. *Phys.Rev.*, D81:064017, 2010. 4.1

[342] Carlos Palenzuela, Luis Lehner, and Steven L. Liebling. Dual Jets from Binary Black Holes. *Science*, 329:927, 2010. 4.1

[343] R.D. Blandford and R.L. Znajek. Electromagnetic extractions of energy from Kerr black holes. *Mon.Not.Roy.Astron.Soc.*, 179:433–456, 1977. 4.1

[344] David Neilsen, Luis Lehner, Carlos Palenzuela, Eric W. Hirschmann, Steven L. Liebling, et al. Boosting jet power in black hole spacetimes. 2010. arXiv:astro-ph.HE/1012.5661. 4.1

[345] Olindo Zanotti, Luciano Rezzolla, Luca Del Zanna, and Carlos Palenzuela. EM counterparts of recoiling black holes: general relativistic simulations of non-Keplerian discs. *Astron.Astrophys.*, 523:A8, 2010. 4.1

[346] Brian D. Farris, Yuk Tung Liu, and Stuart L. Shapiro. Binary Black Hole Mergers in Gaseous Environments: 'Binary Bondi' and 'Binary Bondi-Hoyle-Lyttleton' Accretion. *Phys.Rev.*, D81:084008, 2010. 4.1

[347] Brian D. Farris, Yuk Tung Liu, and Stuart L. Shapiro. Binary black hole mergers in gaseous disks: Simulations in general relativity. 2011. arXiv:astro-ph.HE/1105.2821. 4.1

[348] K. R. Bell and D. N. C. Lin. Using FU Orionis outbursts to constrain self-regulated protostellar disk models. *Astrophys. J.*, 427:987–1004, June 1994. 4.2.1.1

[349] Eduardo Rubio-Herrera and William H. Lee. Oscillations of thick accretion discs around black holes. *Mon.Not.Roy.Astron.Soc.*, 357:L31–L34, 2005. 4.4.1

[350] Eduardo Rubio-Herrera and William H. Lee. Oscillations of Thick Accretion Discs Around Black Holes - II. *Mon. Not. Roy. Astron. Soc.*, 362:789–798, 2005. 4.4.1

[351] Jr. Lombardi, James C., Z.F. Proulx, K.L. Dooley, E.M. Theriault, N. Ivanova, et al. Stellar collisions and ultracompact x-ray binary formation. *Astrophys.J.*, 640:441–458, 2006. 4.4.2

[352] Evghenii Gaburov, James Lombardi, and Simon Portegies Zwart. On the onset of runaway stellar collisions in dense star clusters - II. Hydrodynamics of three-body interactions. *Mon. Not. R. Astron. Soc.*, 402:105–126, February 2010. 4.4.2

[353] Volker Springel and Lars Hernquist. Cosmological SPH simulations: The Entropy equation. *Mon.Not.Roy.Astron.Soc.*, 333:649, 2002. 4.4.2

[354] J. J. Monaghan and D. J. Price. Variational principles for relativistic smoothed particle hydrodynamics. *Mon.Not.R.Astron.Soc.*, 328:381–392, December 2001. 4.4.2

[355] J. J. Monaghan and J. C. Lattanzio. A refined particle method for astrophysical problems. *Astron. Astrophys.*, 149:135–143, August 1985. 4.4.2

[356] Daniel J. Price and J.J. Monaghan. An energy-conserving formalism for adaptive gravitational force softening in SPH and N-body codes. *Mon.Not.Roy.Astron.Soc.*, 374:1347–1358, 2007. 4.4.2, 4.4.2

[357] D. S. Balsara. von Neumann stability analysis of smooth particle hydrodynamics–suggestions for optimal algorithms. *Journal of Computational Physics*, 121:357–372, 1995. 4.4.2

[358] Daniel J. Price. Smoothed Particle Hydrodynamics and Magnetohydrodynamics. 2010. arXiv:astro-ph.IM/1012.1885. 4.5

[359] D. C. Homan, Y. Y. Kovalev, M. L. Lister, E. Ros, K. I. Kellermann, M. H. Cohen, R. C. Vermeulen, J. A. Zensus, and M. Kadler. Intrinsic brightness temperatures of agn jets. *The Astrophysical Journal Letters*, 642(2):L115, 2006. 4.6

[360] Yutaka Fujita. Long-Term Evolution of and X-ray Emission from a Recoiling Supermassive Black Hole in a Disk Galaxy. *Astrophys. J.*, 691:1050–1057, 2009. 4.6

[361] Yutaka Fujita. X-Ray Emission from a Supermassive Black Hole Ejected from the Center of a Galaxy. 2008. 4.6

[362] L. Lehner and F. Pretorius. Final State of Gregory-Laflamme Instability. *ArXiv e-prints*, June 2011. arXiv:gr-qc/1106.5184. 5.1

[363] M. E. Rossi, G. Lodato, and P. Armitage. private communication, 2011. 5.1

[364] M. R. Bate, I. A. Bonnell, and N. M. Price. Modelling accretion in protobinary systems. *MNRAS*, 277:362–376, November 1995. 5.1

[365] P. Crane, M. Stiavelli, I. R. King, J. M. Deharveng, R. Albrecht, C. Barbieri, J. C. Blades, A. Boksenberg, M. J. Disney, P. Jakobsen, T. M. Kamperman, F. Machetto, C. D. Mackay, F. Paresce, G. Weigelt, D. Baxter, P. Greenfield, R. Jedrzejewski, A. Nota, and W. B. Sparks. High resolution imaging of galaxy cores. *The Astronomical Journal*, 106:1371–1393, October 1993. 5.1

[366] P. Rafanelli, H. Schulz, C. Barbieri, S. Komossa, U. Mebold, A. Baruffolo, and M. Radovich. Subarcsec structures in the double nucleus of NGC6240 disclosed with HST at 370, 430 and 500 NM. *Astronomy and Astrophysics*, 327:901–908, November 1997. 5.1

[367] G. Risaliti, E. Sani, R. Maiolino, A. Marconi, S. Berta, V. Braito, R. Della Ceca, A. Franceschini, and M. Salvati. The Double Active Galactic Nucleus in NGC 6240 Revealed through 3-5 μm Spectroscopy. *Astrophys. J. Lett.*, 637:L17–L20, January 2006. 5.1

[368] B. F. Gerke, J. A. Newman, J. Lotz, R. Yan, P. Barmby, A. L. Coil, C. J. Conselice, R. J. Ivison, L. Lin, D. C. Koo, K. Nandra, S. Salim, T. Small, B. J. Weiner, M. C. Cooper, M. Davis, S. M. Faber, and P. Guhathakurta. The DEEP2 Galaxy Redshift Survey: AEGIS Observations of a Dual AGN at z = 0.7. *Astrophys. J. Lett.*, 660:L23–L26, May 2007. 5.1

[369] J. M. Comerford, R. L. Griffith, B. F. Gerke, M. C. Cooper, J. A. Newman, M. Davis, and D. Stern. 1.75 h $^{-1}$ kpc Separation Dual Active Galactic Nuclei at z = 0.36 in the Cosmos Field. *Astrophys. J. Lett.*, 702:L82–L86, September 2009. 5.1

[370] R. S. Barrows, D. Stern, K. K. Madsen, F. A. Harrison, M. C. Cushing, C. D. Fassnacht, R. L. Griffith, A. H. Gonzalez, J. D. Kirkpatrick, and D. J. Lagattuta. A Candidate Binary Black Hole System at z=1.175. In *American Astronomical Society Meeting Abstracts #217*, volume 43 of *Bulletin of the American Astronomical Society*, pages #430.12–+, January 2011. 5.1

[371] U. Munari, A. Henden, S. Kiyota, D. Laney, F. Marang, T. Zwitter, R. L. M. Corradi, S. Desidera, P. M. Marrese, E. Giro, F. Boschi, and M. B. Schwartz. The mysterious eruption of V838 Mon. *Astronomy and Astrophysics*, 389:L51–L56, July 2002. 5.1

[372] Stephan Rosswog. Astrophysical Smooth Particle Hydrodynamics. *New Astron.Rev.*, 53:78–104, 2009. 5.1

[373] S. Rosswog. Conservative, special-relativistic smoothed particle hydrodynamics. *J.Comput.Phys.*, 229:8591–8612, 2010. 5.1

[374] S. Rosswog. Special-relativistic Smoothed Particle Hydrodynamics: a benchmark suite. 2010. arXiv:astro-ph.IM/1005.1679. 5.1

[375] Stephan Rosswog. Relativistic smooth particle hydrodynamics on a given background spacetime. *Class.Quant.Grav.*, 27:114108, 2010. 5.1